

SURFACE REACTIVITY OF IRON, MANGANESE MINERALS AND THEIR ENVIRONMENTAL IMPLICATIONS

A Dissertation
Submitted
to the Temple University Graduate Board

In Partial Fulfillment
of the Requirements for the Degree of
Doctor of Philosophy

By
Soujanya Singireddy
August, 2013

Examining Committee Members:

Dr. Daniel R. Strongin, Research Advisor and Committee Chair, Chemistry
Dr. Frank C. Spano, Committee member, Chemistry
Dr. Michael J. Zdilla, Committee Member, Chemistry
Dr. Huichun (Judy) Zhang, external Committee Member, Civil and
Environmental Engineering

©
Copyright
2013

by

Soujanya Singireddy
All Rights Reserved

ABSTRACT

The focus of the thesis research was to investigate the surface reactivity of three different minerals, pyrite (FeS_2), an ordered form of ferrihydrite (an iron oxyhydroxide phase), and birnessite (MnO_2), toward environmentally relevant aqueous reactants. In particular, research was carried out with the goals of 1) understanding the redox chemistry of nitrite (NO_2^-) and nitrate (NO_3^-) on pyrite and 2) understanding the redox (photo) chemistry of arsenite (AsO_2^- , As(III)) on ordered ferrihydrite and birnessite. A motivation for all these studies stemmed in part from the recognition that NO_2^- , NO_3^- , and As(III) are all environmental pollutants when they are present at sufficiently high concentration in the environment. The removal of these species or conversion of each of them on mineral surfaces to more benign chemical species is of importance in the realm of environmental chemistry. In the case of NO_2^- and NO_3^- on pyrite, an additional and primary motivation for the research was that it has been hypothesized in the “origin-of-life” community that the reaction of NO_2^- and NO_3^- with iron sulfide (e.g., pyrite) may have played a role in the production of ammonia (NH_3) on early Earth. Such prebiotic chemistry had been hypothesized to an essential step in the production of biomolecules that included proteins.

With regard to the NO_2^- reaction with pyrite, results detailed in this thesis showed that ammonia in $\mu\text{mol/kg}$ quantities could be produced by reacting NO_2^- in the presence of pyrite under anaerobic conditions. The concentration of NH_3 (detected as ammonium, NH_4^+ , in solution) was a strong function of the reaction temperature. At the lower temperatures studied (22°C and 70°C), a small amount of NH_4^+ was formed, but $\mu\text{mol.kg}^{-1}$ amounts of NH_4^+ were formed at a reaction temperature of 120°C . Only about 5% of the initial NO_2^- concentration was converted to NH_4^+ . In the $\text{NO}_3^-/\text{pyrite}$ system, the

NO_3^- reactant concentration remained unchanged at all the three reaction temperatures studied, consistent with the low amounts of NH_4^+ formed in these experiments. Finally, it was shown using in situ infrared spectroscopy that surface-bound NO formed on pyrite during the conversion of the nitrogen oxides to ammonia. Overall, it was shown that the kinetics of NH_4^+ formation was slower for NO_3^- than that observed for NO_2^- .

Studies presented in this thesis that focused on the surface reactivity of As(III) on ordered ferrihydrite and birnessite nano particles showed that As(III) could be oxidized to arsenate (referred to as As(V)) in the presence of simulated solar radiation. In the ordered ferrihydrite circumstance the adsorption of As(III) and photo-induced oxidation to As(V) was compared to the same reaction on the more disordered and smaller ferrihydrite particles (known as “2-line” ferrihydrite). A comparison of the adsorption rate of As(III) on the two surfaces in the presence of light after normalizing for differences in surface area showed that the ordered ferrihydrite exhibited a higher arsenic adsorption rate. Also, the oxidation rate of As(III) to As(V) in the presence of light on the ordered ferrihydrite showed a strong dependence on the amount of dissolved oxygen in solution while the oxidation rate on the more disordered form showed no such dependence. It was proposed that differences in the rates of the heterogeneous oxidation rate of ferrous iron with dissolved oxygen on the two surfaces were the reason for this behavior.

Finally, the photo-induced oxidation of As(III) to As(V) on Na- and K-birnessite at solution pHs of 5.0 and 7.4 was investigated. It was shown that the oxidation rate of As(III) to As(V) occurred at a faster rate on birnessite in the presence of light when compared to the same system in the dark. Mn(II) formed during the reductive dissolution of birnessite during the oxidation of As(III) was experimentally observed at pH 5.0, but not at pH 7.4. Experiments were also conducted that investigated the reductive dissolution of Na- and K-birnessite (having different sizes and average oxidation states) by As(III) under more alkaline conditions. These experiments were conducted at pH 8.5

and the post-reaction samples were analyzed with X-ray diffraction (XRD) and X-ray photoelectron spectroscopy (XPS). It was shown under these alkaline conditions using X-ray diffraction that structural changes occurred in/on both the Na- and K-birnessite during the As(III) oxidation reaction.

ACKNOWLEDGMENTS

First and foremost I wish to acknowledge my thesis advisor and mentor Dr. Daniel Strongin, who constantly guided and supported me throughout my PhD. His approach towards research, understanding and expertise motivated me all throughout my graduate career. His working style had always given me the intellectual freedom and enhanced my scientific curiosity. I cherish the moments spent working with him and I thank him for being such a great mentor.

I wish to thank my graduate committee members Dr. Frank Spano and Dr. Michel Zdilla for their constant support and valuable suggestions, guidance, and willingness to serve on my doctoral dissertation committee. I thank Dr. Zdilla for helping me gain the knowledge and expertise about XRD instrument. I would like to thank Dr. Huichun (Judy) Zhang for her willingness to serve on my doctoral dissertation committee. I would like to thank our research collaborators Dr. Martin Schoonen, Dr. Alex Smirnov, Dr. Richard Reeder, Dr. Robert Szilagy, and Dr. Mike Vince. I really appreciate their help in reviewing my manuscripts. I thank Dr. Charlie Johnson, Department of Physics, University of Pennsylvania for giving me an opportunity for a visit to his lab.

I wish to convey my warm love and gratefulness to my family, Murali (Venkat), Kamala, Satya reddy, Bhoom reddy, Bharathi, Raju, Abhi, Archana, Bakkavva, Kavita (Lavanya), Mutyam reddy, Indira, Malla reddy, and Rajita. I also appreciate my family members Vijaya, Vishnuvardhan Rao, Sharma, Sumona, Sai, Ram and Priya for their concern and love. I cannot forget losing my grandmother (Ramavva) during my 3rd year of PhD. She was a constant support all throughout my life.

I thank my friends Kapila, Sandya, Kittu, Pramida, Shilpa, Raghu, Archu, Srujana, Guna, Sudheshna, Swetha, Ramya, Kiranmayi, Sudha aunty, and Bhaskar Uncle. I would like to thank Sushma, Srikanth, Sharvan, Swapna, Lavanya, Mohit, Sudipto, and all my friends at Temple University. I also thank Dr.Sudeep Debnath and Sandeep for initial studies on birnessite reductive dissolution.

I feel fortunate to have interaction with Dr. Goutham Kodali, Dr. Gilbert, Dr. Madhavan Narayanan (Maddy), Dr. Michel, Dr. Mascavage, Dr.Vassil, Dr. Muruganandam (Murugan), Dr. Gangadhar Andaluri, and Dr. Rominder Suri. I appreciate their help through different phases of my graduate studies. I am indebted to my high school teachers Laxmirajam, Srinivas, Nagabushanam, Indrasena Reddy, and Saleem Khan, college teachers Upender Reddy, V.V.S Moorthy, Dr. Sarbani Pal, Dr. Srinivas Reddy (Principal Sir), Dr. Sarita Rajender, Praveen Reddy, Srinivas Reddy, and Mamata.

I also wish to express my appreciation to my fellow graduate students Riley Murphy, Kristin, Andro, Sam, Leanne, Amber, Narayan, and Liz. I would like to thank NSF for providing financial support to the transmission electron microscopy (grant # CHE-0923077), partial support for the birnessite research. I would like to acknowledge Brookhaven National laboratory for allowing us to use the National Synchrotron Light Source (D.O.E. grant # DE-AC02-98CH10886). I would like to thank the Department of Chemistry at Temple University for their financial support through teaching and research assistantships and providing an opportunity to pursue my graduate studies.

Overall I feel nothing is possible without the blessings of “*Shirdi Saibaba*” to whom I owe everything.

DEDICATION

“I dedicate this dissertation to my dear husband *Venkata Muralidhar Velvadapu* and my parents *Kamala, Satyareddy*, who supported me at every moment of my life”.

TABLE OF CONTENTS

	PAGE
ABSTRACT.....	iii
ACKNOWLEDGMENTS	vi
DEDICATION.....	viii
LIST OF TABLES.....	xiv
LIST OF FIGURES	xv
LIST OF SCHEMES.....	xxi
CHAPTER	
1. INTRODUCTION	1
1.1. Redox reactions at mineral surfaces	1
1.2. Environmental pollutants.....	3
1.3. Nitrite and nitrate in the environment.....	4
1.4. Heavy metal pollutants in the environment.....	5
1.5. Remediation methods.....	6
1.6. Why iron and manganese minerals	6
1.7. Importance of NO_2^- and NO_3^- remediation	8
1.8. Arsenic in the environment.....	9
1.9. Importance of arsenic remediation.....	10
1.10. Overview of photochemistry.....	12

1.11. Organization of the thesis	13
1.12. References.....	16
2. EXPERIMENTAL METHODS.....	21
2.1. Materials	21
2.1.1. Chemicals.....	21
2.1.2. Minerals	22
2.1.2.1. Pyrite	22
2.1.2.2. Synthesis of ferrimagnetic ferrihydrite or ordered ferrihydrite	22
2.1.2.3. Synthesis of birnessite.....	23
2.2. Instrumental methods and experimental setup.....	23
2.2.1. Xenon lamp (simulated solar light source)	25
2.2.2. Attenuated total reflection-fourier transform infrared (ATR-FTIR) spectroscopy.....	26
2.2.3. Batch experiments.....	30
2.2.4. Ion exchange chromatography (IC)	34
2.2.5. Brauner-Emmett-Teller (BET) surface area analyzer.....	35
2.2.6. UV-Visible spectroscopy	36
2.2.7. Gas chromatography	37
2.2.8. Fluorescence spectroscopy.....	38
2.2.9. X-ray diffraction (XRD)	39
2.2.10. Transmission electron microscopy (TEM)	40
2.2.11. Quick x-ray absorption spectroscopy (QXAS)	41
2.2.12. X-ray photoelectron spectroscopy (XPS)	43
2.2.13. Atomic absorption spectroscopy (AAS)	45

2.3. References.....	46
3. REDUCTION OF NITRITE AND NITRATE ON PYRITE	51
3.1. Introduction.....	51
3.2. Results and discussion	54
3.2.1. Kinetic data associated with the reduction of aqueous NO_2^- and NO_3^- on pyrite	55
3.2.2. Density functional theory (DFT) modeling of surface bound nitrogen oxide species.....	64
3.2.3. ATR-FTIR of NO_2^- (aq) adsorption on FeS_2	69
3.2.4. ATR-FTIR of NO_3^- (aq) adsorption on FeS_2	76
3.3. Mechanistic implications	78
3.5 Conclusions.....	79
3.6 References.....	81
4. PHOTO-OXIDATION AND ADSORPTION OF ARSENIC BY FERRIMAGNETIC FERRIHYDRITE OR ORDERED FERRIHYDRITE	85
4.1. Introduction.....	85
4.2. Structural models for ferrihydrite	86
4.3. Motivation behind using Ferrifh as a substrate for arsenic redox chemistry..	88
4.4. Characterization of Ferrifh.....	88
4.5. Results and discussion	92
4.5.1. ATR-FTIR experiments	92
4.5.2. Batch experiments.....	97
4.6. Comparison of the mechanism of the CB-, CF-Ferrifh, and 2-line Fh with As(III) in presence of light.....	105
4.7. Comparison of the reactivity of the CB-, CF-Ferrifh, and 2-line Fh with As(III) in presence of light.....	108
4.6. References.....	111

5. LIGHT INDUCED OXIDATION OF ARSENIC BY BIRNESSITE.....	113
5.1. Introduction.....	113
5.2. Prior investigation on As(III) oxidation by birnessite	115
5.3. Characterization of Na-birnessite	119
5.4. Results and discussion	121
5.4.1. Effect of light on the redox chemistry of As(III) on birnessite at pH 5.00.....	122
5.4.2. Effect of light on the redox chemistry of As(III) on birnessite at pH 7.40.....	129
5.4.3. Effect of dissolved O ₂ on As(III) oxidation by birnessite in presence of light.....	134
5.4.4. Detection of ROS formed during the photo-oxidation of As(III) in presence of Na-birnessite	137
5.5. Reaction mechanism	144
5.6. Summary	146
5.7. References.....	149
6. REDUCTIVE DISSOLUTION OF BIRNESSITE BY ARSENITE- AT HIGH PH - XRD STRUDY	155
6.1. Introduction.....	155
6.2. Characterization of synthesis of K-and Na-birnessite	158
6.3. Results and discussion	162
6.3.1. Batch experiments	162
6.3.2. Compositional changes in k- and na-birnessite during the exposure to As(III)	165
6.3.3. Morphological and structural changes in K- and Na-birnessite during the exposure to As(III)	169
6.4. Summary and conclusion.....	173

6.5. References.....	174
7. SUMMARY.....	178
BIBLIOGRAPHY.....	181

LIST OF TABLES

Table	Page
1.1. Common forms of iron sulfides, oxides and manganese oxides and their abundance in the environment	7
1.2. Countries affected by arsenic contamination and maximum permissible concentration.....	11
3.1. Calculated and experimental vibrational frequencies of the intermediates and the products formed during NO_2^- and NO_3^- reduction on FeS_2 surface at 70°C and 120°C	75
6.1. Relative proportions of various Mn oxidation states in the near surface region of K- and Na-birnessite before, after the reaction with As(III) for 15 min and 1 h at pH 8.5 obtained from Mn $2p_{3/2}$ XPS spectra analysis. Relative proportions of As(III), As(V) in the near surface region of K and Na-birnessite after reaction with As(III) for 15 min and 1 h at pH 8.5 obtained from As 3d XPS spectra analysis	167

LIST OF FIGURES

Figure	Page
1.1. Processes involved during the transformation of a reactant to product on a mineral surface.....	3
2.1. List of different techniques used in this study	25
2.2. The spectral output of the light coming from the Xe lamp used in this study after passing through the Pyrex glass, which was analyzed using a BRC111A high CCD spectrometer (B& W TEK, Inc.). Adapted from reference ³⁰	26
2.3. Schematic of the Ge multi bounce (left figure) and Diamond single bounce (right figure) ATR.....	29
2.4. Image of the smart orbit diamond ATR accessory, mounted on a Nicolet Magna 750 FTIR spectrometer was shown with the flow reaction cell and the syringe pumps, which were used to conduct the in-situ ATR-FTIR flow experiments. One syringe pumps the required [As(III) or As(V)] solution into the reaction cell placed on the diamond ATR, while the other syringe draw the solution from the same reaction cell, during which a constant pH is maintained.....	31
2.5. Image showing the batch experimental setup using pH STAT titrino and Xenon lamp. pH STAT titrino was used to maintain the required solution pH.....	33
2.6. Energy diagram showing the absorption of the X-rays and simultaneous emission of the fluorescence photon and auger electron.....	43
3.1. Batch experimental data showing NO ₂ ⁻ reduction to NH ₄ ⁺ in presence of pyrite at 22°C, 70°C and 120°C. (Blank experiments are shown as single data points)	56
3.2. Batch experimental data showing NO ₃ ⁻ reduction to NH ₄ ⁺ in presence of pyrite at 22°C, 70°C and 120°C. (Blank experiments are shown as single data points)	57
3.3. Concentration of NO ₂ ⁻ reactant and NO ₃ ⁻ product as a function of time when the pyrite containing reaction solution is at a temperature of (a) 22°C, (b) 70°C, and (c) 120°C	60
3.4. First generation coordination chemical model of single iron site in bulk pyrite (all S-S and Fe-S distances are as specified. Trans Fe-S-Fe angles are all 180°)	64

3.5. Computational models for a representative set of surface bound nitrogen oxide intermediates with optimized Fe-N, N-O bond lengths, and Fe-N-O bond angles. Calculated and experimental (in parenthesis) N-O stretching frequencies for the free and coordinated forms	67
3.6. ATR-FTIR spectra obtained during the reaction of NO_2^- with pyrite at room temperature (22°C) after (a) 30 min (b) 60 min (c) 120 min, and (d) 180 min. The vibrational mode at $\sim 1630 \text{ cm}^{-1}$ is due to O-H bending vibrations of water	70
3.7. ATR-FTIR spectra obtained during the reaction of NO_2^- with pyrite at 70°C (Top spectrum) after reaction times of (a) 9 min (b) 30 min (c) 130 min, and (d) 180 min. The vibrational mode at $\sim 1630 \text{ cm}^{-1}$ is due to O-H bending vibrations of water. Bottom spectra is the ATR-FTIR spectra obtained during the reaction of NO_2^- with pyrite at 120°C after reaction times of (a) 30 min (b) 60 min (c) 120 min, and (d) 180 min. The vibrational mode at $\sim 1630 \text{ cm}^{-1}$ is due to O-H bending vibrations of water	72
3.8. Top spectra is the ATR-FTIR spectra obtained during the reaction of NO_3^- with pyrite at 70 °C after reaction times of (a) 9 min (b) 30 min (c) 130 min, and (d) 180 min. The vibrational mode at $\sim 1630 \text{ cm}^{-1}$ is due to O-H bending vibrations of water. Bottom spectra ATR-FTIR spectra obtained during the reaction of NO_3^- with pyrite at 120 °C after reaction times of (a) 30 min (b) 60 min (c) 120 min, and (d) 180 min. The vibrational mode at $\sim 1630 \text{ cm}^{-1}$ is due to O-H bending vibrations of water	77
4.1. ATR-FTIR spectra of the citrate bound and citrate free ferrifh. ATR-FTIR spectrum of the 2 line fh was shown for comparison	89
4.2. X-ray diffraction pattern of the citrate bound (before Ozone cleaning) and citrate free (after Ozone cleaning) ferrifh, showing that the structure and particle size of the ferrifh was not changed after Ozone cleaning	91
4.3. TEM micrograph of the citrate bound ferrifh (a), TEM micrograph of the citrate free ferrifh (b)	92
4.4. ATR-FTIR spectrum showing the As(III) and As(V)-O stretching modes obtained when citrate bound and citrate free ferrifh was exposed to 0.41 mM As(III), 5 mM NaCl solution at pH 5.00. 0 h spectrum in both the cases was obtained after the 24 h exposure of citrate bound ferrifh to As(III) in dark. In case of citrate bound ferrifh the subsequent spectra were collected after 0.5, 1, 2, 3, 4, 6, and 7 h of light irradiation. Inset shows the desorbed carbonate and citrate modes observed, when the clean citrate bound ferrifh spectrum was subtracted from ferrifh exposed to As(III) before light irradiation (top) and the citrate bound ferrifh exposed to light for 7 h (bottom). Negative modes are desorbed citrate and carbonate modes. The subsequent spectrum in case of citrate free ferrifh were collected after 0, 0.5, 1, 2, 3, and 4 h of As(III) exposure in presence of light. Inset shows the difference	

spectrum obtained after the subtraction of 0 h dark spectrum and the 4 h light spectrum from the clean fh spectrum. The negative modes at 1472 and 1355 cm^{-1} are the desorbed carbonate modes, which were replaced by As(III) or As(V) during the As(III) exposure94

4.5. Top spectrum shows the ATR-FTIR spectrum of As(V)-O stretching modes obtained when citrate bound ferrifh was exposed to 0.41 mM As(V), 5 mM NaCl solution in dark at pH 5 for 0.5, 1, 2, 3, 4 and 5 h. Bottom spectrum shows the ATR-FTIR spectrum of As(V)-O stretching modes at 838, 880 cm^{-1} obtained when citrate free ferrifh was exposed to 0.41 mM As(V), 5 mM NaCl solution for 0.5, 1, and 4 h in dark96

4.6. Amount of As(V) formed in solution when 470 μM of aqueous As(III) solution was exposed to simulated solar light at pH 5.0098

4.7. The amount of arsenic adsorbed in mole.kg⁻¹ on CB-Ferrifh (top plot), when exposed to As(III) in dark (closed circles), in presence of light (closed diamonds), in presence of light under anoxic conditions (closed triangles), and As(V) exposure in dark (closed squares). The amount of arsenic adsorbed on CF-Ferrifh (bottom plot), when exposed to As(III) in dark (open circles), in presence of light (open diamonds), and in presence of light under anoxic conditions (open triangles).99

4.8. The amount of As(V) released into the solution when CB-Ferrifh was exposed to As(III) , in dark (closed circles), in presence of light (closed diamonds), and in presence of light under anoxic conditions (closed triangles). There is no As(V) released into the solution when CF-Ferrifh was exposed to As(III) (bottom plot), in dark and in presence of light under anoxic conditions indicated with open triangles. Open diamonds represent the amount of As(V) released when CF Ferrifh was exposed to As(III) in presence of light100

4.9. Normalized K-edge XANES data of the arsenite, arsenate adsorbed on CF-Ferrifh in dark, and the As(III) and As(V) adsorbed on CF-Ferrifh, when exposed to As(III) or As(III) for 8h. All these spectra were collected in Q-EXAFS mode. XANES spectra of As(III) and As(V) aqueous solutions were used as oxidation state references.101

4.10. The amount of Fe(II) released in μM when CB-Ferrifh is exposed to As(III) , in presence of light, absence of dissolved O₂ (closed triangles), in presence of dissolved O₂ (closed diamonds). Closed circles represent the Fe(II) released into the solution, when CB-Ferrifh was exposed to light in the absence of As(III) and dissolved O₂. Open triangles represent the amount of Fe(II) released into the solution when CF Ferrifh was exposed to As(III) in presence of light and the absence of dissolved O₂, Open diamonds represent the Fe(II) released when the CF Ferrifh was exposed As(III) in the presence of light and dissolved O₂ and the closed circles represent the Fe(II) released when CF Ferrifh was exposed to light in the absence of As(III), and dissolved O₂.103

4.11. The figure represents the surface area normalized total As adsorption on CB- and CF-Ferrifh, and 2-line Fh, when exposed to 0.41 mM of As(III), 5 mM NaCl solution in presence of light for 8 h at pH 5. The bottom figure illustrates the comparison between the total amount of As(V) released into the solution, when CB and CF-Ferrifh, and 2-line Fh was exposed to 0.41 mM of As(III) in 5 mM NaCl, in presence of light for 8 h at pH 5. These amounts are normalized according to the surface area of the respective minerals.	109
5.1. Layers structure of birnessite showing the inter layer cations Na ⁺ and K ⁺ , with an interlayer spacing of 7 Å.....	114
5.2. UV-Vis absorption spectrum of the Na-birnessite.....	118
5.3. X-ray powder diffraction pattern of synthetic Na-birnessite	120
5.4. TEM image of the clean Na-birnessite	121
5.5. The amount of arsenate released into the solution during the oxidation of 470 μM of As(III) at pH 5.00 as a function of time in dark (closed diamonds) and light (open diamonds). The amount of As(V) that was released into solution during the oxidation of As(III) by Na-birnessite in the absence and presence of light at pH 5.00, under anoxic conditions is shown with closed and open circles respectively. The inset shows the amount of arsenic adsorbed on the birnessite during the oxidation of As(III) under dark (closed diamonds) and light (open diamonds) conditions.....	123
5.6. The concentration of dissolved Mn ²⁺ released during the oxidation of 470 μM of As(III) by Na birnessite at pH 5.00 in presence of light, oxic (open triangles), light, anoxic (open diamonds), dark, oxic (closed triangles), dark, anoxic (closed diamonds) as a function of time.....	124
5.7. Bottom spectrum shows the X-ray diffraction pattern of the Na birnessite before reacting with As(III) and top spectrum shows the X-ray diffraction pattern of the Na birnessite after reaction with arsenite at pH 5.00. Completer transformation of triclinic Na-birnessite to hexagonal H-birnessite was observed after the reaction. For clarity reflections and d-spacings of the both birnessite samples were shown in the Figure. X-ray diffraction patterns of the birnessite reacted with arsenite at pH 5.00 is same both in dark and in presence of light. Hence, only images of the birnessite reacted in light was shown for clarity.....	126
5.8. TEM images of the Na-birnessite particles reacted with Arsenite at pH 5, (a) 8 h in dark, (b,c) 8 in light, and (d) 48 h in dark. (e) and (f) are the TEM images of the Na-birnessite particles reacted with As(III) for 8 h at pH 7.4 in the absence and presence of light respectively. Etching of the particles was shown with the arrows and circles	128

5.9. The amount of As(V) released into the solution during the oxidation of As(III) at pH 7.40 in dark (closed diamonds), in light (open diamonds) as a function of time. The amount of As(V) that was released into solution during the oxidation of As(III) by Na-birnessite in the absence and presence of light at pH 7.40, under anoxic conditions is shown with closed and open circles respectively. Inset shows the concentration of arsenic adsorbed at pH 7.40 during As(III) oxidation in dark (closed diamonds), light (open diamonds). The initial concentration of As(III) used was 470 μM	129
5.10. Arsenic K-edge EXAFS spectrum of the Na-birnessite exposed to As(III)/As(V) for 8 h. As K-edge spectrum of the As(III) and As(V) solution were used as the reference. (All the plots were offset for clarity).	131
5.11. (a) XRD pattern of the un reacted Na-birnessite, (b) XRD pattern of the Na-birnessite exposed to Mn^{2+} for 1h at pH 7.40, (c) XRD pattern of the Na-birnessite reacted with As(III) in dark at pH 7.40, and (d) XRD pattern of the Na-birnessite reacted with As(III) at pH 7.40 in presence of light. Arrows indicates the peaks, which reduced in intensity, while stars indicate the peaks, which are growing during the reaction of Na-birnessite with As(III).	132
5.12. XRD pattern of the Na-birnessite exposed to 80 μM of Mn^{2+} solution for different time intervals. The peaks which are growing with time indicated as stars and peaks which are disappearing with time are indicated with arrows. (All the plots were offset for clarity).	134
5.13. Relative intensity of the OH radicals formed in presence of birnessite, light, and dissolved O_2 (open circles), birnessite, light, in the absence of dissolved O_2 (open reverse triangles), birnessite, dark, dissolved O_2 (closed triangles), Birnessite, As(III), light, and dissolved O_2 (open squares), APF and light (Open diamonds) .	138
5.14. The fluorescence intensity of the OH radicals observed when the birnessite was irradiated with light and the probe APF was added ex-situ	139
5.15. Concentration of H_2O_2 observed when the probes HRP and APF were added to the Na-birnessite suspension and irradiated with light (closed diamonds). Open diamonds indicate the H_2O_2 formed in control experiment where the probes HRP and APF were added to the phosphate buffer and irradiated with light	140
5.16. Concentration of H_2O_2 formed in presence of birnessite, light, and dissolved O_2 (open diamonds), in presence of birnessite, light, and in the absence of dissolve O_2 (diamonds with cross hairs), in presence of birnessite, in the absence of light (closed diamonds), in presence of birnessite, light, As(III) (open circles)	141
5.17. Amount of Mn^{2+} released into the solution when 200 μM of H_2O_2 was added to Na-birnessite (0.10g/L H_2O) at pH 5.00 and stirred in dark (Without irradiating the light)	143

5.18. Concentration of H ₂ O ₂ remained in solution when 200 nM H ₂ O ₂ was exposed to Na-birnessite at pH 7.40 for 4 h.....	144
6.1. X-ray diffractograms of K- and Na-birnessite	159
6.2. Mn 2p _{3/2} XPS spectra of (a) K-birnessite and (b) Na-birnessite.....	160
6.3. TEM micrographs of unreacted K- birnessite (a) and Na-birnessite (b)	161
6.4. Results from batch experiments of As(III) oxidation by birnessite: Open diamonds and open triangles indicate the As(V) released into the solution during the oxidation of As(III) over a 24 h period at pH 8.5, in presence of K- and Na-birnessite respectively. Inset shows the amount of arsenic adsorbed on K- (solid diamonds) and Na- (solid triangles) birnessite during As(III) oxidation over a 24 h period ...	163
6.5. Mn 2p _{3/2} XPS spectra after K-birnessite is exposed to As(III) for (a) 15 min and (b) 1 h, and after Na-birnessite is exposed to As(III) for (c) 15 min and (d) 1 h exposure to As(III) at pH 8.5. The spectral contribution due to Mn(IV), Mn(III), and Mn(II) is indicated for each spectrum. The relative proportions of the different Mn oxidation state species after the each As(III) exposure time is listed in Table 6.1.....	165
6.6. As 3d XPS spectra and associated fits after K-birnessite was exposed to As(III) for (a) 15 min and (b)1 h, and after Na-birnessite was exposed to As(III) for (c) 15 min and (d)1 h at pH 8.5. The peak represented with solid lines and the dashed lines is related to As(III) and As(V) respectively. The spectral fitting parameters for the As 3d data is given in the experimental section	168
6.7. X-ray diffraction pattern of the unreacted K-birnessite (bottom), K-birnessite exposed to As(III) for 24 h at pH 8.5 (middle), K-birnessite exposed to Mn ²⁺ for 24 h at pH 8.5 (top). The star at the d-spacing 1.82 Å represents the difference in XRD patterns of the unreacted and reacted samples.....	170
6.8. X-ray diffraction pattern of the unreacted Na-birnessite (bottom), Na-birnessite exposed to As(III) for 24 h at pH 8.5 (middle), Na-birnessite exposed to Mn ²⁺ for 24 h at pH 8.5 (top). The stars indicate the new diffraction peaks developed during the reaction.....	171

LIST OF SCHEMES

Scheme	Page
4.1. Mechanism showing the hole induced oxidation of As(III) by CB- and CF-Ferrifh in presence of light.....	107
4.2. Mechanism showing the citrate induced reduction Fe^{3+} to Fe^{2+} and the oxidation of Fe(II) to Fe(III) and H_2O_2 by dissolved O_2 on CB-Ferrifh in presence of light. During this process citrate was desorbed from the surface (citrate desorption was proposed based on the ATR-FTIR experiments and not studied or quantified the oxidized citrate products using the batch experiments).....	107
4.3. Mechanism of As(III) oxidation by 2-line Fh.....	108
5.1. Mechanism of As(III) oxidation by birnessite in presence of light	145

CHAPTER 1

INTRODUCTION

1.1. Redox Reactions on Mineral Surfaces

Minerals that are abundant in soils and modern sediments have surface characteristics (such as surface charge and particle size), which give them the unique ability to interact with aqueous solutions, gases, and living organisms. Mineral surface reactions play an important role in the sequestration and transport of the chemical elements and pollutants within the environment. In some cases, mineral surfaces adsorb pollutants and oxidize or reduce the adsorbed species via electron transfer.^{2a 14,15} In general, the mineral/aqueous interface has received an increasing amount of interest and the location where chemical reactions take place play a significant role in the control of the composition of environmental waters.^{2a}

Redox reactions of minerals occur on their surface where there is proper physical and chemical interactions of the reactants.^{14, 15, 16} Surface mediated reactions occur when the molecules are adsorbed on the surface of a mineral.^{16, 17} Over the past few decades, a number of spectroscopic and microscopic techniques have seen a rapid development along with the computational methods like density functional theory (DFT) methods to study the products of red-ox reactions.¹⁷

Redox reactions at solid-liquid interfaces involve the following steps,

- a) Adsorption of the reactants to the surface

- b) Formation of the products by the electron transfer between the mineral and the adsorbate
- c) The newly formed products are either desorbed from the surface or remain attached on the surface depending on the interactions between the product and the mineral surface.

A schematic showing the different processes involved during the transformation of a reactant to product on the surface of a mineral are shown in Figure 1.1. The focus of the research presented in this thesis focuses on the surface reactivity and redox chemistry of iron (pyrite, ferrimagnetic ferrihydrite) and manganese (birnessite) bearing mineral phases in the removal of environmental pollutants nitrate (NO_2^-), nitrite (NO_3^-), and arsenic. In short the research is interesting in understanding the oxidation and reduction (red-ox) reactions of the environmental pollutants on the surfaces of these minerals under environmentally relevant conditions.

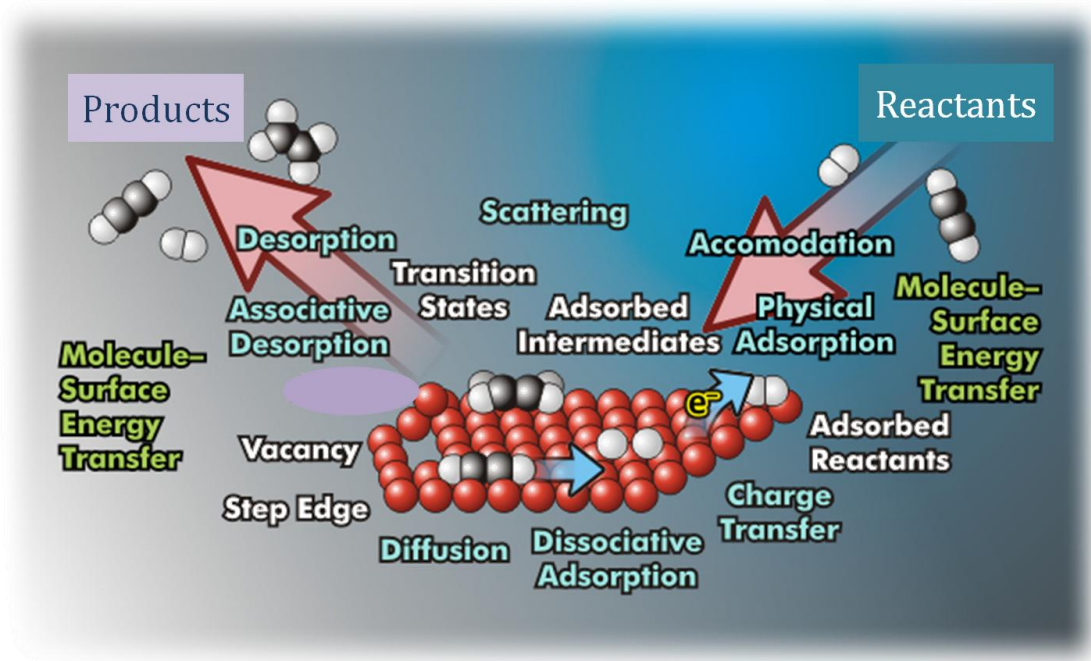


Figure 1.1. Processes involved during the transformation of a reactant to product on a mineral surface.¹⁷

1.2. Environmental Pollutants

Pollutants are the contaminant elements, molecules, or chemical compounds, which are present in sufficient quantities in the environment that affect the health of living organisms.^{1,2} Pollutants pose significant health hazards to humans when inhaled, ingested, or during contact with their skin. Some of these pollutants exist on the Earth's surface and are released into aquatic environments and the atmosphere due to processes such as chemical weathering. A variety of other pollutants also get released into the atmosphere and water by direct or indirect anthropogenic activities.^{1,2a} Improper waste handling and disposal is one such activity that has contributed to a significant raise in the

growth of environmental/water related pollution. One might speculate that these environmental issues will become more prevalent due to the ever increasing global population of industrialized countries.

The spread of environmental pollution is acute in developing countries where the short-sighted view is that environmental regulations impede a rapid economic growth. The long-term reality is not encouraging; for example the World Health Organization (WHO) predicts that about a one fourth of the diseases caused in humans today are due to prolonged exposure to environmental pollutants.^{2b} The bottom line is that while industrialization has been key to the improvement of living conditions for countries, it has also led to increased pollution that has lessened the supply of clean air and water to many societies. Consequently, new methods for the treatment and remediation of harmful environmental pollutants are needed.

There are different kinds of pollutants that exist in the environment. The research presented in this thesis has been divided into two parts. The first part of the thesis presents the remediation of the aqueous pollutants nitrite and nitrate, while the second part discusses the remediation of arsenic, a metalloid pollutant.

1.3. Nitrite and Nitrate in the Environment

Through microbial reduction of dinitrogen (N_2), aqueous NO_2^- and NO_3^- enter the surface and ground waters due to the use of fertilizers, rodenticides, concentrated livestock, and poultry farming.⁵ NO_2^- and NO_3^- are also naturally present in the environment. Microbes convert nitrogen to NO_3^- , which in turn is utilized by plants.^{25, 26,}

²⁷ Animals consume the plants and excess NO_3^- is eliminated in animal feces. Microbial degradation of dead plants and animals also introduces NO_3^- into the environment. Microbes can also convert NO_3^- and NO_2^- to nitrogen in the environment, as a part of the nitrogen cycle, and prevent accumulation of excessive NO_3^- or NO_2^- in the environment. The kinetics of these natural processes are often slow, thus allowing these pollutants to find their way into the ecosystem.^{26, 27} Also, NO_3^- and NO_2^- enter the surface and ground waters from runoff of fertilizers, rodenticides, concentrated livestock, and poultry farming leading to the increased concentrations of these species in the environment.

1.4. Heavy Metal Pollutants in the Environment

Metals with an atomic density greater than 6 g/cm^3 are referred to as heavy metals.³ Compared to other pollutants, heavy metal pollutants are difficult to remove from a contaminated environment and instead accumulate in the ecosystem posing severe health risks to humans.³ Some of the common heavy metal pollutants found in water in environmental settings are As, Cr, Se, Zn, Hg, and Pd. Certain heavy metals like Zn and Cr are essential elements for the human body in small quantities³, but are poisonous when present in large amounts. Heavy metals often exist on the Earth's surface in combination with minerals and enter the surface and ground waters by natural and direct/indirect human activities.³ For example, calcite (CaCO_3) contains Pb^{2+} cations⁶ and oxyanions like chromate (CrO_4^{2-} or Cr(VI)),⁷ selenite (SeO_3^{2-} or Se(IV)),⁸ selenate (SeO_4^{2-} or Se(VI)),⁹ arsenite (AsO_3^{2-} or As(III))¹⁰ and arsenate (AsO_4^{3-} or As(V))¹¹. These oxyanions replace CO_3^{2-} groups in calcite and upon dissolution of the calcite, the heavy

metals can become mobilized. Arsenic exists abundantly in nature in the form of arsenopyrite. Pyrite can accommodate significant amounts (upto 10 wt %) of arsenic¹² and As(III) is released from this arsenopyrite via dissolution processes like those occurring during acid mine drainage¹³. In general, the heavy metal pollutants enter the human body via consumption of contaminated ground or surface water. The short and/or long term exposure of these heavy metal pollutants can lead to various organ damage, nervous system failure, and cancer in humans.

1.5. Remediation Methods

There are various strategies that have developed over the years for the remediation of these pollutants. Strategies include the adsorption and oxidation/reduction of these pollutants on mineral surfaces.^{2a} Mineral carbonates, sulfates, phosphates, metal sulfides, oxides, and oxyhydroxides can transform toxic pollutants to lesser or non-toxic forms through redox reactions and also act as sorbents of the pollutants.³ In the context of environmental remediation, the research presented in this thesis mainly investigated 1) the chemistry of NO_2^- and NO_3^- on an iron sulfide mineral (pyrite) and 2) the chemistry of arsenic bearing oxyanions on iron oxyhydroxide (ferrihydrite) and manganese oxide (birnessite) mineral phases.

1.6. Why Iron and Manganese Minerals?

Iron and manganese are the first and third most abundant elements in the Earth's crust, respectively and are believed to naturally catalyze various chemical and biological reactions in the environment.¹⁸⁻²¹ The cations that are associated with naturally occurring iron and manganese minerals occur in variable oxidation states that include Fe(II) and Fe(III) for iron bearing minerals and Mn(II), Mn(III), and Mn(IV) for the manganese bearing minerals. Pyrite (FeS_2), also referred to as "fools gold", is one of the iron minerals of interest in this thesis. This iron sulfide is characterized by a disulfide bond and is the most abundant iron mineral on the Earth's surface. Pyrite is abundant in terrestrial sediments, marine environments and also in hydrothermal vents on the oceanic floor. This latter environment has even been postulated to have facilitated chemistry relevant to the origin of life.^{22,23,24} A second iron bearing mineral discussed in this thesis is Ferrimagnetic ferrihydrite (Ferrifh) which was investigated in the context of arsenic remediation. Ferrifh is an ordered form of ferrihydrite, which is also an abundant and nano-dimensioned mineral in the soil environment. With regard to manganese minerals, birnessite, a manganese oxide mineral was investigated. Birnessite is found in Mn-rich ore deposits and is formed by precipitation in oceans and ground water. The surface chemistry of this manganese based mineral showed good potential applications in the areas of bio-inorganic, alternative energy, and environmental remediation.²⁰

Some commonly occurring forms of iron and manganese minerals on the Earth's crust are shown in Table 1.1.

Table 1.1. Common forms of iron sulfides, oxides and manganese oxides and their abundance in the environments.¹⁸⁻²¹

	Fe sulfides	Fe oxides	Mn oxides
Occurrence	Anoxic environments, hydrothermal vents, terrestrial sediments, and marine environments	Common in soils subjected to prolonged weathering or in subsoils/aquifers	Occur together with Fe oxides at a lower abundance
Common forms	Pyrite (FeS_2) Pyrrhotite (Fe_{1-x}S) Mackinawite (Fe_{1+x}S)	Ferrihydrite ($\text{Fe}_{10}\text{O}_{14}(\text{OH})_2$) Goethite (α - FeOOH) Hematite (α - Fe_2O_3)	Birnessite (δ MnO_2)

The objective of this thesis is two-fold. First, research is designed to develop a microscopic picture of the surface reactivity of the above mentioned iron and manganese mineral phases toward arsenic, NO_2^- and NO_3^- . Second, a goal of the research is to use the microscopic understanding to help develop methods for the remediation of harmful environmental pollutants utilizing pyrite, ferrihydrite, and birnessite minerals.

1.7. Importance of NO_2^- and NO_3^- Remediation

NO_3^- that enters the human body is generally non-toxic. However, when it is converted to NO_2^- it can then react with hemoglobin in the blood, thus forming methemoglobin.^{26,27} Methemoglobin is ineffective in the transportation of oxygen from the lungs to the body tissues and cannot bind to oxygen, which is of course the primary function of hemoglobin.

Conversion of the NO_2^- and NO_3^- occurs at high pH.²⁶ Infants and children have a greater risk of accumulation of nitrite in their body as the pH of their gastrointestinal tract is higher than that of adults. Also, long term exposure causes increased urination and hemorrhage of the spleen.²⁶ According to the environmental protection agency (EPA), the maximum allowed concentration of NO_2^- and NO_3^- in drinking water is 10 and 1 ppm, respectively. Unfortunately, due to natural processes and anthropogenic activities, the concentration of these species can exceed the EPA recommendation and thus methods are needed for the remediation of NO_2^- and NO_3^- .²⁶

Results presented in this thesis show that pyrite can potentially be used as a substrate to remove NO_3^- and NO_2^- from water. In particular, it will be shown that the adsorption of NO_3^- and NO_2^- species on pyrite under specific experimental conditions results in NH_4^+ formation. The importance of NO_3^- and NO_2^- chemistry on pyrite also has relevance in a very different arena. In particular it has been postulated by others that the reduction of NO_3^- and NO_2^- on iron sulfide surfaces may have played a role in ammonia production on a prebiotic early Earth. Results presented later in this thesis help to evaluate the possible role of pyrite in NH_4^+ formation on an early Earth, a process that was presumably essential for the formation of biomolecules such as amino acids and proteins that led to life on Earth.

1.8. Arsenic in the Environment

Arsenic is a metalloid and oxyanion forming element, typically found in ground waters both under oxidized and reduced environments.²⁸ Arsenic is a common ground water pollutant in over 21 countries worldwide, including the United States, Bangladesh,

India, China, and Nepal. In the western United States, high arsenic concentrations (50-48,000 $\mu\text{g/L}$) are known to exist in ground water due to gold, pyrite, uranium ore mining areas, basin fill deposits, and geothermal areas.^{29, 30}

Arsenic in these systems exists mainly in the inorganic oxyanions of arsenite (H_3AsO_3^0 , $\text{pK}_a = 9.2$, As(III)) and arsenate (H_3AsO_4 , $\text{pK}_a1 = 2.19$; H_2AsO_4^- , $\text{pK}_a2 = 6.94$; HAsO_4^{2-} , $\text{pK}_a3 = 11.5$; As(V)).³²⁻³⁵ Even though both oxyanions of these forms are toxic, As(III) is more toxic and mobile than the pentavalent As(V) form. These oxyanions adsorb onto many mineral surfaces, but the adsorption is mainly dependent on pH. Even though both As(III) and As(V) are common in natural waters, As(V) predominates in aerobic waters, while As(III) is the primary species in moderately reducing anaerobic ground waters. In this latter environment, the kinetics of the redox transformation of As(III) to As(V) is very slow.³¹ Arsenic contamination in the ecosystem is mainly due to the use of arsenic containing pesticides, burning fossil fuels, and volcanic eruptions. Methods to remove arsenic from ground and subsurface waters is an active area of scientific interest and is a focus of research in this thesis.

1.9. Importance of Arsenic Remediation

Arsenic severely affects human health, causing neurological and other disorders. Short-term exposure and drinking of arsenic containing water causes esophageal, abdominal pain, vomiting and diarrhea, while long term-exposure and drinking causes lung, kidney and skin cancer, neurological disorders, nausea, and loss of appetite.³¹ Worldwide, more than 100 million people are affected by arsenic poisoning, hence the development of

treatment methods is needed to achieve arsenic-free water. Even though arsenic removal treatments are generally focused on reducing arsenic to undetectable levels, the World Health Organization has set a maximum allowed concentration of arsenic in drinking water to be 10 µg/L (10 ppb).^{28, 31}

Table 1.2. Countries affected by arsenic contamination and maximum permissible concentration.³¹

Country	Maximum permissible limits (µg/L)
Bangladesh	50
Nepal	50
India	10
USA	10
China	10
Chile	50
Argentina	50
Mexico	50
New Zealand	10
Taiwan	10
Vietnam	10

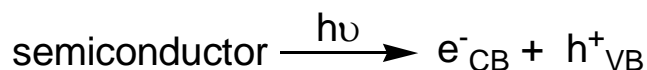
Arsenic removal methods currently in use are based on activated charcoal, TiO₂, iron oxides, iron hydroxides, and manganese oxide (birnessite).³¹ Activated charcoal can remove both As(III) and As(V) from water, but it is expensive and not affordable by poor and developing countries. Metal oxide catalyst such as TiO₂ can effectively remove arsenic from water, but works only in presence of UV light, which is a small component of the solar spectrum. Arsenic can also be removed by adsorption using iron oxides,

oxyhydroxides and manganese oxides (birnessite). Most of these methods work effectively in water containing high concentrations of arsenic (see reference³¹ and references there in), hence finding an effective method to remove arsenic from water containing low arsenic concentrations is still a matter of interest. Methods that can also use sunlight as a source of energy (i.e., photochemistry) to activate (mineral) surfaces for the remediation of environmental pollutants such as arsenic are of interest.

1.10. Overview of Photochemistry

Photoinduced surface chemistry has gained interest in recent years mainly due to its application in degradation of the pollutants present in water and effectively controlling environmental pollution.³⁶ The most ideal method would involve the use of visible light (large part of the solar spectrum) over the use of UV light sources (only a small component of the solar spectrum).

Semiconductors can often drive light-induced redox processes due to photophysical processes that can occur in the valence (VB) and conduction band (CB) of the material.³⁷⁻³⁹ When irradiated with photons having an energy equal to or greater than the band gap of the material, excitation of an electron (e^-) from the filled VB to the empty CB can occur resulting in the creation of a hole (h^+) in the VB.



The h^+ and e^- formed in the semiconductor can migrate to the surface of the material from the bulk³⁷ to the surface and can act as powerful oxidizing and reducing agents, respectively.^{38,39} In the presence of dissolved O_2 , the photoexcited semiconductor can in specific cases reduce the O_2 , resulting in the formation of ROS that include hydroxyl radicals ($\cdot OH$), hydroperoxyl radicals ($\cdot O_2H$) and hydrogen peroxide (H_2O_2). These ROS are strong oxidizing agents. The irradiation of TiO_2 , for example, has been shown to result in the rapid oxidation of aqueous As(III) to As(V) and has been used as a method to remove arsenic from water.⁴⁰⁻⁵¹ TiO_2 , however, only is active in the presence of UV light and thus is a drawback.

Methods that can use visible light as the energy source to activate the semiconductor for photochemical applications have a wider scope. Iron oxides and oxyhydroxides have been shown to adsorb and oxidize arsenic in the absence of light.⁵²⁻⁵⁷ Upon irradiating with visible light, some of these oxides have shown greater arsenic adsorption.^{32,58} Later research presented in this thesis use these results as motivation to study the scope of the reactivity of ferriferous and birnessite in the presence of light.

1.11. Organization of the Thesis

The main objective of this thesis is to understand some fundamental surface chemistry of iron and manganese bearing minerals toward environmentally relevant species. An additional objective of this thesis is to evaluate the use of naturally abundant minerals as useful substrates for the removal of harmful agents present in the environment. This idea has been put forth above with a brief introduction to various

pollutants and the different procedures used for their remediation. The role of minerals and their surface redox chemistry in the environmental remediation process will be shown and the necessity for the remediation of nitrate, nitrite, and arsenic will be stressed. The experimental methods, such as the synthesis and characterization of the minerals, and a brief description of the instrumental techniques used in each study will be explained in chapter 2.

Chapter 3 deals with the adsorption of nitrate and nitrite on the surface of pyrite and the reduction of these species are characterized in situ using attenuated total reflectance Fourier transform infrared spectroscopy (ATR-FTIR). The vibrational modes of these species involved on pyrite surfaces had to be compared on iron oxides and zeolites surfaces. Computational calculations were used to compare and confirm the vibrational modes of the formed species. Also presented in chapter 3 will be the aspect of environmental remediation of NO_3^- and NO_2^- using pyrite, along with the connection of this chemistry to current theories of the evolution of life on Earth.

The photocatalytic oxidation and adsorption and/or oxidation of arsenic by iron oxyhydroxide (ferrimagnetic ferrihydrite) will be discussed in chapter 4. The mechanism of arsenic oxidation and the surface reactivity of ferrimagnetic ferrihydrite (Ferrifh) was studied in the presence and absence of dissolved O_2 . The reactivity and mechanism of arsenic photo-oxidation on Ferrifh will be compared with the reactivity and mechanism of arsenic photo-oxidation and adsorption on 2-line ferrihydrite studied previously by Bhandari et al in 2011.³² The reduction of Ferrifh and simultaneous release of Fe(II) during the arsenic photo-oxidation was studied and compared in presence and absence of dissolved O_2 .

Arsenic photo-oxidation by manganese oxide (birnessite) will be introduced and discussed in chapters 5 at pH 5.00 and pH 7.40. The reductive dissolution of birnessite during arsenic photo-oxidation was studied and compared at two different pH conditions. Mn(II) formed and released or adsorbed onto the surface of birnessite during this process was analyzed with ion chromatography. The primary challenges of this study was to understand the mechanism of As(III) photo-oxidation and to understand the reductive dissolution at pH 7.40. To understand the As(III) photo-oxidation mechanism by birnessite, the formation of ROS were studied, as ROS have been shown to oxidize aqueous phase As(III) in the literature.^{59,60}

It was difficult to prove the reductive dissolution of birnessite during the As(III) photo-oxidation above pH 6.00, as the Mn(II) formed during the reductive dissolution of birnessite was not observed in the solution. However, the understanding of the reductive dissolution of birnessite by arsenic under alkaline conditions, along with the fate of formed Mn(II) from the birnessite, will be discussed in chapter 6 using X-ray photo electron spectroscopy (XPS) and X-ray diffraction (XRD) studies.

1.12. References

- (1) Alloway, B.J.; Ayres, D.C., *Chemical principles of environmental pollution*. Blackie Academic & Professional, London, **1993**, 291 p.
- (2) (a) Brown, G. E. Jr.; Calas, G., *C. R. Geoscience*. **2011**, 343, 90–112. (b) http://www.unep.org/urban_environment
- (3) Akpor, O. B.; Muchie, M., *Int. J. Phys. Sci.* **2010**, 5 (12), 1807-1817.
- (4) Rubasinghege, G. R. S., "Chemical and photochemical reactions on mineral oxide surfaces in gaseous and liquid phases: environmental implications of fate, transport and climatic impacts of mineral dust aerosol." *doctoral dissertation*, University of Iowa, **2011**
- (5) Al-Abadleh, H. A.; Grassian, V. H., *Surf. Sci. Rep.* **2003**, 52 (3-4), 63-161.
- (6) Reeder, R.J., Lamble, G.M., Northrup, P.A., *Am. Mineral.* **1999**, 84, 1049–1060.
- (7) Tang, Y.Z., Elzinga, E.J., Lee, Y.J., Reeder, R.J., *Geochim. Cosmochim. Acta*, **2007**, 71, 1480–1493.
- (8) Aurelio, G., Fernandez-Martinez, A., Cuello, G.J., Roman-Ross, G., Alliot, I., Charlet, L., *Chem. Geol.* **2010**, 270, 249–256.
- (9) Reeder, R.J., Lamble, G.M., Lee, J.F., Staudt, W.J. *Geochim. Cosmochim. Acta*.**1994**, 58, 5639–5646.
- (10) Roman-Ross, G., Cuello, G.J., Turrillas, X., Fernandez-Martinez, A., Charlet, L., *Chem. Geol.* **2006**, 233, 328–336.
- (11) Alexandratos, V.G., Elzinga, E.J., Reeder, R.J., 2007. *Geochim. Cosmochim. Acta*. **2007**, 71, 4172–4187.

- (12) Savage, K.S., Tingle, T.N., O'Day, P.A., Waychunas, G.A., Bird, D.K., *Appl. Geochem.* **2000**, 15, 1219–1244.
- (13) Blanchard, M., Alfredsson, M., Brodholt, J., Wright, K., Catlow, C.R.A., *Geochim. Cosmochim. Acta.* **2007**, 71, 624–630
- (14) Gabor A. Somorjai, Y. L., *Introduction to surface chemistry and catalysis*. 2nd ed.; John Wiley & Sons, Inc.: Hoboken, Newjersey, **2010**.
- (15) Zaera, F., *Surf. Sci.* **2011**, 605 (13-14), 1141-1145.
- (16) Somorjai, G. A.; Li, Y., *Proc. Natl. Acad. Sci. U. S. A., Early Ed.* **2010**, 1-8.
- (17) http://www.bnl.gov/chemistry/programs/Surface_dynamics. In BNL.
- (18) Stone, A. T.; Ulrich, H. J., *J. Colloid Interface Sci.* **1989**, 132 (2), 509-522.
- (19) Summers, D. P., *Origin. Life. Evol. Biosph.* **1999**, 29 (1), 33-46.
- (20) Walker, J. C. G.; Brimblecombe, P., *Precambrian. Res.* **1985**, 28 (3-4), 205-222.
- (21) Zohner, A.; Broda, E., *Orig. Life.* **1979**, 9 (4), 291-298.
- (22) Wächtershäuser, G., *Microbiol. Rev.* **1988**, 52 (4), 452-484.
- (23) Wächtershäuser, G., *Syst. Appl. Microbiol.* **1988**, 10 (3), 207-210.
- (24) Corliss, J. B.; Baross, J. A.; Hoffman, S. E., *Oceanologica Acta* **1981**, Supplement, 59-69.
- (25) Al-Abadleh, H. A.; Grassian, V. H., *Surf. Sci. Rep.* **2003**, 52 (3-4), 63-161.
- (26) Argonne National Laboratory, E., Human Health Fact Sheet. In August **2005**
- (27) (<http://toxnet.nlm.nih.gov/cgi-bin/sis/htmlgen?HSDB>). In The National Library of Medicine Hazardous Substances DataBank.
- (28) Smedley, P. L.; Kinniburgh, D. G., *Appl. Geochem.* **2002**, 17 (5), 517-568.
- (29) Welch, A. H.; Lico, M. S., *Appl. Geochem.* **1998**, 13 (4), 521-539.

- (30) Scott, M. J. In *Kinetics of Adsorption and Redox Processes on Iron and Manganese Oxides: Reactions of As(III) and Se(IV) at Goethite and Birnessite Surfaces*. California Institute of Technology, Pasadena, CA, **1991**.
- (31) Mohan, D.; Pittman, C. U., *J. Hazard. Mater.* **2007**, 142 (1-2), 1-53.
- (32) Bhandari, N.; Reeder, R. J.; Strongin, D. R., *Environ. Sci. Technol.* **2011**, 45 (7), 2783-2789.
- (33) Cherry, J. A.; Shaikh, A. U.; Tallman, D. E.; Nicholson, R. V., *J. Hydrol. (Amsterdam)* **1979**, 43 (1-4), 373-392.
- (34) Goldberg, S.; Johnston, C. T., *J. Colloid Interface Sci.* **2001**, 234 (1), 204-216.
- (35) Voegelin, A.; Hug, S. J., *Environ. Sci. Technol.* **2003**, 37 (5), 972-978.
- (36) Markham, M. C.; Hannan, M. C.; Evans, S. W., *J. Am. Chem. Soc.* **1954**, 76, 820-823.
- (37) Henderson, M. A., *Surf. Sci. Rep.* **2011**, 66 (6-7), 185-297.
- (38) Kormann, C.; Bahnemann, D. W.; Hoffmann, M. R., *Environ. Sci. Technol.* **1988**, 22 (7), 798-806.
- (39) Kormann, C.; Bahnemann, D. W.; Hoffmann, M. R., *Envir. Sci. Technol.* **1991**, 25 (3), 494-500.
- (40) Choi, W. Y.; Termin, A.; Hoffmann, M. R., *J. Phys. Chem. B* **1994**, 98 (51), 13669-13679.
- (41) Jegadeesan, G.; Al-Abed, S. R.; Sundaram, V.; Choi, H.; Scheckel, K. G.; Dionysiou, D. D., *Water Res.* **2010**, 44 (3), 965-973.
- (42) Leng, W. H.; Li, X.; Fei, H.; Zhang, J. Q.; Cao, C. N., *Environ. Sci. Technol.* **2011**, 45 (5), 2028-2029.

- (43) Yoon, S.-H.; Lee, J. H.; Oh, S.; Yang, J. E., *Water Res.* **2008**, 42 (13), 3455-3463.
- (44) Bissen, M.; Vieillard-Baron, M. M.; Schindelin, A. J.; Frimmel, F. H., *Chemosphere* **2001**, 44 (4), 751-757.
- (45) Monllor-Satoca, D.; Tachikawa, T.; Majima, T.; Choi, W., *Environ. Sci. Technol.* **2011**, 45 (5), 2030-2031.
- (46) Sharma, V. K.; Dutta, P. K.; Ray, A. K., *J. Environ. Sci. Health, Part A: Toxic/Hazard. Subst. Environ. Eng.* **2007**, 42 (7), 997-1004.
- (47) Xu, Z.; Meng, X., *J. Hazard. Mater.* **2009**, 168 (2-3), 747-752.
- (48) Ferguson, M. A.; Hering, J. G., *Environ. Sci. Technol.* **2006**, 40 (13), 4261-4267.
- (49) Ferguson, M. A.; Hoffmann, M. R.; Hering, J. G., *Environ. Sci. Technol.* **2005**, 39 (6), 1880-1886.
- (50) Xu, T.; Cai, Y.; O'Shea, K. E., *Environ. Sci. Technol.* **2007**, 41 (15), 5471-5477.
- (51) Yoon, S.-H.; Lee, J. H., *Environ. Sci. Technol.* **2005**, 39 (24), 9695-9701.
- (52) Amstaetter, K.; Borch, T.; Larese-Casanova, P.; Kappler, A., *Environ. Sci. Technol.* **2010**, 44, 102-108.
- (53) Appelo, C. A. J.; Van Der Weiden, M. J. J.; Tournassat, C.; Charlet, L., *Environ. Sci. Technol.* **2002**, 36, 3096-3103.
- (54) Carabantea, I.; Grahna, M.; Holmgrena, A.; Kumpienez, J.; Hedlunda, J., *Colloids and Surfaces A: Physicochem. Eng. Aspects*, **2009**, 346, 106-113.
- (55) Dixit, S.; Hering, J. G., *Environ. Sci. Technol.* **2003**, 37, 4182-4189.
- (56) Dixit, S.; Hering, J. G., *Chemical Geology* 228 (2006) 6-15.
- (57) Fuller, C. C.; Davis, J. A.; Wayshunas, G. A., *Geochim. Cosmochim. Acta.* **1992**, 57, 2271-2282.

- (58) Bhandari, N.; Reeder, R. J.; Strongin, D. R., *Environ. Sci. Technol.*, **2012**, *46* (15), 8044–8051.
- (59) Dutta, P. K.; Pehkonen, S. O.; Sharma, V. K.; Ray, A. K., *Environ. Sci. Technol.* **2005**, *39*, 1827-1834.
- (60) Hug, S. J.; Leupin, O., *Environ. Sci. Technol.* **2003**, *37*, 2734-2742.

CHAPTER 2

EXPERIMENTAL METHODS

The information presented in this chapter is divided into two separate sections. The first section provides information about the chemicals and minerals used in this study. The second section provides description of the different instrumentation techniques and experimental setup.

2.1. Materials

2.1.1. Chemicals

All the chemicals used in this study are reagent grade (99.99% or greater) and are used as purchased. Sodium nitrite (NaNO_2) and Potassium nitrate (KNO_3) are purchased from Sigma-Aldrich. Ferrous ammonium sulfate hexahydrate is used to make the Fe(II) standard solutions was obtained from Fisher-Scientific. Ferrous ammonium sulfate was used rather than ferrous sulfate due to its increased stability. Ferrous ammonium sulfate is less prone to oxidation by air to Fe(III) compared to ferrous sulfate and other Fe(II) salts. Fe(II) oxidation by air is pH dependant and increases with increase in pH. Ammonium ions in ferrous ammonium sulfate make it slightly acidic, which slows the oxidation process.¹

Potassium hydroxide (KOH), sodium hydroxide (NaOH), and hydrochloric acid (12 N/HCl) was purchased from Fisher-Scientific. Iron (III) nitrate nonahydrate

[Fe(NO)₃.9H₂O] was purchased from Alfa-Aesar. Sodium (meta) arsenite (NaAsO₂), sodium arsenate dibasic heptahydrate (Na₂HAsO₄. 7H₂O), Aminophenyl fluorescein (APF, 5mM) solution in dimethyl formamide (DMF), and horse radish peroxidase Type (II) was purchase from Sigma-Aldrich. Deionized (DI) water (18 ΩM) was used to make all the solutions and suspensions of interest.

2.1.2. Minerals

2.1.2.1 Pyrite

Pyrite (FeS₂) was obtained from Wards Natural Science. It was crushed and then ground in an agate ball-mill, and filtered using sieves to get the particle sizes of 90 and 38 μm. To remove surface oxides pyrite was washed with O₂-free HCl solution (pH=2) and ultrasonically cleaned for 60 min. It was then transferred into a glove box with an Ar/H₂ atmosphere, washed and filtered three times with Ar-purged O₂-free DI water and allowed to dry. After drying, pyrite was stored in a ~90 %Ar/10 %H₂ atmosphere with a monitored O₂ content ≤ 0.02 ppm.

2.1.2.2. Synthesis of Ferrimagnetic Ferrihydrite or Ordered ferrihydrite

Ferrimagnetic ferrihydrite (Ferrifh) was synthesized by using a modified version of the method published by Michel et al., in 2010.² 0.0003 moles of citric acid and 0.01moles of ferric nitrate nonahydrate [Fe(NO)₃.9H₂O] were dissolved in deionized (DI) water and the pH was adjusted to 7.00 ± 0.02 by slowly adding 1M potassium hydroxide (KOH) solution. Then the 75 mL of reaction mixture was placed in 100 mL Teflon lined stainless steel reactors (High temperature and pressure Parr reactor vessels) under dark,

aerobic conditions at 175°C for 8 h. After 8 h the suspension was centrifuged and rinsed several times with DI water, to remove any salts and unreacted metal ions and dried in a freeze drier.

2.1.2.3. Synthesis of Birnessite

Two synthetic birnessite samples were used in this study; one containing Na and the other containing K in the birnessite interlayers. Na-birnessite was used for the As(III) photo-oxidation experiments explained in chapter 5. The Na- and K-birnessite samples were used for the reductive dissolution of birnessite by arsenite explained in chapter 6. The synthesized Na- and K-birnessite samples have different sizes and average manganese (Mn) oxidation states (AOS). Na-birnessite was synthesized by following the modified procedure reported by yang et al.^{3,4} A mixture of 0.4 M Mn^{+2} solution was mixed with 8 M NaOH in 0.5 L of water, cooled to 0°C and oxidized by bubbling oxygen for 5 h at a rapid rate. The suspension was aged at 90°C for 48 hours with constant stirring. The synthesized particle suspensions were centrifuged and washed ten times with DI water at 13, 000 rpm (15 mins each time), to remove all the excess ions present in the supernatant and then dried in a freeze drier.³ K-birnessite was prepared following the method reported by McKenzie et al.⁵ K-birnessite was synthesized by a drop wise addition of 0.8 M HCl to a boiling solution of 0.4 M $KMnO_4$ while stirring. Boiling is maintained for 10 minutes after the addition of HCl is complete. The resulting K-birnessite was centrifuged and rinsed several times to remove excess ions from the sample. Then the sample was dried using a freeze drier.

2.2. Instrumental Methods and Experimental Setup

Solid samples were characterized by using different spectroscopy, microscopy techniques. The aqueous species were quantified by UV-Vis spectroscopy, fluorescence spectroscopy, and ion chromatography. Gaseous products (NO, N₂) were detected and quantified using gas chromatography. Figure 2.1 shows the list of different techniques used in this study to characterize the minerals, mineral surfaces and the species formed during and after the reaction. A brief description of the light source used in this study is explained first and then explanation of these experimental techniques and experimental setup is given below in separate sections.

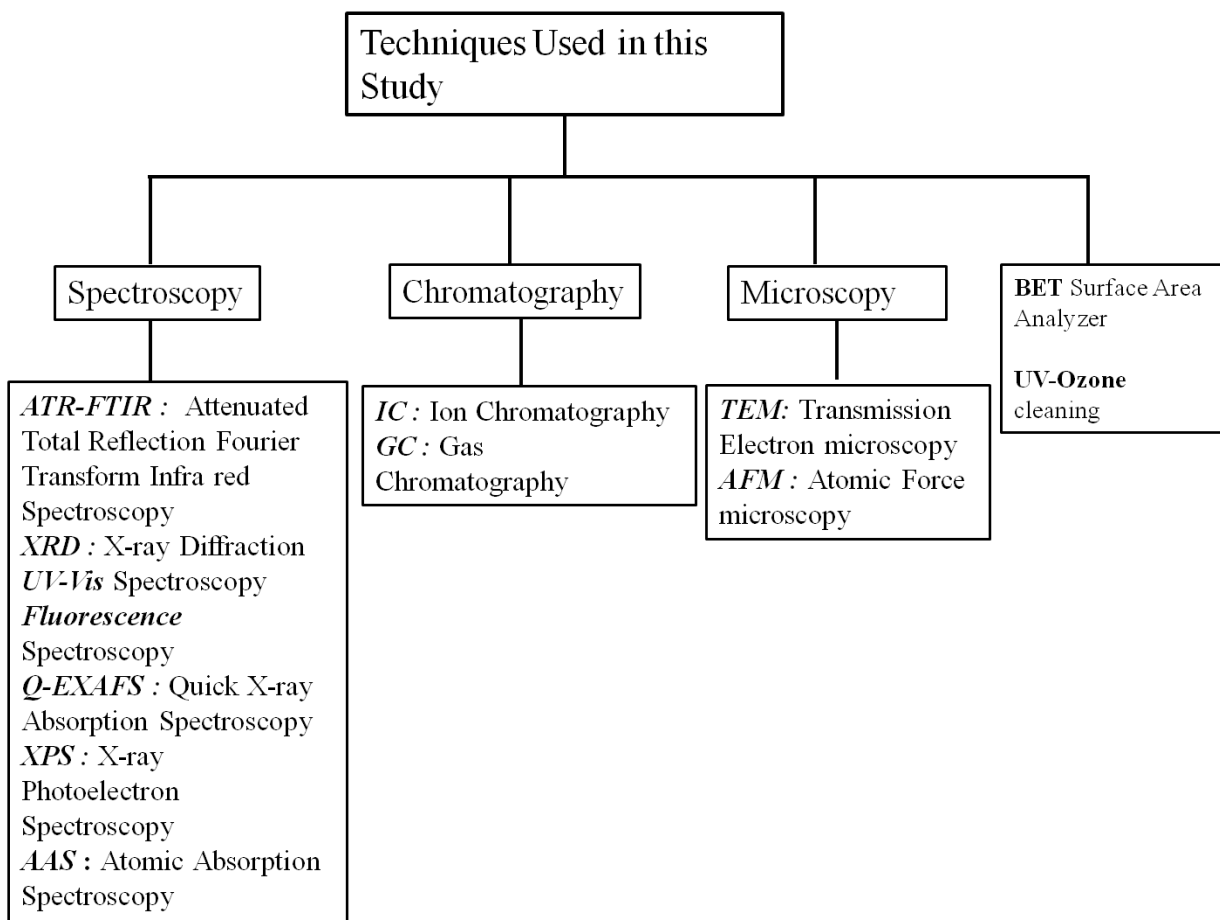


Figure 2.1. List of different techniques used in this study

2.2.1. Xenon lamp (Simulated Solar light Source)

A 900 W high pressure Xenon lamp (Schoeffel instruments, Westwood, NJ), was used to conduct the photo irradiation experiments of birnessite and ferrimagnetic ferrihydrite.^{29, 30} For ATR-FTIR experiments a 4.5 m long fiber optic cable (Fiber Bundle Focusing Assemblies, Newport, RI) was used to irradiate the sample solution. For batch experiments and the ATR-FTIR experiments, Pyrex glass was used as the UV

B (280 to 315 nm) cut off filter, so that UV-A (315 to 400 nm) and visible light reaches the sample solution. The spectral output (Figure 2.2) of the light passed through the Pyrex glass was measured using the BRC111A high speed CCD spectrometer (B&WTEK, Inc.).^{29,30} The radiant flux density of the light irradiated on the sample suspension was measured by using the Melles Griot (USA) 30 W broad band power meter. The a final radiant flux density of light reaching the sample in batch and ATR-FTIR experiments was found to 1450 and $\sim 15 \text{ W.m}^{-2}$ resepctively.^{29,30} The intensity of the light used in batch experiments is slightly higher than the maximum global irradiance of the sunlight, which is 1000 W.m^{-2}

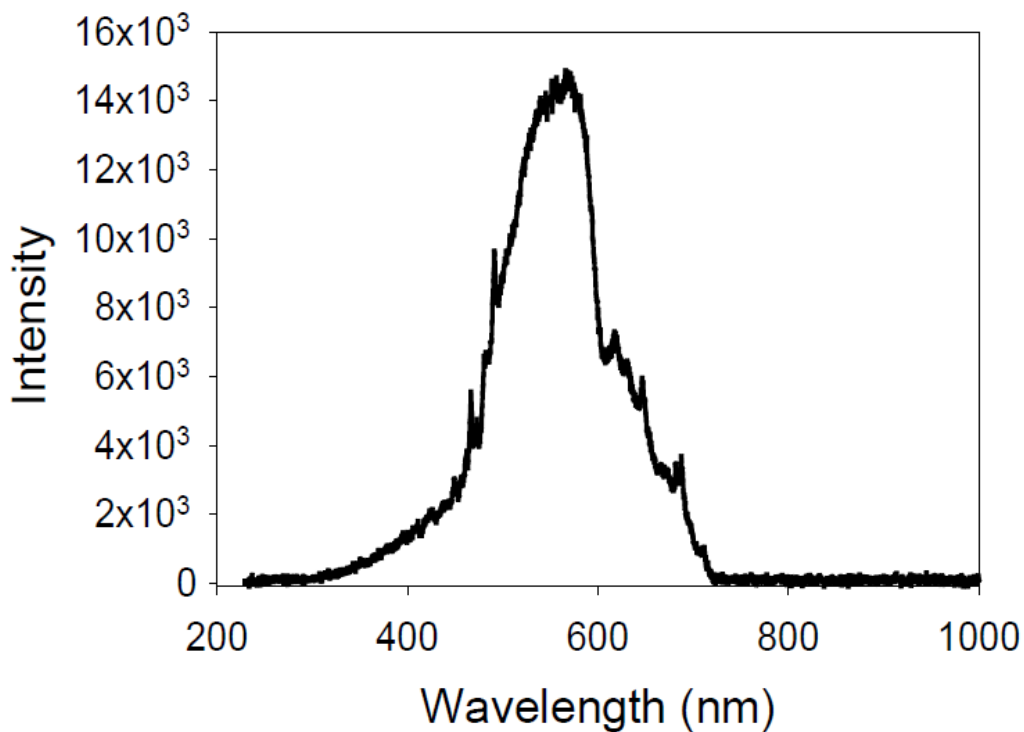


Figure 2.2. The spectral output of the light coming from the Xe lamp used in this study after passing through the Pyrex glass, which was analyzed using a BRC111A high CCD spectrometer (B&W TEK, Inc.). Adapted from reference³⁰.

2.2.2. Attenuated Total Reflection-Fourier Transform Infrared (ATR-FTIR) Spectroscopy.

ATR-FTIR is used to detect the species that are near or on the surface of a mineral. The infrared beam, when passed from the dense medium (ATR crystal) to a less dense medium (sample), gets reflected internally from the surface of the crystal and creates an evanescent wave, and extends into the sample.^{6,7,8} Some of the energy of the evanescent wave is absorbed by the sample and remaining is reflected. The parameters that affect the ATR spectrum are refractive indices of the crystal, sample and depth of penetration of the evanescent wave. Refractive indices of the crystal and the sample are related by the following equation,^{6,8}

$$\theta_c = \sin^{-1}(n_2/n_1)$$

where n_2 is the refractive index of the sample and n_1 is the refractive index of the crystal, and

θ_c is the critical angle. Refractive indices of the crystal must be significantly higher than the refractive index of the sample to get a good quality spectrum. Also a good contact between the sample and the ATR crystal is required as the depth of penetration of evanescent wave into the sample is only upto specific microns. Penetration depth is defined as the distance at which the electric field amplitude equals to the e^{-1} times the value at the surface, which is represented by the following equation,^{6,7,8}

$$d_p = \frac{\lambda}{2 \Pi (n_1^2 \sin^2 \theta - n_2^2)^{1/2}}$$

where d_p is the penetration depth and theta is the angle of incidence.

The ATR crystals are usually made of diamond, zinc selenide (ZnSe), and Germanium (Ge).^{6,9} Among these diamond is a single reflection (bounce) ATR, while ZnSe and Ge are multibounce ATR crystals. Increase in number of reflections result in increased sensitivity of the ATR spectrum. When a single bounce diamond ATR crystal is used pressure should be applied to ensure a good sample contact with the crystal. This gives a spectrum with good sensitivity. For soft or liquid samples ZnSe crystal are good. Often proper care is needed while using ZnSe crystal as it can get scratched quite easily..^{6,8} The Ge crystal has a high refractive index and is ideal for the studies of high absorbing materials such as carbon black. With Ge crystal high surface sensitivity is achieved, even when using a thin layer of sample.

Diamond ATR crystal is highly inert and resistant to scratches. Although expensive, diamond is usually preferred over other crystals. They can be used for small size samples and have good durability. Also, Diamond is ideal for high temperature and pressure studies. Schematics of multi bounce and single bounce ATR are shown in Figure 2.3.

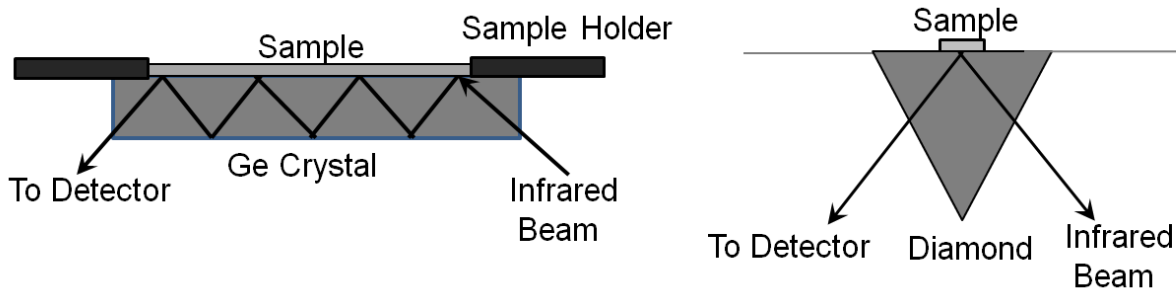


Figure 2.3. Schematic of the Ge multi bounce (left figure) and Diamond single bounce (right figure) ATR.^{8,10}

Germanium (Ge) multibounce ATR was used for the in-situ ATR-FTIR experiments of nitrite and nitrate reduction on pyrite that were conducted at room temperature (22°C) and 70°C. This ATR accessory was mounted on a Nicolet Magna 750 FTIR spectrometer that was equipped with a mercury cadmium telluride A (MCTA) detector. Golden gate diamond ATR cell (SpecacTM) is used to conduct the 120°C FTIR experiments, as Ge crystal is not ideal to use at this temperature. Experiments were conducted using FeS₂ slurry in water containing either 5 mM KNO₂ or KNO₃. The total volume of the sample used in these studies was 1 mL and 0.25 mL for the Ge and the diamond cell, respectively.

In-situ ATR-FTIR flow experiments with photo-irradiation were conducted to determine if the Ferrifh was either oxidizing As(III) and/or adsorbing As(III)/As(V) on the surface. A single bounce smart orbit diamond ATR accessory was mounted in a Nicolet Magna 750 FTIR spectrometer (Thermo Scientific) and used to collect the ATR-FTIR spectrum. It was equipped with a deuterium tryglycine sulfate (DTGS) detector.

12 mg of the solid was suspended in 500 μL of DI water, sonicated for 20 min. 24 μL of the suspension was placed and dried on the diamond under the flow of ultra high purity (UHP) Ar gas. Then 0.41 mM As(III) solution (prepared using 5 mM NaCl solution) at pH 5 was flowed at a flow rate of 20 mL/h through a teflon flow cell (~2 mL volume capacity), surrounded by the film. The solution was flowed continuously through the cell, to maintain constant pH during the study. Samples were irradiated using a 900 W high-pressure xenon lamp using a fiber optic cable. Single beam spectra were recorded as an average of 200 scans with a resolution of 4 cm^{-1} . An initial single beam spectrum of Ferrifh suspended in water was used as the background. To avoid solution phase chemistry and study only the surface chemistry of arsenic, a dry film of ferrifh was used in these experiments.



Figure 2.4. Image of the smart orbit diamond ATR accessory, mounted on a Nicolet Magna 750 FTIR spectrometer was shown with the flow reaction cell and the syringe pumps, which were used to conduct the in-situ ATR-FTIR flow experiments. One syringe pumps the required [As(III) or As(V)] solution into the reaction cell placed on the diamond ATR, while the other syringe draw the solution from the same reaction cell, during which a constant pH is maintained.

2.2.3. Batch Experiments

Dark and photo irradiation batch experiments were conducted by exposing the As(III) to ferrimagnetic ferrihydrite and birnessite separately. To quantify the amount of As(III) oxidized or adsorbed by Ferrifh, batch experiments were conducted in a Pyrex vessel by suspending 0.25 g/L of the Ferrifh suspension in 5 mM NaCl solution and in presence of 0.41 mM (1.64 mole/kg) of As(III) in the dark or in the presence of visible light. 25 mg of the ferrifh was suspended in 99 mL of 5 mM NaCl, sonicated for 20 min and stirred for 20 min. Then the pH of the suspension was adjusted to 5.00 ± 0.02 , and 0.82 mL of 50 mM As(III) solution was added to it. After 24 h equilibration in the dark for 24 h at $\text{pH } 5.00 \pm 0.02$, light was irradiated. For dark experiments samples were collected at regular time intervals after 24 h equilibration in dark at pH 5, without irradiating the light. A 900 W high pressure Xe lamp, with a power density of 1450 W/m^2 , was used to irradiate the suspensions and a Pyrex glass was used in these experiments as a UV cut off filter ($< 300\text{nm}$). A pH titrino (Metrohm[®] 718) in STAT mode was used to maintain the pH during the reaction.



Figure 2.5. Image showing the batch experimental setup using pH STAT titrino and Xenon lamp. pH STAT titrino was used to maintain the required solution pH.

As(III) photo-oxidation experiments using Na-birnessite were conducted in 400 mL volume Pyrex glass bottles for a time period of 8 h. 15 mg of birnessite was suspended in 148.59 mL of DI water in a glass beaker, sonicated for 20 min, stirred for 30 min for homogeneity. Then 1.41 mL of 50 mM As(III) (NaAsO_2) solution was added to the suspension that makes the total concentration of As(III) to $\sim 470 \pm 10 \mu\text{M}$. Experiments were performed at pH of 5.0 and 7.4. In all the reactions pH was adjusted

by adding either 0.1 M HCl or 0.5 M NaOH and maintained by adding either 0.01 M HCl or 0.1 M NaOH depending on the pH. All the suspensions were allowed to equilibrate at the desired pH for 1 hr before adding the known concentration of As(III). A constant pH was maintained throughout these experiments using a pH stat titrino (Metrohm 718 STAT pH titrino). A 900 W high pressure Xe lamp, with a power density of 1450 W/m², was used to irradiate the suspensions and a Pyrex glass was used in these experiments as a UV cut off filter (< 300nm).

As(V), Mn²⁺, released in to the solution during the oxidation of As(III) was analyzed by Ion chromatography (Dionex ICS1000) with a conductivity detector and 4 mm ion pac column. All the samples were filtered with 0.22 µm filters, before being analyzed with IC. Total As (As(III) + As(V)) present in solution was determined by adding H₂O₂, using a method adopted by Hansen et al.,¹¹ Total adsorbed arsenic was determined by subtracting the total arsenic present in solution at that time from the concentration of arsenite added initially. After the experiments all the suspensions were immediately centrifuged, washed once with pH 5.00/pH 7.40 water and the resulting birnessite sample was air dried before being analyzed. Changes in the structure and composition of the birnessite after reaction with As(III) was investigated using several characterization techniques like XRD, TEM. EXAFS is used determine the relative amounts of As(III) and As(V) adsorbed on birnessite

For the birnessite reductive dissolution studies, batch experiments were conducted by using a birnessite suspension density of 0.15 g L⁻¹. Initially, 15 mg of the K or Na-birnessite samples were suspended in 99.6 mL DI water, sonicated for 30 min and stirred for 30 min, and pH was adjusted to 8.5 using 0.1 N NaOH, stirred at this pH for 1h. Then

0.4 mL of 50 mM As(III) solution was added to the birnessite suspension, to get an initial As(III) concentration of 200 μ M. During this reaction time the suspension was stirred at a solution pH of 8.5 and the pH was maintained at 8.5 ± 0.05 with dilute NaOH using a pH titrino (Metrohm 718 pH STAT). For the XRD and XPS, an aliquot of the reaction suspension at desired time was collected, centrifuged, washed with pH 8.5 water once, and air dried. For the analysis of the aqueous arsenic (As(V)) and Mn(II) species, the samples were collected at regular intervals of time (0.25, 0.5, 1, 3, 4, 17, 19, 21, and 24 h for K-birnessite, 0.25, 0.5, 1, 3, 5, 20, and 24 h for Na-birnessite) and filtered with 0.22 μ m (Millipore) filters and analyzed using ion chromatography (IC, Dionex ICS-1000). Quantification was based on a standard curve derived from known solution phase concentrations of As(V) ($\text{Na}_2\text{HAsO}_4 \cdot 7\text{H}_2\text{O}$) and/or Mn(II) (MnCl_2). Concentrations of unreacted As(III) remaining in solution and As(V) product formed during experiments designed to measure As(III) oxidation were determined by a difference method after the addition of H_2O_2 , as explained above.

2.2.4. Ion Exchange Chromatography (IC)

Ion exchange chromatography is used to analyze anions and cations including aminoacids and proteins.¹² An aqueous mobile phase carries the injected sample onto the stationary phase present in the packed column. The stationary phase retains ions of opposite charge based on the columbic interactions.¹² Often a suppressor is placed between the column and the detector. Suppressor is used to increase the sensitivity and to reduce the background conductivity from the eluent. A suppressor in anion chromatography is used to remove cations and the suppressor in cation chromatography

is used to remove anions. These retained ions are displaced by the similarly charged eluent ions. Either conductivity or UV-Visible detector is used in ion chromatography.¹²

A Dionex DX500 ion chromatograph with a 4 mm IonPac[®] AS4A-SC anion column is used to analyze NO₃⁻, NO₂⁻ and SO₄²⁻. It is equipped with a conductivity detector, which measures the conductivity of the species. The samples were injected through an auto sampler. Standard solutions of the respected species are run through the column for calibration and concentrations were calculated from a linear 4-point calibration curve with R² values above 0.99. 1.7/1.8 mM sodium bicarbonate (NaHCO₃)/sodium carbonate (Na₂CO₃) solution was used as the eluent. As(V), Mn(II) were analyzed by using Dionex ICS-1000 Ion chromatography equipped with the conductivity detector. At regular time intervals an aliquot of the sample was collected, filtered through 0.22 µm PVDF (Millex[®], GV) filters and immediately analyzed. Total As (As(III) + As(V)) remained in solution was determined by the oxidation of As(III) remained in the solution to As(V) by adding H₂O₂, using a method adopted by Hansen et al.,¹¹ Total adsorbed arsenic was determined by subtracting the total amount of As(V) in solution at a given point of time, from the concentration of arsenite added initially. As(III), As(V), Mn(II) were analyzed using ion chromatography.

2.2.5. Braunner-Emmett-Teller (BET) Surface area analyzer

BET surface area analyzer calculates the surface area of the sample based on the amount of gas adsorbed (physisorbed) on the surface of the sample at a given pressure.¹³ Surface area of the minerals is very important to study the rate of the surface reactions. Samples are generally prepared by heating while simultaneously evacuating or flowing

gas over the sample to remove adsorbed water and other impurities. The degassing temperature and time were selected so that there is no structural damage to the samples. Then the samples were analyzed by cooling with liquid nitrogen and measuring the volume of gas (typically N₂ or Kr) adsorbed at specific pressures.¹³ 5-point BET surface area of crushed pyrite was determined with a Quantachrome NOVA 2200e surface area analyzer using the ultra-high-purity N₂ adsorbate gas. The BET surface area of pyrite was found to be 0.358 m²/g. Multipoint BET surface area of the Ferrifh, Na-, and K-birnessite samples were determined by using micromeritics ASAP 2020 surface area analyzer. Ferrifh was degassed at 60°C for 3 h and Na-, K-birnessite samples were degassed at 150°C for 2 h.^{14, 15} Ferrifh and birnessite samples were analyzed using N₂ as the adsorbate gas. The surface area of the Ferrifh was 156 m²/g. The surface of the Na- and K-birnessite samples was determined to be 23.10 m² g⁻¹ and 49.86 m² g⁻¹ respectively.

2.2.6. UV-Visible Spectroscopy

UV-Visible (UV-Vis) spectroscopy is widely used in chemistry to detect different analytes. The principle of UV-Vis is based on the Beer-Lambert's law, shown by the following equation¹⁶

$$A = \text{Log} (I_0/I) = E. C. b$$

Where A is the absorption, I₀ is the intensity of the incident radiation, and I is the intensity of the transmitted radiation. E is the extinction co-efficient, C is the

concentration of the solution and b is the path length (length of the sample cell). The amount of light absorbed by a solution is directly proportional to the concentration of the solution.

Ferrous [Fe(II)] and total iron [Fe(II)+Fe(III)] released into the solution were analyzed at 562 nm (using a HACH DR/4000 spectrophotometer). Fe(II) released into the solution during the experiment was measured by adding 0.2 mL of 15 mM ferrozine and 2 mL of DI water to the 0.1 mL sample filtered using 0.22 μm filters. Total Fe released into the solution were analyzed after incubation with ferrozine/30 mmolal aqueous ascorbic acid.^{17,18}

2.2.7. Gas Chromatography (GC)

Gas chromatography or gas liquid chromatography is used to analyze gases or the compounds, which can be vaporized without decomposition.¹⁹ Sample is transported through the column by a gaseous mobile phase (carrier gas). Column contains a liquid stationary phase supported on an inert support. Carrier gas generally includes chemically inert gases such as argon, krypton, and nitrogen. Analytes are eluted from the column based on the interaction between the analyte and the stationary phase inside the column. Stronger the interaction between the analyte and the stationary phase, longer the analyte remains attached to the stationary phase and eluted later and vice versa. Separation of the compounds depends on the column temperature, carrier gas flow, amount of material injected, and the column length. Different types of detectors can be used in GC. Detectors can be used based on the type of the analyte to be detected.

Gas analyses were conducted using a single column SRI 8610c gas chromatograph (GC) equipped with a 6' Molecular Sieve 5A column. Thermal conductivity detector (TCD) was used with Ultra high purity (UHP) Helium as carrier gas. Experiments were conducted at 95°C in a 40 mL Alltech gas sampling vessel. The vial was filled with O₂-free, 5 mmolal solution of NaNO₂ and pyrite in the ratio identical to all other experiments. The vial was then partially closed with a PTFE coated silica septum and a needle was inserted through the septum all the way into the solution and the entire assembly was sparged with UHP He to remove any residual O₂ from the solution or the headspace. After approximately 30 minutes, the needle was withdrawn and the headspace was tested for the absence of O₂ and N₂ prior to the start of the experiment. After 50 hours, two gas samples were collected from each vessel and immediately analyzed by GC. Each data point was the average of these two sample analyses.

2.2.8. Fluorescence Spectroscopy

The instrument which measures the fluorescence is called the Fluoremeter. Molecules are excited at a specific wavelength mainly by using the UV light and the fluorescence emitted by these molecules is measured at 90° angle relevant to the excitation source to avoid interference with the transmitted radiation.²⁰

NH₃ was analyzed using an adapted fluorescence method.²¹ on a Barnstead Quantech FM109515 fluorometer with 360 nm and 420 nm narrow band excitation and emission filters, respectively. 175 µL of the Samples and standards were pipetted into polypropylene vials with 3 mL of working reagent and incubated in the dark for 24-48

hours. NH_3 concentrations were calculated from a linear 9-point calibration curve with R^2 values above 0.99.

OH radicals ($\cdot\text{OH}$) and Hydrogen peroxide (H_2O_2) was analyzed by Fluorometer with 3'-(*p*-amino phenyl) fluoresceine (APF) and horse radish peroxidase (HRP) as the probes.^{22,23} For the ex-situ experiments 100 mL of the 1 mL of the sample was collected at regular intervals, filtered birnessite suspension prepared using the pH 7.4 phosphate buffer and 50 μL of the APF was added and irradiated with light. At regular intervals 1 mL of the sample was collected, filtered using 0.22 μm filters. Excitation wavelength was set to 490 nm and emission was observed at 513 nm. For the ex-situ detection of the $\cdot\text{OH}$, 1 mL of the sample was collected at regular intervals and filtered. To the 1 mL filtered sample 2 μL of the APF was added and analyzed using the Fluoremeter. APF itself is non fluorescent, and becomes fluorescent after reacting with $\cdot\text{OH}$. HRP catalyzes the oxidation of APF by H_2O_2 , hence APF react with H_2O_2 only in presence of HRP. H_2O_2 is detected by the addition of 0.2 μM Horse radish peroxidase (HRP) to the reaction mixture in addition to APF and phosphate buffer. For the in-situ detection of the 25 μL of 0.2 μM HRP was added to the birnessite suspension containing 50 μL of the 10 μL APF. For the ex-situ detection of the H_2O_2 , 1 mL of the sample was collected at regular time intervals, filtered, and 10 μL of 0.2 μM HRP, 2 μL of 10 μM APF was added and analyzed immediately.

2.2.9. X-ray diffraction (XRD)

X-ray diffractograms were collected by using Bruker AXS APEX II duo single crystal X-ray diffractometer. When X-rays pass through the sample, a diffraction pattern

will be formed due to the constructive interference of the beam as explained by the Bragg's law,²⁴

$$n\lambda = 2d \sin \theta$$

where d is the distance between the atomic layers, and λ is wave length of the X-rays used and θ is the angle of incidence. This diffraction pattern is unique to each sample. Selection of the X-ray source generally depends on the type of the analyzing material. Generally Cu $K\alpha$ radiation is employed as the X-ray source for the powder diffraction, but when the sample contains Fe or Co it is better to use other X-ray sources as these elements fluoresce in presence of Cu $K\alpha$ radiation.²⁴ Hence Mo $K\alpha$ radiation was used for the characterization of ferrimagnetic ferrihydrite and Cu $K\alpha$ radiation was used to characterize birnessite samples..

Samples were prepared by filling the powder into the boro-silicate glass capillaries with an internal diameter of 0.1 mm. The resulting spectral pattern contains background peaks from the glass capillary, which were removed by subtracting the XRD data of the empty glass capillary. All the XRD data were processed using the EVA software package.

2.2.10. Transmission electron microscopy (TEM)

Electron microscopy is similar to the optical light microscopy, but electrons are used to illuminate the specimen, instead of the visible light in light microscopy. These electrons are accelerated by the high voltage in the anode. Resolution is based on the wave length of the light and wavelength of the electrons is almost 100,000 times more than the wavelength of light, electron microscopes gives higher resolution than the light

microscope. Higher the speed of the electrons, shorter the wavelength, and hence higher the resolution achieved by the instrument.²⁵ In an electron microscope, electrons are emitted from a tungsten filament under high vacuum and focused as beam by electromagnetic lenses. The electron beam is passed through a specimen and interacts with the specimen. These transmitted electrons carried the information about the structure of the specimen and passed through a series of magnetic lenses and the magnified image is recorded after hitting a fluorescent screen and viewed on charge-coupled device (CCD) camera. But a very good vacuum is needed to prevent the collision of electrons with air molecules and hence the scattering of the electrons.²⁵ TEM was used to characterize the synthesized ferrite and birnessite samples. TEM images of the birnessite samples were also collected before and after the reaction with arsenic to observe the phase changes in birnessite. Images were collected by using a JEOL (JEM 1400) Transmission electron microscope. 2 mg of the sample was suspended in 10 mL of isopropanol and sonicated for 20 min for homogeneity. One drop (~ 5 μ L) of the suspension was deposited on a 300 mesh carbon coated copper grid (light hydrophilic side) and air dried before the analysis.

2.2.11. Quick X-ray Absorption Spectroscopy (QXAS)

Atoms have different core shells (K, L, M, and N) that have different binding energies. When a monochromatic X-ray beam with energy higher than the binding energy the core shell electron hits the surface, a photoelectron is generated, creating a hole in the core level.²⁶ The hole is filled by a radiative emission of a fluorescent photon or by non radiative emission of an auger electron. The intensity of this fluorescence

photons or auger electrons are measured by an appropriate detector. For example fluorescence yield is measured by using a fluorescence detector and the auger electron is measured either by a channeltran or an energy ionizer.²⁶

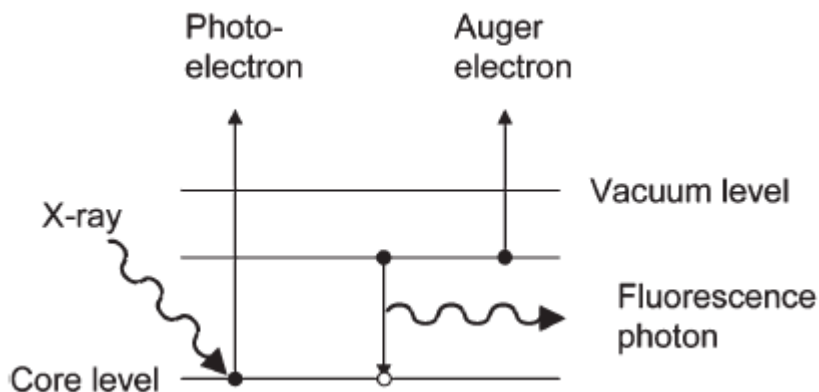


Figure 2.6. Energy diagram showing the absorption of the X-rays and simultaneous emission of the fluorescence photon and auger electron.²⁶

Synchrotron radiation is the commonly used X-ray source in the X-ray absorption spectroscopy. It is the intense pulse of X-rays produced, when electrons are accelerated to high energy. Each absorption edge represents a specific core shell binding energy. These absorption edges are labeled in the order of increasing energy of the core shells. An X-ray absorption edge is mainly divided into three types.

- 1) Pre edge – The energy of the incident radiation is below the absorption edge
- 2) Near edge X-ray absorption fine structure spectroscopy (NEXAFS) – The energy of the incident radiation is near or upto 50 eV above the absorption edge

3) Extended X-ray absorption fine structure spectroscopy (EXAFS)– The energy of the incident radiation is upto 50 to 1000 eV above the absorption edge

Formal oxidation state, , coordination geometry, and local structure of the atoms can be obtained by using X-ray absorption near edge (XANES) spectra.²⁷ Bond length and coordination number can be obtained using EXAFS.

Arsenic K-edge X-ray absorption near-edge structure (XANES) spectroscopy is used to determine the oxidation state of the arsenic adsorbed on Ferrifh and birnessite and to quantify the relative % of the As(III) and As(V) adsorbed on the surface, which is important to determine the mechanism of the As(III) oxidation. Previous researchers have shown that exposure of a sample to a synchrotron- X-ray beam may induce the oxidation of As(III) to As(V) depending on factors such as the X-ray photon flux, exposure duration, and characteristics of the sample.²⁸ This artifact can also minimized by cooling samples to liquid He temperature before making measurements.²⁵ Several authors showed that X-ray beam-induced oxidation of As(III) can be avoided by using quick-scanning X-ray absorption spectroscopy, as implemented at beam line X18B at the National Synchrotron Light Source, Brookhaven National Laboratory.^{29, 30} In this technique a channel-cut Si(111) monochromator is scanned continuously over the absorption edge of interest, allowing a full spectrum to be collected in less than 1 sec, thereby greatly reducing exposure time to the X-ray beam. We have demonstrated the effectiveness of this approach by collecting XANES spectra of As(III)-sorbed iron oxyhydroxide control samples (with no exposure to light) continuously for periods up to 150 sec following exposure to the X-ray beam. Using the non-focusing optics at X18B,

we found no evidence of beam-induced oxidation in As(III)-sorbed goethite, in As(III)-sorbed ferrihydrite, or in As(III) aqueous solutions.

XANES spectra of As-reacted birnessite samples in the current study were collected over a duration of 30 seconds using the quick-scanning technique, with each scan requiring less than 1 sec. As(III)-reacted samples were sealed between two layers of Kapton tape, and mounted at 45° relative to the incident X-ray beam. XANES spectra were measured in fluorescence mode, using a passivated implanted planar silicon detector. For each sample, the spectra within a sequence were compared to confirm the absence of any changes during scanning and then averaged to achieve better signal/noise. A linear pre-edge background function was subtracted from the averaged spectrum, and normalization was performed at an energy value above the absorption edge (11915 eV), as described by Bhandari et al.³⁰ XANES spectra of As(III) and As(V) aqueous solutions were used as oxidation state references. The position of the absorption maximum for As(V) was found to be shifted ~3.5 eV higher than the position for the As(III) solution.

2.2.12. X-ray photoelectron spectroscopy (XPS)

XPS of the dry samples was collected with a Scienta ESCA-300 instrument. Monochromatic Al K α X-rays (1486.7 eV) generated from a rotating anode were used with a high resolution, 300 mm mean radius hemispherical electrostatic analyzer. The base pressure of the analysis chamber was maintained at 1×10^{-9} Torr. Survey scans were collected using fixed pass energy of 300 eV and narrow scans were collected using a fixed pass energy of 150 eV. Data collected for the Mn 2p_{3/2} and As 3d spectral regions were peak fitted using Casa XPS software. To fit the Mn 2p_{3/2} region, the procedure used

by Nesbitt and Banerjee^{31, 32} was employed, which takes into account the multiplet structure resulting from the presence of unpaired valence electrons in the 3d orbitals of manganese in the birnessite sample. This fitting procedure relies on the theoretical calculations by Gupta^{33, 34} of the expected XPS spectra for the free Mn(IV), Mn(III), and Mn(II) ions. Prior work showed that calculated XPS spectra for the free ions (each containing 5 multiplet peaks) allowed the accurate fitting of experimental XPS Mn 2p_{3/2} data for birnessite.^{31,32} We used the fitting parameters published in this prior work with little alteration. The contribution of Mn(IV) to the XPS data were fitted with peaks at 642.15, 643.19, 644.0, 645.05, and 646.06 eV using a relative peak area ratio of 1:0.63:0.32:0.10:0.06. Mn(III) contributions to the XPS data were fitted with peaks at 640.83, 641.53, 642.34, 643.36, and 644.73 eV with a relative peak area ratio of 1.0:1.0:1.16:0.73:0.028. Finally, Mn(II) contributions were fitted to the spectral data with peaks at 639.80, 640.0, 641.79, 642.69, and 644.19 eV with a relative peak area ratio of 1.0:0.71:0.42:0.30:0.030. Peak area ratios for each Mn-species were not changed during the fitting procedure. Peaks with a 50:50 Gaussian:Lorentzian contribution were used in the procedure and the full width half maximum for each peak was 1.15 eV. Using these parameters the spectral data was fitted by varying the relative contribution of individual set of multiplet peaks. Arsenic 3d photoemission peaks were peak fitted using the following parameters. The relative area ratio of the As d_{5/2} and d_{3/2} associated with As(V) and As(III) was constrained to a ratio of 3:2. A value of 0.7 eV was used as the splitting between the 3d_{5/2} and 3d_{3/2} peaks. The 3d_{5/2} peak of As(V) and As(III) were set to 44.8 and 44.1 eV respectively.

2.2.13. Atomic Absorption Spectroscopy (AAS)

Manganese (Mn) in birnessite exists in three different oxidation states [Mn(IV), Mn(III), Mn(II)]. Average oxidation state (AOS) of Mn in K and Na-birnessite were calculated by using the flame atomic absorption spectroscopy (AAS) and titration method.³⁵⁻³⁷ In the first step, the total Mn contents were determined by using AAS by dissolving 0.1 g of the birnessite in 25 mL of 0.25 M hydroxylamine hydrochloride and diluting to 250 mL. Then 1 mL of the dissolved and diluted birnessite sample was taken and diluted to 100 mL. The resulting solution was analyzed with AAS for total Mn. In the second step 0.1 g of the K- or Na-birnessite sample was dissolved in 5 mL of the 0.5 M oxalic acid and 10 mL of the 1 M H₂SO₄. Excess oxalic acid was determined by back titration at 75 °C using a standardized 0.021 M KMnO₄ solution.

2.3. References

- (1) Greenwood, N. N.; Earnshaw, A., *Chemistry of the Elements* (2nd Ed), 1997, Butterworth-Heinemann, ISBN 0080379419.
- (2) Michel, F. M.; Barron, V.; Torrent, J.; Morales Maria, P.; Serna Carlos, J.; Boily, J.-F.; Liu, Q.; Ambrosini, A.; Cismasu, A. C.; Brown Gordon, E., Jr., *Proc. Natl. Acad. Sci. U S A* 2010, 107 (7), 2787-2792.
- (3) Yang, D. S.; Wang, M. K., *Clays Clay Miner.* 2002, 50 (1), 63-69.
- (4) Golden, D. C.; Dixon, J. B.; Chen, C. C., *Clays Clay Miner.* 1986, 34 (5), 511-520.
- (5) McKenzie, R. M., *Mineral. Mag.* 1971, 38 (296), 493-502.
- (6) Mirabella, F. M. Jr., *Practical Spectroscopy Series; Internal reflection spectroscopy: Theory and applications*, Marcel Dekker, Inc.; Marcel Dekker, Inc., 1993, 17-52
- (7) Braun .D.; Böhringer. B.; and Eidam. N., *Polymer Bulletin* 21, 1989, 63-68
- (8) Milosevic, M. Internal Reflectance near Critical Angle, in Internal Reflection and ATR Spectroscopy, *John Wiley & Sons, Inc., Hoboken, NJ, USA.* (2012) doi: 10.1002/9781118309742.ch9
- (9) "FT-IR Spectroscopy—Attenuated Total Reflectance (ATR)". *Perkin Elmer Life and Analytical Sciences.* 2005.
- (10) Coumbs, D., *Int. J. Vibr. Spec.* 1998, 2, 3-4.
- (11) Hansen, L. D.; Richter, B. E.; Rollins, D. K.; Lamb, J. D.; Eatough, D. J., *Anal. Chem.* 1979, 51 (6), 633-637.
- (12) Weiss. T.; Joachim. W., (2005). *Handbook of Ion Chromatography.* Weinheim: Wiley-VCH. ISBN 3-527-28701-9

- (13) Brunauer, S.; Emmett, P. H.; and Teller, E.; *J. Am. Chem. Soc.* 1938, 60, 309-319
- (14) Prieto, O.; del Arco, M.; Rives, V., *Thermochim. Acta* 2003, 401 (2), 95-109.
- (15) Prieto, O.; Del Arco, M.; Rives, V., *J. Mater. Sci.* 2003, 38 (13), 2815-2824.
- (16) Skoog, D. A.; West, D. M.; James Holler, F., *Analytical Chemistry: An Introduction (Saunders Golden Sunburst Series)* 7th Ed., 1999.
- (17) Hao, J.; Murphy, R.; Lim, E.; Schoonen, M. A. A.; Strongin, D. R., *Geochim. Cosmochim. Acta* 2009, 73 (14), 4111-4123.
- (18) Stookey, L. L., *Anal. Chem.* 1970, 42 (7), 779-781.
- (19) Harris, D.C., *Quantitative Chemical Analysis, 6th ed.*, W.H. Freeman and Company, New York, 1982.
- (20) Holler, J. F.; Skoog, D. A.; Crouch, S. R. *Principles Of Instrumental Analysis*, 2006
- (21) Amornthammarong, N.; Zhang, J.-Z., *Anal. Chem.* 2008, 80 (4), 1019-1026.
- (22) Cohn, C. A.; Pedigo, C. E.; Hylton, S. N.; Simon, S. R.; Schoonen, M. A. A., *Geochem Trans* 2009, 10, 8.
- (23) Cohn, C. A.; Simon, S. R.; Schoonen, M. A. A., *Part. Fibre. Toxicol.* 2008, 5, 2.
- (24) Suryanarayana, C.; Grant Norton M., *X -Ray Diffraction: A Practical Approach*, Springer, Jun 30, 1998, 1-292.
- (25) McLaren, A., *Transmission Electron Microscopy of Minerals and Rocks*. 2nd ed.; Cambridge university Press: 1991
- (26) Hähner, G., *Chem. Soc. Rev.*, 2006, 35, 1244-1255
- (27) Ona-Nguema, G.; Morin, G.; Juillot, F.; Calas, G.; Brown, G. Jr., *Environ. Sci. Technol.* 2005, 39, 9147-9155

- (28) Ginder-Vogel, M.; Landrot, G.; Fischel, J. S.; Sparks, D. L., *Proceed. National Acad. Sci.* 2009, 106, (38), 16124-16128.
- (29) Bhandari, N.; Reeder, R. J.; Strongin, D. R., *Environ. Sci. Technol.* **2012**, 46 (15), 8044-8051.
- (30) Bhandari, N.; Reeder, R. J.; Strongin, D. R., *Environ. Sci. Technol.* **2011**, 45 (7), 2783-2789.
- (31) Nesbitt, H. W.; Canning, G. W.; Bancroft, G. M., *Geochim. Cosmochim. Acta* **1998**, 62 (12), 2097-2110.
- (32) Nesbitt, H. W.; Banerjee, D., *Am. Mineral.* **1998**, 83 (3-4), 305-315.
- (33) Gupta, R. P.; Sen, S. K., *Phys. Rev. B : Solid State* **1974**, 10 (1), 71-77.
- (34) Gupta, R. P.; Sen, S. K., *Phys. Rev. B : Solid State* **1975**, 12 (1), 15-19.
- (35) Kijima, N.; Yasuda, H.; Sato, T.; Yoshimura, Y., *J. Sol. State. Chem.* **2001**, 159 (1), 94-102.
- (36) Zhao, W.; Cui, H.; Liu, F.; Tan, W.; Feng, X., *Clays Clay Miner.* **2009**, 57 (5), 513-520.
- (37) Zhao, W.; Feng, X.; Tan, W.; Liu, F.; Ding, S., *J. Environ. Sci. (Beijing, China)* **2009**, 21 (4), 520-526.

CHAPTER 3

REDUCTION OF NITRITE AND NITRATE ON PYRITE

Reprinted from Publication Origins of Life and Evolution of Biospheres, 2012, 42:275–294

Soujanya Singireddy, Alexander D. Gordon, Alexander Smirnov & Michael A. Vance,

Martin A. A. Schoonen, Robert K. Szilagyi, Daniel R. Strongin

Received: 12 January 2012 / Accepted: 27 March 2012 /

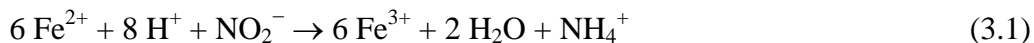
Published online: 6 May 2012

Springer Science+Business Media B.V. 2012

3.1. Introduction

The fixation of N_2 to NH_3 is often cited as a critical chemical transformation on early Earth, since it is assumed that such a reaction would be a prerequisite for the formation of important biomolecules such as amino acids, necessary for the assembly of nucleic acids (DNA, RNA) and proteins.^{1, 2} Using scientific methods to recreate likely scenarios for how this chemical transformation might have occurred has been of intense interest over the past few decades.³⁻⁸ It has been hypothesized previously that the levels of ferrous iron (Fe^{2+}), sulfate (SO_4^{2-}), NO_2^- and NO_3^- in the early ocean were significant and relevant in the context of prebiotic chemistry.^{1, 6, 9-21} Research in this area suggested that the reduction of NO_2^- to NH_3 by aqueous ferrous iron may have been a key reaction

for the reduction of nitrogen according to Eq. (3.1) in a prebiotic chemical environment.^{12, 13}



For oceanic pHs greater than 7.3, it was postulated that a steady-state concentration of ~70 μM NH_3 could be maintained.¹³ Subsequent work by Summers also showed that the ferrous iron bearing sulfide, FeS , could facilitate the transformation of NO_2^- to NH_4^+ .^{1, 12} This result is of potential importance within the context of the early Earth, considering that in an O_2 deficient environment sulfide minerals such as pyrite (FeS_2), pyrrhotite (Fe_{1-x}S), mackinawite (Fe_{1+x}S), and gregite (Fe_3S_4) would be expected to be found in abundance.^{12, 20, 21} Furthermore, it was shown that the FeS facilitated reduction of NO_2^- and NO_3^- ¹ was operative over a wider pH window, than if aqueous ferrous iron was the reductant. For example, while ferrous iron was found to reduce NO_2^- ¹³ only at solution pHs greater than 7, FeS was found to be a viable reductant of NO_2^- (to NH_3) at a solution pH as low as 4.¹

The current study builds on these seminal prior studies and extends research to understand the reduction of nitrogen oxides on pyrite (FeS_2). Pyrite is also of interest in the context of prebiotic chemistry, since it has been hypothesized that the formation of this mineral phase from FeS was a key step in prebiotic synthesis.^{3, 15, 16, 18, 19} The conditions at the Earth's crust and the associated distribution of iron sulfide minerals during the Hadean on the surface remain poorly constrained.²²⁻²⁴ Alteration of ultramafic crust with komatiitic composition is expected to lead predominantly to FeS and preclude

the presence of pyrite in extremely reducing conditions.²³ However, a more recent synthesis of the available data suggests that the Hadean crust was basaltic in composition rather than komatiitic as assumed by many.²⁴ In addition, ancient zircons formed during the Hadean suggest that in addition to basaltic rock there were some rocks with a granitic composition, although the extent of this type of rock was likely limited.²⁴ The implication is that Hadean crust may not have been as reduced as often assumed. Importantly, in all but the most reducing conditions, pyrite becomes the stable iron sulfide phase²⁵ and, therefore, its presence on the early Earth is predicted if the conditions were moderately reducing as suggested by Kasting.²⁶ In fact, it is the stability of pyrite compared to pyrrhotite that is the driving force for the reduction of carbon monoxide and carbon dioxide to reduced carbon compounds that is at the core of the “metabolism-first” theory championed by Wächtershäuser.^{15, 16, 18, 19} Hence, there are compelling reasons to study the efficacy of the conversion of NO_2^- and NO_3^- on the surface of pyrite in the context of the origin of life, even though it is almost certain that the amount of pyrite in the Hadean was more limited since microbial sulfate reduction, which drives most pyrite formation in modern sediments was not active.²⁵

The current study shows for the first time that pyrite can facilitate the reduction of NO_2^- and NO_3^- to NH_3 in the 70-120°C range. We distinguish this work from the prior research by Brandes et al.,³ which showed that pyrite could facilitate the reduction of NO_3^- (NO_2^- was not studied) to NH_3 , but at much higher temperature (500°C). While an important prior study, it did not investigate lower temperatures that may have also been important on early Earth or go into mechanistic detail: an understanding of which that may ultimately allow a molecular level view of prebiotic chemistry. Toward this end, our

study provides the first example for a combined kinetic, spectroscopic and computational modeling of the surface reactivity of pyrite with aqueous NO_2^- and NO_3^- as a function of temperature. We show using *in situ* vibrational spectroscopy that the reduction of NO_2^- on pyrite at temperatures ranging from 22°C to 120°C, and the reduction of NO_3^- on pyrite at 120°C, results in an adsorbed NO intermediate indicating the reduction of NO_3^- to NO by pyrite at this temperature. At the highest temperatures we experimentally observed the liberation of ferrous iron (Fe^{2+}) from the pyrite surface under anoxic solution conditions. Based on the experimentally determined yield of Fe^{2+} it only can account for a minor fraction of the observed NH_3 (via reaction (3.1)). Finally, it is shown that the activation of NO_3^- to form NH_3 on pyrite can only be accomplished at the highest reaction temperatures used in this study (~120°C).

3.2. Results and Discussion

This section is divided into three parts. First, kinetic data obtained from batch experiments are presented that determined the concentration of aqueous phase reactant and product species during the independent exposure of FeS_2 to NO_2^- and NO_3^- at reaction temperatures of 22°C, 70°C and 120°C. The second and third part of this section explains theoretical studies and ATR-FTIR experiments combined with the theory-based spectral assignments respectively. The computational results provide a framework to determine the origin of the stretching frequencies of the surface complexes formed on FeS_2 during exposure to aqueous NO_2^- and NO_3^- . These FTIR experiments are also

interpreted in view of the kinetic data and shed light on the surface reactions that lead to aqueous products.

3.2.1. Kinetic Data Associated with the Reduction of Aqueous NO_2^- and NO_3^- on Pyrite

Figure 3.1 plots the amount of NH_4^+ formed as a function of time for experiments where pyrite was exposed to 5 mM NO_2^- at three different reaction temperatures (22, 70, and 120°C). Also included are control experiments that monitored the amount of NH_4^+ in solution at the three different reaction temperatures for experiments with only pyrite and water present and experiments with only NO_2^- or NO_3^- present. The intent of the pyrite and water control experiments was to determine if residual NH_4^+ is formed in presence of pyrite and water, whereas the $\text{NO}_2^-/\text{NO}_3^-$ -only control experiments were designed to evaluate the stability of these species in the absence of pyrite. The control experiments indicate that after 30 h of reaction there is a low level of NH_4^+ in solution, and this background level is most noticeable at a solution temperature of 120°C ($< 3 \mu\text{mol. kg}^{-1}$). We attribute this residual NH_4^+ formed in the pyrite-only (control) experiment primarily to contamination in the reactants that were used in this study, similar to what was found for FeS surfaces in prior studies that investigated NH_4^+ production.⁵ A lower amount ($\sim 1 \mu\text{mol. kg}^{-1}$) of residual NH_4^+ also was detected at a reaction temperature of 120°C when only NO_3^- was present (pyrite absent), which might be the result of reactions with the interior surface of the reactor despite the fact that we used biocompatible materials rather than alloys.^{5,6}

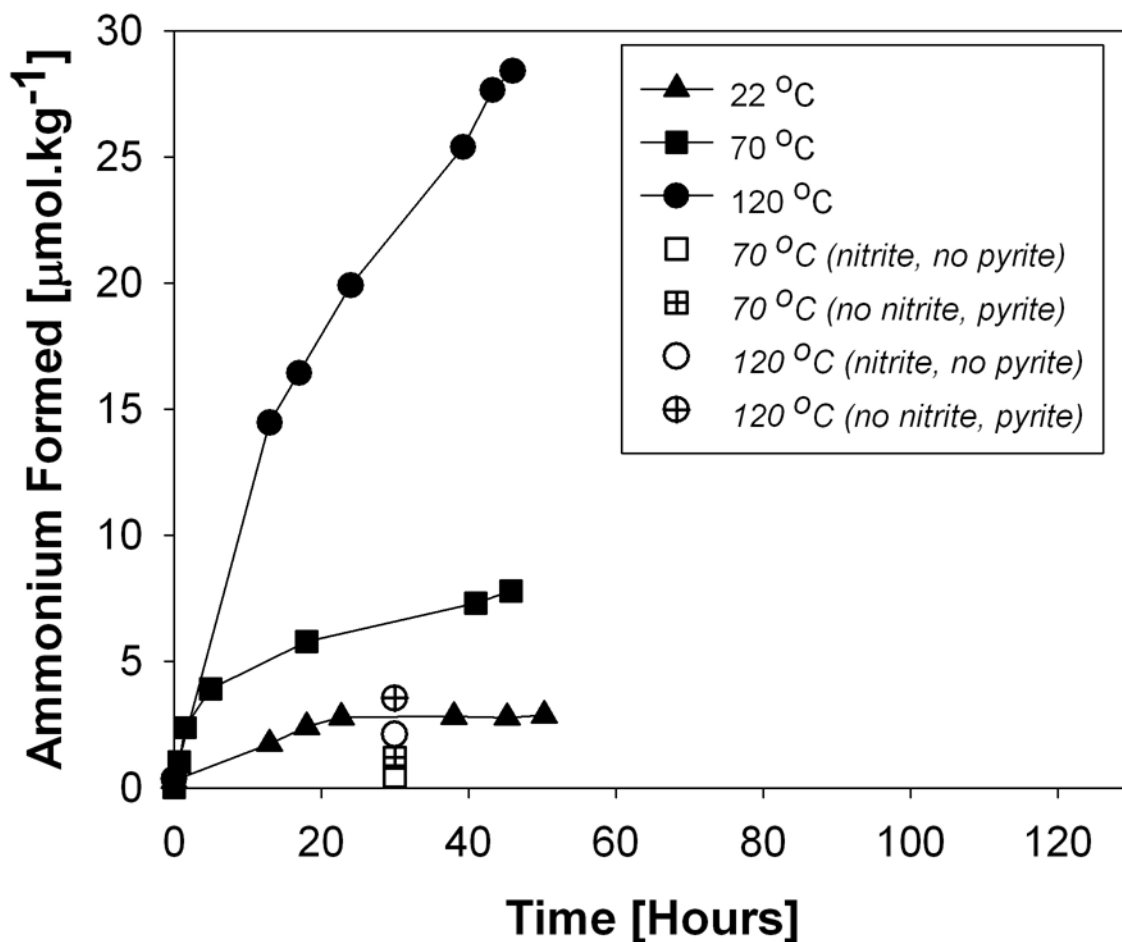


Figure 3.1. Batch experimental data showing NO_2^- reduction to NH_4^+ in presence of pyrite at 22°C, 70°C and 120°C. (Blank experiments are shown as single data points).

Inspection of the plot (Figure 3.1) shows that at a reaction time of 45 h the amount of NH_4^+ formed in the $\text{NO}_2^-/\text{FeS}_2$ reaction at 22°C (trace with triangles) is $\sim 3 \mu\text{mol. kg}^{-1}$ and any NH_4^+ formation at this temperature is unrelated to the reaction between pyrite and NO_2^- , considering that the levels of NH_4^+ in this circumstance are similar to the blank reaction where NO_2^- is not present. Data associated with the NO_2^-

/FeS₂ reaction at 70°C and 120°C, however, shows NH₄⁺ (traces with squares and circles) that can be attributed to formation from the reduction of NO₂⁻ on the pyrite surface. In particular the amount of NH₄⁺ in solution after 30 h for the 70°C and 120°C reactions is 6 and 22 μmol. kg⁻¹, respectively and after 45 h the amount of NH₄⁺ rises to 8 and 27 μmol. kg⁻¹ at 70°C and 120°C respectively.

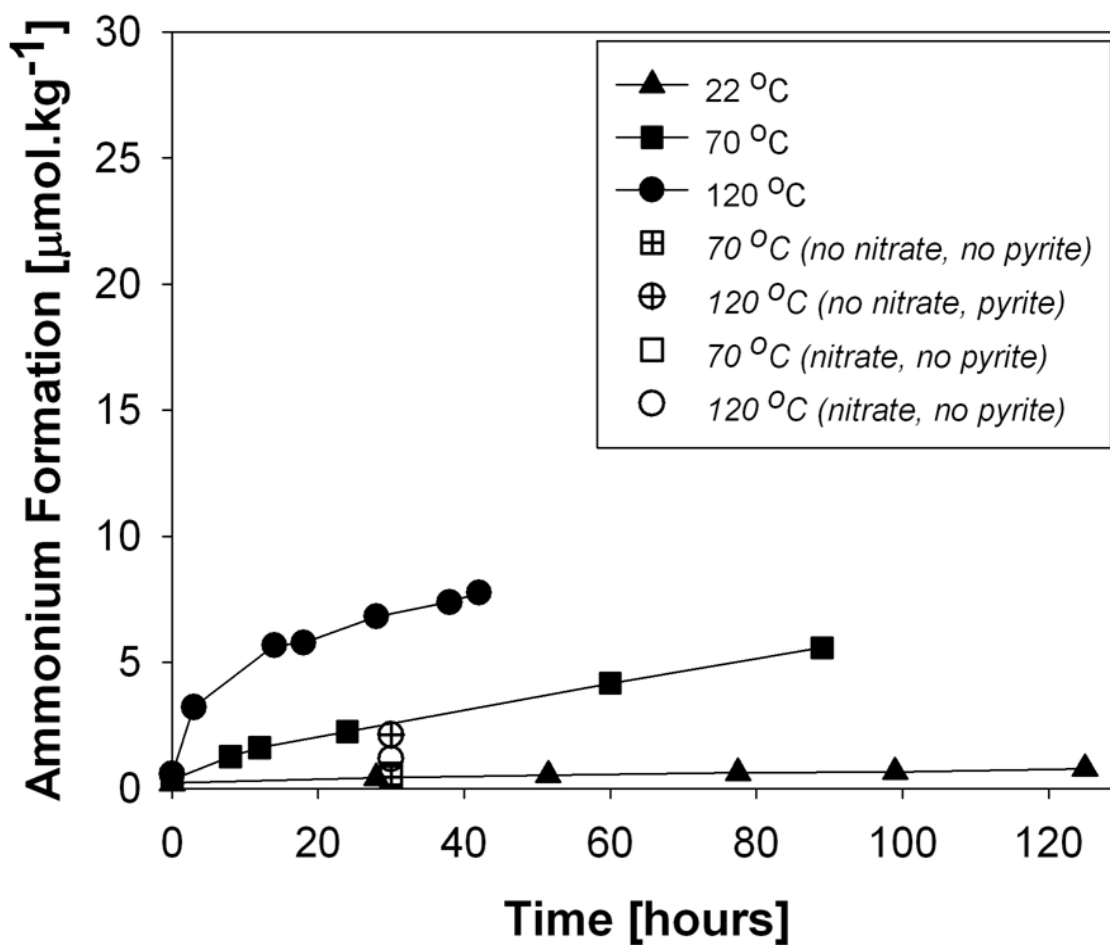


Figure 3.2. Batch experimental data showing NO₃⁻ reduction to NH₄⁺ in presence of pyrite at 22°C, 70°C and 120°C. (Blank experiments are shown as single data points).

Figure 3.2 plots the amount of NH_4^+ formed in solution as a function of time when 5 mmol. kg^{-1} of NO_3^- is exposed to the FeS_2 at reaction temperatures of 22°C , 70°C , and 120°C . Similar to our interpretation of the 22°C $\text{NO}_2^-/\text{FeS}_2$ reaction data, we attribute any NH_4^+ production at 22°C and 70°C (trace with triangles and squares) for the $\text{NO}_3^-/\text{FeS}_2$ reaction to be due to residual reactions not related to the reaction of NO_3^- and pyrite. At reaction temperatures of 120°C , the amount of NH_4^+ in solution (trace with circles) is attributed to the reaction of pyrite and NO_3^- , since the amounts of NH_4^+ produced after 30 h are significantly greater than background levels shown by the relevant control experiment data points. In general, the amount of NH_4^+ formation associated with the reaction of NO_3^- with pyrite is significantly less than what is formed via the reaction of NO_2^- with pyrite at a similar temperature. For example, the amount of NH_4^+ production associated with the 120°C $\text{NO}_3^-/\text{FeS}_2$ and $\text{NO}_2^-/\text{FeS}_2$ systems at a 40 h reaction time is 8 and $26 \text{ } \mu\text{mol. kg}^{-1}$, respectively. The straight-forward interpretation of our experimental data is that NO_2^- is converted to NH_4^+ product on pyrite faster than NO_3^- is.

Figure 3.3 shows plots of the amount of NO_2^- and NO_3^- in solution as a function of time during the exposure of FeS_2 to aqueous NO_2^- at a reaction temperature of 22°C (Figure 3.3a), 70°C (Figure 3.3b), and 120°C (Figure 3.3c). At 22°C the exposure of FeS_2 to NO_2^- (Figure 3.3a), results in no significant change in the NO_2^- reactant concentration, consistent with the lack of NH_4^+ formation in this circumstance (Figure 3.3, traces with triangles and squares). At 70°C , we observed a $\sim 200 \text{ } \mu\text{mol. kg}^{-1}$ decrease in the amount of NO_2^- over 40 h of reaction. The decrease far exceeds the amount of NH_4^+ in solution ($8 \text{ } \mu\text{mol. kg}^{-1}$). At a reaction temperature of 120°C , essentially all of the NO_2^- was

consumed (5 mmol. kg^{-1}), even though the amount of NH_4^+ in solution did not exceed $28 \text{ } \mu\text{mol. kg}^{-1}$. It is emphasized that this loss in NO_2^- only occurs when pyrite is present, based on the control experiment shown for the 120°C reaction, where there is no decrease in NO_2^- in the absence of pyrite over 40 h. Furthermore, the exposure of FeS_2 to NO_3^- reactant did not result in a significant change in NO_3^- concentration at any of the three studied reaction temperatures (data is not shown).

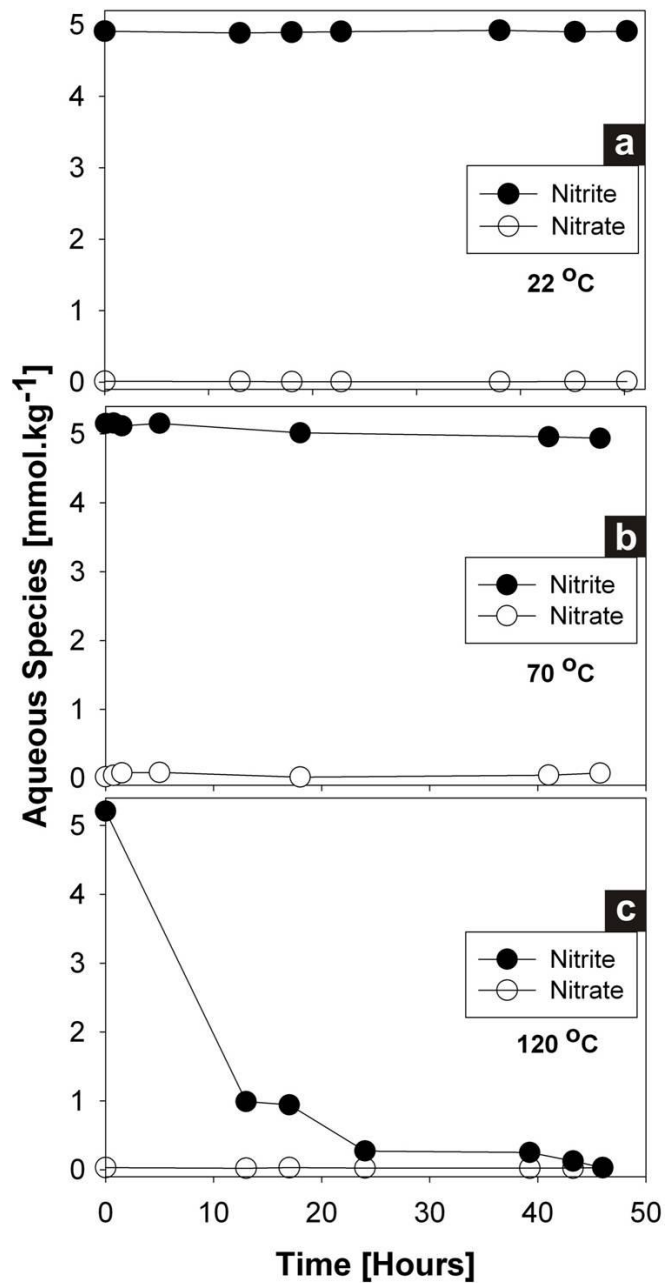
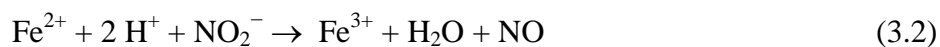


Figure 3.3. Concentration of NO_2^- reactant and NO_3^- product as a function of time when the pyrite containing reaction solution is at a temperature of (a) 22°C , (b) 70°C , and (c) 120°C .

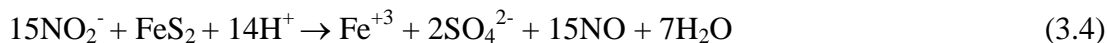
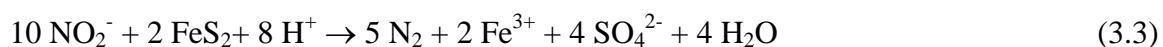
To better understand the chemistry that occurred leading to the loss of NO_2^- in the presence of pyrite at 120°C , we conducted a limited set of measurements to determine the amount of sulfate in solution during 40 h of reaction for the NO_2^- /pyrite and pyrite-only systems at a temperature of 120°C . In the absence of NO_2^- , pyrite heated to 120°C in the reactor led to a SO_4^{2-} concentration of $320 \mu\text{mol. kg}^{-1}$ and in the presence of NO_2^- the concentration of SO_4^{2-} was $500 \mu\text{mol. kg}^{-1}$. SO_4^{2-} generation in absence of NO_2^- is likely due to the reaction of water with defects on pyrite at this temperature.²⁷ We attribute the extra amount of sulfate (i.e., $180 \mu\text{mol. kg}^{-1}$) formed in the presence of NO_2^- to the oxidation of the sulfur component of pyrite with the simultaneous reduction of NO_2^- . Additional analyses of the solution phase for both systems showed ferrous iron in solution in the absence of NO_2^- ($30 \mu\text{mol. kg}^{-1}$). Taken together with SO_4^{2-} formation, this observation suggests that defect or non-stoichiometric sites on pyrite, highlighted in prior work,²⁷ react at hydrothermal conditions i.e. at high temperatures and pressures resulting in some dissolution of the pyrite particles. In fact, this observation is the first to show that dissolution of pyrite and the formation of aqueous Fe^{2+} and SO_4^{2-} can occur in anoxic water at elevated temperature.

In the presence of NO_2^- , there was no aqueous Fe^{2+} after 40 h of reaction with pyrite. Based on this experimental observation, we speculate that at least a portion of the aqueous NO_2^- was reduced by $\text{Fe}^{2+}_{(\text{aq})}$ (see reaction. 3.1), since prior studies have shown that the reduction of NO_2^- by Fe^{2+} could result in the formation of either NO (equation 3.2)²⁸ or NH_4^+ (equation 3.1),^{12, 13} albeit, at room temperature.



These prior studies, however, showed that the reduction of NO_2^- by aqueous Fe^{2+} only showed measureable NH_4^+ formation at pH 7 or higher. Thus, we cannot state with confidence at this point that a similar reduction process occurred in our experiments, considering that our solution pH was near 5. What we can state is that even if such a reduction process was operative under our experimental conditions, it could not account for the entire yield of NH_4^+ . For example, as mentioned above we experimentally observed $30 \mu\text{mol.kg}^{-1}$ of $\text{Fe}^{+2}/\text{Fe}_{\text{TOT}}$, when a pyrite suspension was heated to 120°C for 49 h. If this amount of ferrous iron went on to reduce NO_2^- , then the maximum amount of NH_4^+ (see equation (3.1)) produced would be $5 \mu\text{mol.kg}^{-1}$ of NH_4^+ . Hence, this reaction could only account for <20% of the total NH_4^+ product after 49 h of reaction of the NO_2^- /pyrite system at a solution temperature of 120°C .

Along with NH_4^+ formation, we also suggest additional reaction pathways (reaction 3.3 and 3.4) for the consumption of NO_2^- .



GC analysis of the head space of the reactor shows the presence of $44.19 \mu\text{mol}$ of N_2 product. The initial total amount of NO_2^- in the reactor was $100 \mu\text{mol}$. Hence, based on these results the primary loss mechanism for aqueous NO_2^- is the formation of N_2 product (reaction 3.3). The remaining NO_2^- presumably is involved in the formation of

NH_4^+ and NO (reaction 3.4) with the latter species probably also transforming in part to NH_4^+ as discussed below. Reactions 3.3 and 3.4 are believed to be operative, since pyrite is implicitly involved, NO_3^- is not a reaction product, Fe^{3+} and SO_4^{2-} are reaction products, and spectroscopic results presented below show that NO is adsorbed on the pyrite surface during the consumption of NO_2^- . We, however, find no evidence for gaseous NO product in the reactor headspace.

Finally, the disproportionation of the aqueous NO_2^- could occur in the presence of pyrite.²⁹



This reaction cannot be the primary mechanism for the loss of NO_2^- considering that we do not observe a significant amount of NO_3^- in solution. We, however, see evidence for adsorbed NO_3^- on pyrite when the mineral is exposed to NO_2^- (presented in the following section).

In order to identify the intermediates and products formed during the batch reactions we carried out *in situ* reactions using ATR-FTIR spectroscopy. The assignments of vibrational bands were made by comparing with literature reference data and the calculated N-O stretching frequencies from our computational model. We present the theoretical studies first, since they provide a basis by which the experimental results can be interpreted.

3.2.2. Density Functional Theory (DFT) Modeling of Surface Bound Nitrogen Oxide Species

Theoretical estimates of N-O stretching frequencies were obtained from density functional theory calculations using Becke exchange and Perdew correlation functionals (BP86)^{30, 31} with triple- ζ quality Gaussian type basis set (TZVP)³² as implemented in Gaussian03³³.

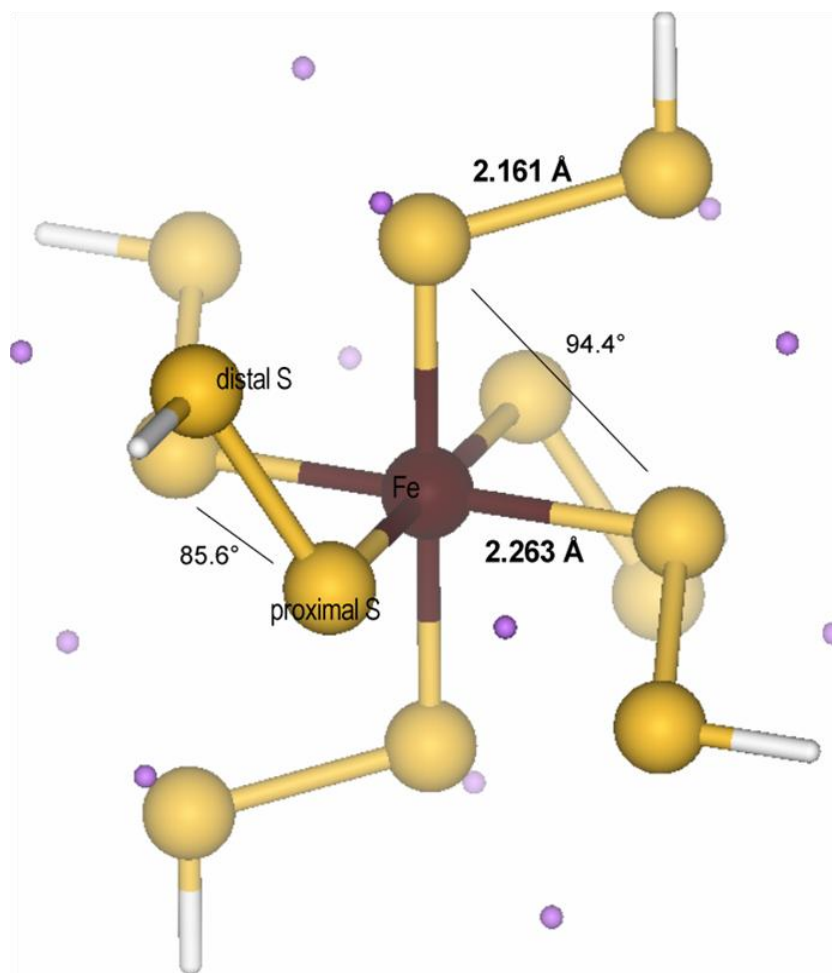


Figure 3.4. First generation coordination chemical model of single iron site in bulk pyrite (all S-S and Fe-S distances are as specified. Trans Fe-S-Fe angles are all 180°).

The coordination chemical model (Figure 3.4) for a mononuclear iron site on a pyrite surface was constructed from the highest resolution crystal structure (R value of 0.0173, ICSD # 109377) of cubic pyrite with a lattice constant of 5.416 Å³⁴. In this model, the central Fe²⁺ ion was coordinated by persulfhydryl ligands (HSS⁻). The position of the hydrogen atom was chosen based on the shortest Fe-S distance from the first sphere of iron sites around the inner sphere of persulfide ligands of the central Fe²⁺ ion. We used this replacement to recapture some of the covalent bonding interactions that a persulfide ligand experiences when bound to neighboring iron sites. For charge neutrality, all other first sphere iron sites (12 in a bulk model, see pink dots in Figure 3.4) were replaced by a point charge. In order to distinguish between the two sulfur sites, the one directly attached to the iron will be referenced as the proximal site, while the one attached to the terminating hydrogen is the distal site. This computational model was considered as a first generation, coordination chemical model for a single iron site, because it only contains the inner sphere coordination environment of the iron ion. The elimination of the top sulfhydryl group as shown in Figure 3.4 opens up a coordination site for various nitrogen oxide species studied and hence provides a reasonable molecular model for the surface bound nitrogen-oxide species. Considering the charge of the central iron ion (Fe²⁺) and the five surrounding persulfhydryl ligands (HSS⁻), the surface model was neutralized by 8 counter ions, each having +0.375 e⁻ charge.

In order to approximate the upper limit of steric, electronic, and electrostatic influence of mineral bulk on a single iron site on a pyrite surface, we kept the positions fixed for the hydrogen atoms and the attached distal sulfur atoms in structural optimizations. All plausible spin states for the central iron ion were evaluated.

Vibrational analyses were carried out only for the lowest energy, ground state spin state. Due to the highly constrained nature of the computational model, imaginary frequencies were obtained for normal modes involving H-S and S-S bond stretches and associated angle bending modes and their combinations; however, these would mainly affect the results of thermo chemistry calculations and not the N-O stretches that are of interest here.

A critical component of predicting N-O stretching frequencies, which then can be used to aid the assignment of spectral features observed in our experiments, is how well the iron site that is coordinated by nitrogen-oxide species is represented electronically and geometrically. Due to the small size of the studied nitrogen-oxide species, we do not expect any considerable steric interaction between the surface and the coordinating substrate or product ligand. Although simplified, this computational model can be considered as suitable for identifying distinct nitrogen-oxide species by their unique set of vibrational frequencies.

Figure 3.5 summarizes a representative set of adsorbate/surface models that were used in the DFT calculations. Shown alongside the models are selected vibrational frequencies calculated for each complex configuration. Before the ATR-FTIR experimental results are presented, it is useful to comment on some issues brought forward by the calculations. An analysis of the calculated frequencies shows that the studied spectral range can be separated into two general regions. The highest frequency or wave number region, which lies above the water bending frequency region (at around $\sim 1600\text{ cm}^{-1}$), contains vibrational modes associated with surface bound NO species ($\sim 1737\text{ cm}^{-1}$). This vibrational frequency is red-shifted by about 100 cm^{-1} relative to

gaseous NO ($\sim 1875\text{ cm}^{-1}$),³⁵ which is due to the NO ligand accepting electron density from the formally Fe^{2+} ion that is effectively reduced approximately to Fe^{1+} level due to the ligand to metal donation from the persulfide anionic persulfide ligand. The $\text{Fe}\rightarrow\text{NO}$ donation results in increased electron density of the π^* orbitals (π backbonding) of NO, which decreases the vibrational frequency of surface bound NO compared to that of gaseous NO.³⁵ Thus, the $[\text{L}(\text{S}^-)\text{-Fe}^{\text{II}}]\text{-NO}$ species can also be described with a probable resonance structure pair of $[\text{L}(\text{S}^-)\text{-Fe}^{\text{I}}]\text{-NO} \leftrightarrow [\text{L}(\text{S}^-)\text{-Fe}^{\text{II}}]\text{-NO}^-$.

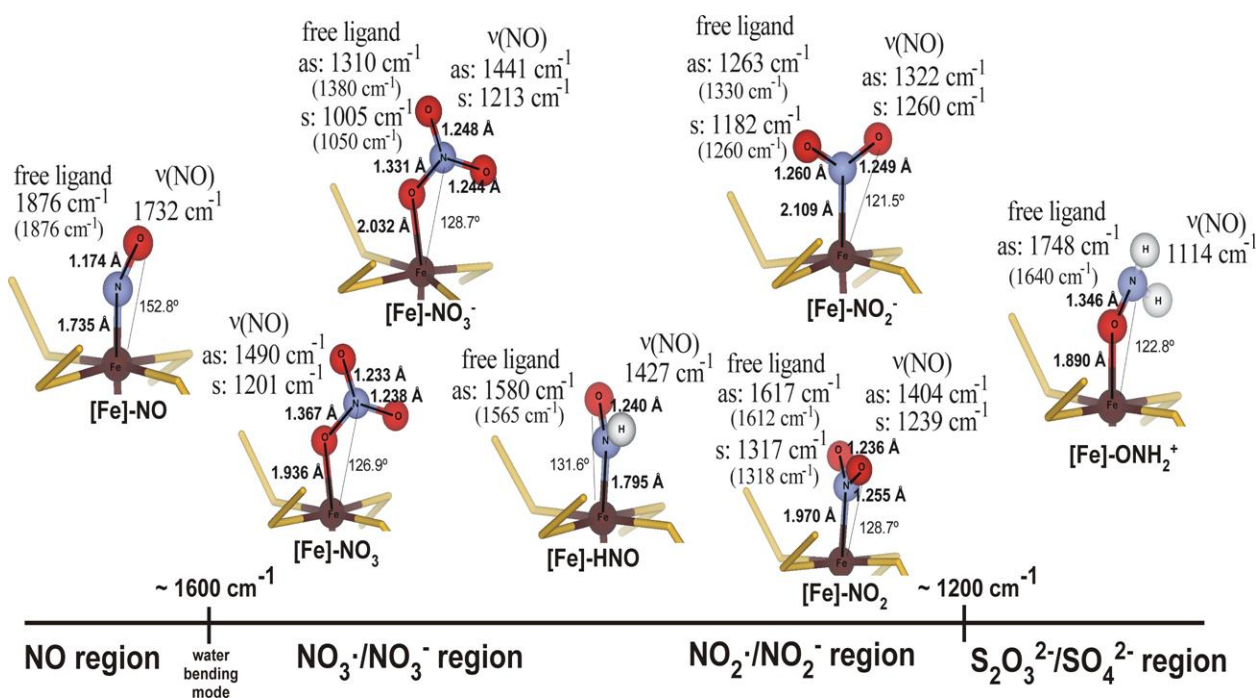


Figure 3.5. Computational models for a representative set of surface bound nitrogen oxide intermediates with optimized Fe-N, N-O bond lengths, and Fe-N-O bond angles. Calculated and experimental (in parenthesis) N-O stretching frequencies for the free and coordinated forms.

The NO_3^- and NO_2^- region, between 1600 cm^{-1} and 1200 cm^{-1} , is somewhat overlapped especially when the radical forms of the anions are considered. The higher energy vibrations originate from $\text{NO}_3\cdot$ ($\sim 1490\text{ cm}^{-1}$) and NO_3^- ($\sim 1441\text{ cm}^{-1}$) species, with the asymmetric N-O stretching modes of these species being at significantly higher wave numbers than the corresponding modes associated with $\text{NO}_2\cdot$ ($\sim 1402\text{ cm}^{-1}$) or NO_2^- species ($\sim 1322\text{ cm}^{-1}$), respectively. Interestingly, calculations show that the N-O stretch in NO_3^- shifts up by about 200 cm^{-1} upon binding to the surface. This particular theoretical observation is rationalized by noting that there is a reduction in the electron-electron repulsion (upon complexation with the Fe-S cluster) among the peripheral O atoms as well as formation of better N-O bond overlap resulting from an increase in the O effective nuclear charge. The latter is due to the ligand-to-metal donation from the O atoms to the formally Fe^{2+} centers. In contrast, surface bound NO_2^- shows a downward shift in N-O stretching frequency relative to the free aqueous species (by $\sim 100\text{ cm}^{-1}$). We mention that in the case of NO_2^- , calculations indicate that the N-coordinated NO_2^- (nitro) configuration is about 60 kJ/mol more stable than the O-coordinated nitrito isomer. In short, the N-O bonds become stronger in the NO_3^- species, since NO_3^- coordinates via oxygen lone pairs to the surface, relative to the NO_2^- that directly binds to Fe through an N-atom. Based on these theoretical results, it is perhaps not surprising that NO_3^- showed less propensity to reduction to NH_4^+ in the experimental results presented above.

Inspection of Figure 3.5 also shows that the N-O stretching frequency range between ~ 1200 and 1600 cm^{-1} is populated by protonated, surface bound, and effectively reduced NO species due to electron donation from the Fe center. Of note is that the N-O

stretch associated with the coordinated HNO ligand (1427 cm^{-1}) shows a red shift of $\sim 140\text{ cm}^{-1}$ compared to the free HNO ligand at 1565 cm^{-1} ³⁶ suggesting that a significant weakening of the N-O bond is caused by the complexation with the Fe-S surface. Calculation suggests that the second N-protonated form, ONH_2^+ changes its coordination mode from N- to O-bound (relative to the HNO ligand). The difference between the N-O stretch associated with the free and coordinated ligand is $\sim 600\text{ cm}^{-1}$, indicating that the O=N bond is expected to be broken upon coordination. Such a bond breaking step is expected to precede the additional two electron reduction and consecutive or simultaneous protonation steps that ultimately lead to NH_4^+ formation.

3.2.3. ATR-FTIR of NO_2^- (aq) Adsorption on FeS_2

Figure 3.6 shows time-dependent ATR-FTIR data associated with an aqueous suspension of FeS_2 that had been exposed to NO_2^- at $22\text{ }^\circ\text{C}$. Based on these ATR-FTIR data, we propose that NO_2^- (aq) adsorption on pyrite results primarily in the formation of adsorbed $(\text{NO})_2$. We base this suggestion on the presence of a vibrational mode at 1776 cm^{-1} that we attribute to the $\nu_{\text{as}}(\text{N}=\text{O})$ stretching vibration of adsorbed $(\text{NO})_2$. It is noted that this assignment also is consistent with prior research that has shown a similar vibrational mode of $(\text{NO})_2$ attached to iron in iron nitrosyl complexes.³⁷ This mode was also observed by Andrews et al.³⁸ when NO and sulfur were codeposited in argon and also observed by several authors, when gaseous NO was adsorbed on a variety of metal surfaces.³⁹⁻⁴³

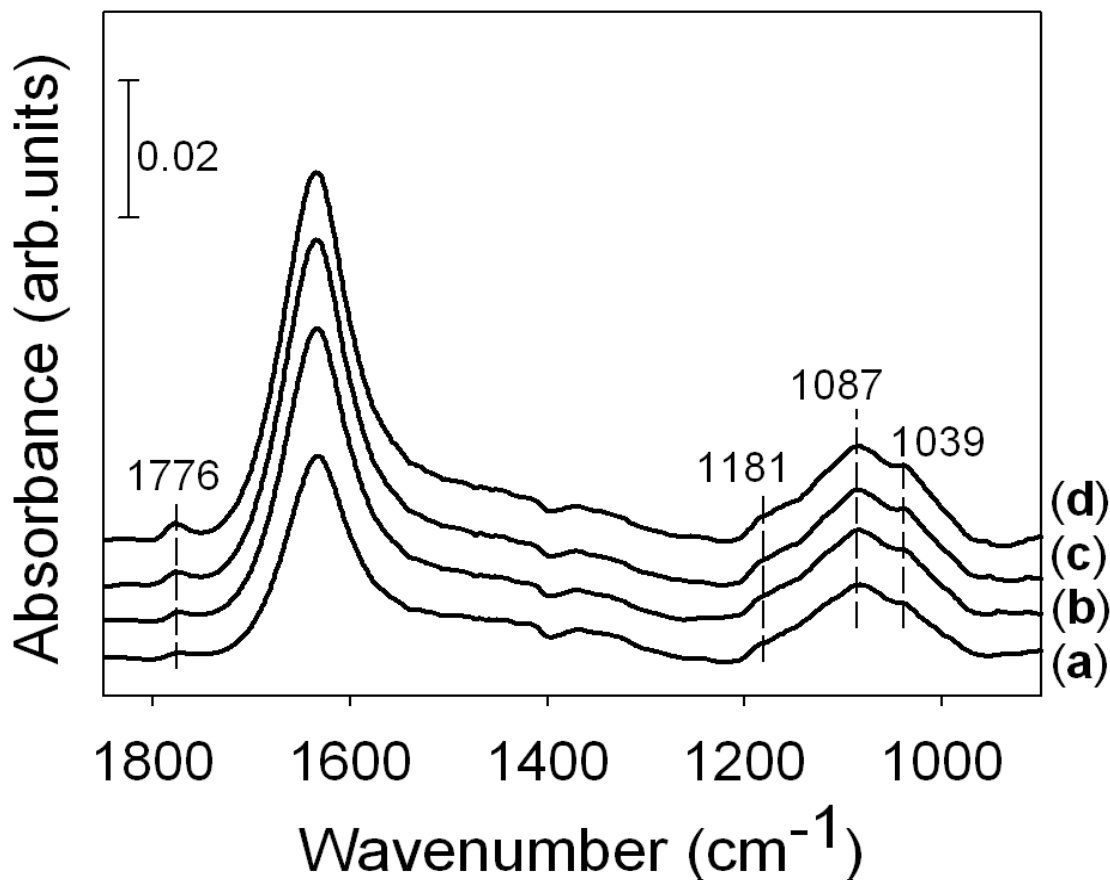


Figure 3.6. ATR-FTIR spectra obtained during the reaction of NO_2^- with pyrite at room temperature (22°C) after (a) 30 min (b) 60 min (c) 120 min, and (d) 180 min. The vibrational mode at $\sim 1630\text{ cm}^{-1}$ is due to O-H bending vibrations of water.

In addition to the modes that are assigned to NO_{ad} , modes are present below 1200 cm^{-1} . The absence of modes near 1450 cm^{-1} (where $\nu_{\text{as}}(\text{NO}_2)$ modes appear) would call into question the assignment of the 1181 , 1087 , and 1039 cm^{-1} modes to the symmetric stretching mode of adsorbed NO_2 species. Instead we favor the assignment of these modes to adsorbed sulfur oxyanions based on prior studies⁴⁴. While speculative at this

point, the reduction of NO_2^- to NO (which we do observe) is likely coupled with the oxidation of the sulfur component of pyrite to form sulfate as shown in reaction (3.5), where the SO_4^{2-} exists as an adsorbed and aqueous species and NO as an adsorbed and/or gaseous species (existing in the reaction headspace). Prior research^{44, 45} has shown that pyrite oxidation includes SO_4^{2-} production as a result of persulfide/ sulfide oxidation and the subsequent attack of the electron deficient sulfur by water. This mechanism is supported in earlier work primarily by the experimental observation (using isotopic labeling) that the vast majority of the oxygen in the sulfate product is derived from water.^{44, 45}

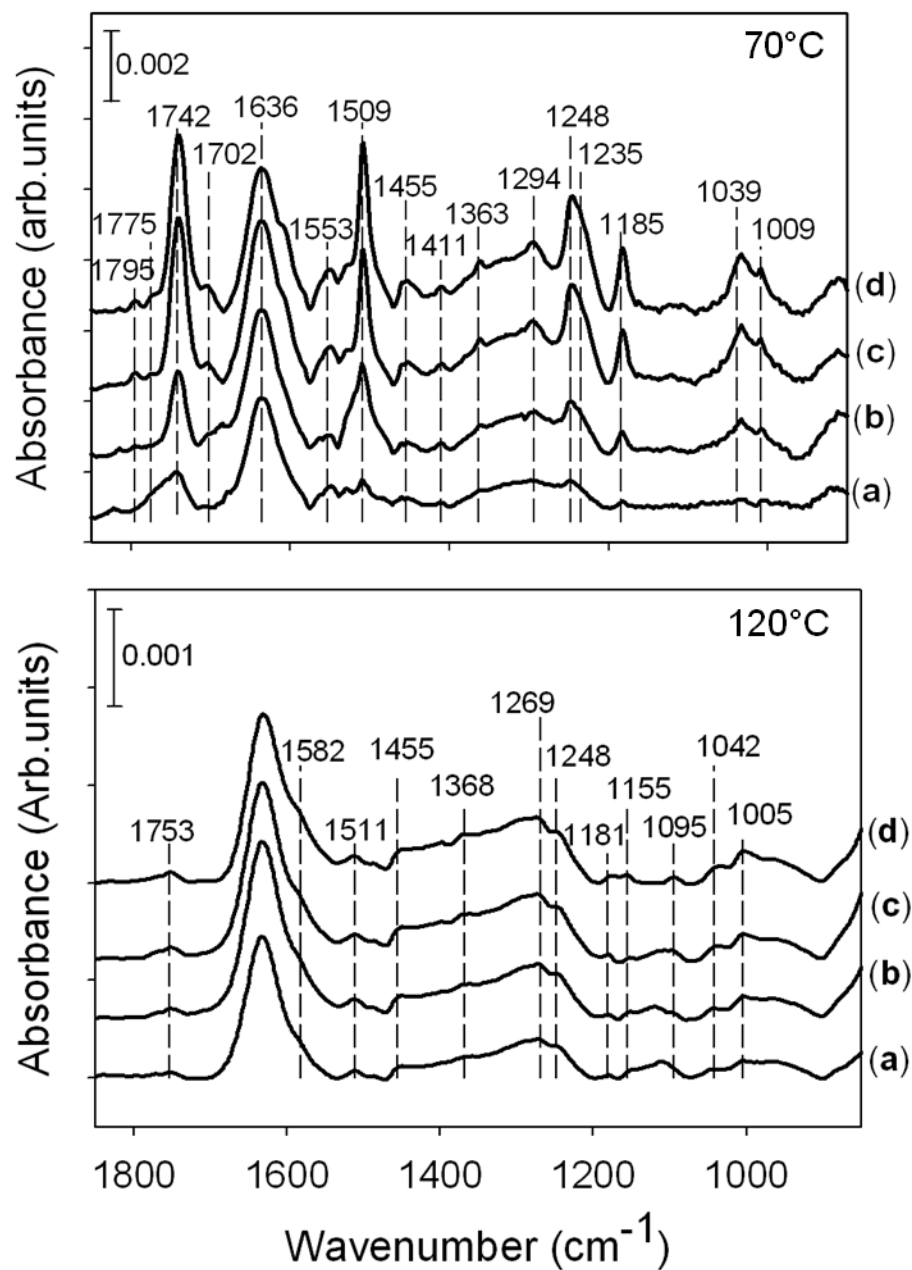


Figure 3.7. ATR-FTIR spectra obtained during the reaction of NO_2^- with pyrite at 70°C (Top figure) after reaction times of (a) 9 min (b) 30 min (c) 130 min, and (d) 180 min. The vibrational mode at $\sim 1630\text{ cm}^{-1}$ is due to O-H bending vibrations of water. Bottom figure is the ATR-FTIR spectra obtained during the reaction of NO_2^- with pyrite at 120°C

after reaction times of (a) 30 min (b) 60 min (c) 120 min, and (d) 180 min. The vibrational mode at $\sim 1630\text{ cm}^{-1}$ is due to O-H bending vibrations of water.

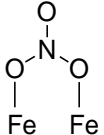
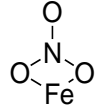
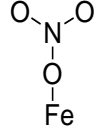
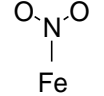
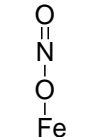
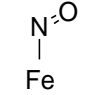
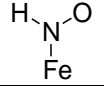
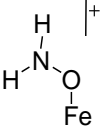
The reaction of NO_2^- with pyrite at a solution temperature of 70°C leads to a significantly higher concentration of surface species as evidenced by the ATR-FTIR data presented in Figure 3.7. This increased concentration of surface species suggests in general the activation of NO_2^- by the pyrite surface and is consistent with the increased amount of NH_4^+ formation at 70°C relative to the 22°C reaction from the batch reactions presented above. Data in Figure 3.7 shows that in contrast to the 22°C reaction, the exposure of FeS_2 to NO_2^- at 70°C results in the appearance of peaks at 1742, 1636, 1509, and 1248 cm^{-1} (broad peak with a shoulder at 1235 cm^{-1}). We assign the peak at 1742 cm^{-1} to surface bound NO species based on calculation and prior research.^{41, 43} After a reaction time of 1 h weak vibrational modes appear at 1795, 1775, and 1702 cm^{-1} . Based on prior studies, we assign the 1795/1775 cm^{-1} pair and 1742/1702 cm^{-1} pair to dinitrosyl species, where two NO molecules are adsorbed individually on the same Fe atom in contrast to a coordinated N_2O_2 dimer.^{46, 47} Using the first generation computational model of a S rich pyrite surface, we could not verify this mode due to the unlikeliest presence of a seven-coordinate iron site. The inspection of the vibrational data of $\text{FeS}_2/\text{NO}_2^-$ reaction at 70°C (Figure 3.7) also brings forward some surface complexes that are likely relevant to the adsorption of NO_2^- on the surface of FeS_2 . Specifically, based on our calculations peaks in the 1235 to 1455 cm^{-1} vibrational window are assigned to NO_2^- surface complexes (Table 3.1). In addition to NO_2^- , we attribute vibrational modes between 1009 - 1553 cm^{-1} to NO_3^- surface complexes (Table 3.1). An additional mode at

1411 cm^{-1} was assigned to the adsorbed HNO species, based on the calculations. The batch geochemical results presented above do show the presence of aqueous NO_3^- , although in very low amounts ($< 3 \mu\text{mol kg}^{-1}$). We propose that the NO_3^- was formed in these experiments due to the disproportionation of NO_2^- (see reaction 3.5) and/or due to the oxidation of NO_2^- to NO_3^- via the generation of reactive oxygen species that has been shown to occur by Borda et al.⁴⁸ in a prior study of pyrite oxidation. SO_4^{2-} modes were observed at 1185 and 1009 cm^{-1} ⁴⁴.

The increase in reaction temperature from 70°C to 120°C (Figure 3.7) results in an overall decrease in intensity of the modes associated with surface complexes. This experimental observation suggests that the steady-state concentration of surface species on pyrite at 120°C is less than at 70 °C. Kinetic results show that the formation of NH_4^+ at this higher temperature is significantly greater than at the lower temperatures, suggesting that the lower concentration of surface intermediates adsorbed on pyrite may be simply due to an enhanced turnover rate to form product. The majority of the vibrational modes are similar to the 70°C reaction temperature data. Surface NO (ν_{as} (N=O) at 1753 cm^{-1}) and NO_3^- , for example, are observed at this temperature similar to the 70 °C experiment (Table 3.1). In addition to these modes a single mode due to the ONH_2^+ was observed around 1155 cm^{-1} . We assign modes at 1181, 1095 and 1005 cm^{-1} modes to sulfate⁴⁴.

In no circumstance we experimentally observe modes on the pyrite surface that can be attributed to adsorbed NH_4^+ , suggesting that NH_4^+ formed at the 70 and 120°C partitions rapidly from the FeS_2 surface to the aqueous phase.

Table 3.1. Calculated and experimental vibrational frequencies of the intermediates and the products formed during NO_2^- and NO_3^- reduction on FeS_2 surface at 70°C and 120°C

Assignments	Representation	Calculated modes (cm^{-1})	Experimental modes (cm^{-1}) $\text{FeS}_2/\text{NO}_2^-$, 70°C	Experimental modes (cm^{-1}) $\text{FeS}_2/\text{NO}_2^-$, 120°C	Experimental modes (cm^{-1}) $\text{FeS}_2/\text{NO}_3^-$, 70°C	Experimental modes (cm^{-1}) $\text{FeS}_2/\text{NO}_3^-$, 120°C
Bridging bidentate Nitrate		1041	1039	1039	1042	1042→1036
Bidentate nitrate		1549	1553	1582	1556	1582
Monodentate nitrate		1441, 1213	1455, 1248	1455, 1248	1447, 1248	1455, 1248
Monodentate Nitrate radical		1490, 1201	1509	1511	1509	1511
Monodentate Nitro		1444, 1176	1455	1455	1447	1455
Monodentate nitrito		1322, 1260	1294	1269	1305, 1248	1285
Monodentate nitrite radical		1402, 1239	1363, 1235	1368	1363, 1230	-
NO		1737	1795, 1775, 1742, 1702	1753	-	1753, 1702
HNO		1427	1411	-	-	-
H_2NO^+		1114	-	1155	-	1155

3.2.4. ATR-FTIR of NO_3^- (aq) Adsorption on FeS_2

Figure 3.8 shows ATR-FTIR data for FeS_2 exposed to NO_3^- at 70°C . The batch experiments presented above showed that NH_4^+ production from the reaction of NO_3^- with FeS_2 was insignificant up to 70°C . Perhaps the most revealing aspect of the vibrational data is the absence of mode(s) that can be associated with an adsorbed NO on the FeS_2 surface above the water bend of 1633 cm^{-1} . These observations are in stark contrast to the chemistry associated with NO_2^- and suggest that the reduction of NO_3^- is not a facile process on FeS_2 . The vibrational data does, however, show that NO_3^- adsorbs on FeS_2 , as suggested by the presence of vibrational peaks at 1509 cm^{-1} (monodentate nitrate radical, NO_3^\cdot), 1447 and 1248 cm^{-1} (monodentate nitrate). Interestingly, all these modes are consistent with the modes observed when NO_3^- was formed from NO_2^- in presence of FeS_2 at 70°C . We did not observe NO, as a stable species, but the peaks associated with NO_2^- are apparent between 1230 and 1447 cm^{-1} (see Table 3.1 for assignments) that agrees well with the calculated vibrational frequencies of the NO_2^- complexes. SO_4^{2-} modes were observed at 1181 , 1090 and 1005 cm^{-1} . This result suggests that there is some reduction of NO_3^- to NO_2^- on pyrite, but further reduction to NO and ultimately to NH_4^+ is likely kinetically hindered. Kampschreur et al. ²⁸ stated that the further reduction of NO occurs mainly through the Fe(II) adsorbed to the surface of the mineral (solid bound Fe(II)) as solid bound Fe(II) is a strong reducing agent than the dissolved Fe(II). Hence the reduction of NO to NH_4^+ has not occurred at 70°C as there is no Fe^{2+} formed at this temperature.

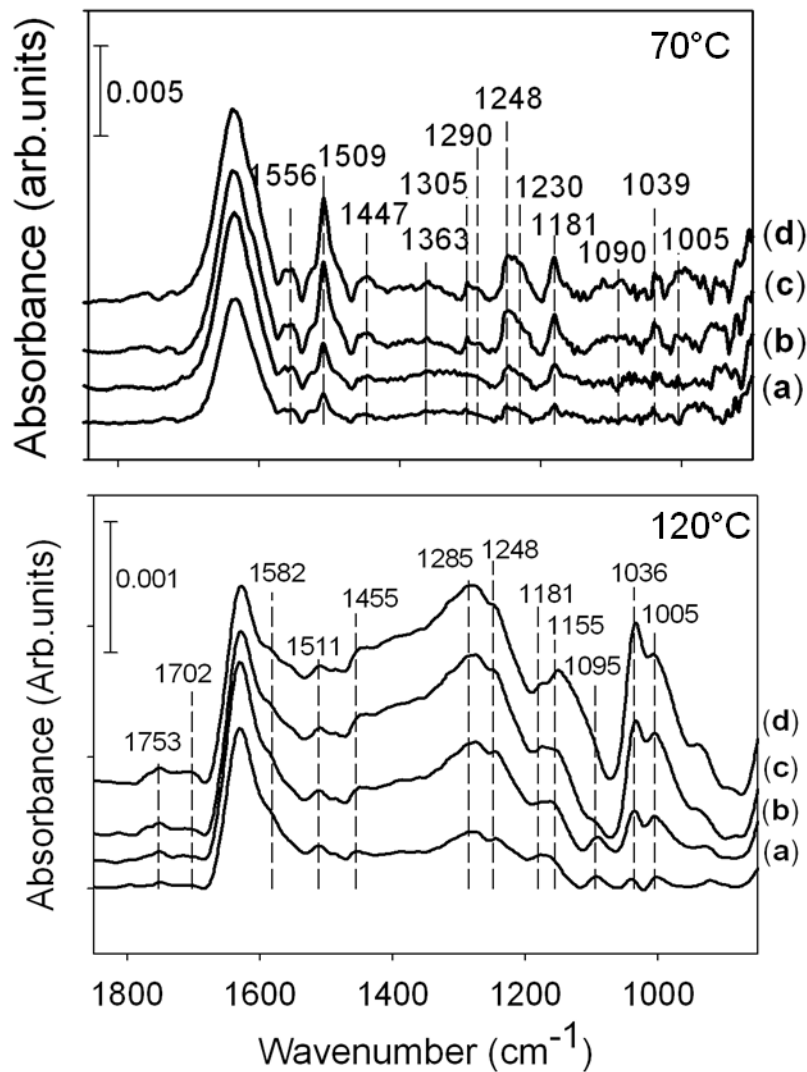


Figure 3.8. Top figure is the ATR-FTIR spectra obtained during the reaction of NO_3^- with pyrite at 70°C after reaction times of (a) 9 min (b) 30 min (c) 130 min, and (d) 180 min. The vibrational mode at $\sim 1630\text{ cm}^{-1}$ is due to O-H bending vibrations of water. Bottom figure is ATR-FTIR spectra obtained during the reaction of NO_3^- with pyrite at 120°C after reaction times of (a) 30 min (b) 60 min (c) 120 min, and (d) 180 min. The vibrational mode at $\sim 1630\text{ cm}^{-1}$ is due to O-H bending vibrations of water.

The increase in temperature from 70°C to 120°C (Figure 3.8) results in significant changes in the IR spectrum of the surface complexation of the pyrite, consistent with the kinetic results that show significant ammonium production at this elevated temperature. Inspection of Figure 3.8 shows that after 1 h of reaction, modes appear at 1753 and 1702 cm^{-1} , which we attribute to NO_{ad} . Hence, nitrate is activated to NO at 120°C and not at 70°C. The majority of the modes observed for the NO_3^- /pyrite system are similar to those modes that appear when FeS_2 is exposed to NO_2^- at 120°C (see Table 3.1 for assignments), indicating that stable NO_2 species are forming on the pyrite surface under these elevated conditions in addition to the NO complex.

3.3. Mechanistic Implications

Iron⁶ and iron mono sulfide^{1, 13} minerals have already been shown to facilitate ammonia formation from NO_2^- and NO_3^- in solution over a wide range of pH values. This study establishes that pyrite, an iron disulfide mineral-pyrite being the most abundant iron sulfide mineral on Earth²⁵, can facilitate the formation of NH_4^+ . Based on our NO_2^- and NO_3^- reduction experiments using pyrite, we suggest that nitric oxide is a likely intermediate during the formation of NH_4^+ . Hence, nitric oxide gas formed in the atmosphere by lightning and electric discharges¹⁴ can be a source of NH_3 or dissolved NH_4^+ once it becomes the part of the hydrosphere through dissolution and reaction with pyrite in addition to FeS, Fe(II).^{1, 13} The overall reduction of adsorbed NO can be

represented by reaction 3.6. It is postulated that the stable intermediate surface complexes formed in our experiments is a reason for the relatively low NH_4^+ yields.



We propose that pyrite is the electron donor, which leads to the formation of SO_4^{2-} and/or Fe^{3+} ; with the former product being found to be present on the pyrite surface as well as in the aqueous phase. As mentioned above, we also believe that the reduction of NO_2^- by aqueous Fe^{2+} is another pathway to NH_4^+ in our experiments, but our data does not allow us to determine the relative contribution of each reaction pathway.

Overall, experimental observations and theoretical modeling suggest that N-bound species to the pyrite surface tend to be more reactive, because of considerable Fe→ligand donation. This donation facilitates the protonation at the N-site to form HNO. Interestingly, the second protonation toward the ONH_2^+ intermediate likely results in a change of the coordination mode and spontaneous activation of the O-N bond for the final cleavage. It is expected that the proximal sulfur atom will be involved in the last step either as a catalytic site for electron acceptor or stoichiometric reaction partner forming a thiosulfate/sulfate by-product upon NH_4^+ formation.

3.4. Conclusions

NH_4^+ was synthesized in $\mu\text{mol.kg}^{-1}$ solution quantities under anaerobic conditions from pyrite in the presence of aqueous NO_2^- and NO_3^- . Aqueous NO_2^- was reduced to NO and NH_4^+ at 70°C and 120°C and produced $\mu\text{mol.kg}^{-1}$ quantities of NH_4^+ , while NO_3^- was

reduced only at 120°C. The amount of NH_4^+ formed is increased significantly with increasing temperature. At 22°C and 70°C, the initial NO_2^- concentration was nearly unchanged, whereas at 120°C NO_2^- concentration rapidly decreased, indicating the formation of intermediates and NH_4^+ . However, the NH_4^+ yields observed in this study with pyrite are significantly lower than those obtained in the only other related experimental study by Summers,¹ in which commercial FeS and NO_2^- were reacted at room temperature to give yields between 18 and 53% in terms of starting NO_2^- concentration. In the experiments presented here the yields are less than 5% of the initial NO_2^- concentration. Even though at this point we can not compare the reactivity of FeS_2 used in this study to the reactivity of the FeS used by Summers, as the reaction conditions (temperature, pH, surface area of the minerals) used in this study are different from that study. A study of the reduction of NO_2^- and NO_3^- in the presence of FeS is underway to understand the apparent difference in reactivity of pyrite and FeS. In the NO_3^- /pyrite system, the NO_3^- reactant concentration (measured from batch experiments with IC) remained unchanged at all the three reaction temperatures, consistent with the low amounts of NH_4^+ formed in these experiments. We conclude that NO_2^- reduction is faster than NO_3^- reduction on FeS_2 at all the three reaction temperatures used in this study. In the NO_3^- /pyrite system, the nitrate reactant concentration remained unchanged at all the three reaction temperature, consistent with the low amounts of NH_4^+ formed in these experiments. Although we observe surface-bound species, including the postulated NO intermediate, NH_4^+ formation from NO_3^- is slower than from NO_2^- .

3.5. References

- (1) Summers, D. P., *Origin. Life. Evol. Biosph.* **2005**, 35 (4), 299-312.
- (2) Summers, D. P.; Basa, R. C. B.; Khare, B.; Rodoni, D., *Astrobiology* **2012**, 12 (2), 107-114.
- (3) Brandes, J. A.; Boctor, N. Z.; Cody, G. D.; Cooper, B. A.; Hazen, R. M.; Yoder, H. S., Jr., *Nature* **1998**, 395 (6700), 365-367.
- (4) Dörr, M.; Kassbohrer, J.; Grunert, R.; Kreisel, G.; Brand, W. A.; Werner, R. A.; Geilmann, H.; Apfel, C.; Robl, C.; Weigand, W., *Angew. Chem. Int. Ed.* **2003**, 42 (13), 1540-1543.
- (5) Schoonen, M. A. A.; Xu, Y., *Astrobiology* **2001**, 1 (2), 133-142.
- (6) Smirnov, A.; Hausner, D.; Laffers, R.; Strongin, D. R.; Schoonen, M. A. A., *Geochem. Trans.* **2008**, 9, 5.
- (7) Wander, M. C. F.; Kubicki, J. D.; Schoonen, M. A. A., *Origin. Life. Evol. Biosph.* **2008**, 38 (3), 195-209.
- (8) Wander, M. C. F.; Schoonen, M. A. A., *Origin. Life. Evol. Biosph.* **2008**, 38 (2), 127-137.
- (9) Cody, G. D., *Annu. Rev. Earth. Planet. Sci.* **2004**, 32, 569-599.
- (10) Navarro-Gonzalez, R.; McKay, C. P.; Mvondo, D. N., *Nature* **2001**, 412 (6842), 61-64.
- (11) Russell, M. J.; Hall, A. J., *J. Geol. Soc.* **1997**, 154 (3), 377-402.
- (12) Summers, D. P., *Origin. Life. Evol. Biosph.* **1999**, 29 (1), 33-46.
- (13) Summers, D. P.; Chang, S., *Nature* **1993**, 365, 630-633.

- (14) Summers, D. P.; Khare, B., *Astrobiology* **2007**, 7 (2), 333-341.
- (15) Wächtershäuser, G., *Prog. Biophys. Mol. Biol.* **1992**, 58 (2), 85-201.
- (16) Wächtershäuser, G., *Microbiol. Rev.* **1988**, 52 (4), 452-484.
- (17) Wächtershäuser, G., *Syst. Appl. Microbiol.* **1988**, 10 (3), 207-210.
- (18) Wächtershäuser, G., *Origin. Life. Evol. Biosph.* **1990**, 20 (2), 173-176.
- (19) Wächtershäuser, G., *Proc. Natl. Acad. Sci. U. S. A* **1990**, 87 (1), 200-204.
- (20) Walker, J. C. G.; Brimblecombe, P., *Precambrian. Res.* **1985**, 28 (3-4), 205-222.
- (21) Zohner, A.; Broda, E., *Orig. Life.* **1979**, 9 (4), 291-298.
- (22) Schoonen, M. A. A.; Smirnov, A.; Cohn, C., *Ambio* **2004**, 33 (8), 539-551.
- (23) Taylor, S. R., *Solar system evolution : a new perspective*. Cambridge University Press: Cambridge, UK, 2001; p 460.
- (24) Taylor, S. R., McLennan, S.M., , *Planetary Crusts: Their composition, Origin and Evolution*. . Cambridge University Press: Cambridge, UK, 2009.
- (25) Schoonen, M. A. A., *Geol. Soc. Am. Special Papers* **2004**, 379, 117-134.
- (26) Kasting, J. F., *Science* **1993**, 259 (5097), 920-926.
- (27) Guevremont, J. M.; Bebie, J.; Elsetinow, A. R.; Strongin, D. R.; Schoonen, M. A. A., *Environ. Sci. Technol.* **1998**, 32 (23), 3743-3748.
- (28) Kampschreur, M. J.; Kleerebezem, R.; de, V. W. W. J. M.; van, L. M. C. M., *Water Res.* **2011**, 45 (18), 5945-5952.
- (29) Samouilov, A.; Kuppusamy, P.; Zweier, J. L., *Arch. Biochem. Biophys.* **1998**, 357 (1), 1-7.
- (30) Becke, A. D., *Phys. Rev. A* **1988**, 38 (6), 3098-3100.
- (31) Perdew, J.P., *Phys. Rev. B, Cond. Matter* **1986**, 33 (12), 8822-8824.

- (32) Schaefer, A.; Huber, C.; Ahlrichs, R., *J. Chem. Phys.* **1994**, 100 (8), 5829-5835.
- (33) Frisch, M. J.; Trucks, G. W.; Schlegel, H. B.; Scuseria, G. E.; Robb, M. A.; Cheeseman, J. R.; Montgomery, J. J. A.; Vreven, T. K.; Kudin, N.; Burant, J. C.; Millam, J. M.; Iyengar, S. S.; Tomasi, J.; Barone, V.; Mennucci, B.; Cossi, M.; Scalmani, G. R., N. ; Petersson, G. A.; Nakatsuji, H.; Hada, M.; Ehara, M.; Toyota, K.; Fukuda, R.; Hasegawa, J.; Ishida, M.; Nakajima, T.; Honda, Y.; Kitao, O.; Nakai, H.; Klene, M.; Li, X.; Knox, J. E.; Hratchian, H. P.; Cross, J. B.; Bakken, V.; Adamo, C.; Jaramillo, J.; Gomperts, R.; Stratmann, R. E.; Yazyev, O.; Austin, A. J.; Cammi, R.; Pomelli, C.; Ochterski, J. W.; Ayala, P. Y.; Morokuma, K.; Voth, G. A.; Salvador, P.; Dannenberg, J. J.; Zakrzewski, V. G.; Dapprich, S.; Daniels, A. D.; Strain, M.; Farkas, C.; Malick, D. K.; Abuck, A. D.; Raghavachari, R.; Foresman, J. B.; Ortiz, J. V.; Cui, Q.; Baboul, A. G.; Clifford, S.; Cioslowski, J.; Stefanov, B. B.; Liu, G.; Liashenko, A.; Piskorz, P.; Komaromi, I.; Martin, R. L.; Fox, D. J.; Keith, T.; Al-Laham, M. A.; Peng, C. Y.; Nanayakkara, A.; Challacombe, M.; Gill, P. M. W.; Johnson, B.; Chen, W.; Wong, M. W.; Gonzalez, C.; and Pople, J. A. Gaussian 03, Revision E.01, Gaussian, Inc.,
- (34) Rieder, M.; Crelling, J. C.; Sustai, O.; Drabek, M.; Weiss, Z.; Klementova, M., *Int. J. Coal. Geol.* **2007**, 71 (2-3), 115-121.
- (35) Goodman, A. L.; Miller, T. M.; Grassian, V. H., *J. Vac. Sci. Technol. A* **1998**, 16 (4), 2585-2590.
- (36) Ling, Y.; Mills, C.; Weber, R.; Yang, L.; Zhang, Y., *J. Am. Chem. Soc.* **2010**, 132 (5), 1583-1591.
- (37) Cullen, W. R.; Crow, J. P.; Herring, F. G.; Sams, J. R.; Tapping, R. L., *Inorg. Chem.* **1971**, 10 (8), 1616-1623.

- (38) Andrews, L.; Hassanzadeh, P.; Brabson, G. D.; Citra, A.; Neurock, M., *J. Phys. Chem.* **1996**, 100 (20), 8273-8279.
- (39) Dinerman, C. E.; Ewing, G. E., *J. Chem. Phys.* **1970**, 53 (2), 626-631.
- (40) Dumas, P.; Suhren, M.; Chabal, Y. J.; Hirschmugl, C. J.; Williams, G. P., *Surf. Sci.* **1997**, 371 (2/3), 200-212.
- (41) Hess, C.; Ozensoy, E.; Yi, C.-W.; Goodman, D. W., *J. Am. Chem. Soc.* **2006**, 128 (9), 2988-2994.
- (42) Kim, C. M.; Yi, C. W.; Goodman, D. W., *J. Phys. Chem. B* **2002**, 106 (28), 7065-7068.
- (43) Yoshinobu, J.; Kawai, M., *Chem. Lett.* **1995**, (7), 605-606.
- (44) Usher, C. R.; Paul, K. W.; Narayansamy, J.; Kubicki, J. D.; Sparks, D. L.; Schoonen, M. A. A.; Strongin, D. R., *Environ. Sci. Technol.* **2005**, 39 (19), 7576-7584.
- (45) Usher, C. R.; Cleveland, C. A., Jr.; Strongin, D. R.; Schoonen, M. A. A., *Environ. Sci. Technol.* **2004**, 38 (21), 5604-5606.
- (46) Brown, W. A.; King, D. A., *J. Phys. Chem. B* **2000**, 104 (12), 2578-2595.
- (47) Enemark, J. H.; Feltham, R. D., *Coord. Chem. Rev.* **1974**, 13 (4), 339-406.
- (48) Borda, M. J.; Elsetinow, A. R.; Schoonen, M. A.; Strongin, D. R., *Astrobiology* **2001**, 1 (3), 283-288.

CHAPTER 4

PHOTOOXIDATION AND ADSORPTION OF ARSENIC BY FERRIMAGNETIC FERRIHYDRITE OR ORDERED FERRIHYDRITE

4.1. Introduction

Iron oxides, hydroxides, and oxy-hydroxides are abundantly found in nature. These minerals can also be synthesized readily in the laboratory. Iron oxides in the environments are formed via abiotic and biotic pathways (see reference¹ and references there in). Iron oxy-hydroxides under certain environmental conditions are metastable and act as precursors for the formation of iron oxides and hydroxides. The surface chemistry of iron oxides have received considerable interest in different scientific disciplines for example in mineralogy, soil science, geology, industrial chemistry, geochemistry, environmental chemistry, biology, and medicine etc.²

There are 16 types of iron oxide minerals that exist in nature, which includes oxides, hydroxides, and oxy-hydroxides.³⁻⁶ Ferrihydrite (Fh) is one of the naturally occurring, nano dimensioned iron oxy-hydroxide mineral. Fh is not only abundant on the Earth's surface but also in extra-terrestrial environments.³ Under certain conditions, Fh becomes thermodynamically unstable mainly in soils and sediments, where it becomes

converted into more stable iron oxide phases such as hematite (α -Fe₂O₃) and goethite (α -FeOOH).³

Fh also forms the core of ferritin, which is an iron storage protein in biological systems. Ferritin plays an important role in human body as it stores and sequesters iron, thus maintaining the homeostasis process.³ Fh is intrinsically a nano size material (diameter of 2 to 6 nm) with a high surface area (often > 300 m²/g). This high surface area associated with Fh facilitates its ability to sorb reactants as well as enhancing reaction kinetics. Hence Fh can be utilized to sequester contaminants found in ground water by adsorbing on to its surface.³⁻⁶

4.2. Structural models for Ferrihydrite

Fh exists in so-called 2-line and 6-line forms in nature. The number originates from the number of poorly defined and broadened diffraction lines in the respective XRD patterns.³ Due to the variable water content in its structure, assignment of a single formula to the Fh, is often problematic. The exact structure of Fh remains a matter of debate as many structural models have been proposed.¹⁻⁹ According to the well-accepted model of Michel et al., the chemical formula of ferrihydrite is Fe_{8.2}O_{8.5}(OH)_{7.4} · 3H₂O.³

Ferrimagnetic ferrihydrite (Ferrifh) is an ordered form of ferrihydrite (Fe₁₀O₁₄(OH)₂). It was recently synthesized by Michel et al., in 2010.⁸ They named it as the ordered-ferrihydrite or ferrimagnetic ferrihydrite (Ferrifh) based on the new structural

model they proposed for the Fh.^{3, 8} Ferrifh is a Fh phase with enhanced magnetism, obtained when Fh was aged at 175°C in presence of citrate (Fe/citrate = 3%) under dark aerobic conditions.⁸

Fh is smaller in size (2-6 nm) when compared to Ferrifh (10-12 nm). Also, Fh exhibits antiferromagnetism, where as Ferrifh shows ferrimagnetism (see reference⁸ and references there in). Ferrifh has fewer cationic vacancies and less lattice strain compared to Fh. Upon aging of Fh at ambient-temperature for more than a hundred days in presence of several anions, a magnetic enhancement was observed. A similar transformation may be possible in magnetically enhanced soils in the presence of anions such as citrate and phosphate for the conversion of Fh to Ferrifh. This would be plausible explanation for the existence of ferrifh in the environment.⁸

In 2011, the Manceau research group mentioned that the Fh model proposed by Michel et al.,⁸ has few drawbacks.⁶ According to Manceau, Fh does not contain tetrahedral iron and the Ferrifh structure is similar to the structure of the hydromaghemite synthesized by Barron et al.,⁷ in 2003.⁶ Hydromaghemite is a mixture of maghemite (γ -Fe₂O₃), hematite, and 6-line Fh.⁷ The main difference between the hydromaghemite and maghemite is the presence of structural water. Recently Maillot et al., proved the presence of tetrahedral iron in Fh with extended X-ray absorption fine structure spectroscopy (EXAFS), which supports the Michel model of Fh.⁹

4.3. Motivation behind using the Ferrifh as a substrate for arsenic redox chemistry

A Prior study by Bhandari et al., showed that 2-line Fh adsorbs and oxidizes arsenic in presence of simulated solar light.¹⁰ The newly synthesized Ferrifh was proposed to be the ordered form of Fh by Michel et al.⁸ The motivation of this study was to compare the reactivities of Ferrifh and Fh with As(III) in presence of simulated solar light, As(III) photooxidation and adsorption by Ferrifh was investigated. Also the differences in mechanism of As(III) oxidation by Fh and Ferrifh were explained in this chapter.

4.4. Characterization of Ferrifh

Ferrifh was synthesized by using the method published by Michel et al., in 2010.⁸ The synthetic protocol of Ferrifh was explained in section 2.1.1.2 of chapter 2. The synthesized material was characterized with ATR-FTIR- Spectroscopy, X-ray Diffraction Spectroscopy (XRD), Brauner-Emmett-Teller (BET) surface area analyzer, and Transmission Electron Microscopy (TEM).

Infrared spectrum of the synthesized Ferrifh (Figure 4.1) showed several modes due to citrate (between 1650 and 1200 cm^{-1}) along with Fe-O (425, 575, and 699 cm^{-1}) and carbonate (1355 cm^{-1}) modes (Figure. 4.1).¹⁰ Citrate was used during the synthesis of Ferrifh to delay the transformation of 2 line Fh to hematite and to ensure the intermediate

Ferrifh phase could be isolated⁸ It is important to note that the synthesized Ferrifh contains citrate and its modes in FTIR. A significant amount of citrate was removed by using the Ultraviolet (UV)-Ozone (O₃) cleaner.

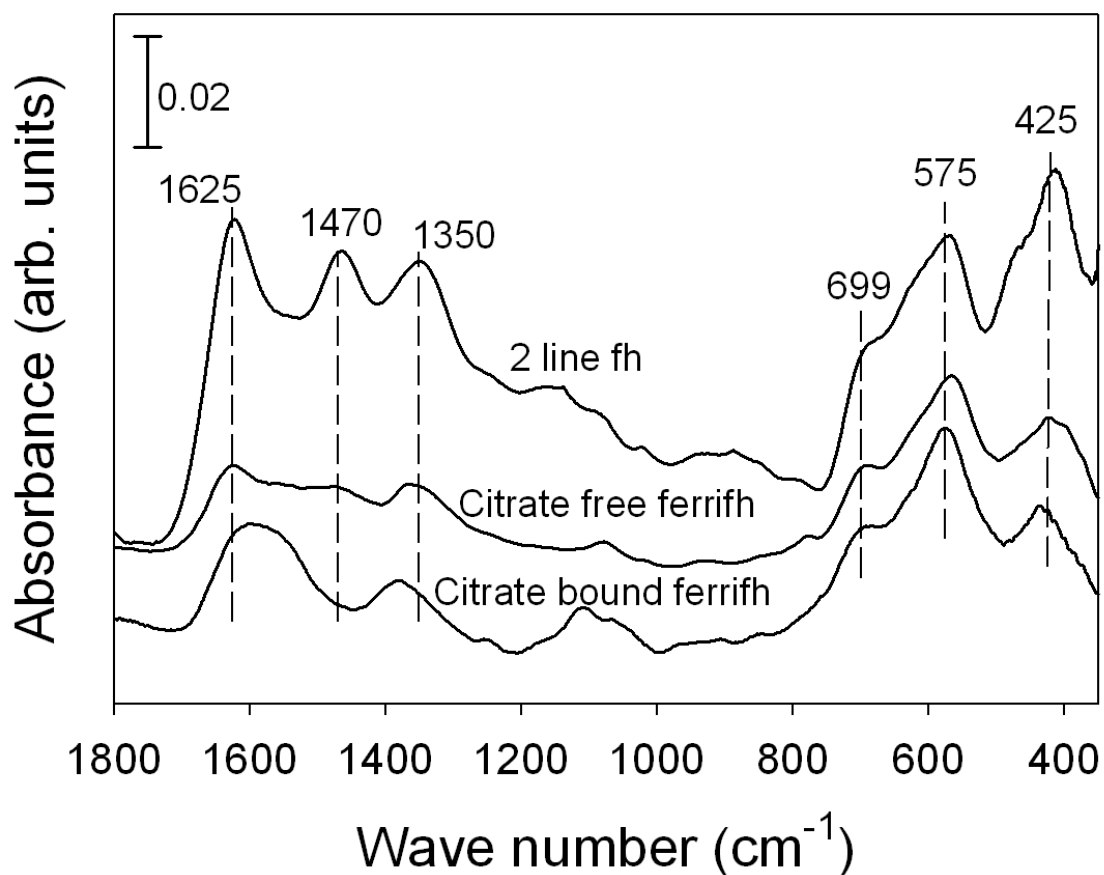
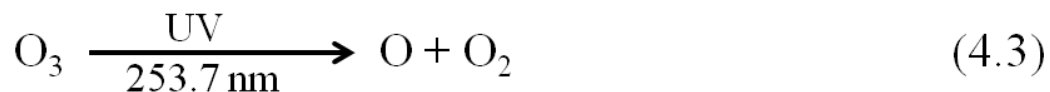


Figure 4.1. ATR-FTIR spectra of the citrate bound and citrate free ferrifh. ATR-FTIR spectrum of the 2 line Fh was shown for comparison.

The UV-O₃ cleaner is generally used for the removal of organic contaminants; it is not effective for the removal of inorganic contaminants from the surface.^{11, 12} The UV-O₃ cleaner can decompose and oxidize the organic contaminants to volatile substances like CO₂, H₂O, O₂, and N₂ etc. These volatile components then desorb from the surface and the then surface is free from the contaminants. The UV-Ozone cleaner contains mercury vapor pressure lamp that emits radiation of 184.9 and 253.7 nm. The energy of 184.9 and 253.7 nm light is 647 and 472 KJ. mol⁻¹. The organic compounds whose bond energy is less than the energy of the UV light emitted from the UV-O₃ cleaner can be decomposed first by photolysis.

Simultaneously, oxygen when irradiated by 184.9 nm wavelength UV light, absorbs UV light and forms atomic oxygen (O). The atomic O is a strong oxidizing agent; it reacts with O₂ in presence of 184.9 nm UV light and generates O₃ as shown by the following equations.¹¹



The O_3 absorbs 253.7 nm UV radiation and then decomposes to O and O_2 . This process continues and the generated atomic O causes the oxidation of products formed by the photolysis of the contaminants by UV light to volatile substances like CO_2 , H_2O , O_2 , and N_2 .¹¹ The volatile contaminants are evaporated from the surface. Citrate is a tri carboxylate and binds to the surface OH groups of the Ferrifh through the CO bonds. For example O=O (828 KJ. mol⁻¹), O-H (704 KJ. mol⁻¹) can be readily decomposed.

When the citrate bound Ferrifh was placed inside a UV- O_3 cleaner, it is suspected that the atomic oxygen breaks the C-O, C-C bonds, resulting in desorption of CO_2 from the surface of Ferrifh. The XRD pattern and TEM images of the Ferrifh before and after O_3 cleaning was shown in Figure 4.2 and Figure 4.3, respectively. Hereafter, citrate bound and citrate free Ferrifh are called as CB-Ferrifh and CF-Ferrifh, respectively.

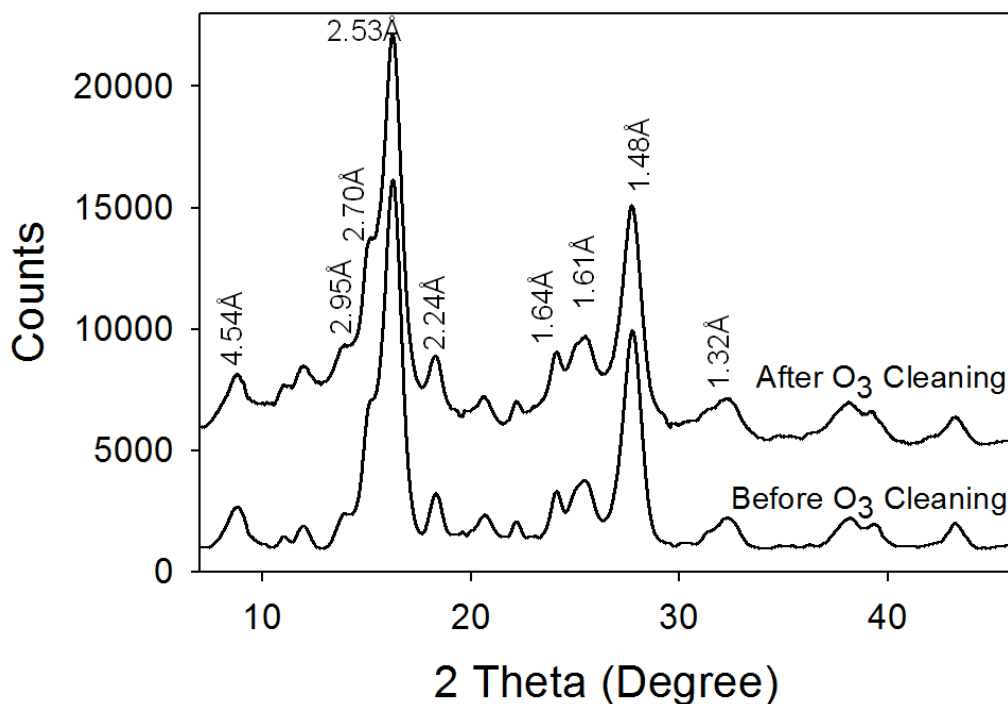


Figure 4.2. X-ray diffraction pattern of the citrate bound (before Ozone cleaning) and citrate free (after Ozone cleaning) Ferrifh, showing that the structure and particle size of the Ferrifh was not changed after Ozone cleaning.

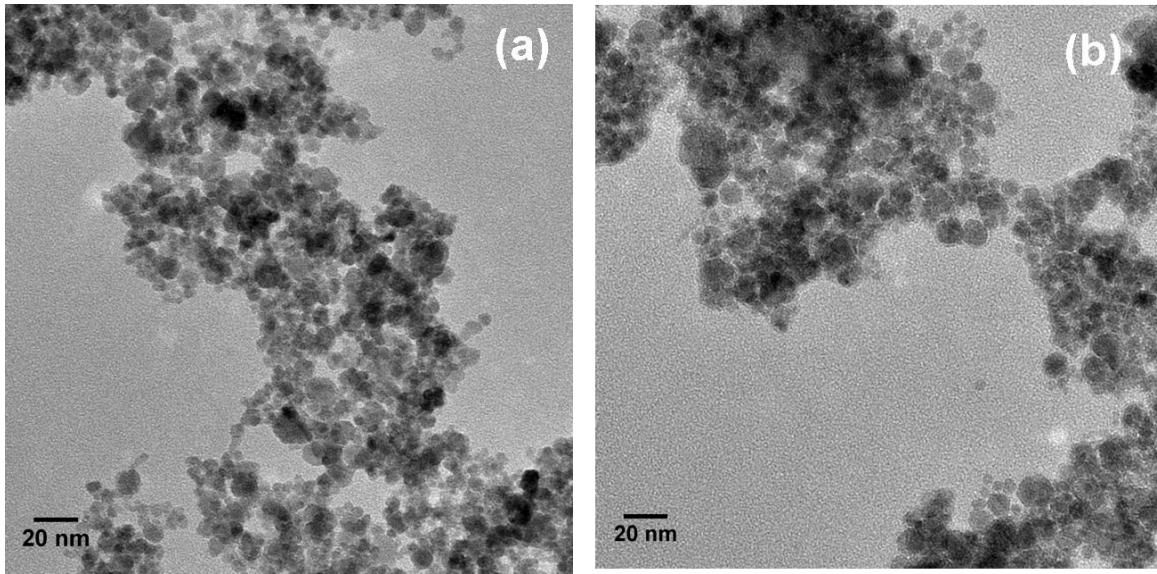


Figure 4.3. TEM micrograph of the CB-Ferrifh (a), TEM micrograph of the CF-Ferrifh (b)

4.5. Results and Discussion

4.5.1. ATR-FTIR Experiments

In-situ ATR-FTIR flow experiments with photo-irradiation were conducted to determine, qualitatively, whether the Ferrifh oxidize As(III) and/or adsorb As(III)/As(V) on the surface. To complement these experiments, batch experiments were then

conducted under similar conditions to quantify the amount of As(III) oxidized/adsorbed and to also quantify the amount of As(V) adsorbed on the surface of Ferrifh. ATR-FTIR experiments were conducted, as the solution phase As(III) and As(V) were detected only at higher concentration using ATR-FTIR, while the adsorbed species can be detected even at low concentrations.¹³

Control experiments were conducted, where CF-Ferrifh samples were individually exposed to As(III) and As(V) in the dark. A thin film of Ferrifh was prepared on the diamond (ATR crystal). Ferrifh (12 mg) was suspended in 500 μL of 5 mM aqueous NaCl solution at pH 5.00 and sonicated 20 min for homogeneity. A 24 μL volume of the suspension was placed on the diamond and dried by gently flowing of ultra high purity (UHP) N_2 . A 0.41 mM of solution of As(III) in 5 mM NaCl at pH 5.00 was flowed over the Ferrifh film at a flow rate of 20 mL/h to maintain a constant pH. After 24 h, a peak due to the As(III)-O stretching mode developed around 785 cm^{-1} (Fig 4.4, 0 h).¹³ No peaks due to As(V) were observed during this time period. This experimental observation indicates that As(III) oxidation was not favored by Ferrifh in dark.

Similarly 0.41 mM of As(V) solution containing 5 mM NaCl was flowed over the dried Ferrifh film at a rate of 20 mL/h. Spectra were collected until there was no increase in the intensity of As(V)-O modes. CB-Ferrifh showed As(V)-O stretching modes at 845 and 889 cm^{-1} (Figure 4.5), while CF-Ferrifh showed As(V)-O stretching modes at 838 , and 880 cm^{-1} (Figure 4.5).

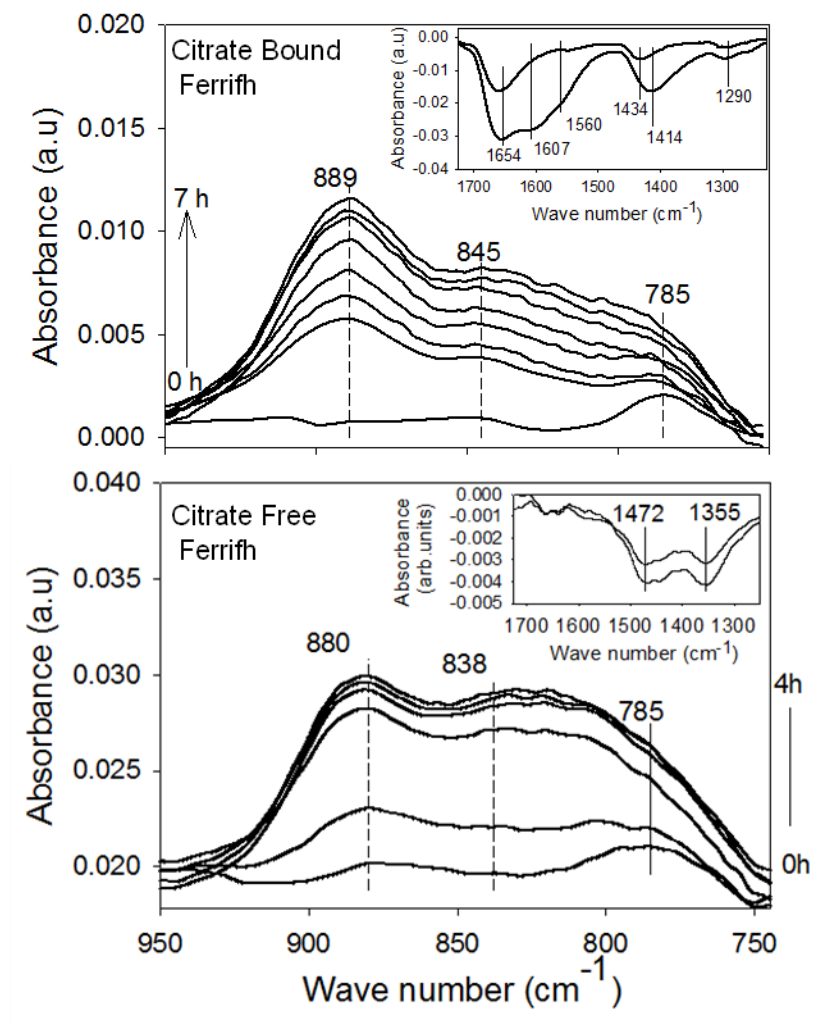


Figure 4.4. ATR-FTIR spectrum showing the As(III) and As(V)-O stretching modes obtained when CB- and CF-Ferrifh was exposed to 0.41 mM As(III), 5 mM NaCl solution at pH 5. 0 h spectra in both the cases were obtained after the 15 h exposure of CB-Ferrifh to As(III) in dark. In the CB-Ferrifh case, the subsequent spectra were collected after 0.5, 1, 2, 3, 4, 6, and 7 h of light irradiation. The inset shows the difference spectra, which were obtained by subtracting the clean CB-Ferrifh spectrum from the CB-Ferrifh exposed to As(III) before light irradiation (top) and the CB-Ferrifh

exposed to light for 7 h (bottom). Negative modes are desorbed citrate modes. The subsequent spectra in the case of CF-Ferrifh was collected after 0, 0.5, 1, 2, 3, and 4 h of As(III) exposure in the presence of light. The inset to Figure shows difference spectra, which were obtained by subtracting the clean CF-Ferrifh spectrum from the CF Ferrifh exposed to As(III) before light irradiation (top) and the CF-Ferrifh exposed to As(III) after 4h of light irradiation (bottom). The negative modes at 1472 and 1355 cm^{-1} are the desorbed carbonate modes, which were replaced by As(III) or As(V) during the As(III) exposure. An initial single beam spectrum of Ferrifh suspended in water was used as the background

Figure 4.4 displays in situ ATR-FTIR experiments, which were carried out by flowing a solution containing 0.41 mM As(III) and 5 mM NaCl at pH 5.00 onto a thin film of CB- and CF-Ferrifh on the diamond ATR element. As(III)-O stretching modes were observed at 785 cm^{-1} . There was no increase in the As(III)-O mode after 15 h. After 15 h, the sample was exposed to light, while maintaining the solution flow. After 30 min of irradiation, As(V)-O stretching vibrations developed at 845, 889 cm^{-1} ,¹³ in presence of CB-Ferrifh and at 838, 880 cm^{-1} in presence of CF-Ferrifh, indicating the oxidation of As(III) to As(V) in the presence of light.

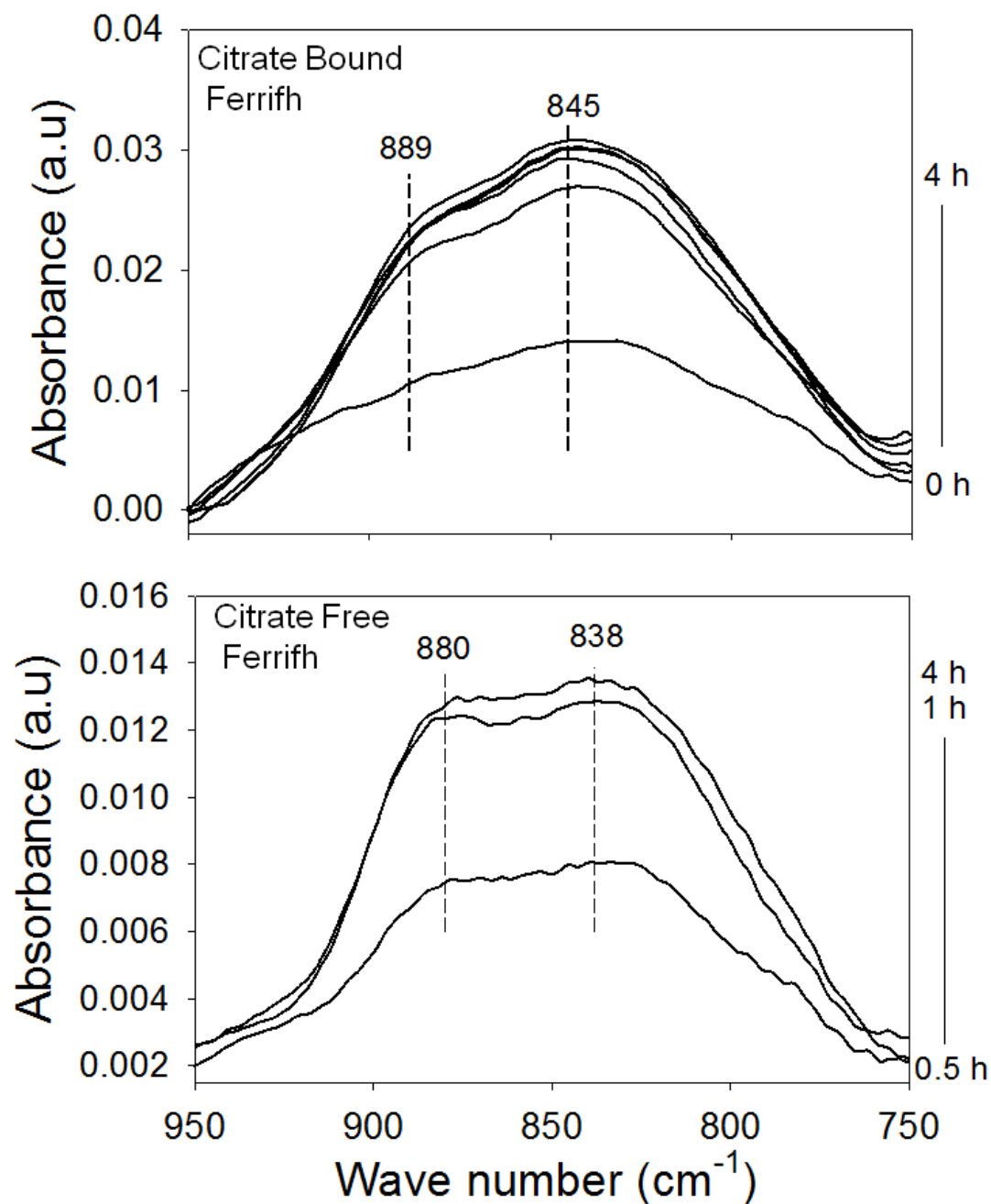


Figure 4.5. Top spectrum shows the ATR-FTIR spectrum of As(V)-O stretching modes obtained when CB-Ferrifh was exposed to 0.41 mM As(V), 5 mM NaCl solution in dark at pH 5.00 for 0.5, 1, 2, 3, and 4 h. Bottom spectrum shows the ATR-FTIR spectrum of

As(V)-O stretching modes at 838, 880 cm^{-1} obtained when CF-Ferrifh was exposed to 0.41 mM As(V), 5 mM NaCl solution for 0.5, 1, and 4 h in dark. An initial single beam spectrum of Ferrifh suspended in water was used as the background.

There was a red shift in the As(V)-O stretching modes after citrate was removed from the Ferrifh. The difference spectrum (Final vs. initial 0 h spectrum) shows that the CB-Ferrifh lost citrate modes (Inset to Figure 4.5), while CF-Ferrifh showed the loss of carbonate modes (Inset to Figure 4.5) with the adsorption of As(III) or As(V). This observation indicates that arsenic was replaced by citrate on CB-Ferrifh and carbonate on CF-Ferrifh. Additional citrate and carbonate were lost on CB and CF Ferrifh respectively in presence of light and replaced by arsenic in presence of light. This indicates that As(III) adsorbed on Ferrifh in the absence of light, but oxidized to As(V) in presence of light. To quantify the amount of As(III) adsorbed and oxidized by CB- and CF-Ferrifh in the absence and presence of light, batch experiments were conducted.

4.5.2. Batch Experiments.

Photo irradiation experiments were conducted using CB and CF Ferrifh to quantify the surface and solution species formed during the exposure of Ferrifh to aqueous As(III) in the dark and in presence of light and to identify the effect of citrate present on the surface of Ferrifh.. A control experiment was conducted where 470 μM of As(III) solution was exposed to simulated solar light at pH 5.00 for 8 h (Figure 4.6). Only 2.5 μM of As(V) was observed in solution after 8 h.

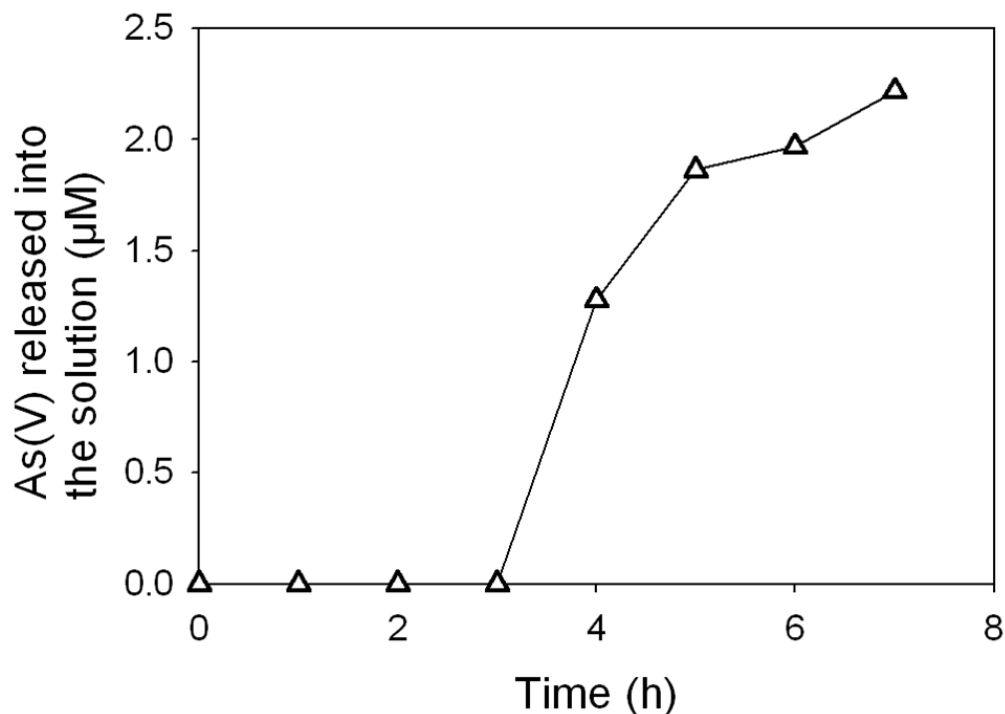


Figure 4.6. Amount of As(V) formed in solution when 470 µM of aqueous As(III) solution was exposed to simulated solar light at pH 5.00

Figure 4.7 plots the amount of arsenic adsorbed on CB Ferrifh and CF Ferrifh when exposed to 0.41 mM of As(III) in presence of light at pH 5.00. The Ferrifh sample was equilibrated with As(III) solution for 24 h in dark. CB Ferrifh and CF Ferrifh showed $\sim 0.38 \pm 0.03$ mole/kg and 0.30 ± 0.03 mole.kg⁻¹ of As adsorption, respectively after 24 h of As(III) exposure in the dark. After this 24 h of As(III) exposure the sample was exposed to light. After 8 h of irradiation, 30 and 23 µM of As(V) was released into the solution respectively in the presence of CB- and CF-Ferrifh (Figure 4.8). The amount of arsenic that was adsorbed on CB- and CF-Ferrifh after 8 h of irradiation was 0.70 ± 0.03 mol/kg and 0.51 ± 0.03 mole/kg, respectively (Figure 4.7). This result indicates

that the CB-Ferrifh showed high arsenic adsorption both under dark and light conditions. The reason for the high reactivity of the CB-Ferrifh sample than the CF-Ferrifh sample will be discussed below.

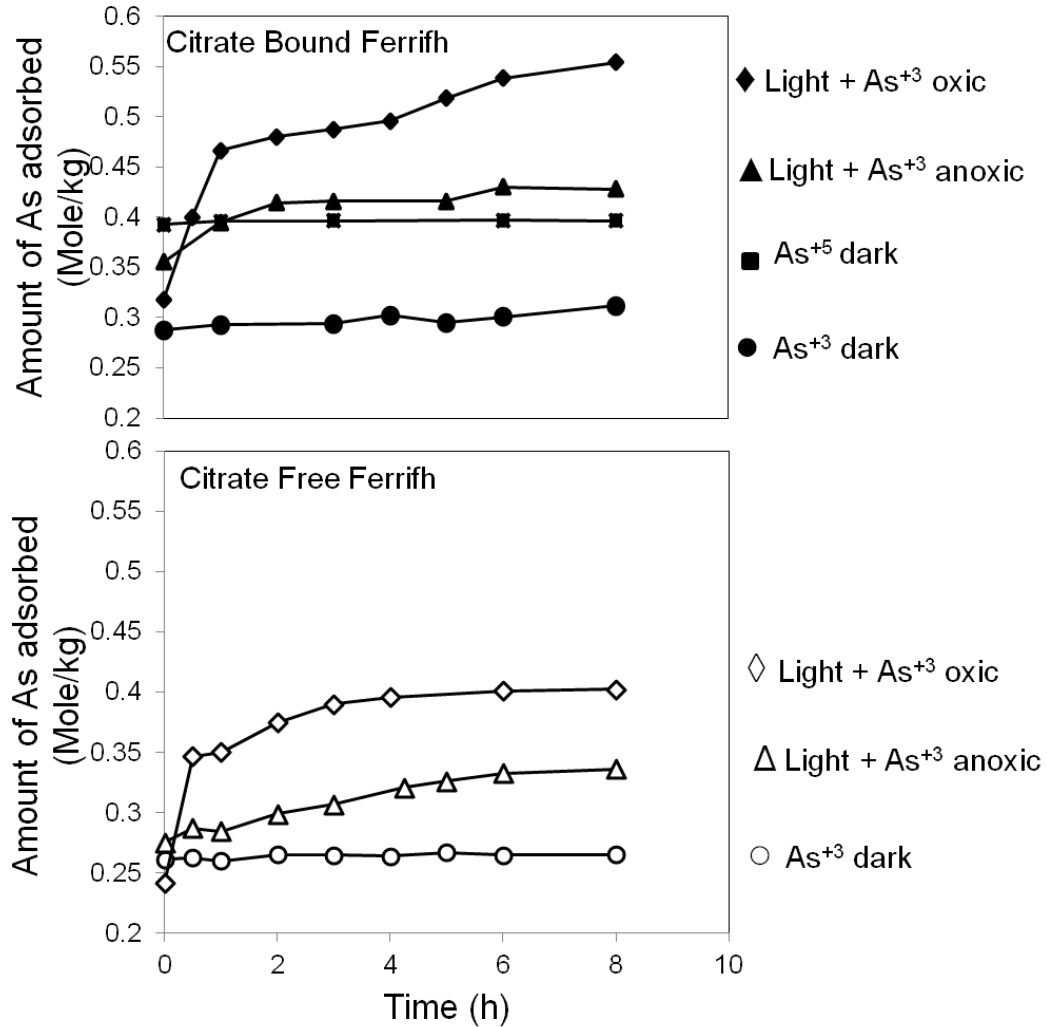


Figure 4.7. The amount of arsenic adsorbed in mole.kg⁻¹ on CB-Ferrifh (top plot), when exposed to As(III) in dark (closed circles), in presence of light (closed diamonds), in presence of light under anoxic conditions (closed triangles), and As(V) exposure in dark (closed squares). The amount of arsenic adsorbed on CF-Ferrifh (bottom plot), when

exposed to As(III) in dark (open circles), in presence of light (open diamonds), and in presence of light under anoxic conditions (open triangles).

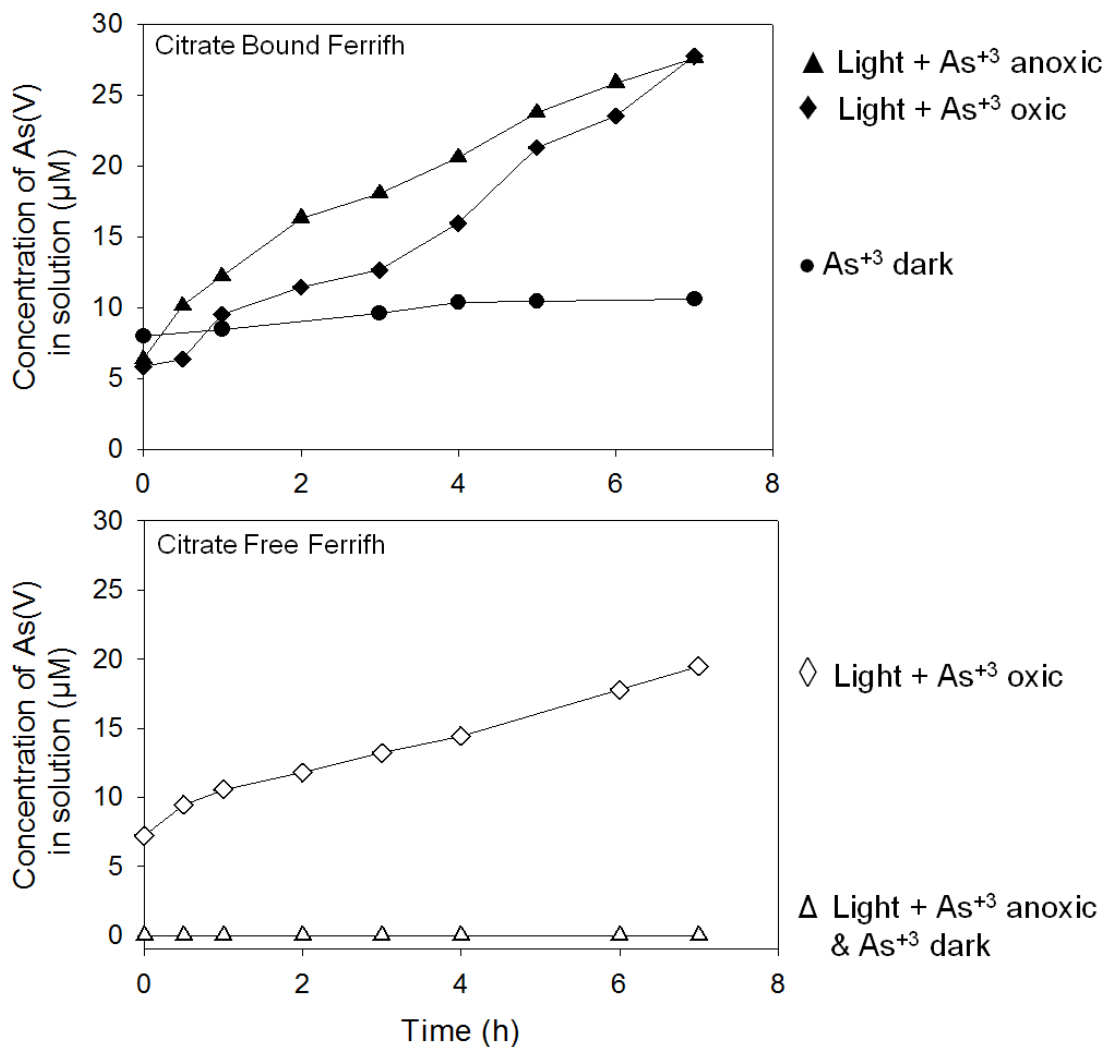


Figure 4.8. The amount of As(V) released into the solution when CB-Ferrifh was exposed to As(III) , in dark (closed circles), in presence of light (closed diamonds), and in presence of light under anoxic conditions (closed triangles). There is no As(V) released into the solution when CF-Ferrifh was exposed to As(III) (bottom plot), in dark and in presence of light under anoxic conditions indicated with open triangles. Open diamonds

represent the amount of As(V) released when CF Ferrifh was exposed to As(III) in presence of light.

To determine the relative concentration of adsorbed As(III) and As(V), arsenic K-edge XANES analysis was performed on the CF-Ferrifh reacted with As(III) in dark and in presence of light (Figure. 4.9). Based on the Q-EXAFS analysis (experimental details were given in section 2.2.11 of chapter 2) there is insignificant amount of As(V) adsorbed on the surface of CF-Ferrifh when it was exposed to As(III) in dark at pH 5, while 29% of As(III), 71% of As(V) was adsorbed on the CF-Ferrifh, in presence of light. The energy difference between the absorption maxima in XANES of As(III) and As(V) bonds is 3.7 eV, which is consistent with the previous reports by several authors.^{10, 16}

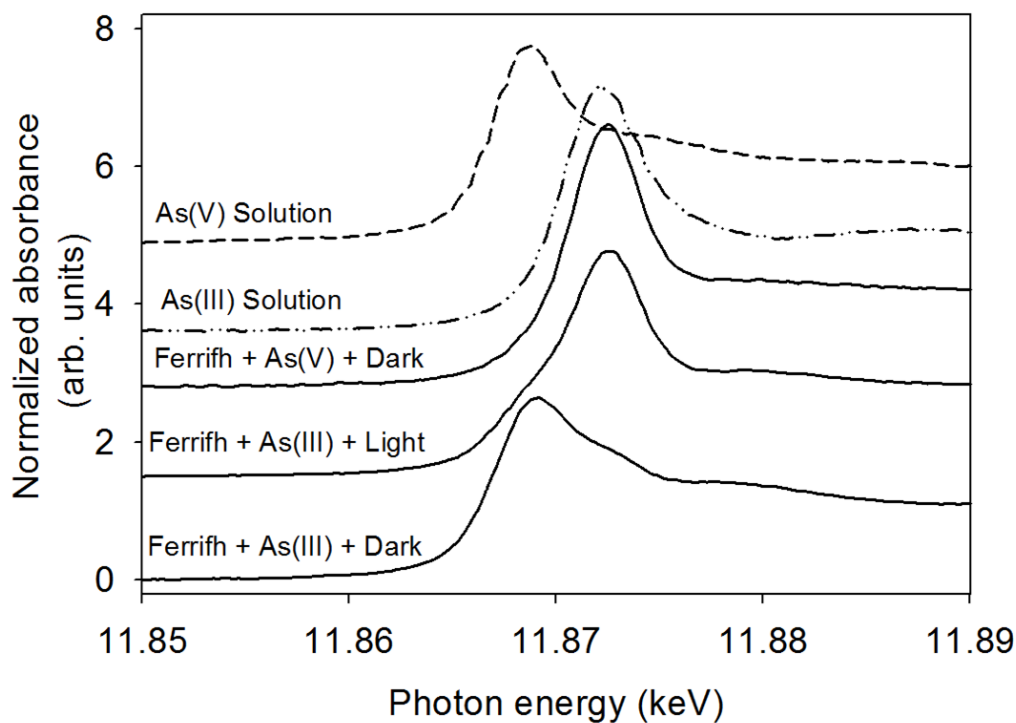


Figure 4.9. Normalized K-edge XANES data of the arsenite, arsenate adsorbed on CF-Ferrifh in dark, and the As(III) and As(V) adsorbed on CF-Ferrifh, when exposed

to As(III) or As(III) for 8h. All these spectra were collected in Q-EXAFS mode. XANES spectra of As(III) and As(V) aqueous solutions were used as oxidation state references.

According to the reaction stoichiometry, for every mole of As(III) that is oxidized, there should be 2 mol of Ferric iron (Fe(III)) reduced to ferrous iron (Fe(II)).¹⁴ Fe(II) is a water soluble species and can be observed in solution as an aqueous species. According to the Q-EXAFS and batch experimental data, the total concentration of As(V) formed, when CF-Ferrifh was exposed to As(III) in the presence of light is 105 μM . Hence, approximately 210 μM Fe(II) should be observed in solution. In these experiments only ~ 25 μM of Fe(II) is released (Figure. 4.10), which was approximately 8 times lower than the amount of Fe(II) expected to be formed during this redox reaction.

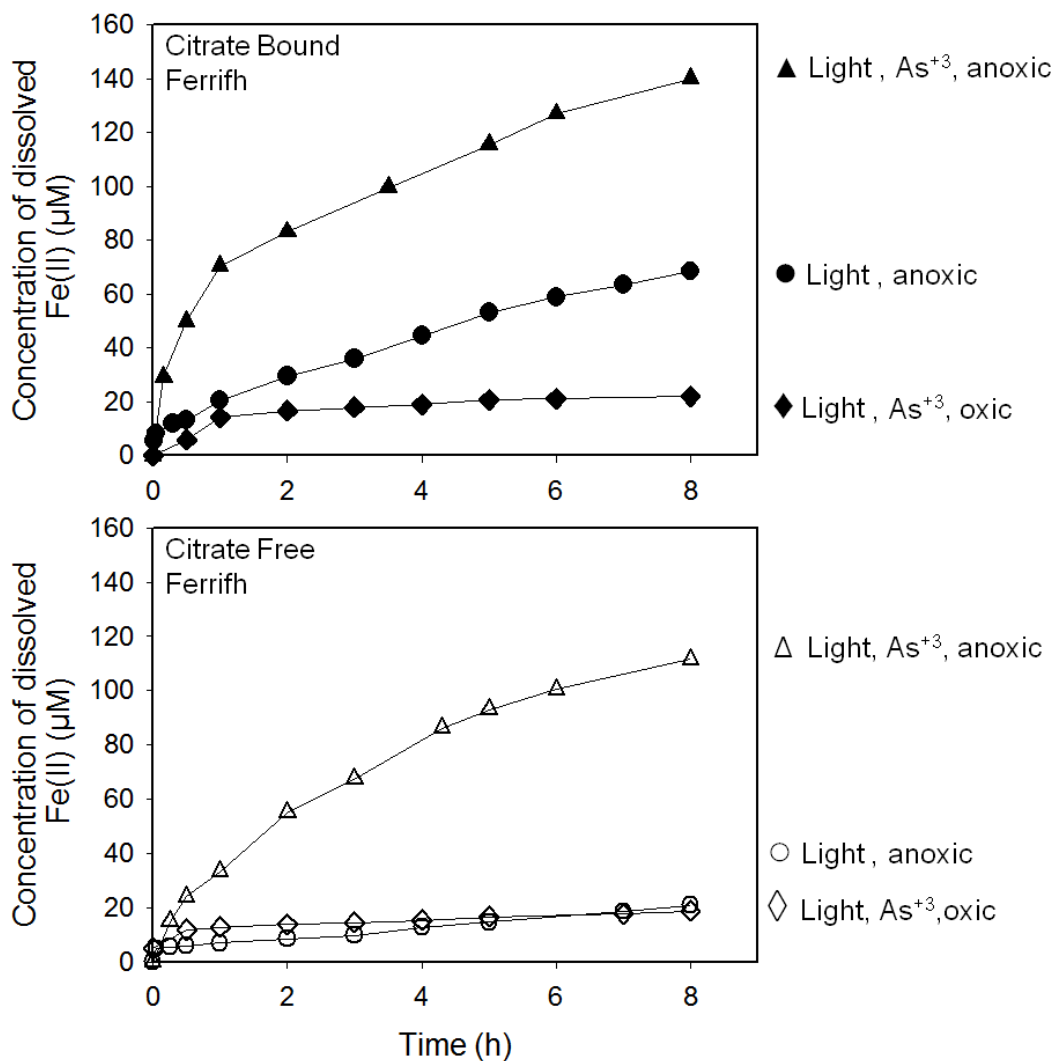


Figure 4.10. The amount of Fe(II) released in μM when CB-Ferrifh is exposed to As(III), in presence of light, absence of dissolved O_2 (closed triangles), in presence of dissolved O_2 (closed diamonds). Closed circles represent the Fe(II) released into the solution, when CB-Ferrifh was exposed to light in the absence of As(III) and dissolved O_2 . Open triangles represent the amount of Fe(II) released into the solution when CF Ferrifh was exposed to As(III) in presence of light and the absence of dissolved O_2 , Open diamonds represent the Fe(II) released when the CF Ferrifh was exposed As(III) in the presence of

light and dissolved O_2 and the closed circles represent the Fe(II) released when CF Ferrifh was exposed to light in the absence of As(III), and dissolved O_2 .

Several experiments were conducted to determine the fate of Fe(II) during As(III) oxidation in these experiments in presence and absence of dissolved O_2 . A photo irradiation experiment was conducted, where CF-Ferrifh was exposed to As(III) under anoxic conditions. To achieve anoxic conditions the pre-reaction solution was Purged with Ar 30 min prior to light exposure(after 24 h equilibration with As(III) in dark). The total amount of Fe(II) released during these experiments after 8 h light irradiation was 115 μM (Figure. 4.10), and the amount of arsenic oxidized was 60 μM . The ratio between Fe(II) released and As(III) oxidized is 1.9:1, which was close to the expected stoichiometry. The amount of arsenic adsorbed was also significantly reduced under anoxic conditions, and this experimental observation indicates that Fe(II), dissolved O_2 were playing a major role in these photoirradiation experiments. The extra amount of arsenic oxidized and observed in the presence of dissolved O_2 in the light experiments is attributed to the reactive oxygen species (ROS) such as O_2^- , OH^- , and H_2O_2 formed due to the reaction between Fe(II) and O_2 .¹³⁻¹⁷ The formation of these species from the aqueous/adsorbed Fe(II) and dissolved O_2 was mentioned by several authors;¹³⁻¹⁷ Interestingly, the photooxidation and adsorption of As(III) by 2 line Fh was independent of dissolved O_2 .³

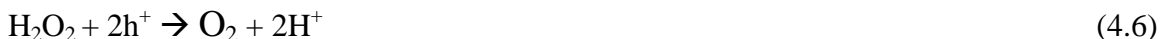
To determine the influence of citrate on Fe(II) release and As(III) oxidation in the presence of light, control experiments were conducted by exposing the CB- and CF-

Ferrifh to light in the absence of As(III) and dissolved oxygen. The amount of Fe(II) released, when CB- and CF-Ferrifh was exposed to light in the absence of As(III) and dissolved O₂, was 60 and 18 μM, (Figure. 4.10) respectively. From this result we conclude that, in presence of light citrate was facilitating the reduction of Fe(III) to Fe(II) and ths Fe(II) product in the presence of dissolved O₂ formed ROS, which oxidized As(III) to As(V). Hence, the extra amount of arsenic oxidized and adsorbed on CB-Ferrifh was due to the reduction of Fe(III) to Fe(II) by citrate. In the presence of CB-Ferrifh, the amount of As(V) released into the solution is the similar in the presence and absence of oxygen, while the total amount of arsenic oxidized and adsorbed was high in the presence of oxygen. This result indicates that some of the As(V) formed on the surface of CB-Ferrifh in the absence of oxygen desorbs into solution. CF-Ferrifh behaved different way in that the amount of As(V) in solution; the amount adsorbed on the surface was high in the presence of oxygen compared to the amount of As(V) in solution. This amount adsorbed in the absence of oxygen indicates that As(V) binds stronger on the surface of the CF-Ferrifh than CB-Ferrifh.

4.6. Comparison of the mechanism of the CB-, CF-Ferrifh, and 2-line Fh with As(III) in presence of light

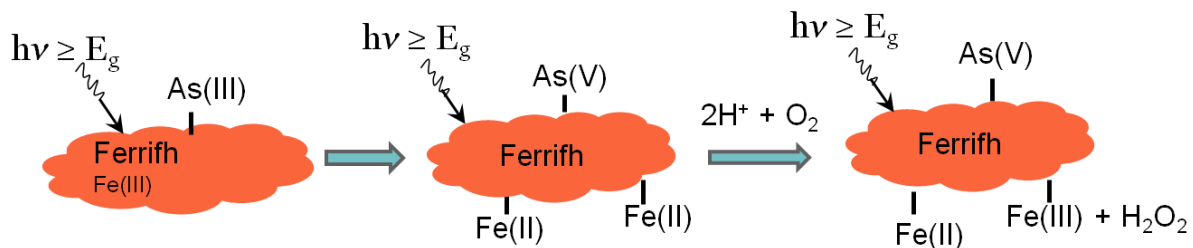
From the above results we conclude that, there are two possible As(III) oxidation pathways in the presence of light by Ferrifh as shown in Scheme 4.1 and Scheme 4.2.

In the presence of CF-Ferrifh, reaction Scheme 4.1 is favored in the presence of dissolved O₂, i.e. As(III) is oxidized by the holes formed during irradiation of light and simultaneously 2 moles of Fe(III) present in Ferrifh are reduced to 2 moles of Fe(II). An additional amount of As(III) is oxidized by the ROS like H₂O₂ and •OH. These ROS are formed by the oxidation of Fe(II) by dissolved O₂ by fenton like processes.¹⁴⁻¹⁷ •OH are postulated to be formed from H₂O₂ by the following reactions,¹⁶

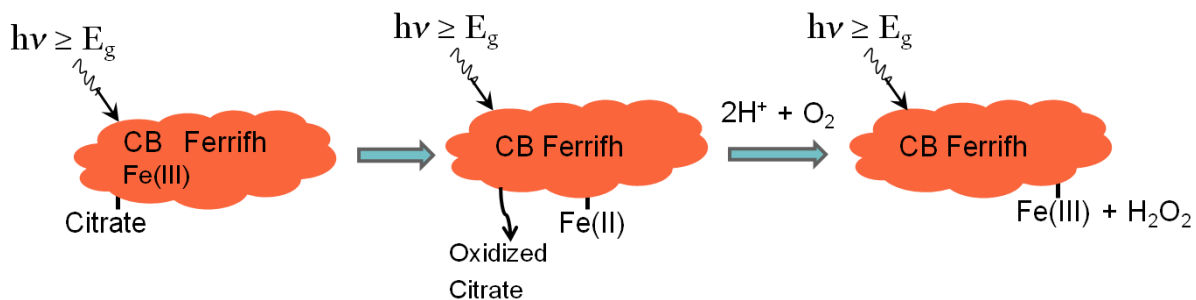


In the presence of CB-Ferrifh along with reactions mentioned in Scheme 4.1, additional reactions occur on the surface as shown in Scheme 4.2. Citrate present on the surface of Ferrifh reduces Fe(III) to Fe(II) and Fe(II) participates in fenton like processes to produce ROS. Hence, additional As(III) oxidation occurs in the presence of CB-Ferrifh by these ROS, making CB-Ferrifh more reactive when compared to CF-Ferrifh. During this process, oxidized forms of citrate also desorb from the surface of Ferrifh and create more adsorption sites for the arsenic. Hence there is greater amount of arsenic oxidized and adsorbed on CB-Ferrifh compared to CF-Ferrifh. In the absence of dissolved O₂, only hole induced As(III) oxidation takes place. ROS species are not formed from Fe(II) due to the unavailability of the dissolved O₂ to produce ROS. Hence

the amount of As(III) oxidized and adsorbed by CB- and CF-Ferrifh in the absence of dissolved O₂, is less than the amount of As(III) oxidized and adsorbed in the presence of dissolved O₂.



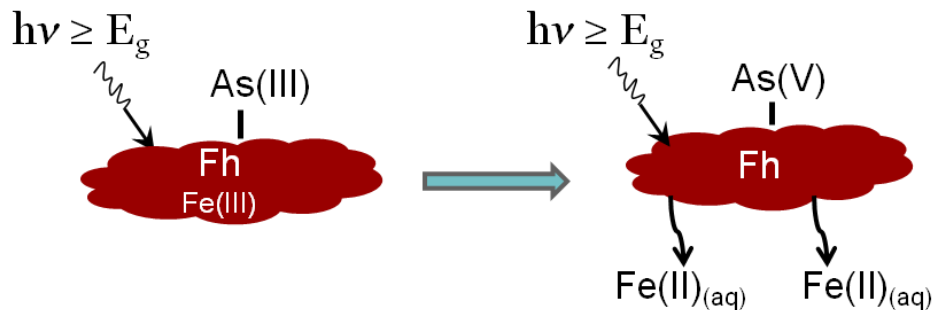
Scheme 4.1. Mechanism showing the hole induced oxidation of As(III) by CB- and CF-Ferrifh in presence of light.



Scheme 4.2. Mechanism showing the citrate induced reduction Fe³⁺ to Fe²⁺ and the oxidation of Fe(II) to Fe(III) and H₂O₂ by dissolved O₂ on CB-Ferrifh in presence of light. During this process citrate was desorbed from the surface (citrate desorption was

proposed based on the ATR-FTIR experiments and not studied or quantified the oxidized citrate products using the batch experiments).

While in the presence of 2-line Fh, As(III) photo-oxidation and adsorption on 2-line Fh is independent of dissolved O₂. Only hole induced As(III) oxidation occurs in presence of light. Fe(II) produced during the As(III) oxidation released into the aqueous phase likely remain in water as stable Fe(II)_{aq} phase and the ROS are not formed even in presence of dissolved O₂.



Scheme 4.3. Mechanism of As(III) oxidation by 2-line Fh.¹⁰

4.7. Comparison of the reactivity of CB-, CF-Ferrifh, and 2-line Fh with arsenic in presence of light

Compared to 2-line Fh, CB- is more reactive towards As(III) in the presence of light (Figure. 4.11), while CF-Ferrifh is slightly more reactive with As(III) when normalized with regard to the surface area.

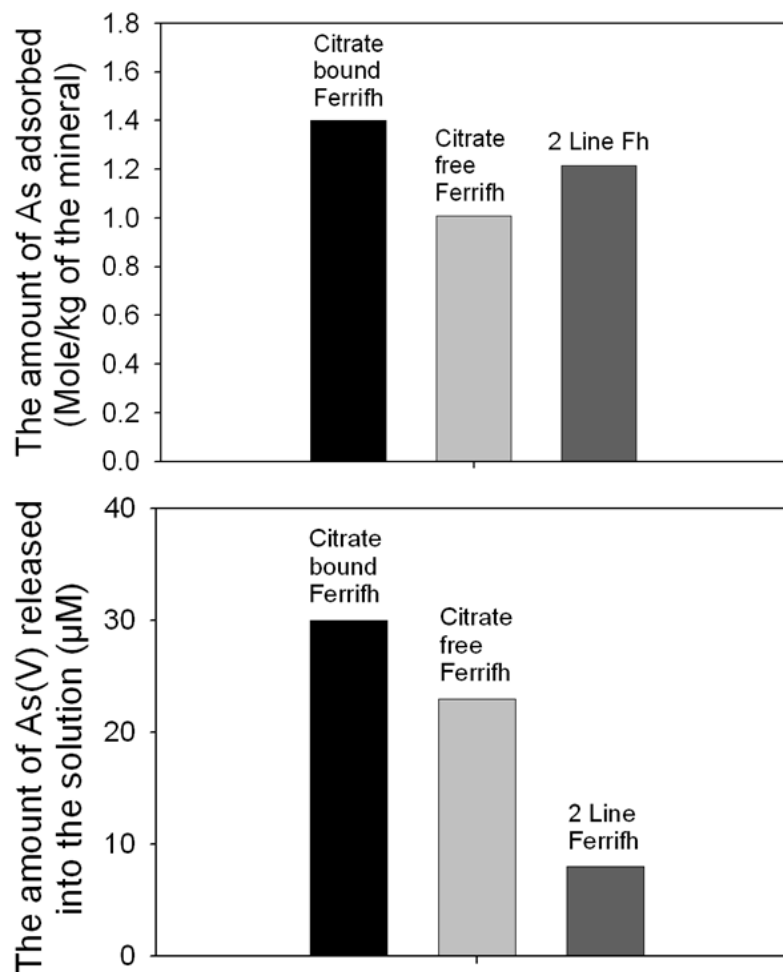


Figure. 4.11. The figure represents the surface area normalized total As adsorption on CB- and CF-Ferrifh, and 2-line Fh, when exposed to 0.41 mM of As(III), 5 mM NaCl solution in presence of light for 8 h at pH 5. The bottom figure illustrates the comparison between the total amount of As(V) released into the solution, when CB and CF-Ferrifh, and 2-line Fh was exposed to 0.41 mM of As(III) in 5 mM NaCl, in presence of light for 8 h at pH 5. These amounts are normalized according to the surface area of the respective minerals.

In the case of 2-line Fh, stoichiometric amounts of Fe(II) was released during As(III) oxidation and adsorption in the presence of light,¹ while ferrifh did not release stoichiometric amounts of Fe(II), due to the adsorption and oxidation of Fe(II) by dissolved O₂ forming reactive intermediates. Due to the competition between Fe(II) and As(III)/As(V) for the reactive sites on Ferrifh, more As(V) was released into the solution in case of Ferrifh compared to 2-line Fh.

4.8. References

- (1). Drits, V. A.; Sakharov, B. A.; Salyn, A. L.; Manceau, A., *Clay Miner.* **1993**, 28, (2), 185-207.
- (2). Jambor, J. L.; Dutrizac, J. E., *Chem. Rev.* **1998**, 98, (7), 2549-2585.
- (3). Michel, F. M.; Ehm, L.; Antao Sytle, M.; Lee Peter, L.; Chupas Peter, J.; Liu, G.; Strongin Daniel, R.; Schoonen Martin, A. A.; Phillips Brian, L.; Parise John, B., *Science* **2007**, 316, (5832), 1726-9.
- (4). Manceau, A., *Clay Miner.* **2009**, 44, (1), 19-34.
- (5). Manceau, A., PDF analysis of ferrihydrite and the violation of Pauling's Principia. *Clay Miner.* **2010**, 45, (2), 225-228.
- (6). Manceau, A., *Am. Mineral.* **2011**, 96, (4), 521-533.
- (7). Rancourt, D. G.; Meunier, J. F., *Am. Mineral.* **2008**, 93, (8-9), 1412-1417.
- (8) Michel, F. M.; Barron, V.; Torrent, J.; Morales Maria, P.; Serna Carlos, J.; Boily, J.-F.; Liu, Q.; Ambrosini, A.; Cismasu, A. C.; Brown Gordon, E., Jr., *Proc. Natl. Acad. Sci. U S A* **2010**, 107 (7), 2787-2792.
- (9). Maillot, F.; Morin, G.; Wang, Y.; Bonnin, D.; Ildefonse, P.; Chaneac, C.; Calas, G., *Geochim. Cosmochim. Acta* **2011**, 75, (10), 2708-2720.
- (10) Bhandari, N.; Reeder, R. J.; Strongin, D. R., *Environ. Sci. Technol.* **2011**, 45 (7), 2783-2789.
- (11). Hazama-cho, Hachioji-shi, Tokyo 193-8533, Japan 1456 Three Bond Technical News 17 Issued March 20, 1987

- (12). Vig. J. R., *IEEE Transactions on Parts, Hybrids, and Packaging*, Vol. Php-12, NO. 4, 1976
- (13) Voegelin, A.; Hug, S. J., *Environ. Sci. Technol.* **2003**, 37 (5), 972-978.
- (14) Gonzalez-Davila, M.; Santana-Casiano, J. M.; Millero, F. J., *J. Sol. Chem.* **2006**, 35 (1), 95-111.
- (15) Hug, S. J.; Leupin, O., *Environ. Sci. Technol.* **2003**, 37 (12), 2734-2742.
- (16) Ona-Nguema, G.; Morin, G.; Wang, Y. H.; Foster, A. L.; Juillot, F.; Calas, G.; Brown, G. E., *Environ. Sci. Technol.* **2010**, 44 (14), 5416-5422.
- (17) Santana-Casiano, J. M.; Gonzalez-Davila, M.; Millero, F. J., *Environ. Sci. Technol.* **2005**, 39 (7), 2073-2079.

CHAPTER 5

LIGHT INDUCED OXIDATION OF ARSENIC BY BIRNESSITE

5.1. Introduction

Birnessite is a major phase in many soils and an important component in desert varnishes and deep-sea manganese nodules.¹⁻¹⁵ Birnessite (δ -MnO₂) is a poorly crystalline, layered manganese oxide mineral composed of sheets having edge sharing MnO₆ octahedra and exchangeable hydrated cations such as H⁺, K⁺, Na⁺, and Ca⁺².^{1-15,29} These cations typically occupy the internal layers, resulting in an interlayer spacing of 7Å.^{1-15,29} The Mn(IV) vacancies in these layers result in an overall negative charge, which is compensated by Mn²⁺ and/or Mn³⁺ ions existing below and above the vacancies in the interlayers.^{1-15,29} A general structural model of a layered birnessite with interlayer cations (Na⁺, K⁺, and water) is shown in Figure 5.1.²⁹

Birnessite is also found in Mn-rich ore deposits as an alteration product. It readily participates in oxidation-reduction and cation-exchange reactions and therefore plays a significant role in soil and groundwater chemistry.¹⁷⁻³³ There are variable Mn oxidation states [Mn(IV), Mn(III), and Mn(II)] present in birnessite where the average oxidation state of these Mn ions in birnessite ranges from 3.5 to 3.99.^{3,7} Natural birnessite typically has an impure composition and poor crystallinity.⁵⁹ This circumstance is at least partially

responsible for the limited studies on the crystal structure and surface reactivity for natural birnessite.⁵⁹

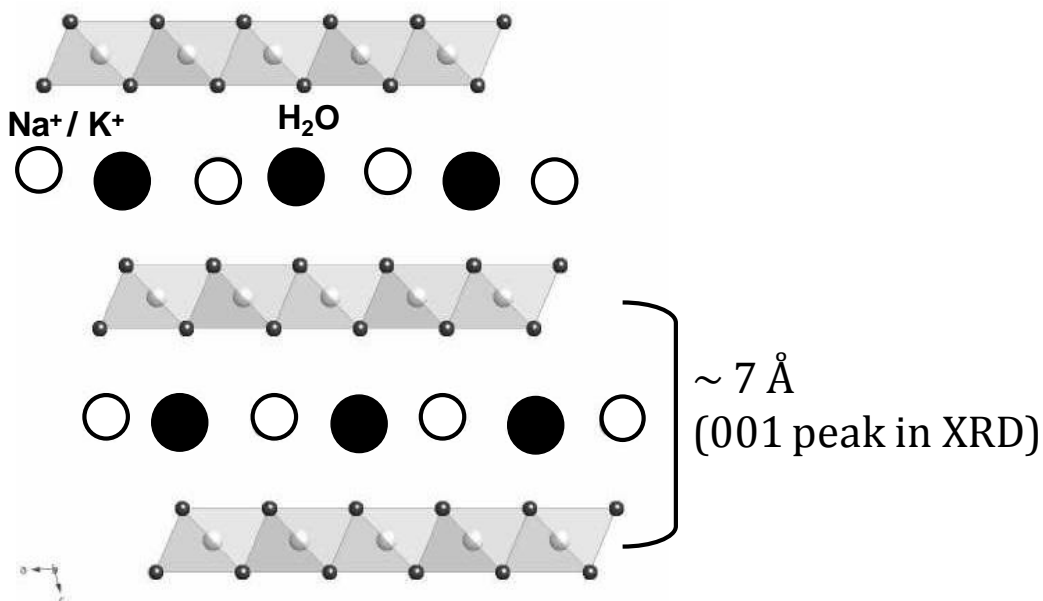


Figure 5.1. Layers structure of birnessite showing the inter layer cations Na⁺ and K⁺, with an interlayer spacing of 7 Å.²⁹

To circumvent the difficulties inherent to naturally occurring birnessite, prior research studied synthetic birnessite which was atomically pure with a high degree of crystallinity (see reference⁵⁹ and references therein). The use of synthetic birnessite is further motivated, because the average Mn oxidation state and crystallinity can be controlled and related to surface reactivity. Parameters such as extent of oxidation, aging process, and the stirring speed affect the ratio of the different Mn oxidation states.¹⁶

Synthetic birnessite can either be in hexagonal or triclinic forms, where as the majority of the natural birnessite exists in the hexagonal form.⁶⁹ Hexagonal birnessite contains Mn(IV) vacancies in octahedral sheets, which gives negative surface charge to

the birnessite.^{6, 9, 69} Triclinic form of birnessite does not contain Mn(IV) vacancies. Negative surface charge of triclinic birnessite is due to the substitution of Mn(III) for Mn(IV) in the layers.^{10, 69} The Na-birnessite used in this study was synthesized following the method reported by Chen et al., (details in chapter 2).³⁶

5.2. Prior Investigation on As(III) Oxidation by Birnessite

Prior studies have shown that birnessite oxidizes toxic compounds like aqueous As(III), Pb(II), Se(IV), and several organic compounds due to the reducibility of Mn in the (III) and (IV) oxidation states in the birnessite structure.¹⁷⁻³³ Studies have shown that this reactive manganese oxide mineral surface can be utilized to adsorb toxic compounds and in certain cases converting toxic compounds to materials having a lesser toxicity via redox chemistry.¹⁷⁻³³ In the context of adsorption, prior studies have shown that that manganese oxides (including birnessite) acts as an active surface for the adsorption of a variety of organic and inorganic compounds [e.g., As(III), Pb(II), Se(VI)].¹⁷⁻³³ IN the context of birnessite acting as a redox active surface, prior studies, for example, have shown that the exposure of birnessite to aqueous arsenite [As(III)] results in the oxidation of this species to arsenate [As(V)] with the concurrent reduction of Mn(IV)/Mn(III) in the mineral.^{7-24, 27-33}

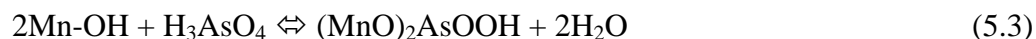
It is interesting to bring forward results from a prior study by Scott and Morgan in 1995 that demonstrated that As(III) was oxidized to As(V) on K-birnessite.³⁰ They proposed a four step reaction mechanism, explaining the red-ox process. The first step

included the formation of an bidentate inner sphere complex by the displacement of As(III) by surface-bound OH⁻ and H₂O. The second step included a two electron transfer from the Mn(IV) to the As(III), breaking the two Mn-O bonds, and the addition of oxygen from water to As(V). The third and fourth steps included the release of As(V) and reduced Mn(II) into the solution. Later in 1998 Nesbitt et al proposed a two step reaction mechanism for the oxidation of As(III) by Na-birnessite, shown by the following reactions,²³



where H₃AsO₃ represents As(III), H₃AsO₄ represents As(V), and MnOOH* is the Mn(III) intermediate reaction product. Mn(II) was simultaneously released into the solution. They proposed an one electron transfer of structural Mn(III) component of the birnessite undergoing reductive dissolution at a different rate than the MnOOH*.

In 2002 Manning et al., (reaction 5.3) have included the adsorption of As(V) by birnessite surface.⁴⁶ They reported that Mn-OH is the reactive hydroxyl group on the surface of MnO₂, and(MnO)₂AsOOH that represents the As(V) surface complex. By using the EXAFS studies they showed that 20 to 30% of the As(V) formed was adsorbed onto the surface of the birnessite at pH 6.5 via an inner sphere bidentate binuclear complex.



The release of Mn(II) was not stoichiometrically related to As(III) oxidation in their studies. This might be due to an one e- transfer to reduce Mn(IV) to Mn(III), with the product remaining in the MnO₂ crystal structure. They have also proposed that the positively charged Mn(II) adsorbs onto the birnessite surface which is negatively charged at pH 6.5.⁴⁶

Light (UV/visible) catalyzed oxidation reactions have gained significant interest in recent years.⁶⁰ Ideal conditions include developing and optimizing those methods that can utilize sunlight as the light source. Relevant to the systems investigated in this thesis work, the photocatalytic oxidation of As(III) using TiO₂ has been extensively studied.⁶¹⁻⁶⁴ However, TiO₂ has a bandgap of 3.2 eV,⁶⁵ hence utilizes UV light to activate the oxidation/adsorption reactions. Due to the abundance of solar radiation in nature, remediation methods that utilize solar radiation are important. Furthermore, recent work reported by Bhandari et al., shows that the oxidation and adsorption of arsenite by two iron oxyhydroxide minerals namely ferrihydrite³⁵ and Goethite,⁶⁰ in the presence of in presence of simulated solar light. These experimental observations drawn from prior studies motivated us in part to understand the reasons and propose that birnessite can be utilized to catalyze the photooxidation of As(III).

Our focus was to utilize the simulated solar light source for photocatalytic oxidation of As(III) using birnessite. The details of the light radiation used in these experiments were explained in section 2.2.1 of chapter 2. Birnessite is a semiconductor. Sherman et al., observed a band gap 1.8 eV for the of Na-birnessite from the oxygen K-

edge absorption and emission spectroscopy.⁶⁶ Sakai et al., calculated the band gap of proton (H)- birnessite from the relationship between the incident photon energy and photon-photon conversion efficiency and reported a band gap of 2.23 eV.⁶⁷ Pinaud et al., observed a band gap of 2.7 eV for the Na-birnessite based on the UV-Vis absorption spectroscopy and Tauc plot.⁶⁸ Bandgap of Na-birnessite used in this study is approximately 2.7 eV. This was calculated based on the λ_{max} (455 nm) from UV-Vis absorption spectroscopy (Figure 5.2).

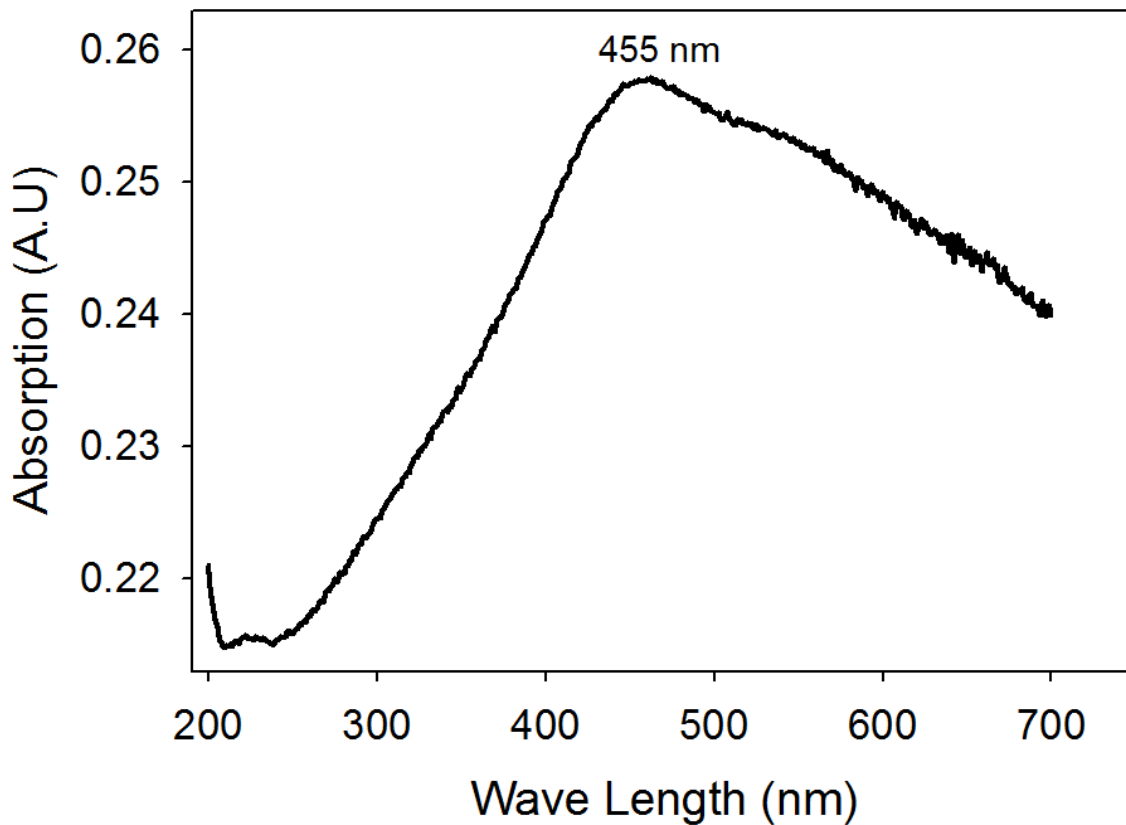


Figure 5.2. UV-Vis absorption spectrum of the Na-birnessite.

Bandgap of the semiconductors changes with the particle size and in case of birnessite bandgap depends on the number of Mn(IV) vacancies.⁶⁹ Band gap decreases with increasing in Mn(IV) vacancies of the birnessite.⁶ Furthermore, the photo-activity of birnessite under visible light conditions was demonstrated by various research groups⁶⁸⁻⁷³, but none of these studies were focused on As(III) photo-oxidation, the focus of this chapter.

5.3. Characterization of Na-birnessite

Na-birnessite was used as the photo-active surface and the material after synthesis was characterized with powder X-ray diffraction (XRD), Brunauer-Emmett-Teller (BET) specific surface area analyzer, X-ray photo electron spectroscopy (XPS), transmission electron microscopy (TEM) and atomic force microscopy (AFM). XRD data was collected with a Bruker AXS single crystal X-ray diffractometer using Cu K α radiation and a graphite monochromator. The voltage and filament current was fixed at 50 kV and 1 mA respectively. XRD of the synthesized Na-birnessite (Figure 5.3) was similar to the previously reported triclinic birnessite samples,^{3, 7, 14, 15, 36-40} which was previously reported as monoclinic birnessite by Drits⁷ and Silvester et al.⁴¹

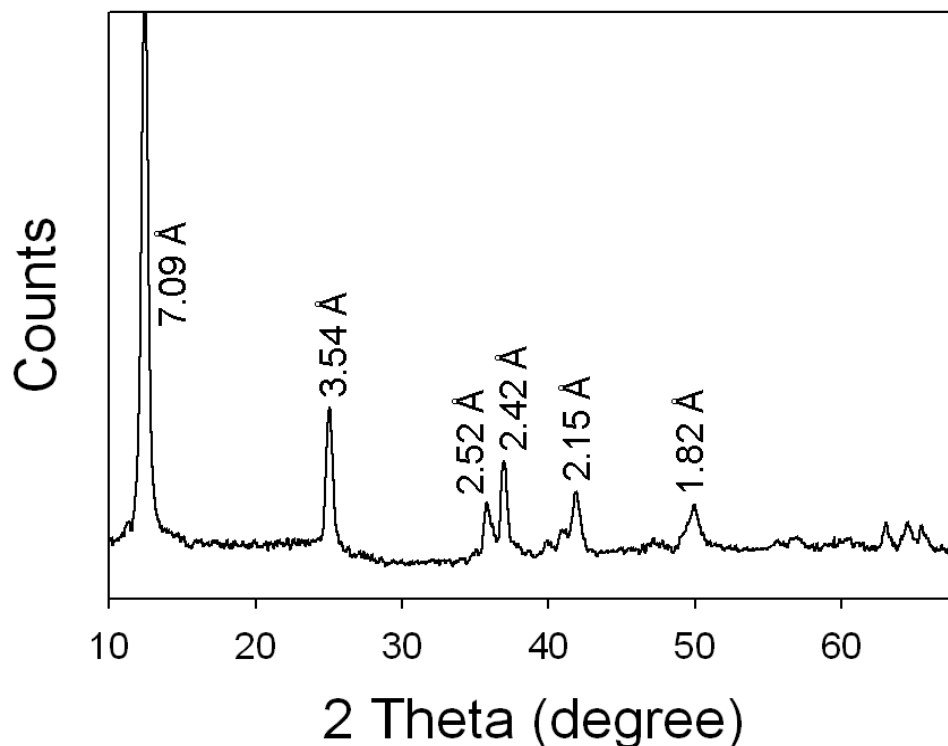


Figure 5.3. X-ray powder diffraction pattern of synthetic Na-birnessite.

The surface area of the Na-birnessite was measured by multi-point BET, N₂ adsorption using a ASAP 2020 surface area analyzer from Micromeritics. Prior to measurement the sample was degassed at 150°C for 2 h.^{42, 43} The BET specific surface area of the Na birnessite was determined to be 23.10 m²/g. TEM images were collected by suspending 2 mg of the solid birnessite sample in 10 mL of isopropanol^{16, 44} and sonicated 20 minutes for homogeneity. One drop (5 μL) of the suspension was deposited onto a 300 mesh carbon coated copper grid and was subsequently air dried. To determine the changes occurring on the birnessite surface during the reaction with As(III) in the presence and absence of light, the reacted samples were analyzed with TEM. Inspection of the synthesized Na-birnessite particles showed them to be similar to the plate or sheet like morphologies reported previously by several authors (Figure 5.4).^{3, 14}

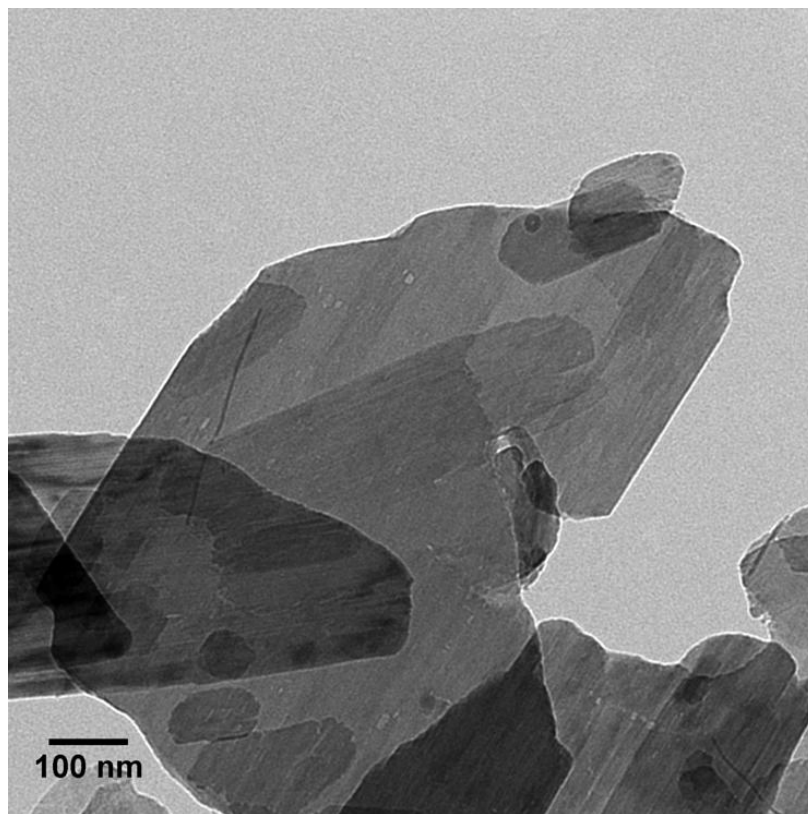


Figure 5.4. TEM image of the clean Na-birnessite

5.4. Results and Discussion

Before conducting the experiments with birnessite, a control experiment was conducted (see Figure 4.7 in chapter 4), where aqueous As(III) is exposed to light for 8 h in the absence of birnessite at pH 5.00. This resulted in a As(V) solution concentration of 2.5 μM after 8h of reaction time. This indicates that that the light induced oxidation of As(III) is a very slow process.

5.4.1. Effect of Light on the Redox Chemistry of As(III) on Birnessite at pH 5.00

Figure 5.5 plots the solution phase concentration of As(V) as a function of time after birnessite was exposed to 470 μM of As(III) at pH 5.00 in the presence and absence of light. Included in the inset to Figure 5.5 is the amount of arsenic adsorbed on the birnessite as a function of reaction time. The amount of arsenic that becomes adsorbed on the birnessite sample is largely independent of whether the solution is irradiated or kept in the dark. For example, $\sim 30 \pm 4 \mu\text{M}$ of arsenic became adsorbed after 8 h on the birnessite surface whether the reaction was carried out in the dark or in presence of light. In contrast, the amount of solution phase As(V) oxidation product shows significant differences between the reaction that was exposed to light and the one that was run under dark conditions. In the dark, for example, $72 \pm 3 \mu\text{M}$ of As(V) product was present after 8 h of reaction, compared to a As(V) aqueous concentration of $158 \pm 4 \mu\text{M}$ when the reacting system was exposed to light for 8 h. The first order (initial) rate constant (k_{obs}) for the As(V) formation was 0.06 and 0.10 h^{-1} respectively in dark and the light experiments. This is calculated by using the following equation, assuming that the initial order of the reaction as the first order reaction,

$$k = \frac{0.693}{t_{1/2}}$$

Where k is the first order rate constant, $t_{1/2}$ is the half life, which is the time, required to reduce the reactant concentration to half. The reason for the higher k_{obs} that is associated with the light experiment will be discussed below.

The concentration of Mn(II) in solution as a function of time during the arsenite oxidation reaction in the absence and presence of light is shown in Figure 5.6. For example, after 8 h of reaction, the concentration of dissolved Mn(II)_(aq) was 97 and 196 μM, in dark and light experiments, respectively.

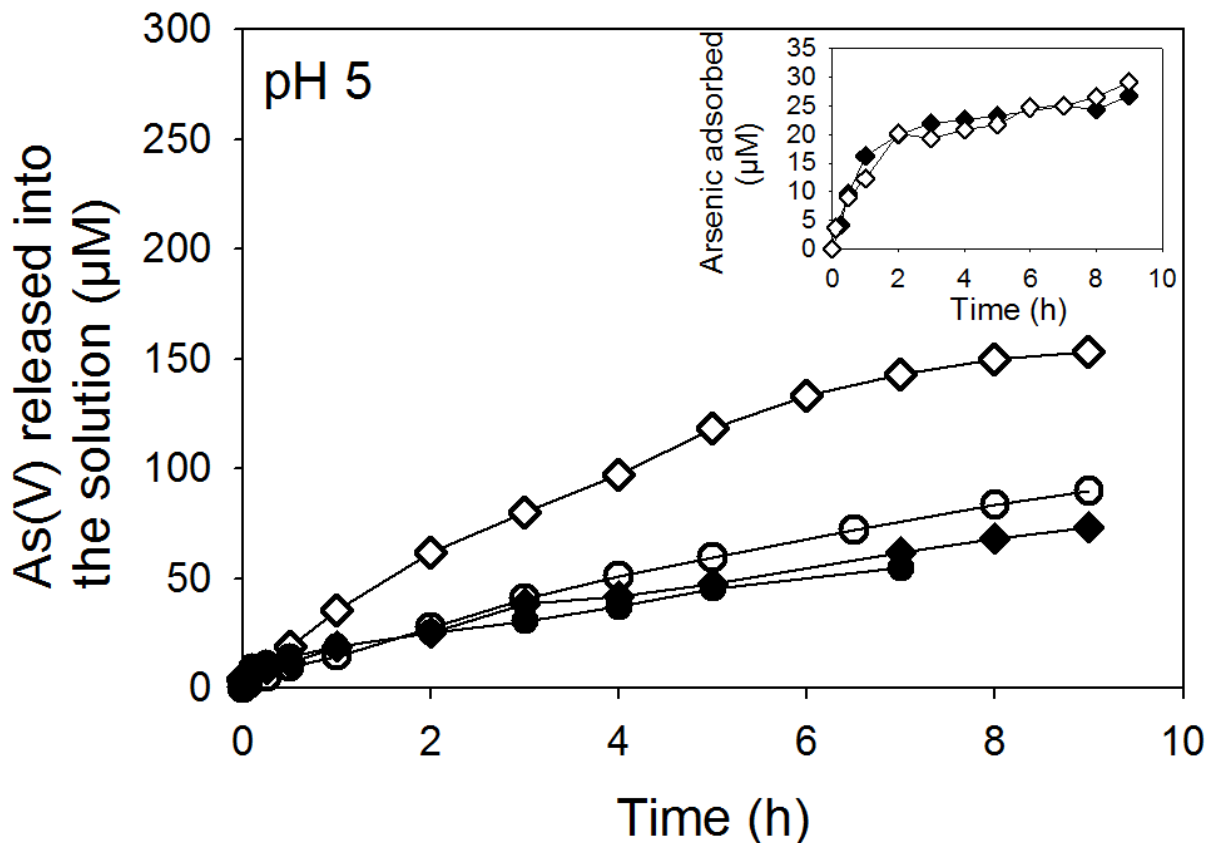


Figure 5.5. The amount of arsenate released into the solution during the oxidation of 470 μM of As(III) at pH 5.00 as a function of time in dark (closed diamonds) and light (open diamonds). The amount of As(V) that was released into solution during the oxidation of As(III) by Na-birnessite in the absence and presence of light at pH 5.00, under anoxic conditions is shown with closed and open circles respectively. The inset shows the

amount of arsenic adsorbed on the birnessite during the oxidation of As(III) under dark (closed diamonds) and light (open diamonds) conditions.

The ratio of the concentration of Mn(II) released into the solution to the concentration of As(III) oxidized (i.e., $\text{As(V)}_{\text{aq}} + \text{As(V)}_{\text{ads}}$) in the dark and in the presence of light was determined from the data to be 1.11:1 and 0.94:1, respectively. This equivalence between As(V) and Mn(II) product under light or dark conditions at pH 5.00 is largely consistent with the stoichiometry associated with As(III) oxidation on birnessite that can be described using the following composite redox reaction.^{23, 46}

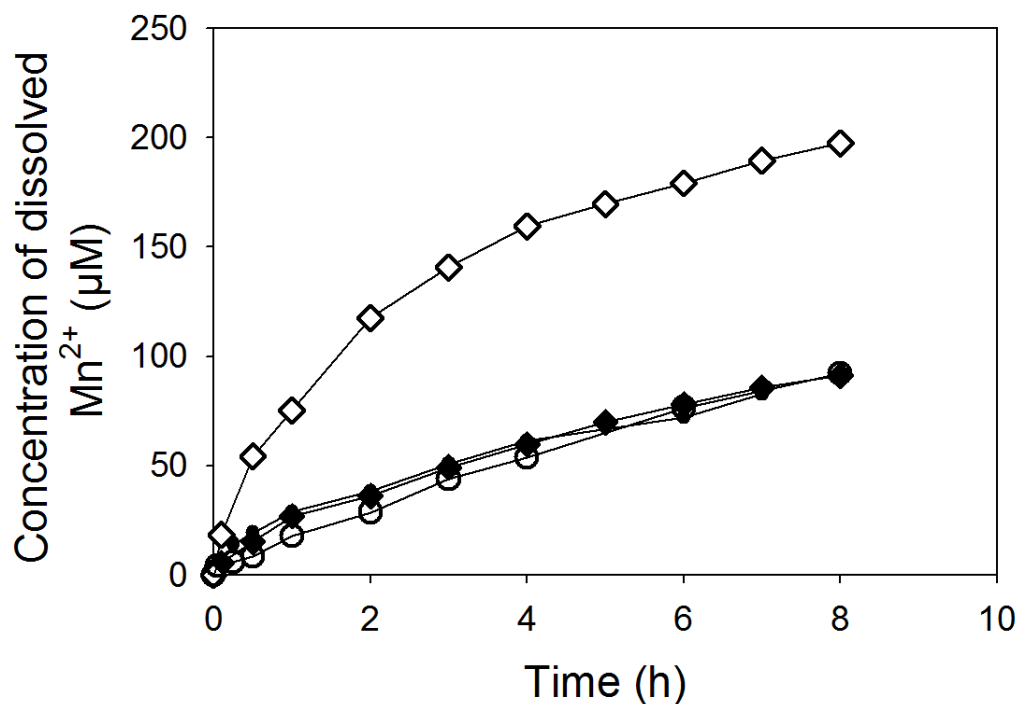


Figure 5.6. The concentration of dissolved Mn^{2+} released during the oxidation of $470 \mu\text{M}$ of As(III) by Na birnessite at pH 5.00 in presence of light, oxic (open triangles), light,

anoxic (open diamonds), dark, oxic (closed triangles), dark, anoxic (closed diamonds) as a function of time.

To investigate any structural changes in the birnessite during the As(III) oxidation reaction at pH 5.00, XRD data were obtained for the post-reaction solid and compared to XRD of the pre-reaction mineral. These data are displayed in Figure 5.7 and suggest that structural changes do occur during the As(III) redox chemistry on birnessite under both dark and light conditions. The most noticeable changes between before-and-after-XRD are emphasized in Figure 5.7. Analysis of these reflections indicates that Na-birnessite converted from the triclinic form^{3, 7, 10, 14, 15, 36-40,45} to hexagonal H-birnessite structure^{7, 41, 45} after reaction with As(III) for 8 h under both light and dark conditions. This type of transformation has been reported by several authors previously^{7, 41} to occur when birnessite was exposed to low pH conditions, even in the absence of arsenite. H-birnessite consists of hexagonal octahedral layers containing predominantly Mn(IV) with variable amounts of Mn(III) and layer vacancies. As explained by Drits⁷ and Silvester et al.,⁴¹ the distribution of layer vacancies is inherited from the former Mn(III) distribution in triclinic Na-birnessite. The driving force of the Na-birnessite to H-birnessite transformation is likely due to the destabilization of Mn(III) rich rows under low pH conditions. At low pH interlayer Na⁺ ions are displaced by H⁺ ions, leading to the destabilization of Mn(III) rich rows.^{7, 41}

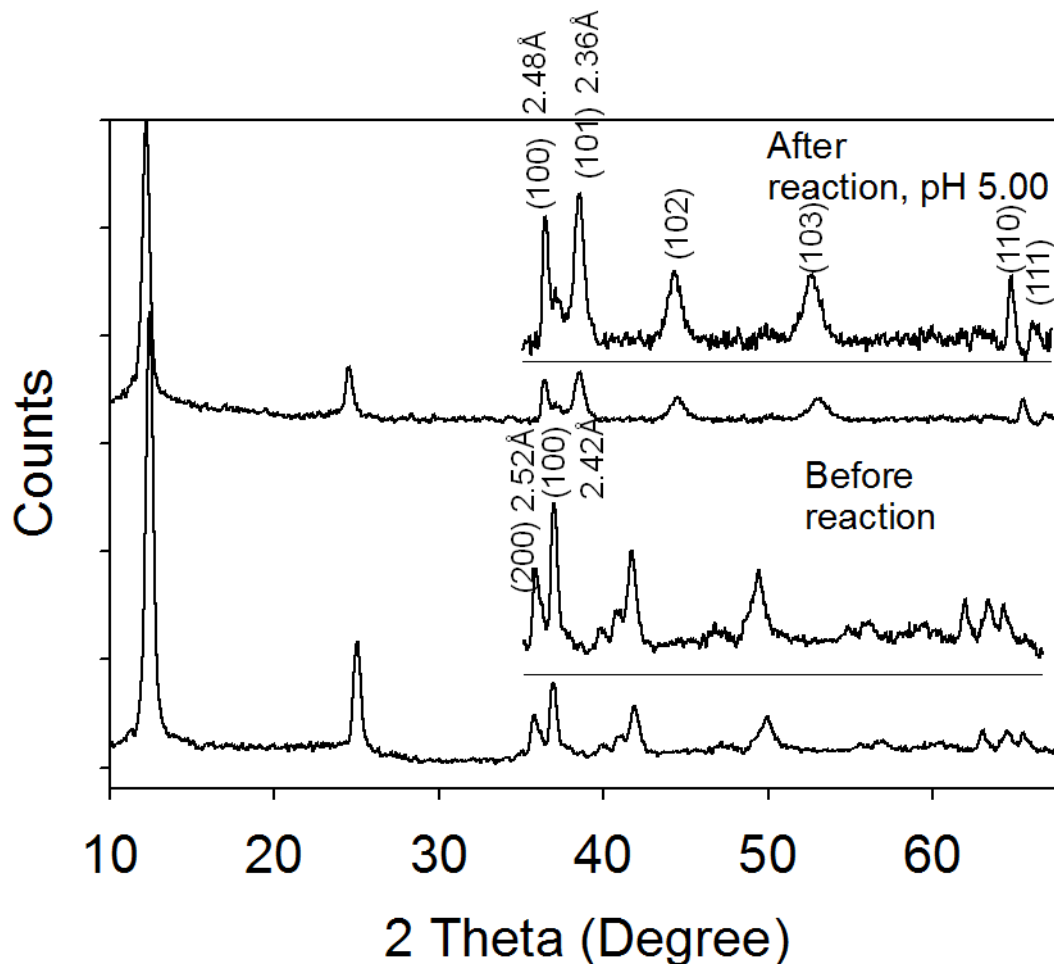


Figure 5.7. Bottom spectrum shows the X-ray diffraction pattern of the Na birnessite before reacting with As(III) and top spectrum shows the X-ray diffraction pattern of the Na birnessite after reaction with arsenite at pH 5.00. Completer transformation of triclinic Na-birnessite to hexagonal H-birnessite was observed after the reaction. For clarity reflections and d-spacings of the both birnessite samples were shown in the Figure. X-ray diffraction patterns of the birnessite reacted with arsenite at pH 5.00 is same both in dark and in presence of light. Hence, only images of the birnessite reacted in light was shown for clarity.

TEM images of the birnessite samples were taken before and after reaction with As(III) both in the presence and absence of light to check any other products formed during the reaction or also to check the phase transformation of the birnessite during the reaction. Figure 5.8 shows the TEM micrographs of the birnessite particles reacted with arsenite for 8 h in dark (Figure 5.8a) and in the presence of light (Figure 5.8b, c) at pH 5.00. Birnessite particle edges are etched after the 8 h of reaction time indicated by arrows and circles in Figure 5.8 and no phases other than birnessite plates were observed.

The etching was more pronounced when the As(III)/birnessite system was exposed to light, indicating the high reactivity of the Na-birnessite in presence of light. To ascertain the effect of light on the birnessite particles, TEM micrographs of the birnessite particles were taken after exposed to arsenite for 48 h in dark. After 48 h of reaction time (Figure 5.8 b) in dark birnessite particle edges are etched and looked similar to the 8 h reaction particles. Hence we conclude that more dissolution and etching of the particles at longer reaction times is due to the more reactivity of the particles in presence of light. Oxidation of more As(III) to As(V) in presence of light compared to the oxidation in dark indicates the high reactivity of Na-birnessite in presence of light compared to dark. From this, we conclude that light did not induce any experimentally observable phase transformation in the birnessite particles. Tournassat et al.,⁴⁵ observed insoluble manganese, arsenate precipitates ($\text{Mn}(\text{H}_2\text{O})(\text{AsO}_3\text{OH})$) during the reaction of birnessite with arsenite at pH 5.00, after 162 h of reaction time, when no Mn^{+2} was released into the solution, due to the reaction of Mn^{2+} with the As(V) during the As(III) oxidation. We did not observe these precipitates in TEM studies, as we have carried out these reactions only for 8 h. There might be small amounts of precipitates formed during

the 8 h of reaction, but the identification of the small amounts of precipitates were not possible with TEM.

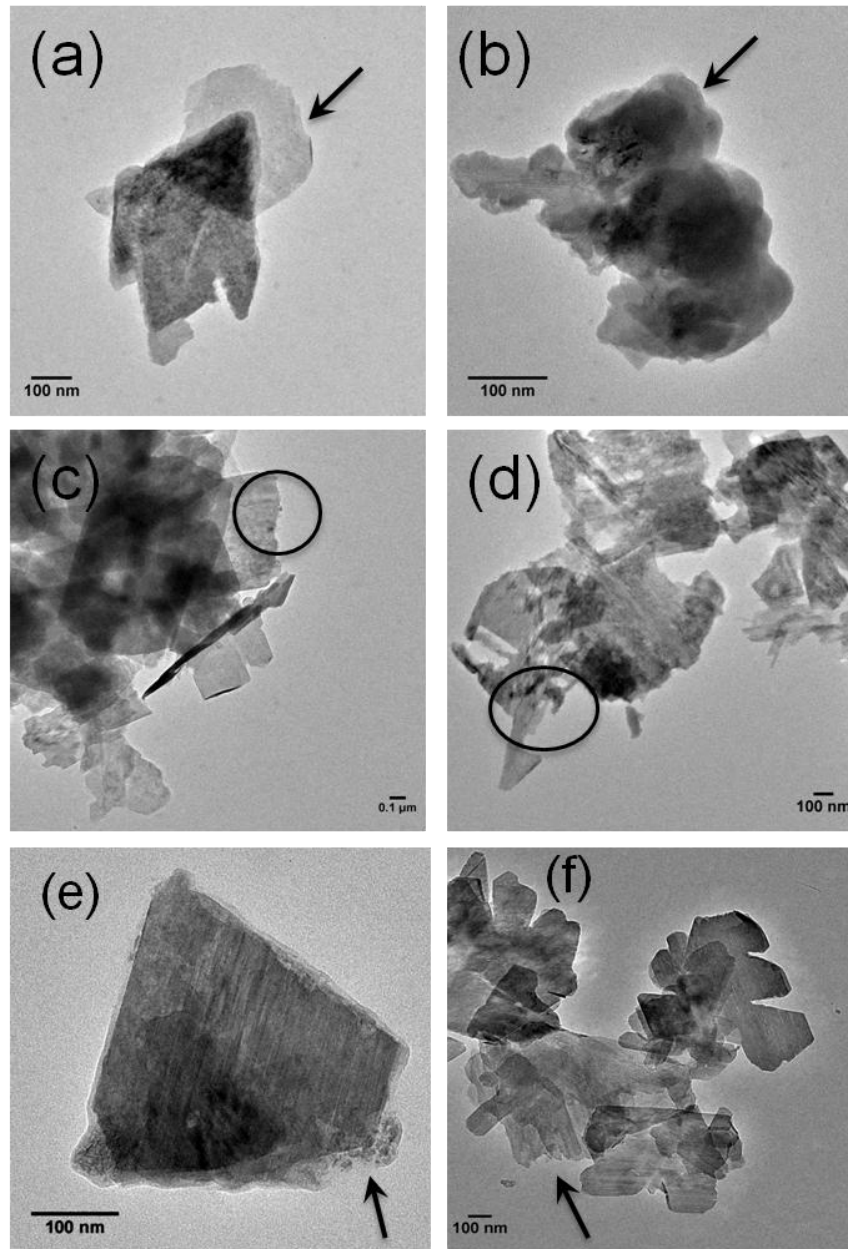


Figure 5.8. TEM images of the Na-birnessite particles reacted with Arsenite at pH 5, (a) 8 h in dark, (b,c) 8 in light, and (d) 48 h in dark. (e) and (f) are the TEM images of the

Na-birnessite particles reacted with As(III) for 8 h at pH 7.4 in the absence and presence of light respectively. Etching of the particles was shown with the arrows and circles.

5.4.2. Effect of Light on the Redox Chemistry of As(III) on Na-Birnessite at pH 7.40

Figure 5.9 plots the aqueous As(V) concentration and the As(V) product that is adsorbed (inset to Figure 5.9) during the oxidation of As(III) on Na-birnessite in the dark and in presence of light at pH 7.40. After an 8 h reaction time the amount of As(V) released into the solution at pH 7.40 in the light ($\sim 25 \pm 4 \mu\text{M}$) is about two times higher than the same reaction under dark conditions ($\sim 15.9 \pm 4 \mu\text{M}$). Similar to the reaction that was run at pH 5.00, the amount of arsenic adsorbed on the birnessite is the same (i.e. within the experimental error) under light and dark conditions at the higher pH of 7.40 ($\sim 25 \pm 4 \mu\text{M}$).

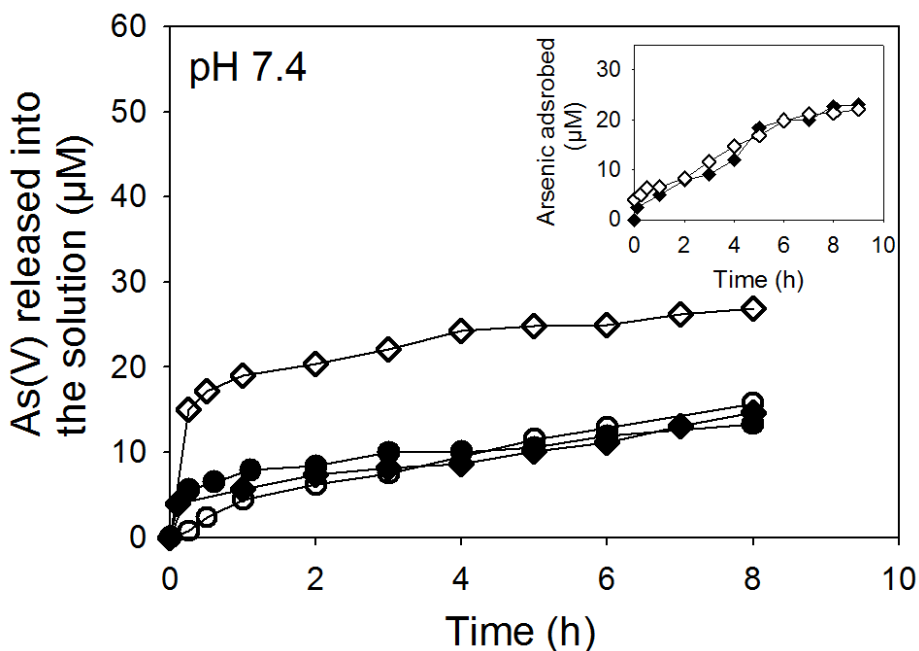


Figure 5.9. The amount of As(V) released into the solution during the oxidation of As(III) at pH 7.40 in dark (closed diamonds), in light (open diamonds) as a function of

time. The amount of As(V) that was released into solution during the oxidation of As(III) by Na-birnessite in the absence and presence of light at pH 7.40, under anoxic conditions is shown with closed and open circles respectively. Inset shows the concentration of arsenic adsorbed at pH 7.40 during As(III) oxidation in dark (closed diamonds), light (open diamonds). The initial concentration of As(III) used was 470 μM .

The k_{obs} for As(V) formation in dark and light experiments were 0.02 and 0.06 h^{-1} respectively and are less than the measured k_{obs} at pH 5.00 in dark (0.06 h^{-1}) and light (0.10 h^{-1}) reactions. Thus the increase in pH leads to a decrease in the As(III) oxidation rate. Similar to the birnessite exposed to As(III) at pH 5.00, arsenic K-edge XANES spectrum of the birnessite samples treated with As(III) in dark, light at pH 7.40 (Figure 5.10) collected in quick EXAFS mode showed the presence of only As(V) on the surface. Consistent with prior studies that have investigated the oxidation of As(III) on birnessite³⁰ at a solution pH > 6.00, there is no measureable release of Mn^{2+} into solution in our experiments at pH 7.40. Instead at the pH of 7.40 used in this particular study, any Mn(II) product formed during the reductive dissolution of the birnessite remains on the surface of the birnessite.^{29, 31, 46, 47}

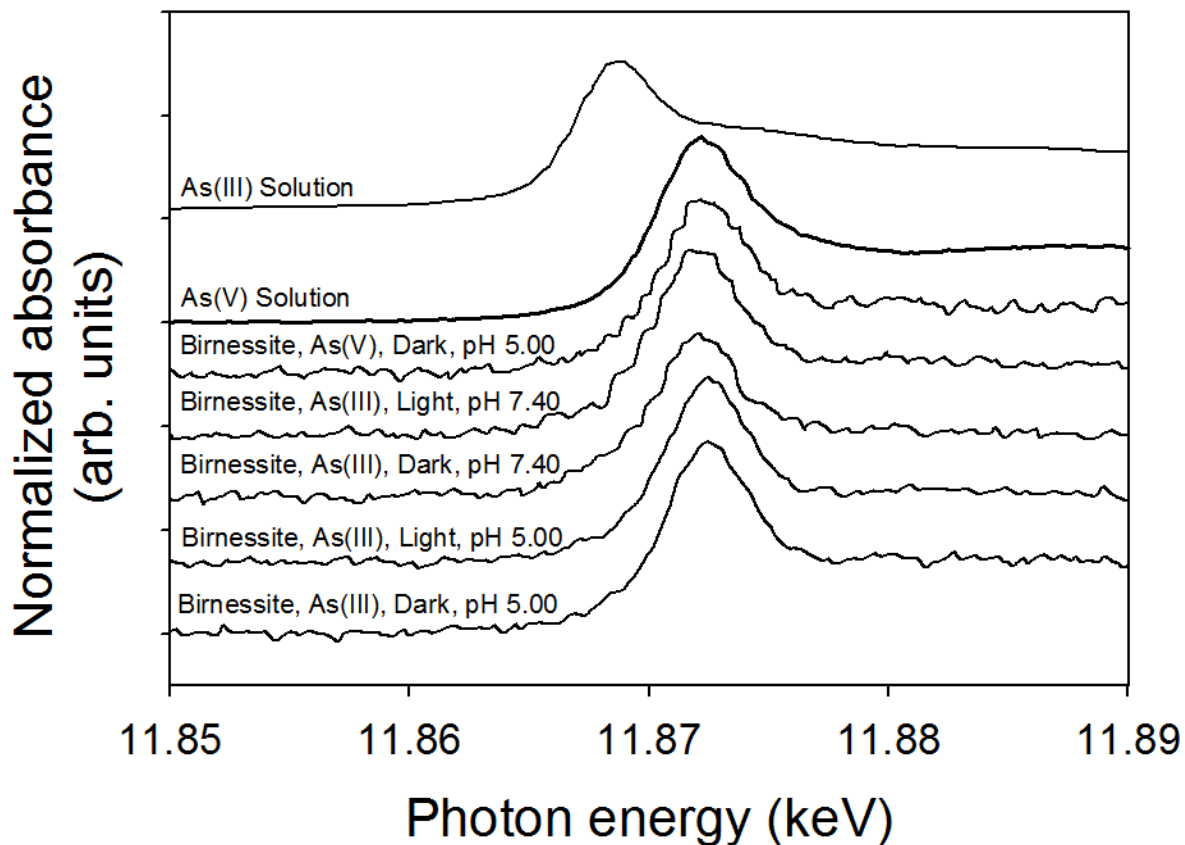


Figure 5.10. Arsenic K-edge EXAFS spectrum of the Na-birnessite exposed to As(III)/As(V) for 8 h. As K-edge spectrum of the As(III) and As(V) solution were used as the reference. (All the plots were offset for clarity).

Prior work by Lafferty et al., showed that Mn(II) released during the oxidation of As(III) by K-birnessite, was adsorbed on the surface of K-birnessite at pH 7.2.^{19, 20} To investigate the adsorption of Mn(II) product onto the Na-birnessite, and to determine the effect of Mn²⁺ adsorption on the birnessite structure we carried out XRD studies for the pre- and post-reaction Na birnessite. Figure 5.11 displays XRD diffractograms for Na-birnessite before and after an 8 h exposure to As(III). Inspection of the XRD data shows

that there are changes after the birnessite is exposed to As(III) for 8 h. In particular there is a decrease in intensity of peaks at 2.52, 2.42, and 1.82 Å, which are due to 200, 100, and 113 reflections respectively (indicated by arrows in Figure 5.11).⁵⁶ Two new peaks are developed at 2.47 and 2.36 Å (indicated by stars in Figure 5.11) that we attribute to the 101, and 101 reflections appeared due to the formation of hexagonal birnessite.^{48,56} Prior research by Le Goff et al.,⁴⁸ suggested that the presence of Mn²⁺ ions in the interlayers of the birnessite results in hexagonal symmetry, due to the decrease in the number of hydrogen bonds between oxygen of the MnO₆ octahedra and the hydrogen of water molecules. Based in part on this prior study we believe it is likely that at pH 7.40 Mn(II) does not partition into the solution phase, but instead adsorbs and resides in the interlayers of the birnessite lattice.

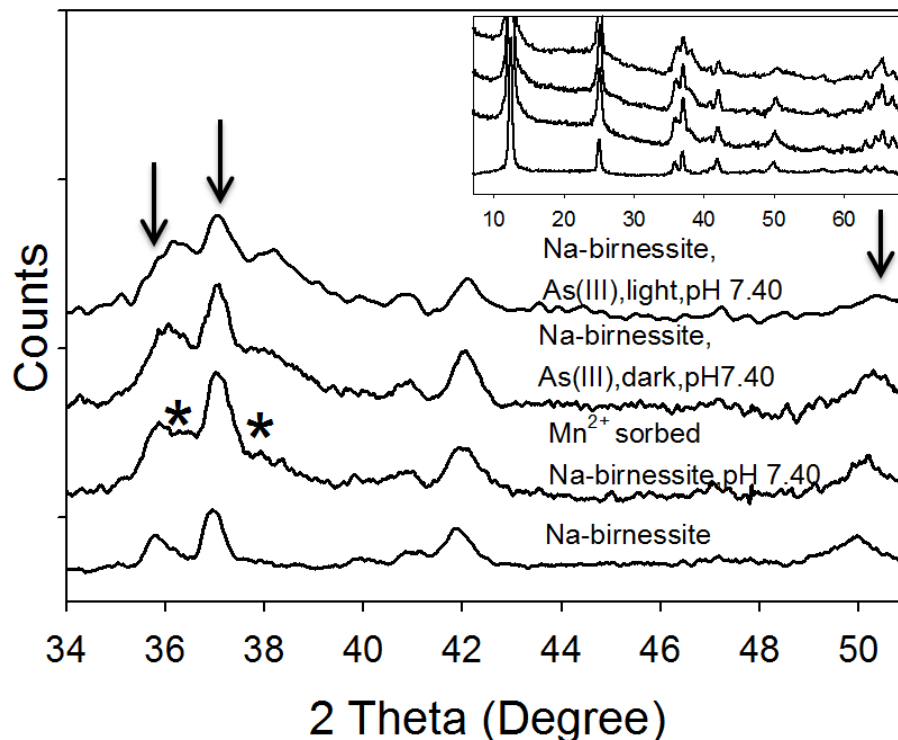


Figure 5.11. (a) XRD pattern of the un reacted Na-birnessite, (b) XRD pattern of the Na-birnessite exposed to Mn²⁺ for 1h at pH 7.40, (c) XRD pattern of the Na-birnessite

reacted with As(III) in dark at pH 7.40, and (d) XRD pattern of the Na-birnessite reacted with As(III) at pH 7.40 in presence of light. Arrows indicates the peaks, which reduced in intensity, while stars indicate the peaks, which are growing during the reaction of Na-birnessite with As(III).

To further support the contention that the retention of Mn(II) in (or on) the birnessite occurred during the oxidation of As(III) at pH 7.40, an experiment was conducted, where Na-birnessite was exposed to 80 μM of Mn^{2+} (Manganese chloride) solution, at pH 7.40 (no As(III) was present). Samples were collected at specific time intervals, centrifuged, washed once with pH 7.40 water, air dried and analyzed with XRD (Figure 5.12). The XRD pattern of Na-birnessite that was exposed to Mn(II) for 8 h was similar to Na-birnessite that was exposed to As(III) at pH 7.40 (see Figure 5.11). Both of these diffractograms show differences relative to birnessite that did not undergo reaction with either As(III) or Mn(II). This experimental observation supports our contention that the presence of Mn(II) product in the birnessite structure after As(III) oxidation was the reason for the structural transformation of the birnessite. TEM images of the Na-birnessite exposed to As(III) for 8 h in dark (Figure 5.8e), in the presence of light (Figure 5.8f) showed that the particles edges are etched similar to the particles at pH 7.40 and there is no other noticeable changes in these particles.

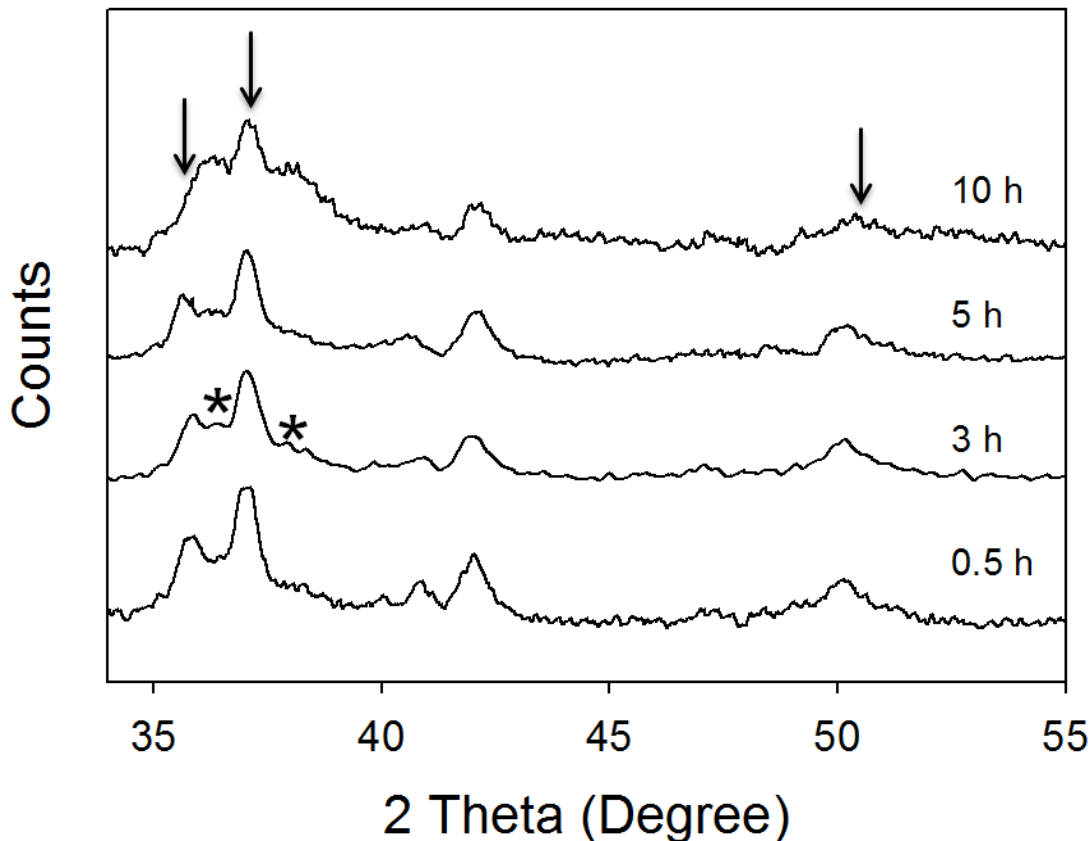


Figure 5.12. XRD pattern of the Na-birnessite exposed to 80 μM of Mn^{2+} solution for different time intervals. The peaks which are growing with time indicated as stars and peaks which are disappearing with time are indicated with arrows. (All the plots were offset for clarity).

5.4.3. Effect of Dissolved O_2 on As(III) Oxidation by Birnessite in the Presence of Light

To better understand the As(III) oxidation mechanism and to elucidate the effect of dissolved oxygen on the oxidation of As(III) by birnessite in presence and absence of light, experiments were conducted, where As(III) was exposed to birnessite in the absence of dissolved O_2 . Dissolved O_2 was removed from the solution by purging ultra high purity (UHP) Ar through the suspension for 1 h in a glove bag filled with UHP Ar.

The oxygen concentration in the reaction mixture and in the glove bag was measured by using an O₂ sensor (Coy laboratories O₂/H₂ monitor) to be ≤ 0.02 ppm and this concentration was maintained throughout the experiment. Figure 5.5 and 5.9 plot the As(V) released into the solution during the oxidation of As(III) in the presence and the absence of dissolved O₂ both in the presence and absence of light at pH 5.00 and pH 7.40 respectively. The amount of As(III) oxidized by birnessite in the dark was the same whether dissolved oxygen was present or not. In contrast, the amount of As(III) oxidized in the presence of light and the dissolved O₂ was approximately 2 times greater than the amount of As(III) that was oxidized under anoxic conditions (no dissolved oxygen present) in the presence of light. This experimental observation brings forward the possibility that in the presence of light, dissolved O₂ was reduced by a photo-excited e⁻ in the conduction band of the birnessite to produce reactive oxygen species (ROS) such as $\cdot\text{OH}$, $\cdot\text{HO}_2$, and H₂O₂ as shown in the following reactions.⁵⁷



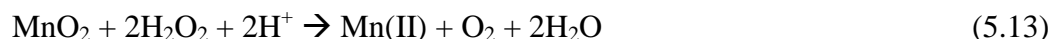
Under both dark and light conditions in either oxic or anoxic solution conditions, 1 mole of Mn(II) was released for every mole of As(III) that was oxidized, which is consistent with the reaction 5.4. ROS are strong oxidizing agents and can oxidize aqueous phase As(III).^{75,76} The formation of ROS under these experimental conditions is confirmed by the fluorescence studies explained below. If ROS are responsible for As(III) oxidation, the ratio of Mn(II) released and As(III) oxidized should not be 1:1 in the oxic experiments conducted in presence of light. In particular, we would assume in this case that the moles of Mn(II) released relative to moles of As(III) that oxidized would be lower, since in the presence of light O₂ would be the terminal electron acceptor and hence not as much Mn(II) product would result. However, in the experiments explained above 0.94 moles of Mn(II) was released for 1 mole of As(III) oxidized, similar to the ratio experimentally observed in the dark or in the light in the absence of O₂. We suspect that the following processes contribute to the formation of Mn(II)_{aq} in these experiments so that the Mn(II):As(V) ratio stays near one in the presence of O₂ and light.

1. Mn(II)_(aq) release may result from the release of Mn(II) trapped in the interlayers of birnessite during the synthesis of the material.³⁰

2. At pH 5.00, Mn(III) present in birnessite layers could presumably undergo a disproportionation reaction to release Mn(II) into solution (reaction 5.12).^{34,55}



3. Another possibility is that H₂O₂, expected to be formed via O₂ reduction by photogenerated electrons, could reduce Mn(IV) to Mn(II) as shown by the following reaction.⁵¹



5.4.4. Detection of ROS Formed During the Photooxidation of As(III) in Presence of Na-Birnessite

Experiments were conducted to determine whether ROS were formed during the photooxidation of As(III) in the presence of birnessite. To determine whether ·OH was formed during the light induced reaction, a fluorescent probe technique was used that utilized 10 μM 3'-(*p*-amino phenyl) fluorescein (APF), and 50 mM phosphate buffer at pH 7.40.^{49, 50} APF itself is non fluorescent, but it becomes fluorescent after reacting with ·OH. ·OH levels were measured at pH 7.40, since APF is stable at pH 7.40 in presence of the phosphate buffer. ·OH formation was measured in-situ, i.e., by adding the APF to the reaction suspension at the beginning the experiment. The excitation wave length was set at 489 nm and emission was observed at 513 nm. Figure 5.13 plots the relative intensity of the ·OH determined using the fluorometer at pH 7.40. The amount of the ·OH formed is more when As(III) is exposed to birnessite in presence of light and dissolved O₂, compared to the ·OH formed when As(III) exposed to birnessite in the presence of dissolved O₂ and the absence of dissolved O₂. The intensity of the ·OH formed when

As(III) was exposed to birnessite in dark, both in the presence and absence of dissolved O_2 is similar to the intensity of the $\cdot OH$ formed when As(III) was exposed to birnessite in presence of light and in the absence of dissolved O_2 . The control experiment where APF was exposed to light in the absence of birnessite also showed the formation of $\cdot OH$ similar to the amount of $\cdot OH$ formed in the absence of light and in the presence and absence of dissolved O_2 . This background signal may be due to the oxidation of APF at room temperature. Further, to rule out any interactions between APF and manganese, APF was added to the reaction mixture after filtering through the 0.22 μm Millipore filters. However, this did not show any $\cdot OH$ formation as shown in Figure 5.14, which was due to the small half life of the $\cdot OH$ (less than 1 ns).⁷⁴

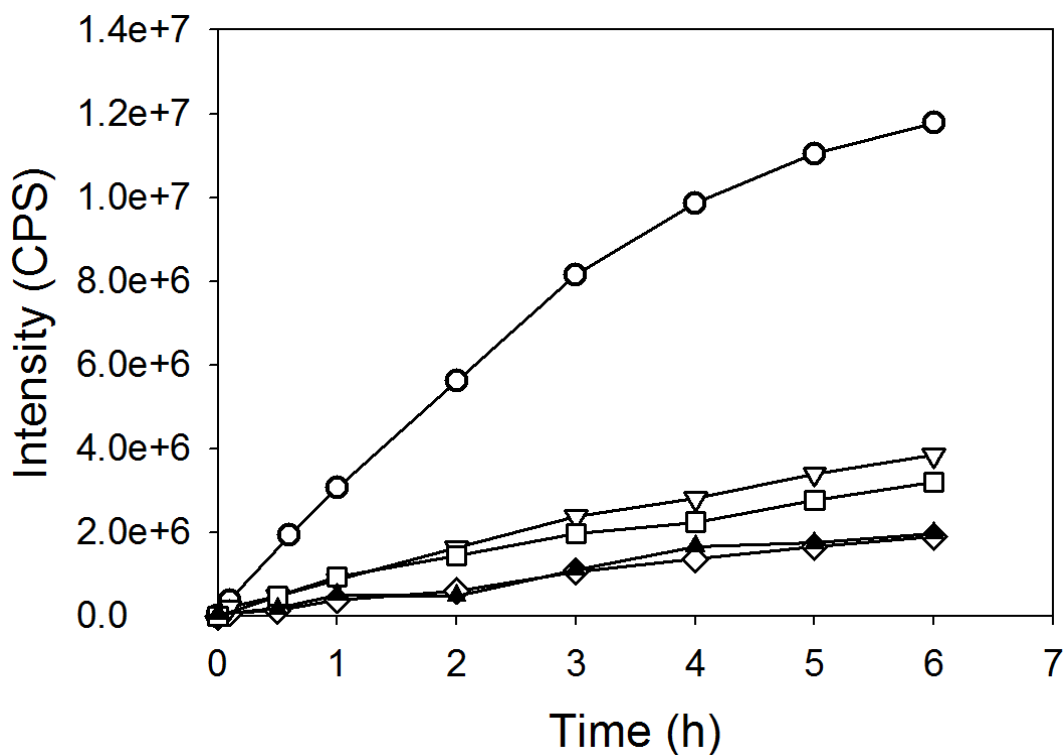


Figure 5.13. Relative intensity of the OH radicals formed in presence of birnessite, light, and dissolved O_2 (open circles), birnessite, light, in the absence of dissolved O_2 (open

reverse triangles), birnessite, dark, dissolved O₂ (closed triangles), Birnessite, As(III), light, and dissolved O₂ (open squares), APF and light (Open diamonds).

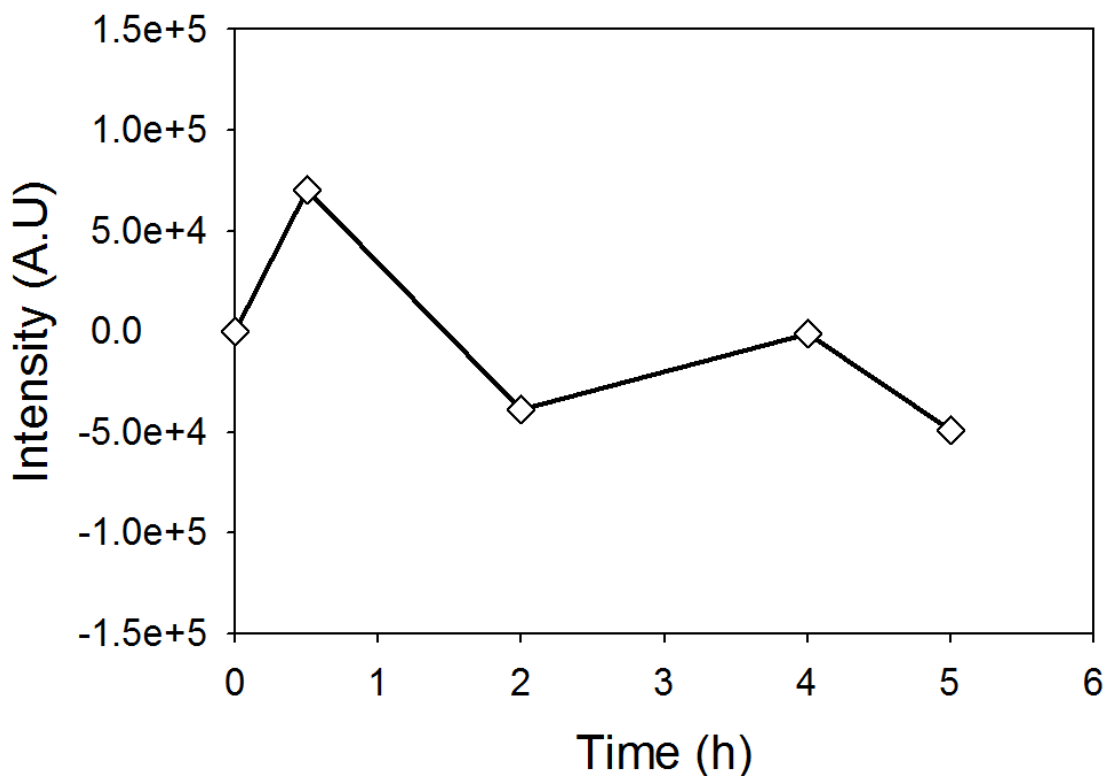


Figure 5.14. The fluorescence intensity of the OH radicals observed when the birnessite was irradiated with light and the probe APF was added ex-situ.

Similarly the production of H₂O₂ was investigated by the addition of 0.2 μM Horse radish peroxidase (HRP) to the reaction mixture in addition to APF and phosphate buffer.^{49, 50} HRP catalyzes the oxidation of APF by H₂O₂, hence APF react with H₂O₂ only in presence of HRP. H₂O₂ are measured at pH 7.40 in presence of the phosphate buffer. In-situ addition of HRP to the reaction mixture showed that it is not stable in

presence of light (Figure 5.15). Hence APF and HRP were added after the sample was filtered. This also prevented the reaction of APF with solution or adsorbed Mn^{2+} .

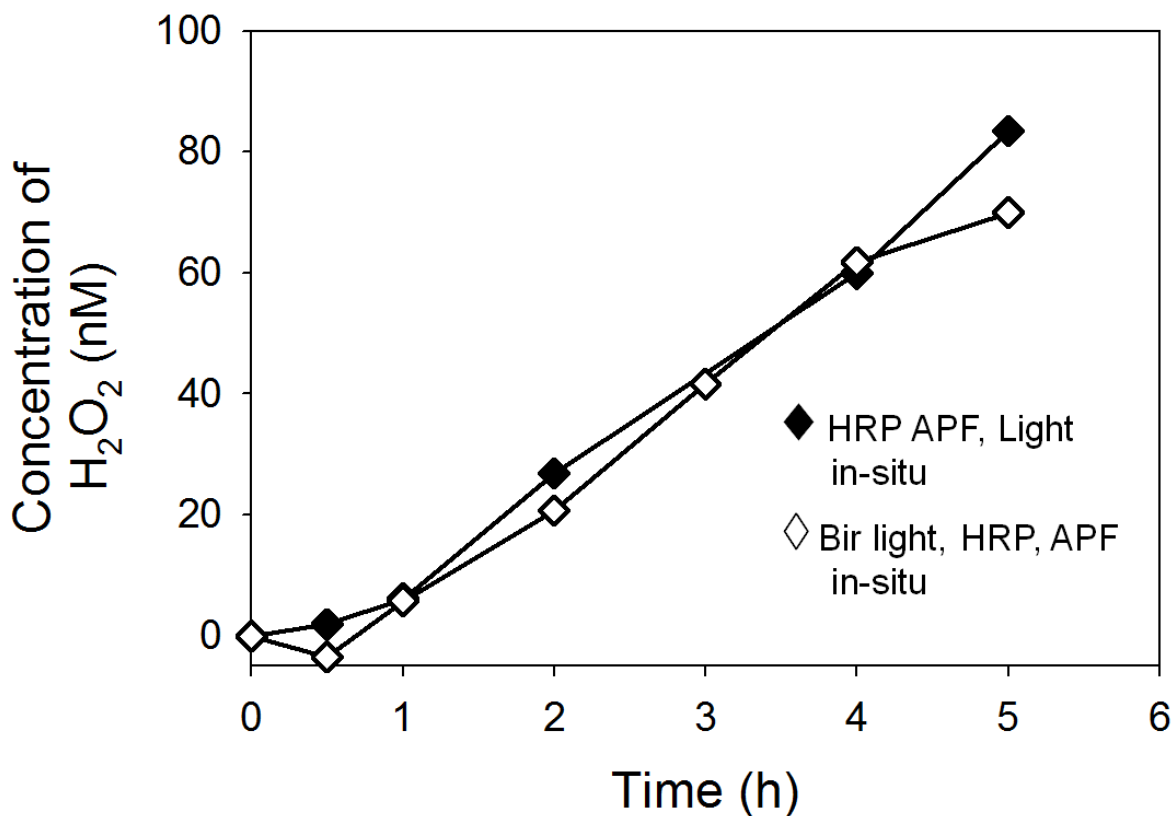


Figure 5.15. Concentration of H_2O_2 observed when the probes HRP and APF were added to the Na-birnessite suspension and irradiated with light (closed diamonds). Open diamonds indicate the H_2O_2 formed in control experiment where the probes HRP and APF were added to the phosphate buffer and irradiated with light.

The concentration of H_2O_2 formed when birnessite is irradiated with light in the absence of As(III) is ~ 27 nM (Figure 5.16) after 12 h, while ~ 4 nM of H_2O_2 was formed when birnessite was irradiated with light in the absence of dissolved O_2 and birnessite is

irradiated with light in presence of As(III), and also when birnessite is exposed to As(III) in the dark. H_2O_2 also has the ability to reduce Mn(IV) to Mn(II) as shown in reaction 5.10.⁵¹ From this result we confirm that H_2O_2 produced during the exposure of As(III) to birnessite in presence of light was consumed due to the reaction of Mn(IV)⁵¹ and As(III) with H_2O_2 separately

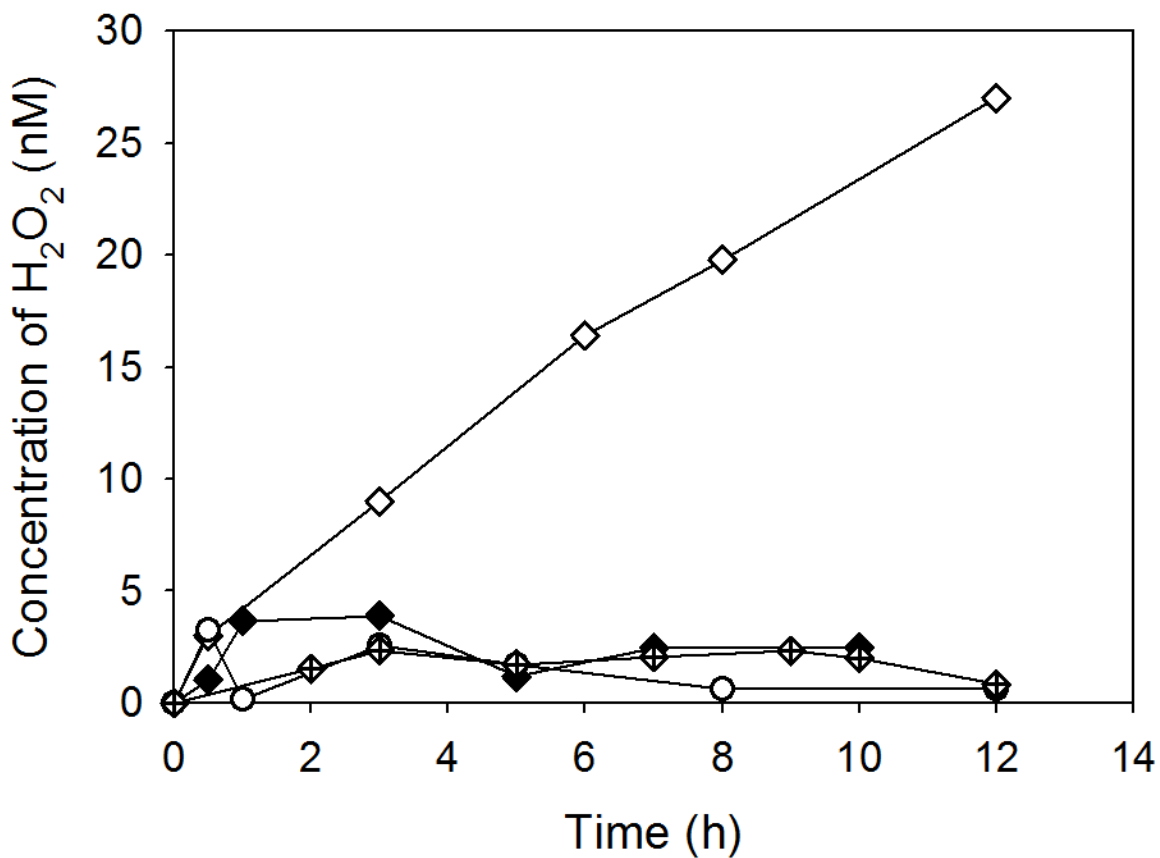


Figure 5.16. Concentration of H_2O_2 formed in presence of birnessite, light, and dissolved O_2 (open diamonds), in presence of birnessite, light, and in the absence of

dissolve O₂ (diamonds with cross hairs), in presence of birnessite, in the absence of light (closed diamonds), in presence of birnessite, light, As(III) (open circles)

To test the possibility that reaction 5.13 was operative under our experimental conditions, Na-Birnessite was exposed to 200 μM H₂O₂ at pH 5.00 in the dark. The solution phase was then tested for aqueous Mn(II) by IC as a function of time. Data for this experiment is shown in Figure 5.17. After 6 h, 31 nM of Mn(II) was released into the solution. We can not rule out the adsorption of some of the Mn²⁺ formed during the reduction of birnessite as Mn²⁺ adsorbs on the birnessite surface. Also Mn(II) release could not be measured at pH 7.40 as it adsorbs onto the birnessite at this pH. The decrease in H₂O₂ concentration could not be measured by the fluorescent techniques, since the probes, APF and HRP, only work well at pH 7.40. Hence another experiment was conducted at pH 7.40, where 200 nM H₂O₂ was exposed to Na-birnessite (0.10g/L H₂O) and H₂O₂ concentration was monitored with the Fluoremeter. These data are shown in Figure 5.18. The H₂O₂ concentration was rapidly reduced after 5 min of reaction, and then a slower rate of decrease was experimentally observed. After 4 h only 26 nM of H₂O₂ remained in solution. From the data in the Figure 5.17 and 5.18 it is possible to show that the H₂O₂ can reduce birnessite and can release Mn²⁺. But the quantification was not possible as these two reactions were conducted at two different pH values. This is because Mn²⁺ adsorbs onto the surface of birnessite at pH 7.40, while H₂O₂ can be detected using Fluoremeter only at pH 7.40.

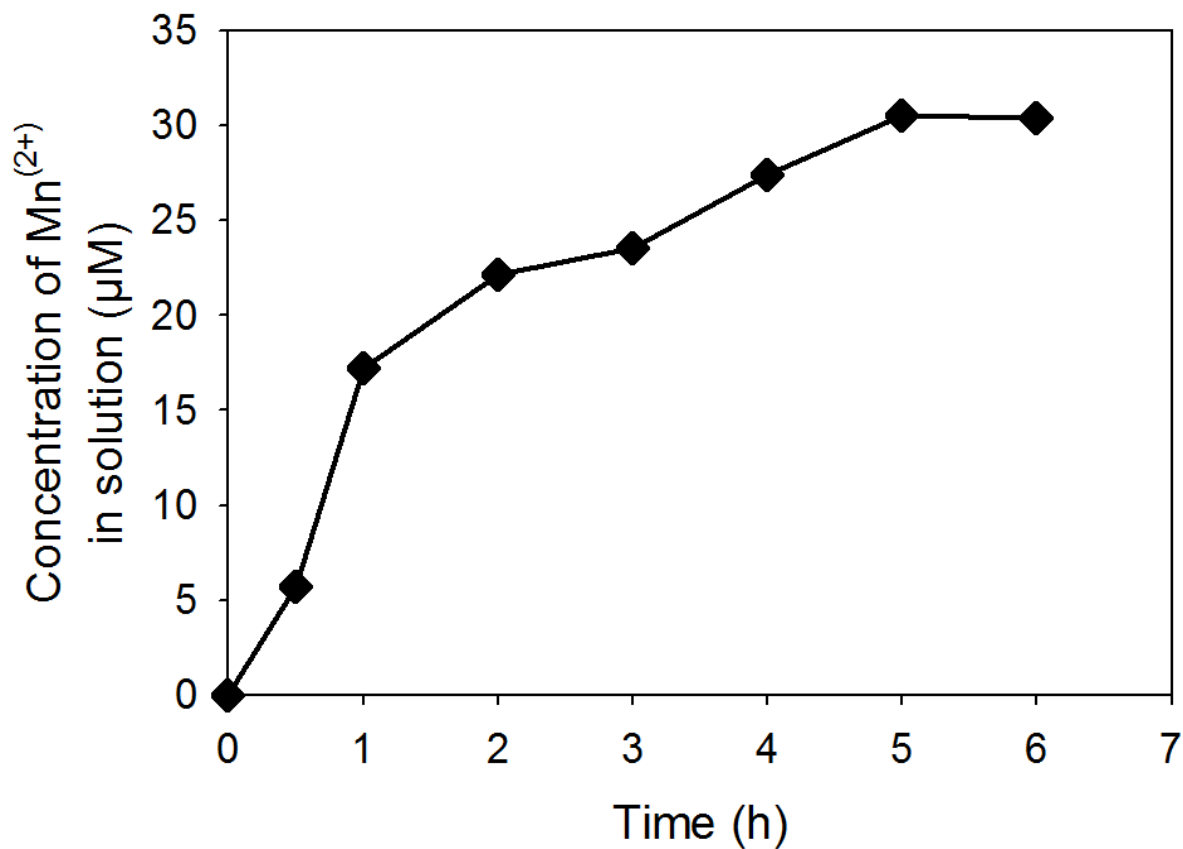


Figure 5.17. Amount of Mn²⁺ released into the solution when 200 µM of H₂O₂ was added to Na-birnessite (0.10g/L H₂O) at pH 5.00 and stirred in dark (Without irradiating the light)

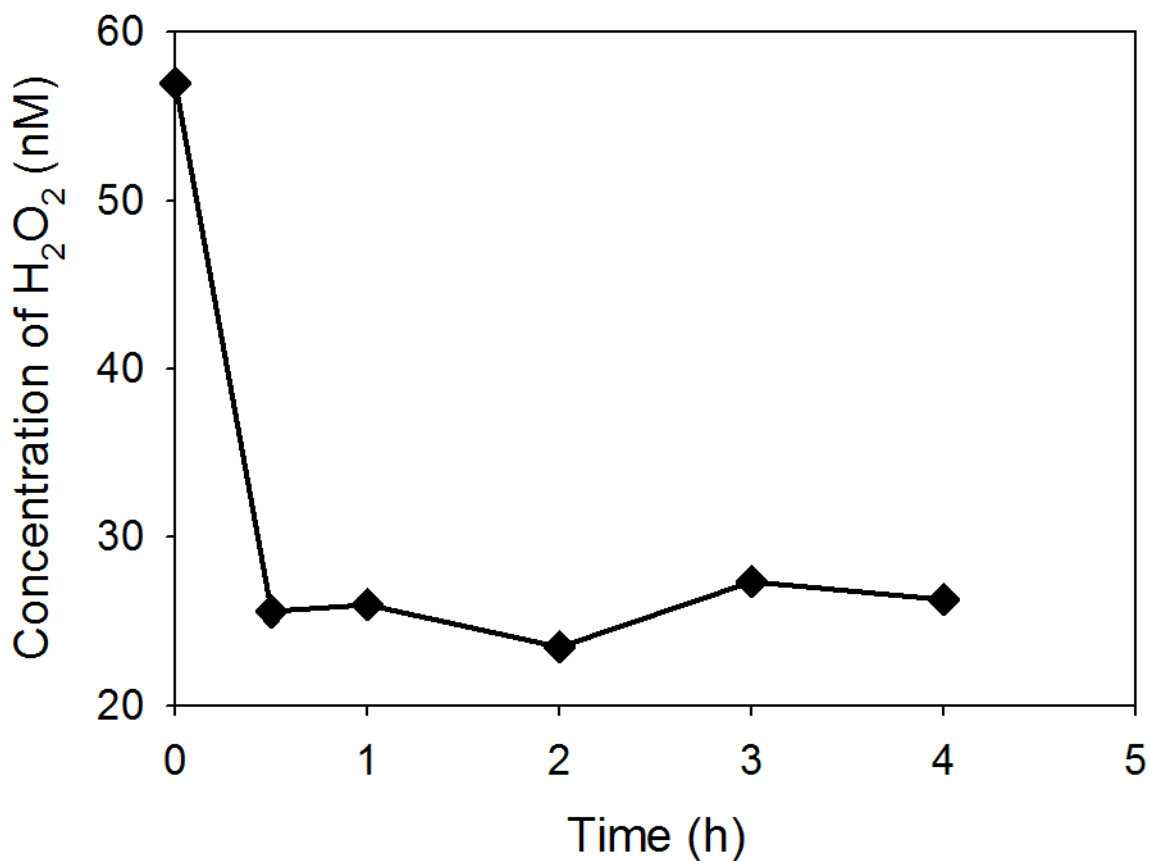
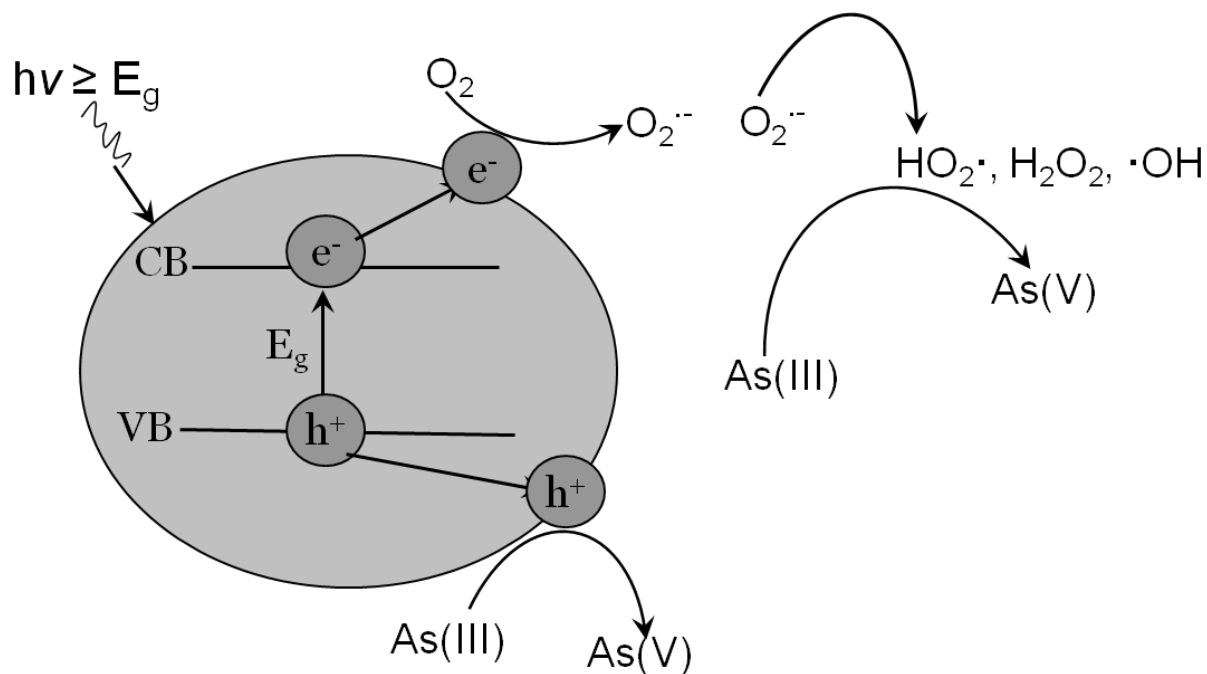


Figure 5.18. Concentration of H₂O₂ remained in solution when 200 nM H₂O₂ was exposed to Na-birnessite at pH 7.40 for 4 h.

5.5. Reaction Mechanism

Birnessite is a semiconductor, with a band gap of ~ 2.7 eV. When irradiated with photons of energy equal to or greater than the band gap energy (2.7 eV,), electrons (e^-) are excited from the valence band (VB) to the empty conduction band (CB), creating a hole (h^+) in the valence band. These h^+ and e^- can act as strong oxidizing and reducing

agents, respectively. Holes can presumably react with As(III) and oxidize it to As(V) and ROS can also oxidize solution phase As(III) (Scheme 5.1).



Scheme 5.1. Mechanism of As(III) oxidation by birnessite in presence of light.⁵⁸

O_2 present near and/or adsorbed on the surface of the birnessite reacts with the e^- resulting in the formation of ROS like HO_2^\cdot , H_2O_2 , and $\cdot OH$. The mechanism of formation of these radicals was shown in reactions 5.5 to 5.11. All these ROS are strong oxidizing agents, and has the ability to oxidize As(III).^{75, 76} At the same time H_2O_2 can also reduce Mn(IV) to Mn(II) (reaction 5.13).⁵¹ Finally the extra amount of As(III) oxidized by birnessite in presence of light can be contributed to the ROS, in addition to the holes in the VB. However, the contribution of these species to the As(III) oxidation is

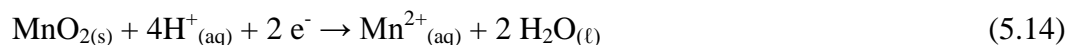
not investigated as catalase, the commonly used H_2O_2 scavenger⁷⁷ is not suitable to use in presence of light as it gets destroyed by light.⁷⁸

5.6. Summary

The results of our study showed that the oxidation of As(III) by Na-birnessite was photochemically enhanced in presence of dissolved O_2 at pH 5.00 and also at pH 7.40. In both the light and dark experiments maximum As(III) oxidation occurred at pH 5.00 compared to pH 7.40. There are several reasons for the increased As(III) oxidation with decreasing pH.

Change in pH results in change of surface charge and redox potential (E_h) of birnessite.⁵² Point of zero charge of birnessite is around pH 2.00, hence birnessite surface is negatively charged above pH 2.00 and positively charged below pH 2.00.⁵³ At pH 7.40 birnessite surface is negatively charged and lowering the pH reduces the negative charge of the surface and As(III), As(V) are negatively charged species at pH 7.40, hence As(III) oxidation decreases with increase in pH as As(III) oxidation by birnessite is surface mediated reaction. With increase in reaction time Mn^{2+} was formed during the reductive dissolution of birnessite, which has high affinity to the negatively charged birnessite surface at pH 7.40.²⁹ Hence with increasing the exposure time, Mn^{2+} competes with As(III) for the surface sites and adsorption of Mn^{2+} was favored at this pH, which lowers the As(III) oxidation by blocking some of the surface sites.^{29, 46}

Higher the red-ox potential of the $\text{MnO}_2/\text{Mn}^{2+}$ couple, greater is the oxidizing ability of MnO_2 . The overall redox reaction of $\text{MnO}_2/\text{Mn}^{2+}$ redox couple is shown by the following reaction,⁷⁹



Redox potential of this reaction at pH 5.00 and pH 7.40 are calculated by using the Nernst equation,⁸⁰

$$E_h = E_h^0 - 2.303 (mRT/nF) \text{ pH}$$

Where E_h is the redox potential of the reaction, E_h^0 is the standard redox potential of the reaction (1.23 V),^{69, 79} m and n are the number of protons (4H^+) and electrons (2e^-) involved in this redox couple. R is the ideal gas constant ($8.314 \text{ J} \cdot \text{mol}^{-1} \cdot \text{K}^{-1}$), T is the standard temperature in Kelvin (298 K), and F is the Faraday's constant ($0.96484 \text{ Coulombs} \cdot \text{mole}^{-1}$). The redox potential of this redox couple at pH 5.00 and pH 7.40 is + 0.64 and + 0.37 V respectively. Hence, the decrease in pH of the MnO_2 suspension increases the E_h of the suspension, which favor electron-transfer to the MnO_2 surface.⁵⁴ Hence As(III) oxidation increases with decrease in pH.

This investigation successfully investigated the utilization of visible light by birnessite for the As(III) remediation from drinking water at near neutral pH and also alkaline pH. This method can be used as an alternative to the currently available As(III) oxidation methods as it used natural sunlight. Also birnessite can be easily synthesized in

the laboratory on a large scale and it can be easily filtered after the As(III) photooxidation.

5.7. References

- (1) Burns, R. G.; Burns, V. M., *Philos. Trans. R. Soc. London, Ser. A: Mathematical, Physical and Engineering Sciences* **1977**, 286 (1336), 283-301.
- (2) Giovanoli, R.; Staehli, E.; Feitknecht, W., *Helv. Chim. Acta* **1970**, 53 (3), 453-464.
- (3) Golden, D. C.; Dixon, J. B.; Chen, C. C., *Clays Clay Miner.* **1986**, 34 (5), 511-520.
- (4) Stouff, P.; Boulegue, J., *Am. Mineral.* **1988**, 73 (9-10), 1162-1169.
- (5) Chukhrov, F. V.; Sakharov, B. A.; Gorshkov, A. I.; Drits, V. A.; Dikov, Y. P., *International Geology Review* **1985**, 27, 1082-1088.
- (6) Drits, V. A.; Lanson, B.; Bougerol-Chaillout, C.; Gorshkov, A. I.; Manceau, A., *Am. Mineral.* **2002**, 87 (11-12), 1646-1661.
- (7) Drits, V. A.; Silvester, E.; Gorshkov, A. I.; Manceau, A., *Am. Mineral.* **1997**, 82 (9-10), 946-961.
- (8) Holland, K. L.; Walker, J. R., *Clays Clay Miner.* **1996**, 44 (6), 744-748.
- (9) Silvester E., Manceau A. and Drits V. A. *Am. Mineral.* **1997**, 82, 962-978.
- (10) Lanson, B.; Drits, V. A.; Feng, Q.; Manceau, A., *Am. Mineral.* **2002**, 87 (11-12), 1662-1671.
- (11) Lanson, B.; Drits, V. A.; Silvester, E.; Manceau, A., *Am. Mineral.* **2000**, 85 (5-6), 826-838.
- (12) Manceau, A.; Lanson, B.; Drits, V. A., *Geochim. Cosmochim. Acta* **2002**, 66 (15), 2639-2663.
- (13) McKenzie, R. M., *Mineral. Mag.* **1971**, 38 (296), 493-502.

- (14) Yang, D. S.; Wang, M. K., *Chem. Mater.* **2001**, 13 (8), 2589-2594.
- (15) Yang, D. S.; Wang, M. K., *Clays Clay Miner.* **2002**, 50 (1), 63-69.
- (16) Cheney, M. A.; Bhowmik, P. K.; Moriuchi, S.; Villalobos, M.; Qian, S.; Joo, S. W., *J. Nanomater.* **2008**, No pp given.
- (17) Hansen, L. D.; Richter, B. E.; Rollins, D. K.; Lamb, J. D.; Eatough, D. J., *Anal. Chem.* **1979**, 51 (6), 633-637.
- (18) He, Y. T.; Hering, J. G., *Water, Air, Soil Pollut.* **2009**, 203 (1-4), 359-368.
- (19) Lafferty, B. J.; Ginder-Vogel, M.; Sparks, D. L., *Environ. Sci. Technol.* **2010**, 44 (22), 8460-8466.
- (20) Lafferty, B. J.; Ginder-Vogel, M.; Zhu, M.-Q.; Livi, K. J. T.; Sparks, D. L., *Environ. Sci. Technol.* **2010**, 44 (22), 8467-8472.
- (21) Manning, B. A.; Suarez, D. L., *Soil Sci. Soc. Am. J.* **2000**, 64 (1), 128-137.
- (22) Moore, J. N.; Walker, J. R.; Hayes, T. H., *Clays Clay Miner.* **1990**, 38 (5), 549-555.
- (23) Nesbitt, H. W.; Canning, G. W.; Bancroft, G. M., *Geochim. et Cosmochim. Acta* **1998**, 62 (12), 2097-2110.
- (24) Oscarson, D. W.; Huang, P. M.; Defosse, C.; Herbillon, A., *Nature* **1981**, 291 (5810), 50-51.
- (25) Oscarson, D. W.; Huang, P. M.; Hammer, U. T.; Liaw, W. K., *Water, Air, Soil Pollut.* **1983**, 20 (2), 233-244.
- (26) Oscarson, D. W.; Huang, P. M.; Liaw, W. K., *Clays Clay Miner.* **1981**, 29 (3), 219-225.

- (27) Oscarson, D. W.; Huang, P. M.; Liaw, W. K.; Hammer, U. T., *Soil Sci. Soc. Am. J.* **1983**, 47 (4), 644-648.
- (28) Parikh, S. J.; Lafferty, B. J.; Sparks, D. L., *J. Colloid Interface Sci.* **2008**, 320 (1), 177-185.
- (29) Power, L. E.; Arai, Y.; Sparks, D. L., *Environ. Sci. Technol.* **2005**, 39 (1), 181-187.
- (30) Scott, M. J.; Morgan, J. J., *Environ. Sci. Technol.* **1995**, 29 (8), 1898-1905.
- (31) Scott, M. J.; Morgan, J. J., *Environ. Sci. Technol.* **1996**, 30 (6), 1990-1996.
- (32) Zhao, W.; Cui, H.; Liu, F.; Tan, W.; Feng, X., *Clays Clay Miner.* **2009**, 57 (5), 513-520.
- (33) Zhao, W.; Feng, X.; Tan, W.; Liu, F.; Ding, S., *J. Environ. Sci. (Beijing, China)* **2009**, 21 (4), 520-526.
- (34) Silvester, E.; Manceau, A.; Drits, V. A., *Am. Mineral.* **1997**, 82 (9-10), 962-978.
- (35) Bhandari, N.; Reeder, R. J.; Strongin, D. R., *Environ. Sci. Technol.* **2011**, 45 (7), 2783-2789.
- (36) Chen, C. C.; Golden, D. C.; Dixon, J. B., *Clays Clay Miner.* **1986**, 34 (5), 565-571.
- (37) Golden, D. C.; Chen, C. C.; Dixon, J. B., *Clays Clay Miner.* **1987**, 35 (4), 271-280.
- (38) Post, J. E.; Heaney, P. J.; Hanson, J., *Powder Diffr.* **2002**, 17 (3), 218-221.
- (39) Post, J. E.; Veblen, D. R., *Am. Mineral.* **1990**, 75 (5-6), 477-489.
- (40) Lopano, C. L.; Heaney, P. J.; Post, J. E.; Hanson, J.; Komarneni, S., *Am. Mineral.* **2007**, 92 (2-3), 380-387.

- (41) Silvester, E.; Manceau, A.; Drits, V. A., *Am. Mineral.* **1997**, 82 (9-10), 962-978.
- (42) Prieto, O.; del Arco, M.; Rives, V., *Thermochim. Acta* **2003**, 401 (2), 95-109.
- (43) Prieto, O.; Del Arco, M.; Rives, V., *J. Mater. Sci.* **2003**, 38 (13), 2815-2824.
- (44) Cheney, M. A.; Bhowmik, P. K.; Qian, S.; Joo, S. W.; Hou, W.; Okoh, J. M., *J. Nanomater.* **2008**.
- (45) Tournassat, C.; Charlet, L.; Bosbach, D.; Manceau, A., *Environ. Sci. Technol.* **2002**, 36 (3), 493-500.
- (46) Manning, B. A.; Fendorf, S. E.; Bostick, B.; Suarez, D. L., *Environ. Sci. Technol.* **2002**, 36 (5), 976-981.
- (47) Stone, A. T.; Ulrich, H. J., *J. Colloid Interface Sci.* **1989**, 132 (2), 509-522.
- (48) Le Goff, P.; Baffier, N.; Bach, S.; Pereira-Ramos, J. P., *Mater. Res. Bull.* **1996**, 31 (1), 63-75.
- (49) Cohn, C. A.; Simon, S. R.; Schoonen, M. A. A., *Part Fibre Toxicol* **2008**, 5, 2.
- (50) Cohn, C. A.; Pedigo, C. E.; Hylton, S. N.; Simon, S. R.; Schoonen, M. A. A., *Geochem Trans* **2009**, 10, 8.
- (51) Waite, T. D.; Wrigley, I. C.; Szymczak, R., *Environ. Sci. Technol.* **1988**, 22 (7), 778-785.
- (52) Zhao, L.; Yu, Z.; Peng, P. a.; Huang, W.; Dong, Y., *Environ. Toxicol. Chem.* **2009**, 28 (6), 1120-1129.
- (53) Feng, X.-h.; Zu, Y.-q.; Tan, W.-f.; Liu, F., *J. Environ. Sci. (Beijing, China)* **2006**, 18 (2), 292-298.
- (54) Petrie, R. A.; Grossl, P. R.; Sims, R. C., *Environ. Sci. Technol.* **2002**, 36 (17), 3744-3748.

- (55) Takashima, T.; Hashimoto, K.; Nakamura, R., *J. Am. Chem. Soc.* **2012**, 134 (3), 1519-1527.
- (56) Drits, V. A.; Lanson, B.; and Gaillot, A. *Am. mineral.* **2007**, 92, 771-788.
- (57) Peral, J.; Casado, J.; Domenech, J., *J. Photochem. Photobiol. A: Chemistry.* **1988**, 44 (2), 209-217.
- (58) Bennett, W. S.; Keller, A. A., *Applied Catal. B. Environmental*, **2011**, 102, 600-607.
- (59) Liu, J.; Durand, J. P.; Espinal, L.; Garces, L.; Gomez, S.; Son, Y.; Villegas, J.; Suib, S. L., *Handbook of Layered Materials - Layered Manganese Oxides: Synthesis, Properties, and Applications*, **2004**, University of Connecticut Storrs, Connecticut, U.S.A.
- (60) Bhandari, N.; Reeder, R. J.; Strongin, D. R., *Environ. Sci. Technol.* **2012**, 46(15), 8044-8051.
- (61) Xiaohong, G.; Juanshan, D.; Xiaoguang, M.; Yuankui, S.; Bo, S.; Qinghai, H., *J. of Hazard. Mater.* **2012**, 215-216, 1-16.
- (62) Yoon, S.-H.; Oh, S.-E.; Yang, J. E.; Lee, J. H.; Lee, M.; Yu, S.; Pak, D. TiO₂ photocatalytic oxidation mechanism of As(III). *Environ. Sci. Technol.* **2009**, 43 (3), 864–869.
- (63) Ohtani, B., *Chem. Lett.* **2008**, 37 (3), 217–229.
- (64) Yoon, S.-H.; Lee, J. H., *Environ. Sci. Technol.* **2005**, 39 (24), 9695–9701.
- (65) Gratzel, M. *Nature*, **2001**, 414, 338.
- (66) Sherman D. M., *Geochim. Cosmochim. Acta*, **2005**, 69, 3249–3255.

- (67) Sakai N., Ebina Y., Takada K. and Sasaki T., *Phys. Chem. B.* **2005**, 109, 9651–9655.
- (68) Pinaud, B. A.; Chen, Z.; Abram, D. N.; Jaramillo, T. F., *J. Phys. Chem. C* **2011**, 115, (23), 11830-11838.
- (69) Kwon, K. D.; Refson, K.; Sposito, G., *Geochim. Cosmochim. Acta* **2009**, 73, (14), 4142-4150.
- (70) Xyla, A. G.; Sulzberger, B.; Luther, G. W., III; Hering, J. G.; Van Cappellen, P.; Stumm, W., *Langmuir* **1992**, 8, (1), 95-103.
- (71) Huerta-Diaz, M. A., *Bull. Environ. Contam. Toxicol.* **2006**, 77, (1), 60-66.
- (72) Jokic, A.; Frenkel, A. I.; Huang, P. M., *Can. J. Soil Sci.* **2001**, 81, (3, Spec. Issue), 277-283.
- (73) Yang, G.; Zhao, X.; Qi, J., *Ocean Univ. Qingdao (Engl. Ed.)* **2003**, 2, (1), 79-84.
- (74) Jomova, K.; Jenisova, Z.; Feszterova, M.; Baros, S.; Liska, J.; Hudecova, D.; Rhodes, C. J.; Valkoc, M., *J. Appl. Toxicol.* **2011**, 31, 95-107.
- (75) Dutta, P. K. ; Pehkonen, S. O.; Sharma, V. K.; Ray, A. K., *Environ. Sci. Technol.* **2005**, 39, 1827-1834.
- (76) Hug, S. J.; Leupin, O., *Environ. Sci. Technol.* **2003**, 37, 2734-2742.
- (77) Liu, W.; Andrews, S. A.; Stefan, M. I.; Bolton, J. R., *Water Research*, **2003**, 37, 3697–3703.
- (78) Shindo, Y.; Witt, E.; Han, D.; Packer, L. J., *Invest. Dermatol.* **1994**, 102(4):470-5.
- (79) www.hwscience.com/chemistry/honors/unit13/srp.pdf.
- (80) Mohammad-Shiri, H.; Ghaemi, M.; Riahi, S.; Akbari-Sehat, A., *Int. J. Electrochem. Sci.*, **2011**, 6, 317 – 336.

CHAPTER 6

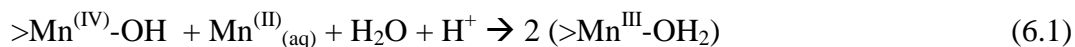
REDUCTIVE DISSOLUTION OF BIRNESSITE BY ARSENITE AT HIGH PH - XRD STUDY

6.1. Introduction

Birnessite, is a layered manganese oxide (δ MnO₂) mineral, composed of edge sharing MnO₆ octahedra, and the layers contain Mn(IV) and Mn(III) with vacant cation layer sites and cation sorption sites. Interlayer regions contain Mn(II), other metal cations (M⁺/M⁺²) and water.¹⁻⁴ It is well known that manganese oxides mainly birnessite acts as redox catalyst in the systems that sequesters and adsorbs a variety of organic and inorganic compounds [e.g., As(III), Pb(II), Se(VI)],⁵⁻²¹ due to the presence of vacant cation layer sites and cation sorption sites.²²⁻²⁵

The surface chemistry of arsenic on birnessite at pH 8.5 was studied using XPS and XRD, as there are controversies over the reductive dissolution of birnessite by arsenite at high pH (Under alkaline conditions) and the surface chemistry of arsenite (As(III)) on mineral phases within soils plays an important role in determining the environmental fate of arsenic. In the context of arsenite oxidation cation vacancies present in birnessite have been proposed to be important sites for the binding of Mn²⁺, which results from either the 2-electron reduction of Mn⁴⁺ or 1 electron reduction of Mn⁴⁺ to Mn³⁺ at octahedral sheet edge sites during the transformation of As(III) to As(V).⁷⁸ The buildup of Mn²⁺ on edge sites, which results after the saturation of vacancy

sites, and/or the comproportionation of Mn^{4+} and Mn^{2+} to Mn^{3+} are likely the reason for the experimental observation that the kinetics of As(III) oxidation decreases over time.⁸



It has been largely assumed that the reaction of arsenite primarily occurs at the edges of the octahedral sheets. This is reasonable considering that under-coordinated metal atoms that populate edge sites might be considered to more reactive than more highly coordinated sites on the basal plane. In the case of birnessite the negative charge at vacancy sites that facilitate the adsorption of cationic species might not be expected to accommodate the adsorption and reaction of arsenic bearing anions.

Recent experimental observations have suggested that the number of cation vacancies shows a positive correlation with the average oxidation state (AOS) of the birnessite.^{20, 21} A rationalization for this contention being that excess Mn^{3+} associated with lower AOS birnessite resides in the octahedral sheet structure, thus reducing the number of cation vacancies; sites that are presumed to be active in binding cation adsorbates. Mn^{2+} formed from the reduction of Mn(IV) during the As(III) oxidation to As(V) was generally observed in solution as $\text{Mn}^{2+}_{\text{(aq)}}$ at pH less than or equal to 6.⁷⁸ Above this pH $\text{Mn}^{2+}_{\text{(aq)}}$ was not observed in solution even though As(III) gets oxidized to As(V). This might be due to the high affinity of Mn^{2+} to the birnessite surface and also the adsorption capacity of Mn^{2+} on birnessite increases with pH and with cation vacancies.

The buildup of Mn^{2+} on edge sites, which results after the saturation of vacancy sites, and/or the con-proportionation of Mn^{2+} and structural Mn^{4+} to Mn^{3+} are likely the reason for the experimental observation that the kinetics of As(III) oxidation decreases over time. Surface reactivity and reductive dissolution of birnessite with As(III) is investigated and compared between two synthetic birnessite samples with different AOS. Formation of Mn^{2+} during the reductive dissolution of K-, Na-birnessite by arsenite at pH 8.5 and morphological changes resulted from the adsorption of Mn^{2+} onto these birnessite samples is studied with XRD.

The primary research objective of the current contribution is to investigate how the variability in AOS of birnessite can affect its surface reactivity with As(III). Toward this end, As(III) oxidation was investigated on a crystalline Na-birnessite and a relatively poorly crystalline K-birnessite surface at pH 8.5. Batch reaction data was obtained to compare the As(III) oxidation rate on the two samples. X-ray diffraction (XRD) and X-ray photoelectron spectroscopy (XPS) were used to characterize the long range order and the surface composition, respectively, of the two samples. We mention that prior research has generally investigated As(III) oxidation on birnessite at pH values of 7.00 or below.^{10, 18, 26} Some researchers mentioned the formation of Mn(II) arsenate precipitates, when no Mn(II) was observed in solution during the redox reaction at or above pH 5.00. Lafferty et al.,^{7, 8} mentioned the adsorption of Mn(II) on the surface of K-birnessite, during the As(III) oxidation. Our study builds upon the previous work by Lafferty et al.,^{7, 8} and investigates the adsorption of Mn(II) on the surface of Na-birnessite during As(III) oxidation at alkaline pH (pH 8.5).

6.2. Characterization of Synthetic K- and Na-birnessite

Synthesized K and Na-birnessite samples were characterized by using XRD, XPS, TEM, and AAS. Figure 6.1 exhibits XRD spectra of the K- and Na-birnessite used in this study and these XRD patterns are consistent with previously reported diffratograms for the K-birnessite.^{3, 10, 18, 20, 27-29} and triclinic (monoclinic) Na-birnessite^{3, 30-37} reported previously by several authors. Comparison of the two XRD patterns shows that the broadened Bragg reflections are associated with K-birnessite. An analysis of the full-width-half-maximum of the (001) and (002) reflections yield values of 2.52° and 1.49° for K-birnessite and 0.52° and 0.48° for Na-birnessite. A similar analysis was previously performed by Tournassat *et al.*,³⁸ for K-birnessite (synthesized by Moore *et al.*,^{10, 18} using the method of McKenzie³⁹) and a similar broadening was noted relative to, for example, well crystallized hexagonal (H) birnessite. Broadening of the Bragg reflections was attributed to poor crystallinity of the K-birnessite in the c^* direction. In particular, these prior researchers postulated that the K-birnessite exhibited hk bands characteristic of a turbo stratic stacking of the MnO_6 sheets in contrast to the hkl reflections exhibited by H-birnessite indicative of a hexagonal stacking of the MnO_6 sheets. Based on a similar comparison between our K-birnessite and Na-birnessite (exhibiting hkl reflections) diffratograms, we argue that our Na-birnessite shows an enhanced crystallinity, at least with regard to the stacking of the Mn layers, compared to the K-birnessite used in this study. BET surface area of K and Na-birnessite samples were experimentally determined to be 49.86 m² g⁻¹ and 23.10 m² g⁻¹ respectively.

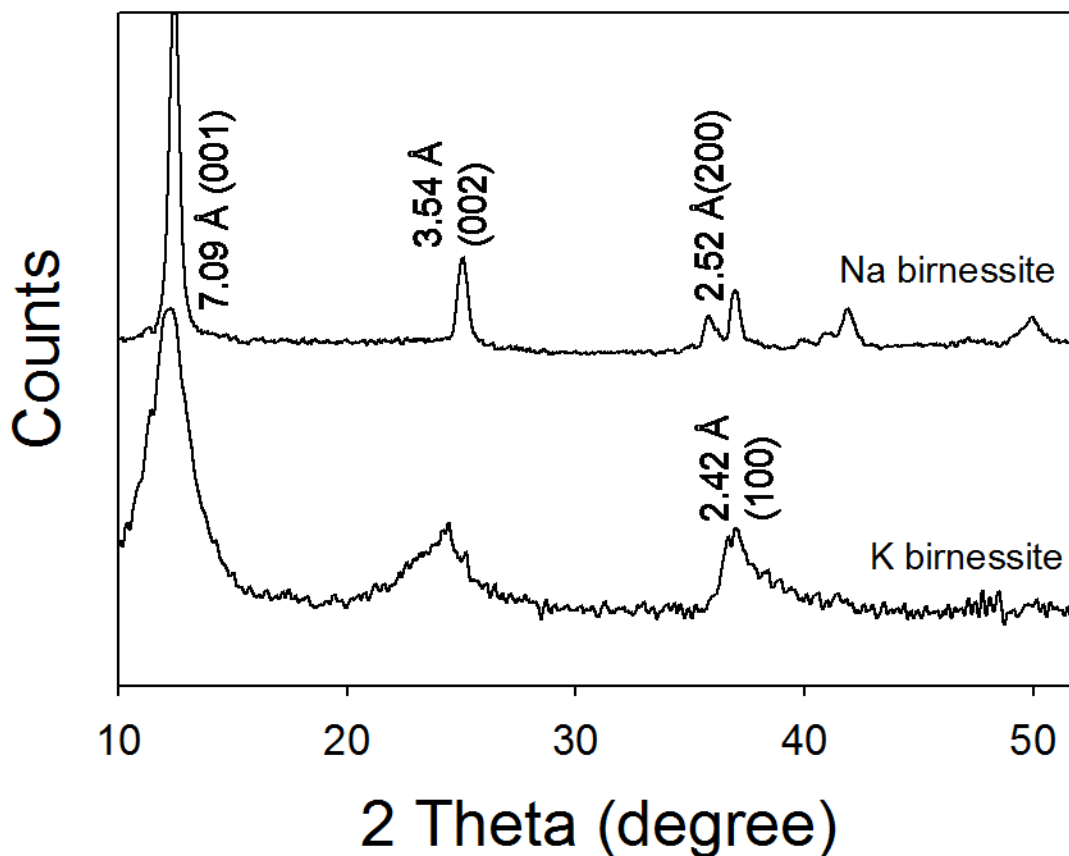


Figure 6.1. X-ray diffractograms of K- and Na-birnessite.

To quantify differences in the composition of the near surface region of each sample, Mn $2p_{3/2}$ data were obtained for both the Na- and K-birnessite samples and these data are shown in Figure 6.2. An analysis of the fitted peaks allows us to estimate the relative proportions of the different valence states of Mn ions (i.e., Mn(IV), Mn(III), and Mn(II)) in the near surface region of each birnessite sample and these results are listed in Table 6.1. The values are close to the relative proportion of the Mn ions (Mn(IV) ~70%, Mn(III) ~25% and Mn(II) ~5%) present in the near surface for a birnessite thin film

described in prior work that was characterized with high-resolution XPS by Nesbitt *et al.*^{26, 40} Interestingly, the XPS-derived relative proportions of Mn(IV), Mn(III), and Mn(II) in the near surface region for the less crystalline K-birnessite (Table 6.1) used in this study are significantly different than those determined for the more crystalline Na-birnessite.

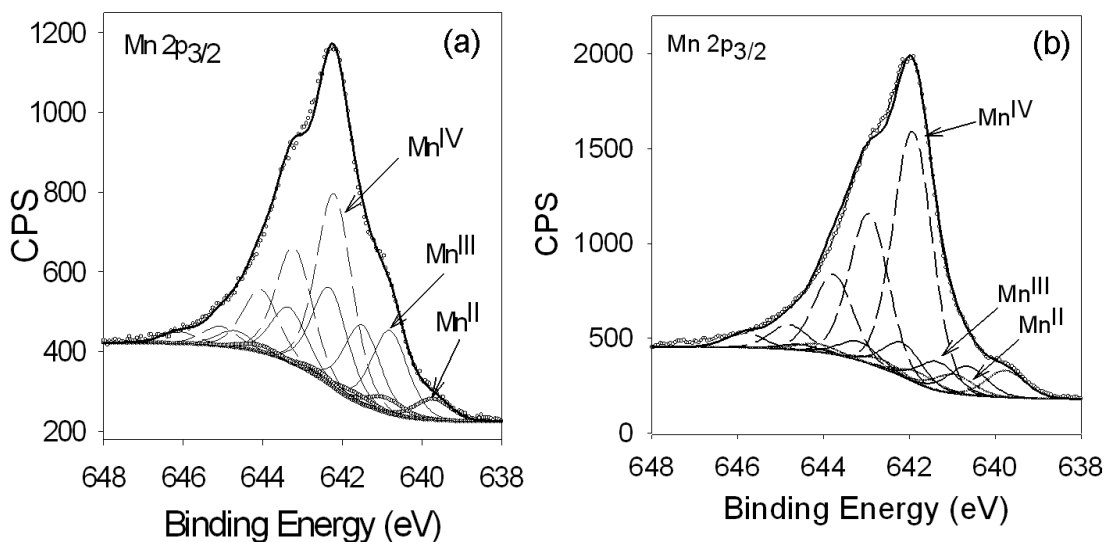


Figure 6.2. Mn $2p_{3/2}$ XPS spectra of (a) K-birnessite and (b) Na-birnessite.

The spectral contribution due to Mn(IV), Mn(III), and Mn(II) is indicated for each spectrum. The relative proportions of the different Mn oxidation state species are listed in Table 6.1. The spectral fitting parameters for the Mn $2p_{3/2}$ data are given in the experimental section. In particular, XPS analysis indicates the relative proportion of Mn(III) in the near surface region of K-birnessite is ~15% higher than the relative proportion of Mn(III) in the near surface region of Na-birnessite. While speculative, we

attribute this higher proportion of Mn(III) in the near surface region to the aggressive conditions in which K-birnessite is synthesized. Essentially, this XPS analysis suggests that the formation of K-birnessite via the relatively harsh synthetic protocol reacting HCl with boiling KMnO_4 results in at least a surface layer that is more reduced and disordered (supported by XRD) when compared to the more crystalline Na-birnessite. We mention at this point that XPS is only sensitive to the near surface region of the material (~ 5 nm) and we cannot then comment on the bulk composition of the material. TEM Morphologies of the K- and Na-birnessite particles (Figure 6.30) is similar to the previously reported K-^{39, 41, 42} and Na- birnessite^{3, 30} morphologies respectively. Average oxidation state of K- and Na-birnessite was 3.60 and 3.89 respectively. These values match with the average oxidation states of different birnessite samples reported in the literature.^{20, 21, 43, 44}

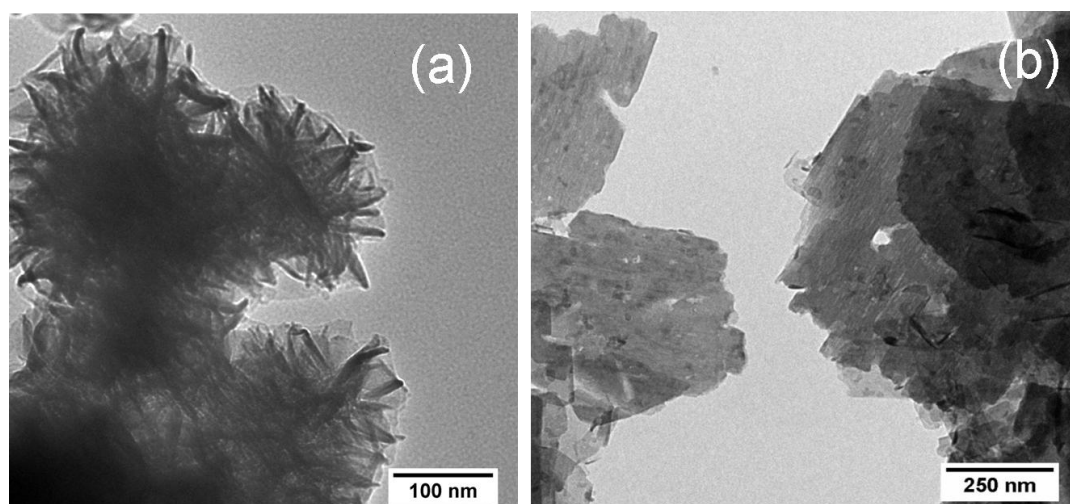


Figure 6.3. TEM micrographs of unreacted K- birnessite (a) and Na-birnessite (b)

6.3 Results and Discussion

6.3.1. Batch experiments.

Figure 6.4 illustrates the solution phase concentration of As(III) and As(V) as a function of exposure time of K and Na-birnessite to 200 μM As(III) at a constant solution pH of 8.5. Inspection of the data shows that for both samples there is a rapid decrease in the concentration of solution phase As(III) and a concomitant increase in the concentration of As(V) within the first 1 h of reaction. After this 1 h period the oxidation rate (slope of the curve at a given time) of As(III) significantly decreases. The amount of arsenic adsorption on the birnessite samples as a function of exposure time to As(III) is quantified in the inset to Figure 6.4. Both K- and Na-birnessite show the most rapid uptake of arsenic bearing species in the first 1 h of reaction, after which the uptake rate shows a decrease consistent with the decrease in As(III) oxidation rate after 1 h. Beyond 5 h of reaction time there is no noticeable uptake of arsenic or As(III) oxidation. In the presence of K-birnessite, 100 % of the As(III) reactant is consumed within 5 h, while in the presence of Na-birnessite 45 % of the As(III) in solution was oxidized in the same reaction time. Based on prior studies we attribute the decrease in the As(III) oxidation kinetics over the course of the reaction to the sorption of strongly bound As(V) product (and likely Mn^{2+} product) by K- and Na-birnessite, resulting in the blocking of redox active sites.^{7,8}

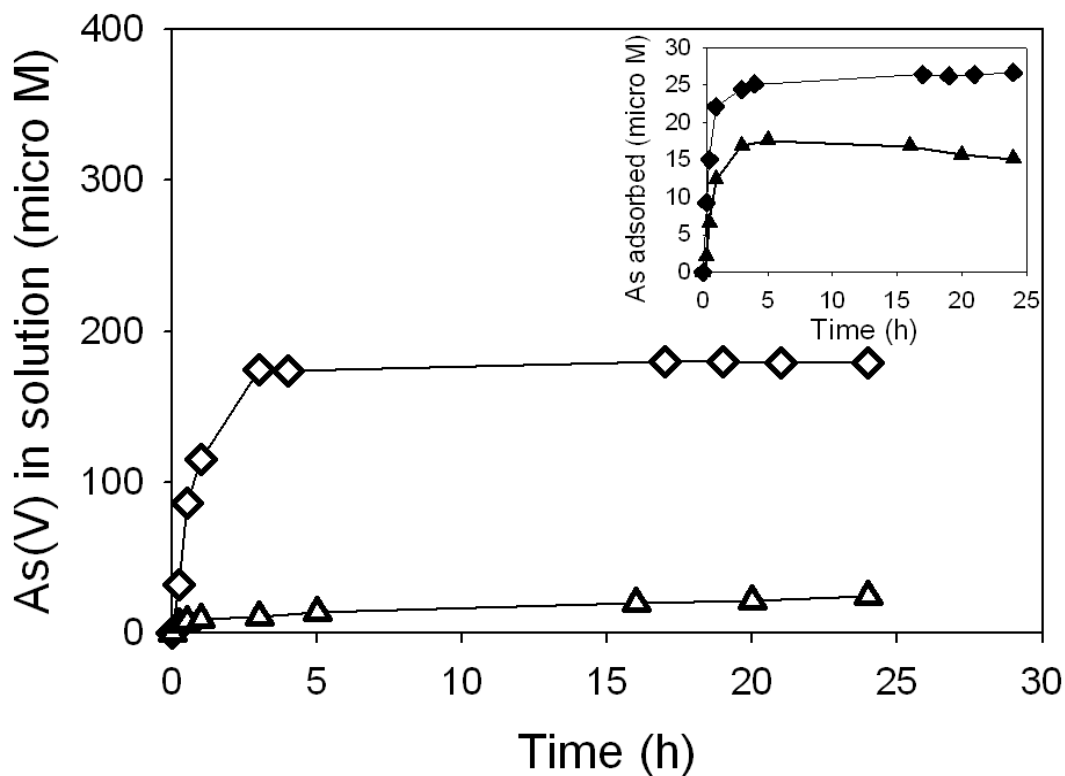


Figure 6.4. Results from batch experiments of As(III) oxidation by birnessite: Open diamonds and open triangles indicate the As(V) released into the solution during the oxidation of As(III) over a 24 h period at pH 8.5, in presence of K- and Na-birnessite respectively. Inset shows the amount of arsenic adsorbed on K- (solid diamonds) and Na- (solid triangles) birnessite during As(III) oxidation over a 24 h period.

Quantification of the data for the first hour of reaction yields a first order rate constant (k) for the depletion of As(III) to be 0.067 h^{-1} and 1.1768 h^{-1} , for Na- and K-birnessite, respectively. These values are relatively consistent with k values found in the literature for As(III) oxidation on different birnessite samples. Our calculated k for Na-birnessite, for example, is similar to the k (0.02 h^{-1}) that was associated with As(III) oxidation on well-crystallized hexagonal birnessite that was measured in the research of

Tournassat *et al.*,³⁸ at pH 5. Since k decreases with increase in pH, we suspect that higher k that we measure for As(III) oxidation on Na-birnessite at pH 8.5 is due to a lower degree of crystallinity in our Na-birnessite sample compared to the hexagonal birnessite used in the prior study. With regard to K-birnessite our experimentally measured k for As(III) oxidation is lower than the k of 1.98 h^{-1} measured by Scott and Morgan²⁸ for As(III) oxidation on a similarly prepared K-birnessite. However, the rate constant from this prior study was for pH 6.8. Our kinetic results as a whole suggest that the more disordered K-birnessite facilitates As(III) oxidation faster than does the more crystalline Na-birnessite.

Prior studies have shown that any partitioning of Mn(II) into solution resulting from As(III) oxidation at a $\text{pH} > 6$ is limited.^{18, 19, 45} Consistent with this prior work, we found no evidence for aqueous phase Mn(II) product during the oxidation of As(III) on Na-birnessite. However, we did measure $\sim 0.5 \mu\text{M}$ of aqueous Mn(II) in solution after 24 h of reaction in the K-birnessite circumstance, with the first measureable amounts of Mn(II) appearing in solution after 3 h of reaction. Mn(II) may adsorb on the birnessite surface and/or diffuse into the interlayers of birnessite.^{7, 8, 10, 18, 19, 45} Consistent with this, in our experiments $\sim 77 \mu\text{M}$ of interlayer K^+ is released into the solution during the exposure of K-birnessite to As(III) for 24 h. Mn(II) adsorption on cation vacancies on the basal plane of birnessite as well as on layer edge sites would also presumably be mechanisms that would inhibit the partitioning of Mn(II) to the solution phase. Prior research has also suggested that redox reactions may also be operative that would convert Mn(II) to Mn(III). Such a redox transformation may conceivably be involved with the experimentally observed phase transformation of birnessite that occurs during As(III)

oxidation or the phase transformation that occurs when the mineral is exposed directly to Mn(II).

6.3.2. Compositional Changes in K- and Na-birnessite During the Exposure to As(III)

XPS was used to quantify differences in the compositional changes in the near surface region of K- and Na-birnessite during the As(III) oxidation reaction. XPS Mn $2p_{3/2}$ data for K- and Na-birnessite that was exposed to As(III) (200 μ M, pH 8.5) solution for 15 min and 1 h are exhibited in Figure 6.5 and the relative proportions of Mn(IV), Mn(III), and Mn(II) derived from these data are presented in Table 6.1.

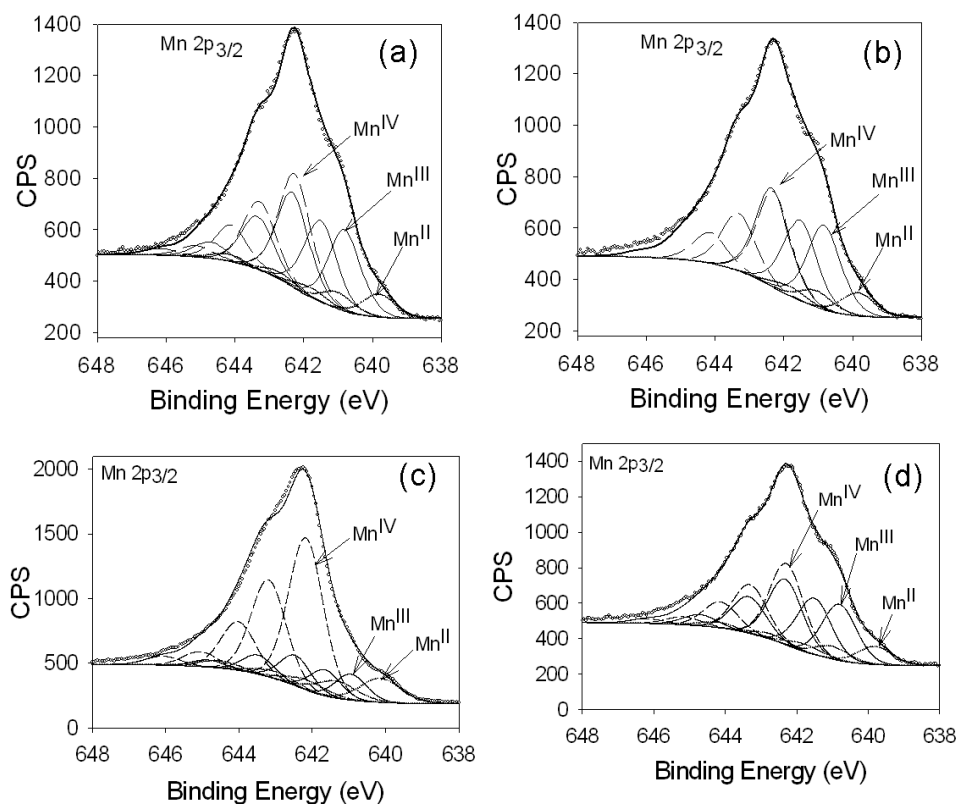


Figure 6.5. Mn $2p_{3/2}$ XPS spectra after K-birnessite is exposed to As(III) for (a) 15 min and (b) 1 h, and after Na-birnessite is exposed to As(III) for (c) 15 min and (d) 1 h

exposure to As(III) at pH 8.5. The spectral contribution due to Mn(IV), Mn(III), and Mn(II) is indicated for each spectrum. The relative proportions of the different Mn oxidation state species after the each As(III) exposure time is listed in Table 6.1.

Analysis of the fitted 15-minute As(III) exposure data shows that for both birnessite samples the relative concentration of Mn(IV) was reduced while the Mn(III) and Mn(II) concentrations increased in the near surface region, when compared to the unreacted samples. The K-birnessite shows the more dramatic change, since the relative proportion of Mn(IV) decreased from 68% to 36% during the 15-minute As(III) exposure at pH 8.5, while the relative proportion of Mn(III) increased from 38% to 52% and Mn(II) increased from 5.1% to 9.8 %. The Na-birnessite shows a decrease in Mn(IV) from 73 to 65%, and an increase in the relative proportion of Mn(III) from a pre-reaction value of 16% to a post-reaction value of 19% along with increase in Mn(II) from 10.32 % to 15.36 %.

The more rapid conversion of Mn(IV) to Mn(III) in the near surface region of K-birnessite is consistent with its faster initial oxidation kinetics over the first 15 min of reaction. The decrease in the relative proportion of Mn(IV) and the increase in relative proportions of Mn(III) and Mn(II) in the near surface region of these birnessite minerals indicates the reductive dissolution of these samples during the As(III) exposure and the retention of Mn(II) product on the surface. This result for Mn(II) supports the batch experimental data, where aqueous Mn(II) was not observed in solution. Analysis of K- and Na-birnessite that was exposed to As(III) for 1 h shows a further decrease in the relative proportion of Mn(IV) and an increase in the proportion of Mn(III).

Table 6.1. Relative proportions of various Mn oxidation states in the near surface region of K- and Na-birnessite before, after the reaction with As(III) for 15 min and 1 h at pH 8.5 obtained from Mn 2p_{3/2} XPS spectra analysis. Relative proportions of As(III), As(V) in the near surface region of K and Na-birnessite after reaction with As(III) for 15 min and 1 h at pH 8.5 obtained from As 3d XPS spectra analysis.

	K-birnessite	Na-birnessite
Before reaction (Unreacted)		
Mn(IV)	56.3 %	73.3 %
Mn(III)	38.6 %	16.4 %
Mn(II)	5.1 %	10.3 %
After 15 minutes of reaction		
Mn(IV)	37.9 %	64.94 %
Mn(III)	52.3 %	19.71 %
Mn(II)	9.8 %	15.36 %
As(V)	72.0 %	87.1 %
As(III)	28.0 %	12.9 %
After 1 h of reaction		
Mn(IV)	33.4 %	38.12 %
Mn(III)	56.3 %	50.89 %
Mn(II)	10.3 %	10.99 %
As(V)	79.4 %	87.0 %
As(III)	20.6 %	13.0 %

It was proposed in prior studies^{11, 27, 40} that the formation of a Mn^{III}OOH* phase and/or adsorption of As(III) or Mn(II) on the birnessite surface region is a likely outcome of this redox chemistry. Nesbitt et al.,¹¹ proposed a 2-step process for the reduction of birnessite by As(III) where there is a rapid reduction of Mn(IV) to Mn(III) (MnOOH*) and then a second slower step where MnOOH* is reduced further to form Mn(II) and As(V) product. Perhaps of note is the higher relative proportion of Mn(III) and lower proportion of Mn(IV) on the K-birnessite sample than on Na-birnessite, consistent with the increased amount of arsenite oxidation on the K-birnessite sample after 1 h of reaction. Increase in Mn(III) is higher than the Mn(II) in these reactions indicate that the higher proportion of Mn(III) on the surface is also due to the conproportionation of Mn(IV) and Mn(II) to Mn(III) indicated by the following reaction.⁴⁶

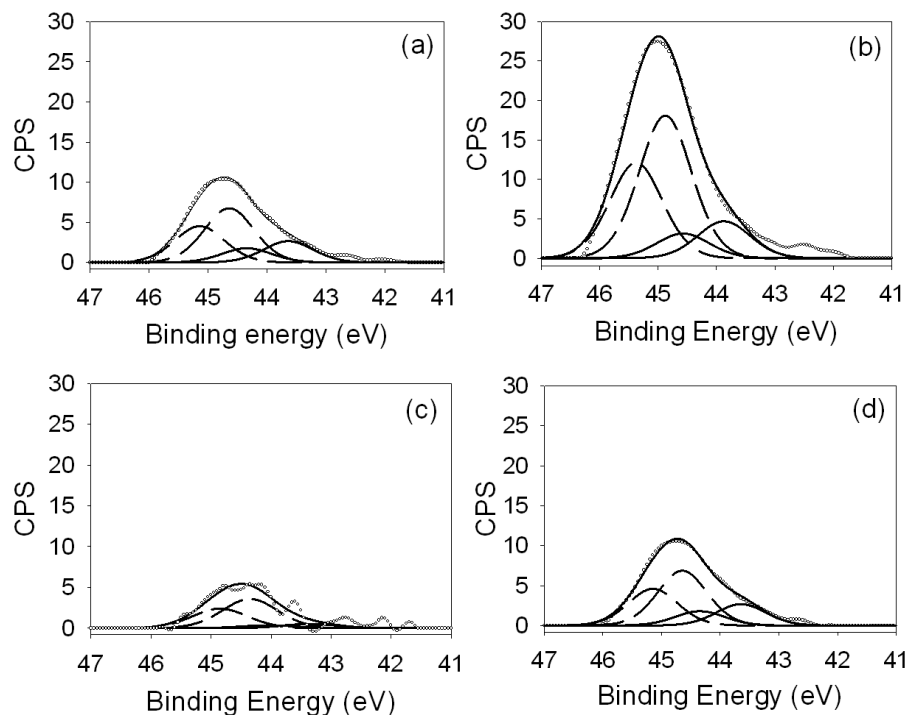


Figure 6.6. As 3d XPS spectra and associated fits after K-birnessite was exposed to As(III) for (a) 15 min and (b) 1 h, and after Na-birnessite was exposed to As(III) for (c) 15

min and (d)1 h at pH 8.5. The peak represented with solid lines and the dashed lines is related to As(III) and As(V) respectively. The spectral fitting parameters for the As 3d data is given in the experimental section.

Figure 6.6 displays As 3d XPS data associated with both birnessite samples after 15- minute and 1-h exposure to As(III). Quantification of this data (Table 6.1) shows that the predominate surface species are As(V) bearing complexes on both K- and Na-birnessite. A further analysis of the spectra by comparing the normalized As 3d signal shows that the amount of arsenic adsorbed on K-birnessite is 50% greater than the amount that is adsorbed on Na-birnessite after a 1 h exposure. This result that the coverage of As(V) is greatest on K-birnessite is shown below to be consistent with differences in morphological changes between the two birnessite samples resulting from As(III) oxidation.

6.3.3 Morphological and Structural Changes in K- and Na-birnessite During the Exposure to As(III)

Up to this point, it has been shown that the birnessite was reduced during the As(III) oxidation. To further investigate the structural changes on the birnessite samples during As(III) oxidation due to the adsorption of Mn^{2+} , released during the reductive dissolution of birnessite, XRD was carried out on samples before and after reaction at pH 8.5 for 24 h. XRD analysis of post reaction K-birnessite (Figure 6.7) showed a new diffraction feature at a d-spacing of 1.80 Å (indicated with the star in Figure 6.7) after reaction with As(III) for 24 h at pH 8.5. A similar experimental observation was made by

Lafferty et al.,⁸ after K-birnessite was reacted with As(III) at pH 7.2 and they attributed this to the sorption of Mn(II) on vacancy sites on the poorly crystalline K-birnessite.

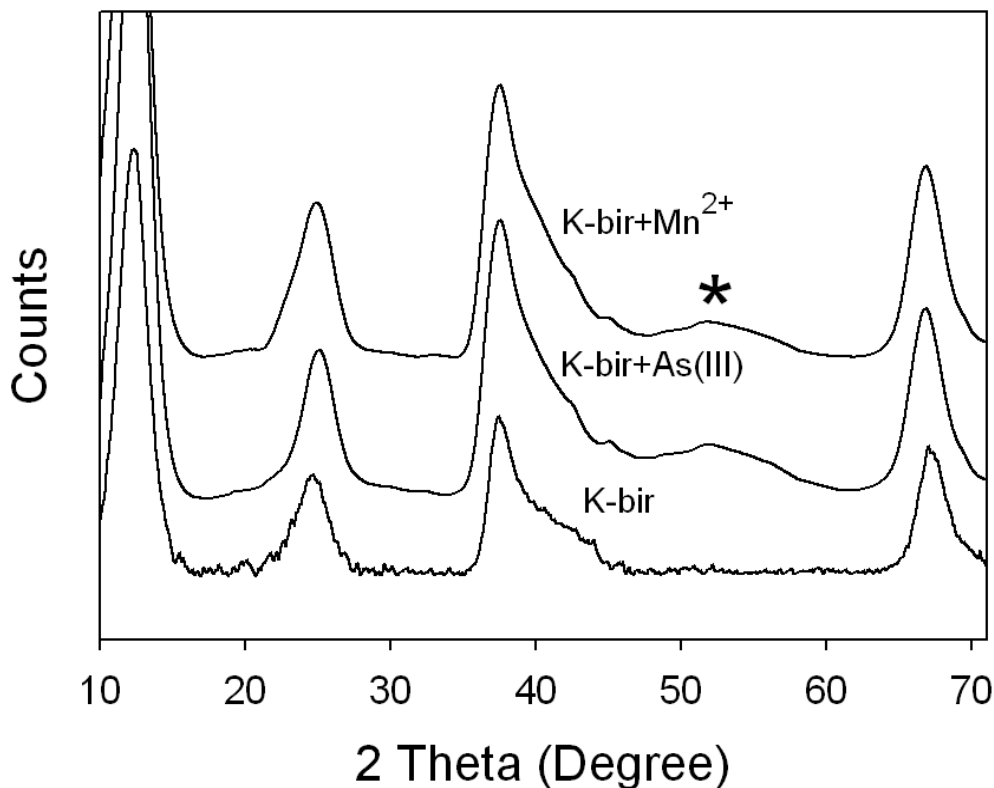


Figure 6.7. X-ray diffraction pattern of the unreacted K-birnessite (bottom), K-birnessite exposed to As(III) for 24 h at pH 8.5 (middle), K-birnessite exposed to Mn²⁺ for 24 h at pH 8.5 (top). The star at the d-spacing 1.82 Å represents the difference in XRD patterns of the unreacted and reacted samples.

Elzinga⁴⁷ in 2011 also proposed that the vacancy sites on hexagonal birnessite basal plane interacts with Mn(II) and promotes the interfacial electron transfer between adsorbed Mn(II) and structural Mn(IV), resulting in the structural transformation of the birnessite with time. To support this contention, and to further support the contention that the growth of this peak was due to the Mn²⁺ sorption, we exposed K-birnessite to 200

μM of Mn^{2+} for 24 h, and the resulting solid suspension was centrifuged, washed with pH 8.5 water, air dried, and analyzed with XRD. The resulting XRD pattern exhibited the same diffraction feature (associated with a d-spacing of 1.80 \AA , indicated with the star in Figure 6.7) that was present in the post As(III) oxidation reaction K-birnessite sample. However, in our experiments the concentration of As(III) used and the amount of Mn(II) expected to be formed during the As(III) oxidation was very low to induce the structural transformation of the birnessite. Based on this we conclude that the Mn^{2+} product became, at least in part adsorbed on cation vacancy sites of the K-birnessite and some of it was exchanged with interlayer K^+ ions, as $\sim 77 \mu\text{M}$ of interlayer K^+ was released into the solution during this reaction. Suppression of this etching over time may in part be due to the buildup of insoluble Mn^{2+} product on redox active sites.

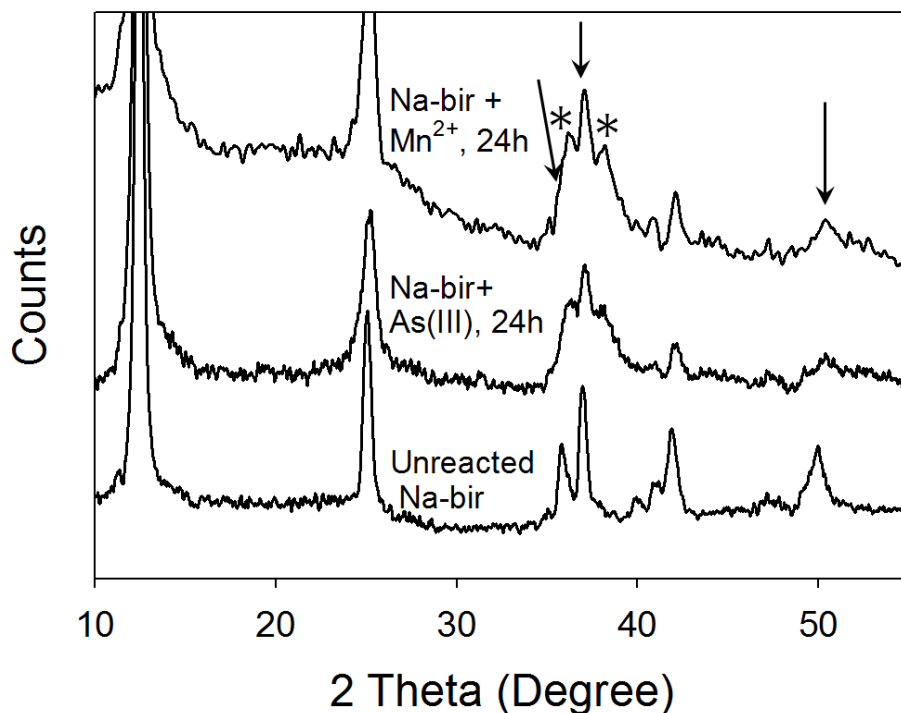


Figure 6.8. X-ray diffraction pattern of the unreacted Na-birnessite (bottom), Na-birnessite exposed to As(III) for 24 h at pH 8.5 (middle), Na-birnessite exposed to Mn^{2+}

for 24 h at pH 8.5 (top). The stars indicate the new diffraction peaks developed during the reaction.

XRD data for Na-birnessite after exposure to As(III) at pH 8.5 for 24 h also showed changes relative to Na-birnessite that had not been exposed to As(III) (Figure 6.8). Specifically, diffraction features at 2.52, 2.42, and 1.82 Å (indicated by arrows in figure 6.8) were reduced and new peaks were developed at 2Θ values of 36° (2.47 Å) and 38° (2.36 Å) (indicated by stars in figure 6.8) that we attribute to the formation of hexagonal birnessite.⁴⁸ We believe this change is due to Mn^{2+} product, based on the results of an experiment where we exposed Na-birnessite to 80 μM of Mn^{2+} solution for 24 h at pH 8.5 (see Figure 5.11 in chapter 5). The XRD associated with birnessite after the Mn^{2+} exposure exhibits the same diffraction 2Θ values of 36° (2.47 Å) and 38° (2.36 Å) indicating that it is the Mn^{2+} product formed during the reductive dissolution of the Na-birnessite by As(III). Similar to the K-birnessite some of the $\text{Mn}^{2+}_{(\text{aq})}$ might be exchanged with interlayer Na ions and part of the $\text{Mn}^{2+}_{(\text{aq})}$ undergoes conproportionation with surface $\text{Mn}^{(\text{IV})}\text{-OH}$ to form $\text{Mn}^{(\text{III})}$ according to the reaction (5.1). Prior research has experimentally observed a similar result when birnessite was directly exposed to Mn^{2+} (no arsenic present in the system) and it was hypothesized that the Mn^{2+} became incorporated into the interlayers of birnessite, leading to the transformation of monoclinic/triclinic birnessite into the hexagonal birnessite.⁴⁸

6.4. Summary and Conclusion

The primary goal of this study was to prove the reductive dissolution of the birnessite at alkaline pH and compare the rate of As(III) oxidation over two birnessite samples with different surface structures (under similar experimental conditions to shed light on the microscopic reasons for experimentally observed differences. The structural nature of this outermost layer, however, is uncertain except that XPS shows that it has a higher proportion of Mn(III) than the outermost surface of Na-birnessite. The new surface that is created through this particular dissolution process likely results in additional As(III) oxidation, consistent with our XPS results that shows that the surface coverage of As(V) is higher on K-birnessite than on Na-birnessite. Aside from morphological changes due to the reductive dissolution of the birnessite samples during As(III) oxidation, XRD results show that there are changes in the crystallinity of both samples that our experiments suggest is due to the interaction of Mn^{2+} product with the birnessite. The implication of these structural changes on As(III) oxidation are not known at this point, although the retention of Mn^{2+} on the surface likely leads at least in part to the suppression of further As(III) oxidation. Taken as a whole, the results presented in this contribution emphasize that the preparation and history of birnessite will undoubtedly affect its surface reactivity due in part to changes in the spatial location of redox active sites.

6.5. References

- (1) Burns, R. G.; Burns, V. M., *Philos. Trans. R. Soc. London, Ser. A: Mathematical, Physical and Engineering Sciences* **1977**, 286 (1336), 283-301.
- (2) Giovanoli, R.; Staehli, E.; Feitknecht, W., *Helv. Chim. Acta* **1970**, 53 (3), 453-464.
- (3) Golden, D. C.; Dixon, J. B.; Chen, C. C., *Clays Clay Miner.* **1986**, 34 (5), 511-520.
- (4) Stoff, P.; Boulegue, J., *Am. Mineral.* **1988**, 73 (9-10), 1162-1169.
- (5) Hansen, L. D.; Richter, B. E.; Rollins, D. K.; Lamb, J. D.; Eatough, D. J., *Anal. Chem.* **1979**, 51 (6), 633-637.
- (6) He, Y. T.; Hering, J. G., *Water, Air, Soil Pollut.* **2009**, 203 (1-4), 359-368.
- (7) Lafferty, B. J.; Ginder-Vogel, M.; Sparks, D. L., *Environ. Sci. Technol.* **2010**, 44 (22), 8460-8466.
- (8) Lafferty, B. J.; Ginder-Vogel, M.; Zhu, M.-Q.; Livi, K. J. T.; Sparks, D. L., *Environ. Sci. Technol.* **2010**, 44 (22), 8467-8472.
- (9) Manning, B. A.; Suarez, D. L., *Soil Sci. Soc. Am. J.* **2000**, 64 (1), 128-137.
- (10) Moore, J. N.; Walker, J. R.; Hayes, T. H., *Clays Clay Miner.* **1990**, 38 (5), 549-555.
- (11) Nesbitt, H. W.; Canning, G. W.; Bancroft, G. M., *Geochim. et Cosmochim. Acta* **1998**, 62 (12), 2097-2110.

- (12) Oscarson, D. W.; Huang, P. M.; Defosse, C.; Herbillon, A., *Nature* **1981**, 291 (5810), 50-51.
- (13) Oscarson, D. W.; Huang, P. M.; Hammer, U. T.; Liaw, W. K., *Water, Air, Soil Pollut.* **1983**, 20 (2), 233-244.
- (14) Oscarson, D. W.; Huang, P. M.; Liaw, W. K., *Clays Clay Miner.* **1981**, 29 (3), 219-225.
- (15) Oscarson, D. W.; Huang, P. M.; Liaw, W. K.; Hammer, U. T., *Soil Sci. Soc. Am. J.* **1983**, 47 (4), 644-648.
- (16) Parikh, S. J.; Lafferty, B. J.; Sparks, D. L., *J. Colloid Interface Sci.* **2008**, 320 (1), 177-185.
- (17) Power, L. E.; Arai, Y.; Sparks, D. L., *Environ. Sci. Technol.* **2005**, 39 (1), 181-187.
- (18) Scott, M. J.; Morgan, J. J., *Environ. Sci. Technol.* **1995**, 29 (8), 1898-1905.
- (19) Scott, M. J.; Morgan, J. J., *Environ. Sci. Technol.* **1996**, 30 (6), 1990-1996.
- (20) Zhao, W.; Cui, H.; Liu, F.; Tan, W.; Feng, X., *Clays Clay Miner.* **2009**, 57 (5), 513-520.
- (21) Zhao, W.; Feng, X.; Tan, W.; Liu, F.; Ding, S., *J. Environ. Sci. (Beijing, China)* **2009**, 21 (4), 520-526.
- (22) Chukhrov, F. V.; Sakharov, B. A.; Gorshkov, A. I.; Drits, V. A.; Dikov, Y. P., *International Geology Review* **1985**, 27, 1082-1088.
- (23) Drits, V. A.; Silvester, E.; Gorshkov, A. I.; Manceau, A., *Am. Mineral.* **1997**, 82 (9-10), 946-961.

- (24) Lanson, B.; Drits, V. A.; Silvester, E.; Manceau, A., *Am. Mineral.* **2000**, 85 (5-6), 826-838.
- (25) Silvester, E.; Manceau, A.; Drits, V. A., *Am. Mineral.* **1997**, 82 (9-10), 962-978.
- (26) Nesbitt, H. W.; Canning, G. W.; Bancroft, G. M., *Geochimica et Cosmochimica Acta* **1998**, 62 (12), 2097-2110.
- (27) Manning, B. A.; Fendorf, S. E.; Bostick, B.; Suarez, D. L., *Environ. Sci. Technol.* **2002**, 36 (5), 976-981.
- (28) Scott, M. J. In Kinetics of Adsorption and Redox Processes on Iron and Manganese Oxides: Reactions of As(III) and Se(IV) at Goethite and Birnessite Surfaces. California Institute of Technology, Pasadena, CA, 1991.
- (29) Holland, K. L.; Walker, J. R., *Clays Clay Miner.* **1996**, 44 (6), 744-748.
- (30) Yang, D. S.; Wang, M. K., *Chem. Mater.* **2001**, 13 (8), 2589-2594.
- (31) Yang, D. S.; Wang, M. K., *Clays Clay Miner.* **2002**, 50 (1), 63-69.
- (32) Chen, C. C.; Golden, D. C.; Dixon, J. B., *Clays Clay Miner.* **1986**, 34 (5), 565-571.
- (33) Drits, V. A.; Silvester, E.; Gorshkov, A. I.; Manceau, A., *Am. Mineral.* **1997**, 82 (9-10), 946-961.
- (34) Golden, D. C.; Chen, C. C.; Dixon, J. B., *Clays Clay Miner.* **1987**, 35 (4), 271-280.
- (35) Lopano, C. L.; Heaney, P. J.; Post, J. E.; Hanson, J.; Komarneni, S., *Am. Mineral.* **2007**, 92 (2-3), 380-387.
- (36) Post, J. E.; Veblen, D. R., *Am. Mineral.* **1990**, 75 (5-6), 477-489.
- (37) Silvester, E.; Manceau, A.; Drits, V. A., *Am. Mineral.* **1997**, 82 (9-10), 962-978.

- (38) Tournassat, C.; Charlet, L.; Bosbach, D.; Manceau, A., *Environ. Sci. Technol.* **2002**, 36 (3), 493-500.
- (39) McKenzie, R. M., *Mineral. Mag.* **1971**, 38 (296), 493-502.
- (40) Nesbitt, H. W.; Banerjee, D., *Am. Mineral.* **1998**, 83 (3-4), 305-315.
- (41) Cheney, M. A.; Bhowmik, P. K.; Moriuchi, S.; Villalobos, M.; Qian, S.; Joo, S. W., *J. Nanomater.* **2008**, No pp given.
- (42) Cheney, M. A.; Bhowmik, P. K.; Qian, S.; Joo, S. W.; Hou., W.; Okoh., J. M., *Journal of Nanomaterials* **2008**.
- (43) Feng, X. H.; Liu, F.; Tan, W. F.; Liu, X. W., *Clays and Clay Miner.* **2004**, 52 (2), 240-250.
- (44) Zhu, M.; Ginder-Vogel, M.; Parikh, S. J.; Feng, X.; Sparks, D. L., *Environ. Sci. Technol.* **2010**, 44 (12), 4465-4471.
- (45) Stone, A. T.; Ulrich, H. J., *J. Colloid Interface Sci.* **1989**, 132 (2), 509-522.
- (46) Takashima, T.; Hashimoto, K.; Nakamura, R., *J. Am. Chem. Soc.* **2012**, 134 (3), 1519-1527.
- (47) Elzinga, E. J., *Environ. Sci. Technol.* **2011**, 45 (15), 6366-6372.
- (48) Le Goff, P.; Baffier, N.; Bach, S.; Pereira-Ramos, J. P., *Mater. Res. Bull.* **1996**, 31 (1), 63-75.

CHAPTER 7

SUMMARY

Results presented in this dissertation successfully studied the remediation of the environmental pollutants like nitrite (NO_2^-), nitrate (NO_3^-), and arsenic using iron and manganese oxide minerals. NO_2^- and NO_3^- are contaminants in water, which cause adverse health effects in human mainly in infants and children. Pyrite was used in the reduction of NO_2^- and NO_3^- to ammonium. During the reduction of NO_2^- and NO_3^- to ammonium by pyrite NO_2^- and NO_3^- were adsorbed on the surface and different intermediates were observed. Surface intermediates were detected using the in-situ ATR-FTIR studies. Computational studies were conducted to assign the ATR-FTIR modes and also previously published literature was used for the assignment of ATR-FTIR modes. GC and UV-Vis Spectrophotometer (or Fluoremeter) was used to observe the gaseous and aqueous intermediates respectively.

Arsenic is also a contaminant in ground water in many parts of the world. Drinking and exposure of arsenic contaminated water causes severe neurological and skin disorders in humans. Ferrimagnetic ferrihydrite (Ferrifh) was effectively oxidized and adsorbed arsenic in presence of simulated solar light than in the absence of light. Arsenic photo-oxidation experiments by Ferrifh were conducted at pH 5.00, in the presence and absence of dissolved O_2 . Synthesized Ferrifh contains citrate on the surface and citrate was successfully removed by using the UV-Ozone cleaner at 45°C . Arsenic remediation experiments were carried out by using citrate bound (CB) and citrate free (CF) Ferrifh. CB- and CF-Ferrifh were shown to oxidize and adsorb arsenic in the presence and

absence of light, however, more amount of arsenic was oxidized in the presence of light. CB- Ferrifh was more active in the photo-remediation of arsenic compared to the CF- Ferrifh. Dissolved O₂ played an important role in the photo-oxidation of arsenic by CB- and CF- Ferrifh. Fe(II) formed from Fe(III) of Ferrifh during As(III) oxidation was reacted with dissolved O₂ and produced reactive oxygen species (ROS) like H₂O₂ and OH. These ROS are strong oxidizing agents and oxidize As(III) to As(V). While extra amount of As(III) oxidation in presence of CB- Ferrifh was due to the formation of additional ROS by Fe(II) formed due to reduction of Fe(III) by citrate.

Compared to the 2-line Fh, CF-Ferrifh was equally reactive in presence of dissolved O₂, while CB- Ferrifh was more reactive when compared to the 2-line Fh in presence of dissolved O₂ after the reactivities are normalized according to the surface area of the minerals. Unlike Ferrifh photo-oxidation of As(III) by 2-line Fh was independent of dissolved O₂. From these studies it was proved that Ferrifh can be successfully used in the remediation of arsenic from water.

Na-birnessite was also utilized for the oxidation of As(III) in presence of simulated solar light at pH 5.00 and 7.40. Similar to Ferrifh dissolved O₂ plays an important role in the photo-oxidation of As(III) by Na-birnessite. Unlike Ferrifh ROS formed in the presence of birnessite by light are due to the oxidation of dissolved O₂ by the photo-excited electrons in the conduction band of Na-birnessite. Mn(II) was released into the solution at pH 5.00, during the As(III) photo-oxidation. An additional amount of Mn(II) was produced during the As(III) photo-oxidation by Na-birnessite. There are three possibilities for the additional Mn(II) release into the aqueous phase. It can be due to the release of Mn(II) trapped in the interlayers of birnessite during the synthesis, or

Mn(II) was formed during the disproportionation of Mn(III)ads to Mn(IV) and Mn(II). The third possibility was the reduction of Mn(III) by H₂O₂ formed during the light irradiation.

Mn(II) was not observed in solution during the As(III) oxidation by birnessite at pH 7.4 both in the presence and absence of light. Previous studies by several authors showed that Mn(II) was not observed in solution during the As(III) oxidation by birnessite in dark above pH 6.00. To prove the reductive dissolution of Mn(III) by birnessite under alkaline conditions experiments were conducted with Na- and K-birnessite with As(III) at pH 8.5 in the absence of light. Birnessite samples were studied with XRD and XPS after reacting with As(III) at definite time intervals. With these techniques it was successfully showed the structural changes in birnessite by Mn(II). Hence the Mn(II) formed by the reductive dissolution of birnessite during the As(III) oxidation at pH 8.5 was either was not released into the aqueous phase or re adsorbed onto the birnessite after releasing into the aqueous phase. The photo-oxidation and/or adsorption of arsenic by ferrimagnetic ferrihydrite and birnessite are the effective and inexpensive methods for the removal of toxic As(III) from water.

BIBLIOGRAPHY

- Akpor, O. B.; Muchie, M., *Int. J. Phys. Sci.* **2010**, 5 (12), 1807-1817.
- Al-Abadleh, H. A.; Grassian, V. H., *Surf. Sci. Rep.* **2003**, 52 (3-4), 63-161.
- Alexandratos, V.G., Elzinga, E.J., Reeder, R.J., 2007. *Geochim. Cosmochim. Acta.* **2007**, 71, 4172–4187.
- Alloway, B.J.; Ayres, D.C., *Chemical principles of environmental pollution.* Blackie Academic & Professional, London, **1993**, 291 p.
- Amornthammarong, N.; Zhang, J.-Z., *Anal. Chem.* 2008, 80 (4), 1019-1026.
- Andrews, L.; Hassanzadeh, P.; Brabson, G. D.; Citra, A.; Neurock, M., *J. Phys. Chem.* **1996**, 100 (20), 8273-8279.
- Appelo, C. A. J.; Van Der Weiden, M. J. J.; Tournassat, C.; Charlet, L., *Environ. Sci. Technol.* **2002**, 36, 3096-3103.
- Applications, **2004**, *University of Connecticut Storrs, Connecticut, U.S.A.*
- Argonne National Laboratory, E., Human Health Fact Sheet. In August **2005**
- Aurelio, G., Fernandez-Martinez, A., Cuello, G.J., Roman-Ross, G., Alliot, I.,
- Bennett, W. S.; Keller, A. A., *Applied Catal. B. Environmental*, **2011**, 102, 600-607.
- Bhandari, N.; Reeder, R. J.; Strongin, D. R., *Environ. Sci. Technol.* **2011**, 45 (7), 2783-2789.
- Bhandari, N.; Reeder, R. J.; Strongin, D. R., *Environ. Sci. Technol.* **2012**, 46(15), 8044-8051.

- Bissen, M.; Vieillard-Baron, M. M.; Schindelin, A. J.; Frimmel, F. H., *Chemosphere* **2001**, 44 (4), 751-757.
- Blanchard, M., Alfredsson, M., Brodholt, J., Wright, K., Catlow, C.R.A., *Geochim. Cosmochim. Acta.* **2007**, 71, 624–630
- Borda, M. J.; Elsetinow, A. R.; Schoonen, M. A.; Strongin, D. R., *Astrobiology* **2001**, 1 (3), 283-288.
- Brandes, J. A.; Boctor, N. Z.; Cody, G. D.; Cooper, B. A.; Hazen, R. M.; Yoder, H. S., Jr., *Nature* **1998**, 395 (6700), 365-367.
- Braun .D.; Böhringer. B.; and Eidam. N., *Polymer Bulletin* 21, 1989, 63-68
- Brown, G. E. Jr.; Calas, G., *C. R. Geoscience.* **2011**, 343, 90–112.
- Brown, W. A.; King, D. A., *J. Phys. Chem. B* **2000**, 104 (12), 2578-2595.
- Brunauer. S.; Emmett, P. H.; and Teller, E.; *J. Am. Chem. Soc.* 1938, 60, 309-319
- Burns, R. G.; Burns, V. M., *Philos. Trans. R. Soc. London, Ser. A: Mathematical, Physical and Engineering Sciences* **1977**, 286 (1336), 283-301.
- Carabantea, I.; Grahna, M.; Holmgrena, A.; Kumpieneb, J.; Hedlunda, J., *Colloids and Surfaces A: Physicochem. Eng. Aspects*, **2009**, 346, 106–113.
- Charlet, L., *Chem. Geol.* **2010**, 270, 249–256.
- Chen, C. C.; Golden, D. C.; Dixon, J. B., *Clays Clay Miner.* **1986**, 34 (5), 565-571.
- Cheney, M. A.; Bhowmik, P. K.; Moriuchi, S.; Villalobos, M.; Qian, S.; Joo, S. W., *J. Nanomater.* **2008**,
- Cheney, M. A.; Bhowmik, P. K.; Qian, S.; Joo, S. W.; Hou., W.; Okoh., J. M., *J. Nanomater.* **2008**.

- Cherry, J. A.; Shaikh, A. U.; Tallman, D. E.; Nicholson, R. V., *J. Hydrol. (Amsterdam)* **1979**, 43 (1-4), 373-392.
- Choi, W. Y.; Termin, A.; Hoffmann, M. R., *J. Phys. Chem. B* **1994**, 98 (51), 13669-13679.
- Chukhrov, F. V.; Sakharov, B. A.; Gorshkov, A. I.; Drits, V. A.; Dikov, Y. P., *International Geology Review* **1985**, 27, 1082-1088.
- Cody, G. D., *Annu. Rev. Earth. Planet. Sci.* **2004**, 32, 569-599.
- Cohn, C. A.; Pedigo, C. E.; Hylton, S. N.; Simon, S. R.; Schoonen, M. A. A., *Geochem Trans* **2009**, 10, 8.
- Cohn, C. A.; Simon, S. R.; Schoonen, M. A. A., *Part Fibre Toxicol* **2008**, 5, 2.
- Corliss, J. B.; Baross, J. A.; Hoffman, S. E., *Oceanologica Acta* **1981**, Supplement, 59-69.
- Coumbs, D., *Int. J. Vibr. Spec.* **1998**, 2, 3-4.
- Cullen, W. R.; Crow, J. P.; Herring, F. G.; Sams, J. R.; Tapping, R. L., *Inorg. Chem.* **1971**, 10 (8), 1616-1623.
- Dinerman, C. E.; Ewing, G. E., *J. Chem. Phys.* **1970**, 53 (2), 626-631.
- Dixit, S.; Hering, J. G., *Chemical Geology* 228, **2006**, 6-15.
- Dixit, S.; Hering, J. G., *Environ. Sci. Technol.* **2003**, 37, 4182-4189.
- Dörr, M.; Kassbohrer, J.; Grunert, R.; Kreisel, G.; Brand, W. A.; Werner, R. A.; Geilmann, H.; Apfel, C.; Robl, C.; Weigand, W., *Angew. Chem. Int. Ed.* **2003**, 42 (13), 1540-1543.
- Drits, V. A.; Lanson, B.; and Gaillot, A. *Am. mineral.* **2007**, 92, 771-788.

Drits, V. A.; Lanson, B.; Bougerol-Chaillout, C.; Gorshkov, A. I.; Manceau, A., *Am. Mineral.* **2002**, 87 (11-12), 1646-1661.

Drits, V. A.; Sakharov, B. A.; Salyn, A. L.; Manceau, A., *Clay Miner.* **1993**, 28, (2), 185-207.

Drits, V. A.; Silvester, E.; Gorshkov, A. I.; Manceau, A., *Am. Mineral.* **1997**, 82 (9-10), 946-961.

Dumas, P.; Suhren, M.; Chabal, Y. J.; Hirschmugl, C. J.; Williams, G. P., *Surf. Sci.* **1997**, 371 (2/3), 200-212. Bhandari, N.; Reeder, R. J.; Strongin, D. R., *Environ. Sci. Technol.* **2012**, 46 (15), 8044-8051.

Dutta, P. K. ; Pehkonen, S. O.; Sharma, V. K.; Ray, A. K., *Environ. Sci. Technol.* **2005**, 39, 1827-1834.

Elzinga, E. J., *Environ. Sci. Technol.* **2011**, 45 (15), 6366-6372.

Enemark, J. H.; Feltham, R. D., *Coord. Chem. Rev.* **1974**, 13 (4), 339-406.

Feng, X. H.; Liu, F.; Tan, W. F.; Liu, X. W., *Clays and Clay Miner.* **2004**, 52 (2), 240-250.

Feng, X.-h.; Zu, Y.-q.; Tan, W.-f.; Liu, F., *J. Environ. Sci. (Beijing, China)* **2006**, 18 (2), 292-298.

Ferguson, M. A.; Hering, J. G., *Environ. Sci. Technol.* **2006**, 40 (13), 4261-4267.

Ferguson, M. A.; Hoffmann, M. R.; Hering, J. G., *Environ. Sci. Technol.* **2005**, 39 (6), 1880-1886.

Frisch, M. J.; Trucks, G. W.; Schlegel, H. B.; Scuseria, G. E.; Robb, M. A.; Cheeseman, J. R.; Montgomery, J. J. A.; Vreven, T. K.; Kudin, N.; Burant, J. C.; Millam, J. M.; Iyengar, S. S.; Tomasi, J.; Barone, V.; Mennucci, B.; Cossi, M.; Scalmani, G. R., N. ;

Petersson, G. A.; Nakatsuji, H.; Hada, M.; Ehara, M.; Toyota, K.; Fukuda, R.; Hasegawa, J.; Ishida, M.; Nakajima, T.; Honda, Y.; Kitao, O.; Nakai, H.; Klene, M.; Li, X.; Knox, J. E.; Hratchian, H. P.; Cross, J. B.; Bakken, V.; Adamo, C.; Jaramillo, J.; Gomperts, R.; Stratmann, R. E.; Yazyev, O.; Austin, A. J.; Cammi, R.; Pomelli, C.; Ochterski, J. W.; Ayala, P. Y.; Morokuma, K.; Voth, G. A.; Salvador, P.; Dannenberg, J. J.; Zakrzewski, V. G.; Dapprich, S.; Daniels, A. D.; Strain, M.; Farkas, C.; Malick, D. K.; Abuck, A. D.; Raghavachari, R.; Foresman, J. B.; Ortiz, J. V.; Cui, Q.; Baboul, A. G.; Clifford, S.; Cioslowski, J.; Stefanov, B. B.; Liu, G.; Liashenko, A.; Piskorz, P.; Komaromi, I.; Martin, R. L.; Fox, D. J.; Keith, T.; Al-Laham, M. A.; Peng, C. Y.; Nanayakkara, A.; Challacombe, M.; Gill, P. M. W.; Johnson, B.; Chen, W.; Wong, M. W.; Gonzalez, C.; and Pople, J. A. Gaussian 03, Revision E.01, Gaussian, Inc.,.

"FT-IR Spectroscopy—Attenuated Total Reflectance (ATR)". *Perkin Elmer Life and Analytical Sciences*. 2005.

Fuller, C. C.; Davis, J. A.; Wayshunas, G. A., *Geochim. Cosmochim. Acta*. **1992**, 57, 2271-2282.

(<http://toxnet.nlm.nih.gov/cgi-bin/sis/htmlgen?HSDB>). In The National Library of Medicine Hazardous Substances DataBank.

Gabor A. Somorjai, Y. L., *Introduction to surface chemistry and catalysis*. 2nd ed.; John Wiley & Sons, Inc.: Hoboken, Newjersey, **2010**.

Ginder-Vogel, M.; Landrot, G.; Fischel, J. S.; Sparks, D. L., *Proceed. National. Acad. Sci.* 2009, 106, (38), 16124-16128.

Giovanoli, R.; Staehli, E.; Feitknecht, W., *Helv. Chim. Acta* **1970**, 53 (3), 453-464.

Goldberg, S.; Johnston, C. T., *J. Colloid Interface Sci.* **2001**, 234 (1), 204-216.

Golden, D. C.; Chen, C. C.; Dixon, J. B., *Clays Clay Miner.* **1987**, 35 (4), 271-280.

Golden, D. C.; Dixon, J. B.; Chen, C. C., *Clays Clay Miner.* **1986**, 34 (5), 511-520.

Gonzalez-Davila, M.; Santana-Casiano, J. M.; Millero, F. J., *J. Sol. Chem.* **2006**, 35 (1), 95-111.

Goodman, A. L.; Miller, T. M.; Grassian, V. H., *J. Vac. Sci. Technol. A* **1998**, 16 (4), 2585-2590.

Gratzel, M. *Nature*, **2001**, 414, 338.

Greenwood, N. N.; Earnshaw, A., *Chemistry of the Elements (2nd Ed)*, 1997, Butterworth-Heinemann, ISBN 0080379419.

Guevremont, J. M.; Bebie, J.; Elsetinow, A. R.; Strongin, D. R.; Schoonen, M. A. A., *Environ. Sci. Technol.* **1998**, 32 (23), 3743-3748.

Gupta, R. P.; Sen, S. K., *Phys. Rev. B : Solid State* **1974**, 10 (1), 71-77.

Gupta, R. P.; Sen, S. K., *Phys. Rev. B : Solid State* **1975**, 12 (1), 15-19.

Hähner, G., *Chem. Soc. Rev.*, 2006, 35, 1244-1255

Hansen, L. D.; Richter, B. E.; Rollins, D. K.; Lamb, J. D.; Eatough, D. J., *Anal. Chem.* **1979**, 51 (6), 633-637.

Hao, J.; Murphy, R.; Lim, E.; Schoonen, M. A. A.; Strongin, D. R., *Geochim. Cosmochim. Acta* 2009, 73 (14), 4111-4123.

Harris, D.C., *Quantitative Chemical Analysis, 6th ed.*, W.H. Freeman and Company, New York, 1982.

Hazama-cho, Hachioji-shi, Tokyo 193-8533, Japan 1456 Three Bond Technical News 17
Issued March 20, 1987

He, Y. T.; Hering, J. G., *Water, Air, Soil Pollut.* **2009**, 203 (1-4), 359-368.

- Henderson, M. A., *Surf. Sci. Rep.* **2011**, 66 (6-7), 185-297.
- Hess, C.; Ozensoy, E.; Yi, C.-W.; Goodman, D. W., *J. Am. Chem. Soc.* **2006**, 128 (9), 2988-2994.
- Holland, K. L.; Walker, J. R., *Clays Clay Miner.* **1996**, 44 (6), 744-748.
- Holler, J. F.; Skoog, D. A.; Crouch, S. R. *Principles Of Instrumental Analysis*, 2006
http://www.bnl.gov/chemistry/programs/Surface_dynamics. In BNL.
http://www.unep.org/urban_environment
- Huerta-Diaz, M. A., *Bull. Environ. Contam. Toxicol.* **2006**, 77, (1), 60-66.
- Hug, S. J.; Leupin, O., *Environ. Sci. Technol.* **2003**, 37 (12), 2734-2742.
- Hug, S. J.; Leupin, O., *Environ. Sci. Technol.* **2003**, 37, 2734-2742
- Jambor, J. L.; Dutrizac, J. E., *Chem. Rev.* **1998**, 98, (7), 2549-2585.
- Jegadeesan, G.; Al-Abed, S. R.; Sundaram, V.; Choi, H.; Scheckel, K. G.; Dionysiou, D. D., *Water Res.* **2010**, 44 (3), 965-973.
- Jokic, A.; Frenkel, A. I.; Huang, P. M., *Can. J. Soil Sci.* **2001**, 81, (3, Spec. Issue), 277-283.
- Jomova, K.; Jenisova, Z.; Feszterova, M.; Baros, S.; Liska, J.; Hudecova, D.; Rhodes, C. J.; Valkoc, M., *J. Appl. Toxicol.* **2011**, 31, 95-107.
- Kampschreur, M. J.; Kleerebezem, R.; de, V. W. W. J. M.; van, L. M. C. M., *Water Res.* **2011**, 45 (18), 5945-5952.
- Kasting, J. F., *Science* **1993**, 259 (5097), 920-926.
- Kijima, N.; Yasuda, H.; Sato, T.; Yoshimura, Y., *J. Sol. State. Chem.* **2001**, 159 (1), 94-102.
- Kim, C. M.; Yi, C. W.; Goodman, D. W., *J. Phys. Chem. B* **2002**, 106 (28), 7065-7068.

Kormann, C.; Bahnemann, D. W.; Hoffmann, M. R., *Envir. Sci. Technol.* **1991**, 25 (3), 494-500.

Kormann, C.; Bahnemann, D. W.; Hoffmann, M. R., *Environ. Sci. Technol.* **1988**, 22 (7), 798-806.

Kwon, K. D.; Refson, K.; Sposito, G., *Geochim. Cosmochim. Acta* **2009**, 73, (14), 4142-4150.

L., *Chem. Geol.* **2006**, 233, 328–336.

Lafferty, B. J.; Ginder-Vogel, M.; Sparks, D. L., *Environ. Sci. Technol.* **2010**, 44 (22), 8460-8466.

Lafferty, B. J.; Ginder-Vogel, M.; Zhu, M.-Q.; Livi, K. J. T.; Sparks, D. L., *Environ. Sci. Technol.* **2010**, 44 (22), 8467-8472.

Lanson, B.; Drits, V. A.; Feng, Q.; Manceau, A., *Am. Mineral.* **2002**, 87 (11-12), 1662-1671.

Lanson, B.; Drits, V. A.; Silvester, E.; Manceau, A., *Am. Mineral.* **2000**, 85 (5-6), 826-838.

Le Goff, P.; Baffier, N.; Bach, S.; Pereira-Ramos, J. P., *Mater. Res. Bull.* **1996**, 31 (1), 63-75.

Leng, W. H.; Li, X.; Fei, H.; Zhang, J. Q.; Cao, C. N., *Environ. Sci. Technol.* **2011**, 45 (5), 2028-2029.

Ling, Y.; Mills, C.; Weber, R.; Yang, L.; Zhang, Y., *J. Am. Chem. Soc.* **2010**, 132 (5), 1583-1591.

Liu, J.; Durand, J. P.; Espinal, L.; Garces, L.; Gomez, S.; Son, Y.; Villegas, J.; Suib, S. L., *Handbook of Layered Materials - Layered Manganese Oxides: Synthesis, Properties, and*

Liu, W.; Andrews, S. A.; Stefan, M. I.; Bolton, J. R.; *Water Research*, **2003**, 37, 3697-3703

Lopano, C. L.; Heaney, P. J.; Post, J. E.; Hanson, J.; Komarneni, S., *Am. Mineral.* **2007**, 92 (2-3), 380-387.

Lopano, C. L.; Heaney, P. J.; Post, J. E.; Hanson, J.; Komarneni, S., *Am. Mineral.* **2007**, 92 (2-3), 380-387.

Maillot, F.; Morin, G.; Wang, Y.; Bonnin, D.; Ildefonse, P.; Chaneac, C.; Calas, G., *Geochim. Cosmochim. Acta* **2011**, 75, (10), 2708-2720.

Manceau, A., *Am. Mineral.* **2011**, 96, (4), 521-533.

Manceau, A., *Clay Miner.* **2009**, 44, (1), 19-34.

Manceau, A., PDF analysis of ferrihydrite and the violation of Pauling's Principia. *Clay Miner.* **2010**, 45, (2), 225-228.

Manceau, A.; Lanson, B.; Drits, V. A., *Geochim. Cosmochim. Acta* **2002**, 66 (15), 2639-2663.

Manning, B. A.; Fendorf, S. E.; Bostick, B.; Suarez, D. L., *Environ. Sci. Technol.* **2002**, 36 (5), 976-981.

Manning, B. A.; Suarez, D. L., *Soil Sci. Soc. Am. J.* **2000**, 64 (1), 128-137.

Markham, M. C.; Hannan, M. C.; Evans, S. W., *J. Am. Chem. Soc.* **1954**, 76, 820-823.

McKenzie, R. M., *Mineral. Mag.* **1971**, 38 (296), 493-502.

McLaren, A., *Transmission Electron Microscopy of Minerals and Rocks*. 2nd ed.; Cambridge university Press: 1991

Michel, F. M.; Barron, V.; Torrent, J.; Morales Maria, P.; Serna Carlos, J.; Boily, J.-F.; Liu, Q.; Ambrosini, A.; Cismasu, A. C.; Brown Gordon, E., Jr., *Proc. Natl. Acad. Sci. U S A* **2010**, 107 (7), 2787-2792.

Michel, F. M.; Barron, V.; Torrent, J.; Morales Maria, P.; Serna Carlos, J.; Boily, J.-F.; Liu, Q.; Ambrosini, A.; Cismasu, A. C.; Brown Gordon, E., Jr., *Proc. Natl. Acad. Sci. U S A* 2010, 107 (7), 2787-2792.

Michel, F. M.; Ehm, L.; Antao Sytle, M.; Lee Peter, L.; Chupas Peter, J.; Liu, G.; Strongin Daniel, R.; Schoonen Martin, A. A.; Phillips Brian, L.; Parise John, B., *Science* **2007**, 316, (5832), 1726-9.

Milosevic, M. Internal Reflectance near Critical Angle, in *Internal Reflection and ATR Spectroscopy*, John Wiley & Sons, Inc., Hoboken, NJ, USA. (2012)
doi: 10.1002/9781118309742.ch9

Mirabella, F. M. Jr., *Practical Spectroscopy Series; Internal reflection spectroscopy: Theory and applications*, Marcel Dekker, Inc.; Marcel Dekker, Inc., 1993, 17-52

Mohammad-Shiri, H.; Ghaemi, M.; Riahi, S.; Akbari-Sehat, A., *Int. J. Electrochem. Sci.*, **2011**, 6, 317 - 336

Mohan, D.; Pittman, C. U., *J. Hazard. Mater.* **2007**, 142 (1-2), 1-53.

Monllor-Satoca, D.; Tachikawa, T.; Majima, T.; Choi, W., *Environ. Sci. Technol.* **2011**, 45 (5), 2030-2031.

Moore, J. N.; Walker, J. R.; Hayes, T. H., *Clays Clay Miner.* **1990**, 38 (5), 549-555.

Moore, J. N.; Walker, J. R.; Hayes, T. H., *Clays Clay Miner.* **1990**, 38 (5), 549-555.

mstaetter, K.; Borch, T.; Larese-Casanova, P.; Kappler, A., *Environ. Sci. Technol.* **2010**, *44*, 102–108.

Navarro-Gonzalez, R.; McKay, C. P.; Mvondo, D. N., *Nature* **2001**, 412 (6842), 61-64.

Nesbitt, H. W.; Banerjee, D., *Am. Mineral.* **1998**, 83 (3-4), 305-315.

Nesbitt, H. W.; Banerjee, D., *Am. Mineral.* **1998**, 83 (3-4), 305-315.

Nesbitt, H. W.; Canning, G. W.; Bancroft, G. M., *Geochim. Cosmochim. Acta* **1998**, 62 (12), 2097-2110.

Nesbitt, H. W.; Canning, G. W.; Bancroft, G. M., *Geochim. et Cosmochim. Acta* **1998**, 62 (12), 2097-2110. Becke, A. D., *Phys. Rev. A* **1988**, 38 (6), 3098-3100.

Nesbitt, H. W.; Canning, G. W.; Bancroft, G. M., *Geochimica et Cosmochimica Acta* **1998**, 62 (12), 2097-2110.

Ohtani, B., *Chem. Lett.* **2008**, 37 (3), 217–229.

Ona-Nguema, G.; Morin, G.; Wang, Y. H.; Foster, A. L.; Juillot, F.; Calas, G.; Brown, G. E., *Environ. Sci. Technol.* **2010**, 44 (14), 5416-5422.

Ona-Nguema, G.; Morin, G.; Juillot, F.; Calas, G.; Brown, G. Jr., *Environ. Sci. Technol.* **2005**, 39, 9147-9155

Oscarson, D. W.; Huang, P. M.; Defosse, C.; Herbillon, A., *Nature* **1981**, 291 (5810), 50-51.

Oscarson, D. W.; Huang, P. M.; Hammer, U. T.; Liaw, W. K., *Water, Air, Soil Pollut.* **1983**, 20 (2), 233-244.

Oscarson, D. W.; Huang, P. M.; Liaw, W. K., *Clays Clay Miner.* **1981**, 29 (3), 219-225.

Oscarson, D. W.; Huang, P. M.; Liaw, W. K.; Hammer, U. T., *Soil Sci. Soc. Am. J.* **1983**, 47 (4), 644-648.

Parikh, S. J.; Lafferty, B. J.; Sparks, D. L., *J. Colloid Interface Sci.* **2008**, 320 (1), 177-185.

Peral, J.; Casado, J.; Domenech, J., *J. Photochem. Photobiol. A: Chemistry.* **1988**, 44 (2), 209-217.

Perdew, J.P., *Phys. Rev. B, Cond. Matter* **1986**, 33 (12), 8822-8824.

Petrie, R. A.; Grossl, P. R.; Sims, R. C., *Environ. Sci. Technol.* **2002**, 36 (17), 3744-3748.

Pinaud, B. A.; Chen, Z.; Abram, D. N.; Jaramillo, T. F., *J. Phys. Chem. C* **2011**, 115, (23), 11830-11838.

Post, J. E.; Heaney, P. J.; Hanson, J., *Powder Diffr.* **2002**, 17 (3), 218-221.

Post, J. E.; Veblen, D. R., *Am. Mineral.* **1990**, 75 (5-6), 477-489. He, Y. T.; Hering, J. G., *Water, Air, Soil Pollut.* **2009**, 203 (1-4), 359-368.

Post, J. E.; Veblen, D. R., *Am. Mineral.* **1990**, 75 (5-6), 477-489.

Power, L. E.; Arai, Y.; Sparks, D. L., *Environ. Sci. Technol.* **2005**, 39 (1), 181-187.

Power, L. E.; Arai, Y.; Sparks, D. L., *Environ. Sci. Technol.* **2005**, 39 (1), 181-187.

Prieto, O.; Del Arco, M.; Rives, V., *J. Mater. Sci.* **2003**, 38 (13), 2815-2824.

Prieto, O.; Del Arco, M.; Rives, V., *J. Mater. Sci.* 2003, 38 (13), 2815-2824.

Prieto, O.; del Arco, M.; Rives, V., *Thermochim. Acta* **2003**, 401 (2), 95-109.

Prieto, O.; del Arco, M.; Rives, V., *Thermochim. Acta* 2003, 401 (2), 95-109.

Rancourt, D. G.; Meunier, J. F., *Am. Mineral.* **2008**, 93, (8-9), 1412-1417.

Reeder, R.J., Lamble, G.M., Lee, J.F., Staudt, W.J. *Geochim. Cosmochim. Acta.* **1994**, 58, 5639-5646.

Reeder, R.J., Lamble, G.M., Northrup, P.A., *Am. Mineral.* **1999**, 84, 1049-1060.

Rieder, M.; Crelling, J. C.; Sustai, O.; Drabek, M.; Weiss, Z.; Klementova, M., *Int. J. Coal. Geol.* **2007**, 71 (2-3), 115-121.

Roman-Ross, G., Cuello, G.J., Turrillas, X., Fernandez-Martinez, A., Charlet, Rubasinghege, G. R. S., "Chemical and photochemical reactions on mineral oxide surfaces in gaseous and liquid phases: environmental implications of fate, transport and climatic impacts of mineral dust aerosol." *doctoral dissertation*, University of Iowa, **2011**

Russell, M. J.; Hall, A. J., *J. Geol. Soc.* **1997**, 154 (3), 377-402.

Sakai N., Ebina Y., Takada K. and Sasaki T., *Phys. Chem. B.* **2005**, 109, 9651–9655.

Samouilov, A.; Kuppusamy, P.; Zweier, J. L., *Arch. Biochem. Biophys.* **1998**, 357 (1), 1-7.

Santana-Casiano, J. M.; Gonzalez-Davila, M.; Millero, F. J., *Environ. Sci. Technol.* **2005**, 39 (7), 2073-2079

Savage, K.S., Tingle, T.N., O'Day, P.A., Waychunas, G.A., Bird, D.K., *Appl. Geochem.* **2000**, 15, 1219–1244.

Schaefer, A.; Huber, C.; Ahlrichs, R., *J. Chem. Phys.* **1994**, 100 (8), 5829-5835.

Schoonen, M. A. A., *Geol. Soc. Am. Special Papers* **2004**, 379, 117–134.

Schoonen, M. A. A.; Smirnov, A.; Cohn, C., *Ambio* **2004**, 33 (8), 539-551.

Schoonen, M. A. A.; Xu, Y., *Astrobiology* **2001**, 1 (2), 133-142.

Scott, M. J. In *Kinetics of Adsorption and Redox Processes on Iron and Manganese Oxides: Reactions of As(III) and Se(IV) at Goethite and Birnessite Surfaces*. California Institute of Technology, Pasadena, CA, 1991.

- Scott, M. J. In *Kinetics of Adsorption and Redox Processes on Iron and Manganese Oxides: Reactions of As(III) and Se(IV) at Goethite and Birnessite Surfaces*. California Institute of Technology, Pasadena, CA, **1991**.
- Scott, M. J.; Morgan, J. J., *Environ. Sci. Technol.* **1995**, 29 (8), 1898-1905.
- Scott, M. J.; Morgan, J. J., *Environ. Sci. Technol.* **1995**, 29 (8), 1898-1905.
- Scott, M. J.; Morgan, J. J., *Environ. Sci. Technol.* **1996**, 30 (6), 1990-1996.
- Scott, M. J.; Morgan, J. J., *Environ. Sci. Technol.* **1996**, 30 (6), 1990-1996.
- Sharma, V. K.; Dutta, P. K.; Ray, A. K., *J. Environ. Sci. Health, Part A: Toxic/Hazard. Subst. Environ. Eng.* **2007**, 42 (7), 997-1004.
- Sherman D. M., *Geochim. Cosmochim. Acta*, **2005**, 69, 3249–3255.
- Shindo, Y.; Witt, E.; Han, D.; Packer, L. J., *Invest. Dermatol.* **1994**, 102(4):470-5.
- Silvester E., Manceau A. and Drits V. A. *Am. Mineral.* **1997**, 82, 962–978.
- Silvester, E.; Manceau, A.; Drits, V. A., *Am. Mineral.* **1997**, 82 (9-10), 962-978.
- Silvester, E.; Manceau, A.; Drits, V. A., *Am. Mineral.* **1997**, 82 (9-10), 962-978.
- Silvester, E.; Manceau, A.; Drits, V. A., *Am. Mineral.* **1997**, 82 (9-10), 962-978.
- Silvester, E.; Manceau, A.; Drits, V. A., *Am. Mineral.* **1997**, 82 (9-10), 962-978.
- Skoog. D. A.; West. D. M.; James Holler. F., *Analytical Chemistry: An Introduction (Saunders Golden Sunburst Series)* 7th Ed., 1999.
- Smedley, P. L.; Kinniburgh, D. G., *Appl. Geochem.* **2002**, 17 (5), 517-568.
- Smirnov, A.; Hausner, D.; Laffers, R.; Strongin, D. R.; Schoonen, M. A. A., *Geochem. Trans.* **2008**, 9, 5.
- Somorjai, G. A.; Li, Y., *Proc. Natl. Acad. Sci. U. S. A., Early Ed.* **2010**, 1-8.
- Stone, A. T.; Ulrich, H. J., *J. Colloid Interface Sci.* **1989**, 132 (2), 509-522.

- Stone, A. T.; Ulrich, H. J., *J. Colloid Interface Sci.* **1989**, 132 (2), 509-522.
- Stone, A. T.; Ulrich, H. J., *J. Colloid Interface Sci.* **1989**, 132 (2), 509-522.
- Stookey, L. L., *Anal. Chem.* 1970, 42 (7), 779-781.
- Stouff, P.; Boulegue, J., *Am. Mineral.* **1988**, 73 (9-10), 1162-1169.
- Stouff, P.; Boulegue, J., *Am. Mineral.* **1988**, 73 (9-10), 1162-1169.
- Summers, D. P., *Origin. Life. Evol. Biosph.* **1999**, 29 (1), 33-46.
- Summers, D. P., *Origin. Life. Evol. Biosph.* **1999**, 29 (1), 33-46.
- Summers, D. P., *Origin. Life. Evol. Biosph.* **2005**, 35 (4), 299-312.
- Summers, D. P.; Basa, R. C. B.; Khare, B.; Rodoni, D., *Astrobiology* **2012**, 12 (2), 107-114.
- Summers, D. P.; Chang, S., *Nature* **1993**, 365, 630-633.
- Summers, D. P.; Khare, B., *Astrobiology* **2007**, 7 (2), 333-341.
- Suryanarayana, C.; Grant Norton M., *X -Ray Diffraction: A Practical Approach*, Springer, Jun 30, 1998, 1-292.
- Takashima, T.; Hashimoto, K.; Nakamura, R., *J. Am. Chem. Soc.* **2012**, 134 (3), 1519-1527.
- Takashima, T.; Hashimoto, K.; Nakamura, R., *J. Am. Chem. Soc.* **2012**, 134 (3), 1519-1527.
- Tang, Y.Z., Elzinga, E.J., Lee, Y.J., Reeder, R.J., *Geochim. Cosmochim. Acta*, **2007**, 71, 1480–1493.
- Taylor, S. R., McLennan, S.M., , *Planetary Crusts: Their composition, Origin and Evolution*. . Cambridge University Press: Cambridge, UK, 2009.

- Taylor, S. R., *Solar system evolution : a new perspective*. Cambridge University Press: Cambridge, UK, 2001; p 460.
- Tournassat, C.; Charlet, L.; Bosbach, D.; Manceau, A., *Environ. Sci. Technol.* **2002**, 36 (3), 493-500.
- Tournassat, C.; Charlet, L.; Bosbach, D.; Manceau, A., *Environ. Sci. Technol.* **2002**, 36 (3), 493-500.
- Usher, C. R.; Cleveland, C. A., Jr.; Strongin, D. R.; Schoonen, M. A. A., *Environ. Sci. Technol.* **2004**, 38 (21), 5604-5606.
- Usher, C. R.; Paul, K. W.; Narayansamy, J.; Kubicki, J. D.; Sparks, D. L.; Schoonen, M. A. A.; Strongin, D. R., *Environ. Sci. Technol.* **2005**, 39 (19), 7576-7584.
- Vig. J. R., *IEEE Transactions on Parts, Hybrids, and Packaging*, Vol. Php-12, NO. 4, 1976
- Voegelin, A.; Hug, S. J., *Environ. Sci. Technol.* **2003**, 37 (5), 972-978.
- Voegelin, A.; Hug, S. J., *Environ. Sci. Technol.* **2003**, 37 (5), 972-978.
- Wächtershäuser, G., *Microbiol. Rev.* **1988**, 52 (4), 452-484.
- Wächtershäuser, G., *Microbiol. Rev.* **1988**, 52 (4), 452-484.
- Wächtershäuser, G., *Origin. Life. Evol. Biosph.* **1990**, 20 (2), 173-176.
- Wächtershäuser, G., *Proc. Natl. Acad. Sci. U. S. A* **1990**, 87 (1), 200-204.
- Wächtershäuser, G., *Prog. Biophys. Mol. Biol.* **1992**, 58 (2), 85-201.
- Wächtershäuser, G., *Syst. Appl. Microbiol.* **1988**, 10 (3), 207-210.
- Wächtershäuser, G., *Syst. Appl. Microbiol.* **1988**, 10 (3), 207-210.
- Waite, T. D.; Wrigley, I. C.; Szymczak, R., *Environ. Sci. Technol.* **1988**, 22 (7), 778-785.
- Walker, J. C. G.; Brimblecombe, P., *Precambrian. Res.* **1985**, 28 (3-4), 205-222.

- Walker, J. C. G.; Brimblecombe, P., *Precambrian. Res.* **1985**, 28 (3-4), 205-222.
- Wander, M. C. F.; Kubicki, J. D.; Schoonen, M. A. A., *Origin. Life. Evol. Biosph.* **2008**, 38 (3), 195-209.
- Wander, M. C. F.; Schoonen, M. A. A., *Origin. Life. Evol. Biosph.* **2008**, 38 (2), 127-137.
- Weiss. T.; Joachim. W., (2005). *Handbook of Ion Chromatography*. Weinheim: Wiley-VCH. ISBN 3-527-28701-9
- Welch, A. H.; Lico, M. S., *Appl. Geochem.* **1998**, 13 (4), 521-539.
- www.hwscience.com/chemistry/honors/unit13/srp.pdf.
- Xiaohong, G.; Juanshan, D.; Xiaoguang, M.; Yuankui, S.; Bo, S.; Qinghai, H., *J. of Hazard. Mater.* **2012**, 215-216, 1-16.
- Xu, T.; Cai, Y.; O'Shea, K. E., *Environ. Sci. Technol.* **2007**, 41 (15), 5471-5477.
- Xu, Z.; Meng, X., *J. Hazard. Mater.* **2009**, 168 (2-3), 747-752.
- Xyla, A. G.; Sulzberger, B.; Luther, G. W., III; Hering, J. G.; Van Cappellen, P.; Stumm, W., *Langmuir* **1992**, 8, (1), 95-103.
- Yang, D. S.; Wang, M. K., *Chem. Mater.* **2001**, 13 (8), 2589-2594.
- Yang, D. S.; Wang, M. K., *Chem. Mater.* **2001**, 13 (8), 2589-2594.
- Yang, D. S.; Wang, M. K., *Clays Clay Miner.* **2002**, 50 (1), 63-69.
- Yang, D. S.; Wang, M. K., *Clays Clay Miner.* **2002**, 50 (1), 63-69.
- Yang, D. S.; Wang, M. K., *Clays Clay Miner.* 2002, 50 (1), 63-69.
- Yang, G.; Zhao, X.; Qi, J., *Ocean Univ. Qingdao (Engl. Ed.)* **2003**, 2, (1), 79-84.
- Yoon, S.-H.; Lee, J. H., *Environ. Sci. Technol.* **2005**, 39 (24), 9695-9701.
- Yoon, S.-H.; Lee, J. H., *Environ. Sci. Technol.* **2005**, 39 (24), 9695-9701.
- Yoon, S.-H.; Lee, J. H.; Oh, S.; Yang, J. E., *Water Res.* **2008**, 42 (13), 3455-3463.

- Yoon, S.-H.; Oh, S.-E.; Yang, J. E.; Lee, J. H.; Lee, M.; Yu, S.; Pak, D. TiO₂ photocatalytic oxidation mechanism of As(III). *Environ. Sci. Technol.* **2009**, 43 (3), 864–869.
- Yoshinobu, J.; Kawai, M., *Chem. Lett.* **1995**, (7), 605-606.
- Zaera, F., *Surf. Sci.* **2011**, 605 (13-14), 1141-1145.
- Zhao, L.; Yu, Z.; Peng, P. a.; Huang, W.; Dong, Y., *Environ. Toxicol. Chem.* **2009**, 28 (6), 1120-1129.
- Zhao, W.; Cui, H.; Liu, F.; Tan, W.; Feng, X., *Clays Clay Miner.* **2009**, 57 (5), 513-520.
- Zhao, W.; Cui, H.; Liu, F.; Tan, W.; Feng, X., *Clays Clay Miner.* **2009**, 57 (5), 513-520.
- Zhao, W.; Cui, H.; Liu, F.; Tan, W.; Feng, X., *Clays Clay Miner.* **2009**, 57 (5), 513-520.
- Zhao, W.; Feng, X.; Tan, W.; Liu, F.; Ding, S., *J. Environ. Sci. (Beijing, China)* **2009**, 21 (4), 520-526.
- Zhao, W.; Feng, X.; Tan, W.; Liu, F.; Ding, S., *J. Environ. Sci. (Beijing, China)* **2009**, 21 (4), 520-526.
- Zhao, W.; Feng, X.; Tan, W.; Liu, F.; Ding, S., *J. Environ. Sci. (Beijing, China)* **2009**, 21 (4), 520-526.
- Zhu, M.; Ginder-Vogel, M.; Parikh, S. J.; Feng, X.; Sparks, D. L., *Environ. Sci. Technol.* **2010**, 44 (12), 4465-4471.
- Zohner, A.; Broda, E., *Orig. Life.* **1979**, 9 (4), 291-298.
- Zohner, A.; Broda, E., *Orig. Life.* **1979**, 9 (4), 291-298.